STELLAR POPULATIONS IN THE MAGELLANIC CLOUDS

A THESIS

SUBMITTED FOR THE DEGREE OF

DOCTOR OF PHILOSOPHY

IN

THE FACULTY OF SCIENCE

CALICUT UNIVERSITY

BY

SMITHA SUBRAMANIAN

INDIAN INSTITUTE OF ASTROPHYSICS
BANGALORE - 560 034, INDIA

AUGUST 2011

DECLARATION

I hereby declare that the matter contained in the thesis entitled **"Stellar Populations in the Magellanic Clouds"** is the result of investigations carried out by me at the Indian Institute of Astrophysics under the supervision of Dr. Annapurni Subramaniam. This thesis has not been submitted for the award of any degree, diploma, associateship, fellowship etc. of any University or Institute.

Smitha Subramanian
(Candidate)

Indian Institute of Astrophysics
Bangalore-560034, India

CERTIFICATE

This is to certify that the matter contained in the thesis entitled "**Stellar Populations in the Magellanic Clouds**" submitted to Calicut University by **Ms. Smitha Subramanian** for the award of the degree of Doctor of Philosophy in the Faculty of Science, is based on the results of investigations carried out by her under my supervision and guidance, at the Indian Institute of Astrophysics. This thesis has not been submitted for the award of any degree, diploma, associateship, fellowship etc. of any University or Institute.

Dr.Annapurni Subramaniam
(Supervisor)

Indian Institute of Astrophysics
Bangalore-560034, India

ACKNOWLEDGEMENTS

First and foremost, I would like to express my sincere thanks to my thesis supervisor, Dr. Annapurni Subramaniam for her guidance. Her immense support, trust and above all, her willingness to provide me full freedom in research enabled me to enjoy the work all throughout the thesis. She made it possible for me to take care of my personal side requirements without having any impact on the work. It would not have been possible to complete the thesis the way it happened unless it was you. The support you gave me cannot be covered with these few statements. Thank you for being an excellent supervisor.

I thank Dr. C.S. Stalin for spending his valuable time to sincerely read a few chapters of the thesis. His comments were valuable. I take this opportunity to thank all the instructors who taught me the fundamentals of astrophysics during course work. I am thankful to Prof. T.P Prabhu for his advice which helped me a lot to choose the research topic.

I thank the Director, Indian Institute of Astrophysics, for providing me all the facilities required for the research work. I thank Prof. S. K. Saha and the members of the Board of Graduate Studies (BGS), IIA for the extended support they have provided me during the five years.

I am grateful to the Council of Scientific and Industrial Research (CSIR), Government of India for providing the financial support for my 5 years of research through the grant, 09/890(0002)/2007-EMR-I.

I thank IIA library staff for providing all the assistance required in making the books and journals available for reference. I thank the Administrative Officer, and the administrative staff of IIA, for their constant help and support. In particular, I would wish to thank Mr. Narasimha Raju, for his help and support in the administrative procedures related to CSIR funding.

I sincerely thank all the faculty members of the Physics Department, Calicut University for their guidance and encouragement during my M.Sc period. I especially thank Prof. B.R.S.Babu, Prof. M.M Musthafa and Prof. K.M. Varier of the Physics Department, Calicut University for their support related to the Phd registration. I thank the administrative staff of the department and the College Development Council (CDC) for all the help

they provided.

Thanks to Ramya.P, Drishya, Vigeesh, Bharat, Koshy, Uday, Sinduja, Hema, Rumpa, Anant, Madhu, Sreeja, Arya, Veena, Mr. Paul and all other students in IIA for their support. Many thanks to Indu for being a wonderful junior as well as a good friend. I enjoyed our discussions on the Magellanic Clouds and related topics. I thank all my seniors, especially Blesson, and Nagaraju. Special thanks to Bhavya and Ramya.S for being there for me always. Both of you had been a great support for me.

I take this opportunity to thank my whole family, who cherished each and every milestone in my life. First of all, a few words about my late father, Prof.K.R.Venkita Subramanian, from whom I inherited the interest towards Physics. His books and notes, introduced me to the fascinating world of physics. I believe that along with the blessings of the Almighty, the blessings of my late father and my late grandparents were also there throughout my work. I am very much thankful to my mother who believed in me and supported me to choose the path of my interest. Thanks to my beloved sister who has always made me happy and proud. I would like to express my sincere thanks to my parents-in-law for their support and encouragement. Many thanks to Vimala akka, whose caring and motherly affection always made me feel happy. Finally a few words about my husband, Hari and my 3 year old son, Pranav. Hari's support was immense and constant, without which I would not have finished my thesis. He was always there for me. *Thank you Hari, for everything*. I would like to thank Pranav, who knowingly and unknowingly supported me a lot. To Hari and Pranav, both of you make my world and make me complete.

TABLE OF CONTENTS

Abstract

The Large Magellanic Cloud (LMC) and the Small Magellanic Cloud (SMC) are two nearby galaxies located at a distance of 50 kpc and 60 kpc respectively. The Magellanic Clouds (MCs) host young, intermediate-age and old stellar populations. In this study, the stellar populations in the MCs are used as a tool to understand the structure and evolution of these galaxies as well as to understand the evolution of the Magellanic system as a whole. The structure of the MCs are studied using stellar populations (standard candles) of different ages (Cepheids - 100 Myr, Red clump stars: 2-9 Gyr & RR Lyrae stars > 9 Gyr) and the quantitative estimates of the structural parameters are derived. This study reveals the structural changes in the two galaxies as a function of time, and help to identify processes like interactions as well as mergers experienced by MCs at different epochs.

The V and I band photometric data from the Optical Gravitational Lensing Experiment (OGLE II, OGLE III) and the Magellanic Cloud Photometric Survey (MCPS) catalogue are used for the study. The J and H band data of the red clump stars in the LMC from the Infrared Survey Facility (IRSF) Magellanic Cloud Point Source Catalogue (MCPSC) are also used for the study of the structure. The de-reddened mean magnitudes of the red clump stars and the RR Lyrae stars are used to estimate the relative distances of different regions within the MCs and the dispersion from their mean magnitudes are used as a measure of the line of sight depth. The period-luminosity relation of Cepheids is used for the estimation of relative distances between the regions within the SMC. The details of the methodology are discussed in chapter 2.

The LMC is believed to be a disk galaxy. Previous kinematical studies suggest that the disk of the LMC is somewhat thicker than the thick disk of the Milky Way. There has not been any direct estimate of the thickness or the line of sight depth of the bar and disk of the LMC so far. The quantitative estimate of depth of different regions in the LMC is important to understand the processes responsible for this large depth as well as to explain the observed microlensing events towards this galaxy. We used the V and I bands data of red clump stars from OGLE II, OGLE III and MCPS data sets to obtain the line of sight depth in different regions of the LMC and the results are presented in chapter 3. A large line of sight depth is found for the LMC disk (3.44 ± 1.16 kpc and 2.88 ± 1.78 kpc from OGLE III and MCPS data sets respectively) as well as for the bar (3.95 ± 1.42 kpc from OGLE II). The northern disk is found to have larger depth compared to other regions. These results suggest that the LMC has experienced heating, probably due to minor mergers.

The knowledge of the location of the bar is important for the estimation of the structure of the LMC. When the off-centered bar of the LMC is a prominent feature in the optical and near infrared, such a feature is not visible in the gas and recent star formation. The study of the optical data of the bar of the LMC is presented in chapter 4. From the study of red clump stars, we found that the bar is coplanar with the disk, within $\sim$ 460 pc. Thus, this study confirms that the bar is very much a part of the LMC and not another component located in front of the LMC disk.

The structural parameters of the LMC disk, such as the inclination (i) and the position angle of the line of nodes (PA_{lon}) had been estimated previously using different tracers. If we combine all these studies we can see a large range in i (23°.5 - 35°.8 degrees) and PA_{lon} (122°.5 to 170°). The study of the inner as well as the outer regions of the LMC using a continuous and homogeneous data is required to understand the variations in the estimated parameters. The intermediate age LMC disk is studied using the optical data of red clump stars from the OGLE III and MCPS data sets. This study is presented in the first part of chapter 5. We found an $i = 23°.0 \pm 0°.8$ and $PA_{lon} = 163°.7 \pm 1°.5$ from the OGLE III data and an $i = 37°.4 \pm 2°.3$ and $PA_{lon} = 141°.2 \pm 3°.7$ from the MCPS data. Regions in the north-west, south-west and south-east of the LMC disk are warped with respect to the disk plane. We also identify a symmetric but off-centered warp in the inner LMC. The structure of the LMC disk inside the 3 degree radius is found to be different from the outside disk such that the inner LMC has relatively less inclination and relatively large position angle of line of nodes. The effect of coverage, adopted center, reddening and the complicated inner structure of the LMC in the estimated parameters are discussed in detail in this chapter. We found that the variation in the planar parameters of the LMC disk is caused by difference in coverage and the complicated inner structure of the disk. Reddening also plays an important role in the estimation of the planar parameters. As the effect of reddening is less in longer wavelengths, the LMC structure estimated using near infrared data of the red clump stars is likely to have reduced effect due to reddening. The IRSF MCPSC data is used for the estimation of structural parameters of the LMC disk and this is presented in the second part of chapter 5. The results obtained from this study are similar to that obtained from the optical study. From the infrared study of the red clump stars in the LMC we obtained an $i = 26°.0 \pm 0°.6$ and $PA_{lon} = 150°.9 \pm 0°.5$. We found that the reddening varies across the LMC and this has to be accounted properly while estimating the structure and detection of extra planar features. The structural parameters and the extra planar features of the LMC disk obtained from the intermediate

age red clump stars are similar to that found from young stars and HI gas.

The halo of the LMC has been an elusive component so far and one of the ideal proxy to study the halo are the RR Lyrae stars. We have studied the distribution of RR Lyrae stars in the LMC to identify the halo of the LMC. This study presented in chapter 6, reveals that a large fraction of the RR Lyrae stars in the LMC are not in a spheroidal system, but in an equatorial plane similar to that of the disk. We estimated the inclination,i and the position angle, PA_{lon} of this plane to be 31°.3 ± 3°.5 and 125° ± 17° respectively. These are found to be very similar to the parameters of the disk found from young and intermediate age stars. We also find that only a small fraction (about 10%) is likely to trace the extended halo. We suggest a major star formation event happened at 10-12 Gyr in the LMC, probably with a gas merger to explain the disk-like distribution of the major fraction of the RRLS.

The SMC is believed to have large line of sight depth, but there is no systematic estimation of this value across the face of the SMC. We estimated the depth of the SMC using red clump stars from OGLE II and MCPS data sets and the results are presented in chapter 7. The SMC bar (4.9 ± 1.23 kpc) and disk (4.23 ± 1.48 kpc) have similar depth, with no significant variation across the SMC. An enhancement in the depth up to 10 kpc is found near the optical center. Increased depth and stellar & HI density near the center suggest that the SMC possibly may have a bulge/nucleus.

The theoretical and observational studies of different stellar populations in the SMC suggest that the intermediate-age and old populations are distributed in a spheroidal system and the young stars are distributed in an extended disk. The intermediate age (red clump stars) and old (RR Lyrae stars) in the SMC are studied in detail to obtain the line of sight depth, density distributions and relative distances. These estimates are compared and we found from both the populations that the north eastern part of the SMC is closer to us. The line of sight depth is found to be large (∼ 14 kpc). This study presented in chapter 8, found that both these populations are distributed in a spheroidal or slightly ellipsoidal system. The orientation measurements of the system in which they are distributed are estimated. An axes ratio of 1:1.5:8.04 , inclination of the longest axis with the line of sight, $i = 0°.5$ and position angle of the projection of the ellipsoid in the plane of the sky, $\phi = 58°.3$ are estimated from the analysis of RR Lyrae stars. Similarly an axes ratio of 1:1.5:7.88 , $i = 0°.6$ and $\phi = 55°.5$ are estimated from the analysis of the red clump stars

assuming them to be also extended to a depth of 3.5-sigma. Our tidal radius estimates and various observational studies of the outer regions of the SMC suggest that the full extent of the SMC in XY plane is similar to the front to the back distance estimated along the line of sight. These results suggest that the actual structure of the SMC is spheroidal or slightly ellipsoidal. We propose that the SMC experienced a merger with another dwarf galaxy at about 4-5 Gyr, and the merger process was completed in another 2-3 Gyr. This resulted in a spheroidal distribution comprising of stars older than 2 Gyr and the young stars (age < 2 Gyr) in a disk.

The study of young stars (Cepheids) in the SMC suggest that they are distributed in a highly inclined ($60^\circ.5 \pm 0^\circ.5$) disk with position angle of line of nodes, $\phi = 137^\circ.2 \pm 1^\circ.0$. The study of young stars also suggest that the north eastern part of the SMC disk is closer to us. This study of the SMC disk using Cepheids is presented in chapter 9.

In this thesis study, we find that the LMC does not have a prominent stellar halo. The disk of the LMC has not changed significantly with time as found from the structural parameters obtained using tracers of different ages. The LMC might have had a couple of minor merger events after the formation of the disk. The highly structured disk of the LMC along with its warps suggests mergers and also interactions with SMC and the Milky Way. The SMC is found to be a spheroidal or slightly ellipsoidal galaxy comprising of old and intermediate age stars, but has a disk consisting of young stars and gas. This structural change is likely to have happened due a major merger event. The SMC also does not have a prominent stellar halo. Our results suggest that the LMC has experienced a major merger at 10-12 Gyr, whereas the SMC experienced a major merger at 4-5 Gyr. Thus the formation and early evolution of the LMC & SMC are found to be different.

List of Publications

- **Refereed Journals**

  - The 3D structure of the Small Magellanic Cloud, **Subramanian, Smitha**., Subramaniam, A., 2011, ApJ (under review)

  - An estimate of the structural parameters of the Large Magellanic Cloud using red clump stars, **Subramanian, Smitha**., Subramaniam, A., 2010, A&A, 520, 24 (5 citations)

  - RR Lyrae stars in the Large Magellanic Cloud, Where did they form?, Subramaniam, A., **Subramanain, Smitha**., 2009, A&A 503L, 9 (5 citations)

  - The Mysterious Bar of the Large Magellanic Cloud: What is it?, Subramaniam, A., **Subramanain, Smitha**., 2009, ApJ, 703L, 37 (6 citations)

  - Depth estimation of the Large and Small Magellanic Clouds, **Subramanian, Smitha**., Subramaniam, A., 2009, A&A, 496 399 (18 citations)

- **In preparation**

  - Structural parameters of the LMC disk using NIR data of red clump stars, **Subramanian, Smitha**., Subramaniam, A., 2011

  - Disk of the SMC: Estimating structural parameters using Cepheids, **Subramanian, Smitha**., Subramaniam.A, 2011

- **Conference proceedings**

  - Line of sight depth of the Large and Small Magellanic Clouds, Subramaniam, A., **Subramanain, Smitha**., 2009, IAUS, 256, 63 (1 citation)

– Internal and foreground reddening maps of the Magellanic Clouds, Subramaniam, A., **Subramanain, Smitha**., 2010, ASInC, 1, 107

LIST OF FIGURES

LIST OF TABLES

LIST OF ABBREVIATIONS

The following table describes various abbreviations used throughout the thesis.

Abbreviation	Description
CMD	Colour Magnitude Diagram
Dec	Declination
IRSF	Infrared Survey Facility
LMC	Large Magellanic Cloud
MB	Magellanic Bridge
MCs	Magellanic Clouds
MCPS	Magellanic Cloud Photometric Survey
MCPSC	Magellanic Cloud Point Source Catalogue
MS	Magellanic Stream
MW	Milky Way
NE	North-East
OGLE	Optical Gravitational Lensing Experiment
PA_{lon}	Position Angle of the Line of Nodes
PL	Period - Luminosity
R.A	Right Ascension
RC	Red Clump
RRLS	RR Lyrae stars
SEHO	South East H I Over density
SMC	Small Magellanic Cloud
SW	South-West

CHAPTER 1

INTRODUCTION

1.1 History

The Magellanic Clouds are two nearby galaxies visible only from the southern hemisphere. The natives on the Sea Islands called them Upper and Lower Clouds of Mist. In 964 A.D, Al Sufi of Persia described their location in the sky and called them the "White Ox of the Southern Arabs". The two objects were also called the Cape Clouds for hundreds of years, as they were the most striking objects appearing in the sky when ships approached the Cape of Good Hope. They were of importance for the navigators of that time for localizing the South Pole, where there is no star corresponding to Polaris in the North Pole. Between 1519 and 1522, an expedition led by Portuguese explorer Ferdinand Magellan became the first to circumnavigate the globe. When they sailed into the Southern Hemisphere, the sailors noticed two cloudy patches in the night sky. The Clouds became connected with the name of Magellan through Antonio Pigafetta's valuable narrative of the first circumnavigation of the globe (Westerlund 1997). Since then these objects were known as Clouds of Magellan. Modern astronomers refer to the Clouds of Magellan as the Large Magellanic Cloud and the Small Magellanic Cloud. The Clouds of Magellan are popular with amateur astronomers. They are relatively easy to find and see on a clear, dark night in the Southern Hemisphere. The Large Magellanic Cloud can be found in the Mensa and Dorado constellations. The Small Magellanic Cloud can be seen in the Tucana constellation.

The Magellanic Clouds were first recognized as stellar systems by Herschel (1847), who identified 224 objects in the Small Magellanic Cloud and 919 objects in the Large Magellanic Cloud. Their nature as the two external galaxies was first summarised by

Abbe (1867). Detailed investigations of the Magellanic Clouds began with the establishment of southern stations of Harvard College Observatory in Peru (1889-1927) and in South Africa. In 1914, the Lick Observatory measured radial velocities of bright-line nebulae in both the Clouds and the results suggested that the MCs are independent of the Milky Way. The most significant result of these early studies was the discovery of the period-luminosity relation for Cepheid variables in the Small Magellanic Cloud by Henrietta Leavitt (Leavitt & Pickering 1912). The subsequent calibration of this relation made it a fundamental tool for measuring extragalactic distances. The first most extensive review on the Magellanic Clouds is the one by Buscombe (1954). Shapley (1956) summarised the significant contributions of the Magellanic Clouds research. Later, Westerlund (1997) gave a detailed review of the topic.

1.2 Magellanic System

The Magellanic system comprises of 4 components: the Large Magellanic Cloud (LMC), the Small Magellanic Cloud (SMC) , the Magellanic Bridge (MB), and the Magellanic Stream (MS). It is located at a distance of ~ 57 kpc (Cioni et al. 2000b). As mentioned earlier, the LMC and the SMC together known as the Magellanic Clouds (MCs) are the two nearby galaxies and are located at a distance of 50 kpc and 60 kpc respectively from our Galaxy. The MB and the MS were discovered by Hindman et al. (1963) and Wannier et al. (1972) respectively. The MB connecting the two galaxies has gas and young stars. The MS attached to the SMC are predominantly formed of neutral H I gas. The H I map taken from Putman et al. (2003) is shown in Fig. 1.1.

MCs were believed to have had interactions with our Galaxy as well as between each other (Westerlund 1997). The MB and the MS are considered as signatures of these interactions. It is also believed that the tidal forces due to these interactions have caused structural changes in the MCs. The recent proper motion estimates by Kallivayalil et al. (2006a), Kallivayalil et al. (2006b) & Besla et al. (2007) indicate that these Clouds may be actually approaching our Galaxy for the first time. Therefore, it is not clear whether the structure of the different components of the Magellanic system are modified due to the interactions with our Galaxy or only due to their mutual interactions and/or previous merger events.

1.2.1 Large Magellanic Cloud (LMC)

The LMC is one of our closest neighbour galaxies at a distance of ~ 50 kpc. The

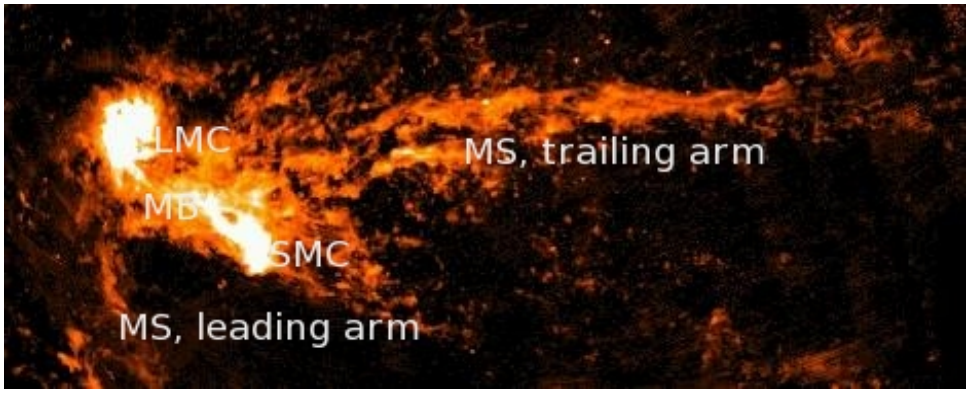

Figure 1.1: The H I map taken from Putman et al (2003). The components of the Magellanic system are shown.

LMC consists of an outer body that appears elliptical in projection on the sky, with a pronounced, off-center bar. The appearance in the optical bands is dominated by the bar, regions of strong star formation, and patchy dust absorption. The LMC is generally considered as an irregular galaxy as a result of these characteristics. It is in fact the prototype of a class of galaxies called Magellanic Irregulars (de Vaucouleurs & Freeman 1972).

Structure of the LMC

- **Disk of the LMC**
  The LMC has long been regarded as a thin flat disk seen nearly face on (de Vaucouleurs & Freeman 1972). By assuming the LMC disk to be circular when viewed face-on, de Vaucouleurs & Freeman (1972) found a disk inclination, $i = 27° \pm 2°$ and a position angle of the line of nodes (PA_{lon}), $\phi = 170° \pm 5°$ from the study of optical and 21 cm H I isophotes. Based on the analysis of spatial variations in the apparent magnitude of asymptotic giant branch (AGB) stars in the near-infrared (NIR) colour-magnitude diagrams (CMDs) extracted from the Deep Near-Infrared Southern Sky Survey (DENIS) and Two Micron All-Sky Survey (2MASS), van der Marel & Cioni (2001) estimated $i = 34°.7 \pm 6°.2$ and $\phi = 122°.5 \pm 8°.3$ for the LMC disk between 2°.5 to 6°.7 from the LMC center. The summary of estimates obtained from the previous studies is given in Table 1.1. The inclination, i has a range from 23°.5 to 35°.8 and PA_{lon} ranges from 122°.5 to 170°. Orientation measurements of the LMC disk obtained from various studies have a large range. This may be due to the structures like warps found by Olsen & Salyk (2002) and Subramaniam (2003)

Table 1.1: Summary of orientation measurements of LMC disk plane

Reference	Inclination, i	PA$_{lon}$, ϕ	Tracer used for the estimate
de Vaucouleurs & Freeman (1972)	27°.0±2°.0	170°.0±5°.0	Isophotes
Feitzinger et al. (1977)	33°.0±3°.0	168°.0±4°.0	H I
Caldwell & Coulson (1986)	28°.0±5°.9	142°.4±7°.7	Cepheids
Luks & Rohlfs (1992)	–	162°.0	H I
Kim et al. (1998)	22°.0±6°.0	168°.0	H I
van der Marel & Cioni (2001)	34°.7±6°.2	122°.5±8°.3	AGB stars
Olsen & Salyk (2002)	35°.8±2°.4	145°.0±4°.0	Red clump stars
Nikolaev et al. (2004)	30°.7±1°.1	151°.0±2°.4	Cepheids
Persson et al. (2004)	27°.0±6°.0	127°.0±10°.0	Cepheids
Koerwer (2009)	23°.5±0°.4	154°.6±1°.2	Red clump stars

in the LMC disk and bar respectively.

Kinematical properties of different LMC tracers like H I (e.g.,Rohlfs et al. 1984, Luks & Rohlfs 1992 and Kim et al. 1998), star clusters (Freeman et al. 1983 and Schommer et al. 1992), planetary nebulae (PNe) (Meatheringham et al. 1988), H II regions and supergiants (Feitzinger et al. 1977), and carbon stars (Kunkel et al. 1997, Graff et al. 2000, Alves & Nelson 2000, van der Marel et al. 2002) have been studied. A common result from all these studies is that the line of sight velocity dispersion of the tracers is generally at least a factor of ~ 2 smaller than their rotation velocity. This implies that the LMC is kinematically cold, and must therefore to the lowest approximation be a disk system. The ratio of the rotational velocity to the dispersion is a measure of the scale height of the disk. This ratio obtained from the carbon stars is 2.9. For comparison, the thin disk of the Milky Way has V /σ ~ 9.8 and its thick disk has V /σ ~ 3.9. In a relative sense, one might therefore expect the LMC disk to be similar, but somewhat thicker than the Milky Way thick disk.

- **Bar of the LMC**

  The off-centered stellar bar is one of the most striking features of the LMC. The NIR star count maps presented by van der Marel & Cioni (2001) found the bar to be a smooth structure. On the other hand, the bar is neither visible in the H I distri-

bution nor in the H I velocity maps (Staveley-Smith et al. 2003). Interestingly, an offset between the LMC bar and disk was previously suggested by Zhao & Evans (2000) as an explanation for the observed LMC microlensing optical depth. Subramaniam (2003) studied the relative distance within the LMC bar using red clump stars and found that the bar is warped and also found structures in the bar. Zaritsky (2004) suggested that the bar of the LMC is a levitating bar and it is the result of viewing a triaxial stellar bulge that is embedded in a highly obscuring thick disk. Nikolaev et al. (2004) found that the bar is located ~ 0.5 kpc in front of the main disk.

- **Halo of the LMC**

  The first possible evidence for the presence of a pressure supported halo of the LMC was presented by Minniti et al. (2003). They measured a dispersion, $\sigma \sim 53 \pm 10$ km s^{-1} for a sample of 43 RR Lyrae stars within 1°.5 from the LMC center. This value is consistent with what would be expected for a pressure supported halo in equilibrium in the gravitational potential implied by the circular velocity (Alves 2004a). The RR Lyrae stars make up ~ $1/50^{th}$ of the visible mass of the LMC, similar to the value for the Milky Way halo. However, it is surprising that the surface density distribution of the LMC RR Lyrae stars stars is well fit by an exponential with the same scale length as inferred for other tracers known to reside in the disk Alves (2004b). This is very different from the Milky Way halo, where RR Lyrae stars follow a power-law density profile. This suggests that the RR Lyrae stars in the LMC might have formed in the LMC disk, instead of in the halo. In this scenario they might simply have attained their large dispersions by a combination of disk heating and Milky Way tidal forces (Weinberg 2000). Subramaniam (2006) found that the RR Lyrae stars in the bar region of the LMC have disk like distribution, but halo like location. The studies on the outer disk regions by Carrera et al. (2011) and Saha et al. (2010) do not find an evidence of a halo in the LMC.

1.2.2 Small Magellanic Cloud (SMC)

The SMC is located at a distance of around 60 kpc. The SMC is characterized by a less pronounced bar, and an eastern extension called the Wing. The Wing and the north-eastern part of the bar are closer than the southern parts (Hatzidimitriou et al. 1993). A large line of sight depth was found in the outer regions of the SMC by Gardiner & Hawkins (1991).

Structure of the SMC

The kinematical studies of PNe and carbon stars (Dopita et al. 1985, Hardy et al. 1989, Suntzeff et al. 1986 & Hatzidimitriou et al. 1997) which represent the old and intermediate-age populations show no evidence of rotation of the main body of the SMC. From the study of 2046 red giant stars, Harris & Zaritsky (2006) found that they have a velocity dispersion of 27.5 km s^{-1} and a maximum possible rotation of 17 km s^{-1}. All these results suggest that the structure of the older stellar component of the SMC is nearly spheroidal, where the SMC is supported by its velocity dispersion.

Viewing the SMC as a triaxial ellipsoid with R.A, Dec and the line of sight depth as the three axes, Crowl et al. (2001) found an axes ratio of 1:2:4. Zaritsky et al. (2000) showed that the older stellar populations (age > 1 Gyr) in the SMC are distributed in a regular, smooth ellipsoid. Similar conclusions were drawn by Cioni et al. (2000a) and Maragoudaki et al. (2001). Detailed studies for the quantitative estimation of the structural parameters of the SMC spheroid/ellipsoid are not done.

In contrast to the old and intermediate-age stars, young stars (age < 200 Myr) in the SMC have an irregular distribution (Zaritsky et al. 2000) similar to that found in the H I morphology (Stanimirović et al. 2004) . The H I observations also show that the SMC has a significant amount of rotation with a circular velocity of approximately 60 km s^{-1} with a gradient from southwest to northeast. The inclination of the SMC disk in which the young stars are believed to be distributed is estimated as $70^\circ \pm 3^\circ$ and $68^\circ \pm 2^\circ$ from the studies of Cepheids by Caldwell & Coulson (1986) and Groenewegen (2000) respectively. The position angle of the line of nodes is estimated to be $\sim 148^\circ$.

Gardiner & Noguchi (1996) modelled the SMC as a two component system consisting of a nearly spherical halo and a rotationally supported disk. They estimated the tidal radius to be 5 kpc. The distribution of their halo particles within 5 kpc radius was in good agreement with the observed distributions of the old (> 9 Gyr) and intermediate age (2-9 Gyr) stellar populations in the SMC. The distribution of disk particles could reproduce the observed irregular distribution of young stars in the SMC.

Thus, both observational and theoretical studies suggest that the old and intermediate-age stellar populations in the SMC are distributed in a nearly spheroidal system and the young stars are distributed in a highly inclined disk.

Another important observed feature in the SMC is the large extension in the line of sight. The studies of Mathewson et al. (1986) & Mathewson et al. (1988) found that the SMC Cepheids extend from 43 to 75 kpc with most Cepheids found in the neighbourhood

of 59 kpc. Later, the line of sight depth of the SMC was estimated (Welch et al. 1987) by investigating the line of sight distribution and period - luminosity relation of Cepheids. They accounted for various factors which could contribute to the larger depth estimated by Mathewson et al. (1986) & Mathewson et al. (1988) and found the line of sight depth of the SMC to be $\sim$ 3.3 kpc. Hatzidimitriou & Hawkins (1989) estimated the line of sight depth in the outer regions of the SMC to be around 10-20 kpc. A sample of 12 populous SMC clusters which possess red clump stars were studied by Crowl et al. (2001) to determine the line of sight depth of the SMC. They found a 1-sigma depth of around 6-12 kpc for the SMC. The depth estimate of the SMC was also done by North et al. (2009) using eclipsing binary stars and estimated a 2-sigma depth of 10.6 kpc.

1.2.3 Magellanic Bridge (MB)

The region between the MCs is known as the MB. Neutral hydrogen was detected in this intercloud region by Hindman et al. (1963). No stellar link was found in the MB till 1980, when Kunkel (1980) found a group of young stars in the extreme eastern tip of the wing of the SMC. Later Irwin et al. (1985) discovered several blue main sequence stars which are the optical counterpart of the H I bridge. The age of these stars were estimated to be around 100 Myr. Demers & Battinelli (1998) observed five fields in the western Bridge and found stars as young as 10-25 Myr in both clusters and in a diffuse field component up to 9° from the SMC. The MB is believed to be a classical bridge formed by the tidal interactions of the MCs (Besla et al. 2010, Diaz & Bekki 2011). Diaz & Bekki (2011) modelled the Magellanic System with the MCs separately bound to the Milky Way for more than 5 Gyr and the MCs became bound to each other in last 1.6 Gyr. The close encounter of the MCs around 250 Myr ago formed the MB. Harris (2007) observed 12 fields in the MB and did not detect an older stellar population belonging to the Bridge in any of the fields, implying that the material that was stripped from the MCs to form the MB was very nearly a pure gas. He estimated the star formation history of the young population in the MB and found that the star formation in the MB started around 200-300 Myr ago and continued until about 40 Myr ago.

1.2.4 Magellanic Stream (MS)

The most famous and the prominent Galactic Halo H I stream is the MS. This is a 10° wide filament with $\sim$ 2 x 10^8 solar mass of neutral hydrogen and stretches over 100° across the southern sky behind the MCs. This was first recognised by Wannier et al.

(1972). Mathewson et al. (1974) associated the Stream with the MCs and more fully demonstrated its ∼ 100° span. Putman et al. (1998) discovered a gaseous leading arm of the MS, that stretches in-front of the MCs. A more thorough history and general review of the MS is given by Putman et al. (2003) and Brüns et al. (2005). Putman et al. (2003) used the high resolution HIPASS data (Barnes et al. 2001) and showed that the trailing MS is spatially bifurcated. Braun & Thilker (2004) suggested that the MS is plausibly longer than previously recognized.

The two primary mechanisms postulated for the MS formation were the ram pressure stripping (Meurer et al. 1985, Sofue 1994, Moore & Davis 1994 and Mastropietro et al. 2005) and tidal stripping (Murai & Fujimoto 1980, Gardiner & Noguchi 1996, Yoshizawa & Noguchi 2003 and Combes et al. 1990). To remove the MS gas effectively, both these mechanisms require the MCs to be relatively close to the Milky Way for a prolonged encounter time. Recent simulations by Besla et al. (2007), motivated by new proper motion measurements for the MCs (Kallivayalil et al. (2006a), Kallivayalil et al. (2006b) and Piatek et al. 2008), conclude that the MCs might be on their first passage around the Milky Way. If the orbits of the MCs have kept them more isolated in the past, then it becomes difficult for either ram pressure or tidal forces alone to create the MS. However, Mastropietro et al. (2009) & Mastropietro (2010) produced a 120° long stream using ram pressure and the new, higher velocity MC orbits. Later Besla et al. (2010) showed that the tidal interactions between the MCs are sufficient to remove a substantial amount of material from the SMC without the aid of Milky Way tides or hydrodynamic interactions. Diaz & Bekki (2011) proposed a new tidal model in which structures resembling the bifurcated MS and elongated leading arm are able to form in a bound orbit consistent with the HST proper motions. The LMC and the SMC have remained bound to each other only recently in their model despite being separately bound to the Milky Way for more than 5 Gyr. They found that the structures of the MS are formed as a consequence of LMC-dominated tidal stripping during the recent dynamical coupling of the LMC and the SMC.

A third mechanism for the formation of the MS was put forward by Nidever et al. (2008) after tracing one filament of the trailing stream as well as the leading arm back to their origin in the southeast H I overdensity (SEHO) region in the LMC, contrary to previous assertions that the MS originates in the SMC and/or in the MB. They also found that the SEHO contains large gaseous outflows from supergiant shells. The blowout hypothesis postulates that supergiant shells in the dense SEHO blow out gas from the LMC to large radii by overcoming a significant portion of the gravitational hold of the

LMC on the gas. This should be an effective solution for explaining a large extent of the MS in the first passage scenario of the MCs around the Milky Way. Nidever et al. (2010) showed that the MS is at least 140° long (~ 40° longer than previously verified) and probably even longer. This additional extension of the MS make the entire MS system (including the leading arm) at least 200° long. Nidever et al. (2010) estimated the age of the MS to be ~ 2.5 Gyr. They found that this timescale coincides with bursts of star formation in both the LMC and the SMC as well as with a possible close encounter between the MCs. They suggested that this encounter could have triggered the new era of star formation of the MS via supergiant shell blowout.

1.3 Scientific Motivation

The overall appearance of the Magellanic system is shaped by the dynamics of the MCs which are on their first passage around the Milky Way (Besla et al. 2007). The study of stellar populations in the MCs is important to understand the structure and evolution of these galaxies as well as to understand the evolution of the Magellanic system as a whole. Stellar populations of different ages (young, intermediate-age and old) can be studied to see the evolution of the MCs, due to processes like interactions as well as mergers experienced by MCs at different epochs.

As described in Section 1.1.1, the structural parameters of the LMC disk are estimated previously using different stellar populations like the AGB stars, the red clump stars and the Cepheids. In order to understand the variations and large range in the estimated parameters (see Table 1) from different tracers, we have to study the structure of the inner as well as the outer LMC from a continuous and homogeneous sample. The knowledge of the location of the bar with respect to the main disk as well as its structure plays a major role in the estimation of the structural parameters of the LMC disk. Previous studies also suggest that the LMC disk is thicker than the disk of normal disk galaxies. The quantitative estimate of the depth in different regions of the LMC is important to understand the processes responsible for the large depth as well as to explain the observed microlensing events towards this galxy. The RR Lyrae stars are used to study the stellar halo of the LMC. But whether the majority of the RR Lyrae stars in the LMC reside in the halo or in the disk is still not clearly understood.

The structure of the SMC is less explored than that of the LMC. Even though the Cepheids and star clusters in the SMC are studied, detailed studies for the quantitative estimation of the spheroidal/ellipsoidal component are not done. A detailed study of young,

intermediate-age and old stellar populations in the SMC is necessary to quantitatively estimate the structural parameters of the SMC as well as to understand the formation of the galaxy.

The aim of this thesis is to understand the structure and evolution of the MCs from the study of different stellar populations which represent the galaxies at different ages. The quantitative estimates of the structural parameters of different components of the MCs are also derived.

1.4 Stellar Populations in the Magellanic Clouds

Stars in a galaxy are mainly divided into two different populations,

- Population I stars which are relatively young are found in spiral arms, disk of a galaxy and in relatively young open clusters. They have an age range of 1-8 Gyr. They are also relatively metal rich.
- Population II stars are those found in galactic halo and in globular clusters. They have an age $\geq$ 10 Gyr. They are observed to be relatively metal poor.

Both the LMC and the SMC show active star formation with H I shells, H II regions, and molecular clouds all linked to young stellar associations. The dominant stellar population in the MCs is the intermediate age stars. MCs host a large number of red giants, red clump stars and AGB stars. MCs also contain stars which are as old as the Universe. Thus these two galaxies host both Population I as well as Population II stars. This extended range of star formation is a valuable source of information to understand the formation and evolution of galaxies in general. Their proximity enables us to resolve individual stars in them. They are also located at a high galactic latitude, where the effect of Galactic reddening is very low. This helps us to detect their faint stellar populations. The MCs have four to five times lower metallicities than the Milky Way, and their gas-to-dust ratio is much higher. Thus, they have environments resembling those of the early universe. Therefore, they may hold information about the Universe at its early stages.

The young, intermediate-age and old stellar populations we have studied in this thesis are Cepheids (age $\sim$ 100 Myr), Red Clump (RC) stars (age $\sim$ 2-9 Gyr) and RR Lyrae stars (RRLS) (age $>$ 10 Gyr) respectively. These three stellar populations which we use as the tracers of the structure and evolution of the MCs, represent stars of different ages at different evolutionary phases. Before the detailed introduction of these tracers, a sneak preview of stellar evolution is given in the next section.

1.5 Stellar Evolution

1.5.1 Star Formation

The star formation takes place in the giant molecular cloud of gas and dust in the local interstellar medium. A number of processes enable these clouds to collapse under their own gravity until they are sufficiently dense and hot for the nuclear fusion process to begin, which converts hydrogen into helium. At this point, we consider a star is born. These stars are located on a diagonal band called the main sequence in the HR diagram and steadily shine for the longest period of their luminous lifetime.

1.5.2 Main sequence

The major factor which determines a main sequence star's position in the HR diagram is its mass. High mass stars expend energy faster than low mass stars. The energy generated, E is proportional to the mass of the star and its luminosity is proportional to M^4. Thus, the lifetime of a star in the main sequence is inversely proportional to M^3. This relation holds for all the stars expect for very high and very low mass stars. Thus, the high mass stars evolve quickly out of the main sequence and the low mass stars evolve slowly. The post main sequence evolution of high mass and low mass stars are different. The evolution of low and intermediate mass stars is explained below.

1.5.3 Evolution of Low and Intermediate Mass Stars

- **The Giant Branch**
  When the hydrogen in the core gets depleted, nuclear reactions switch off, and the core contracts. Hydrogen rich material outside the core is compressed and heated by the contraction and hydrogen burning shifts from core to a shell. However, not all the high luminosity generated in the shell finds its way to the surface (limited by photon diffusion rate). The difference between the luminosity generated in the shell source and that leaving the surface goes into heating the intermediate layers, causing them to expand. This expansion increases the total radius (R) of the star. According to the relation, $L = 4\pi R^2 T^4_{eff}$, for a nearly constant surface luminosity, there must be a decrease in the effective surface temperature of the star. Thus the immediate post-main sequence evolution of a radiative star moves the star more or less horizontally to the right in the HR diagram, turning the dwarf star into a

subgiant. The cooling and expansion of surface layers makes the star appear to be redder.

As the star expands, the effective temperature cannot continue to fall to arbitrarily low values. According to Hayashi, the ability of the photospheric layers to prevent the free streaming of photons drops rapidly with decreasing temperatures. This ease for photon streaming in turn leads to a minimum temperature below which T_{eff} is prevented from falling. The existence of such a temperature barrier forces the evolutionary tracks of low mass stars in the HR diagram to travel almost vertically upward, turning the red subgiant into a red giant. The accompanying increase in the amount of shell luminosity which makes its way to the surface is too much for radiative diffusion to carry out stably, and the entire envelope of the red giant becomes convective.

In lower masses ($\leq 2\ M_{\odot}$), a star develops an electron-degenerate helium core as it ascends the giant branch. This core does not increase in temperature as the pressure increases, and hence will not ignite helium easily. The hydrogen-burning shell adds processed helium to the core, and itself gets progressively hotter and thinner as the mass of the remaining hydrogen envelope is reduced. In principle, the core should be isothermal with the hydrogen burning shell (10^8 K). In practice, pair-production of neutrinos in the dense electron degenerate core removes heat and keeps the center of the core cooler than the outer regions.

- **Core Helium Burning**

  - **Low mass stars**: When the hottest part of the core reaches a critical temperature ($\sim 10^8$ K), triple alpha reactions become increasingly likely. This occurs when the core mass reaches $\sim 0.48\ M_{\odot}$. With the onset of the reaction, energy is liberated and provides immediate local heating. Since the local equation of state is insensitive to temperature, runaway heating occurs and sustained helium-burning reactions begin. Therefore the helium burning turns on in low mass stars with a helium flash. These stabilize once temperature has risen sufficiently to lift the local degeneracy. The energy derived from helium burning heats the helium core and forces it to expand. Thus the hydrogen burning shell may actually get weaker at this point, the overall luminosity drops and the star contracts. Low mass helium core burning stars are identified with horizontal branch stars (horizontal strip of stars extending blue ward

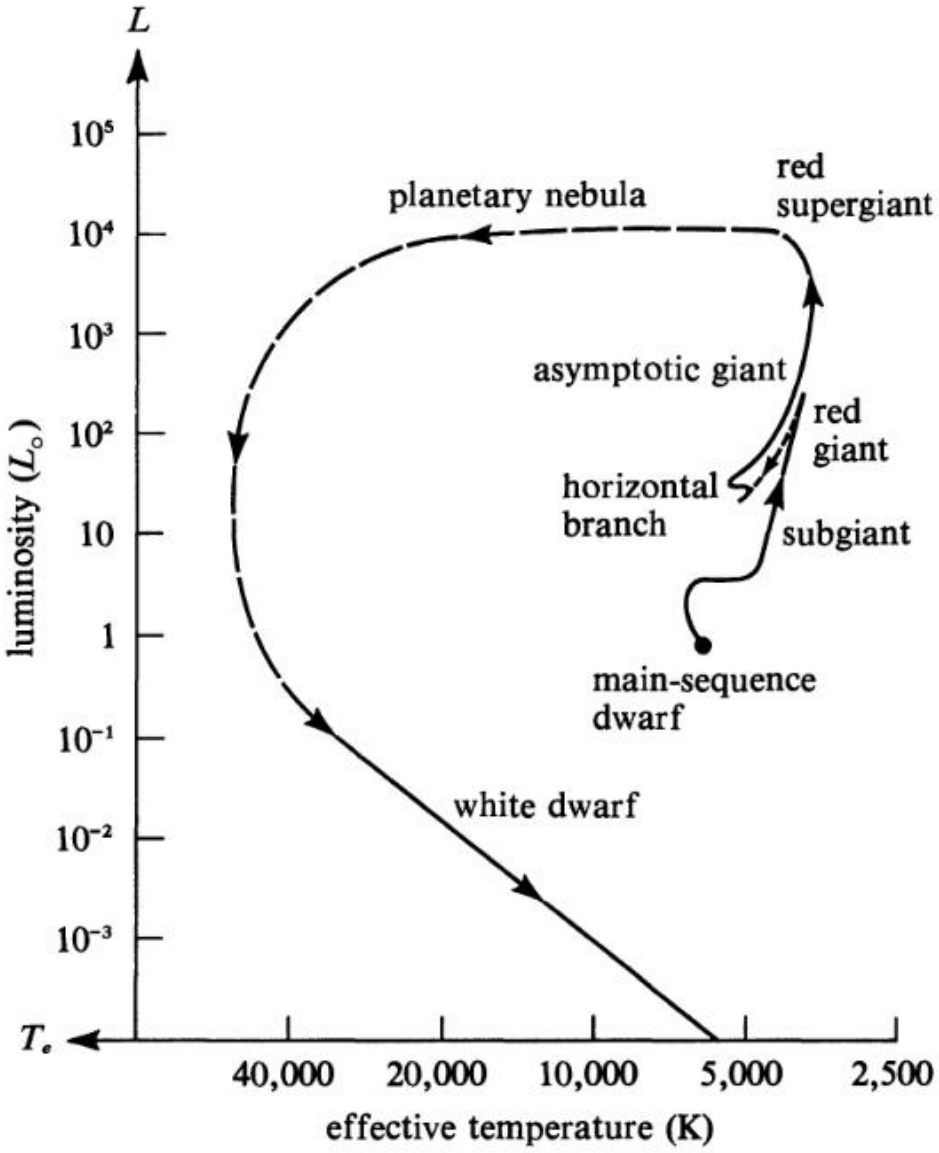

Figure 1.2: Evolution of a low mass star. This figure is taken from the book, The Physical Universe, An Introduction to Astronomy by Frank Shu (1982).

of the giant branch) in the globular clusters. In the HR diagram of stars in the solar neighbourhood, the giant branch contains a dense clump of stars. Clump stars are essentially low mass helium core burning stars belonging primarily to population I, stars which are metal rich and have significant hydrogen envelopes. The post main sequence evolution of a low mass star is shown in Fig. 1.2.

  - **Intermediate mass stars**: In more massive stars (3-8 $M_{\odot}$) helium ignition occurs in a non-degenerate core, hence is not very explosive. Helium burning starts before the core becomes compact and before the hydrogen burning shell becomes very thin. The total luminosity does not drop much. The radius becomes smaller. Core helium burning is associated with a blueward loop through the Cepheid instability strip.

- **Asymptotic Giant Branch (AGB) Stars**
  With core helium exhaustion, the focus of nuclear burning in low and intermediate mass stars shifts to a double shell structure. Because the He-shell is thermally unstable, a process known as thermal pulsing is established. The helium burning shell burns faster and so keeps moving out. When sufficient fresh helium has accumulated below the hydrogen burning, the helium shell reignites, the intershell region is forced to expand, and hydrogen burning is extinguished. When the hydrogen burning shell is operating, it is very thin and very powerful, so the star becomes very luminous and very large.

- **Planetary Nebula and White dwarfs**
  Ultimately, the expansion of the AGB star results in a dynamical instability which causes the expulsion of the outer layers as planetary nebula. When it has cooled sufficiently the star becomes a white dwarf.

1.6 Tracers

1.6.1 Red Clump stars

The RC stars are core helium burning stars, which are metal rich and slightly more massive counter parts of the horizontal branch stars. From the computed evolutionary tracks (Girardi et al. 2000) the mass range of RC stars in the MCs is found to be $\sim$ 1-2.5 $M_{\odot}$. The luminosity of these stars are relatively independent of their masses. The theoretical isochrones (0.5 Gyr to 10 Gyr) for the metallicities Z = 0.008 and Z = 0.004 obtained from the evolutionary tracks of Girardi et al. (2000) are plotted in the $(V-I)_0$ vs M_I colour magnitude diagram (CMD) . The CMDs for Z = 0.008, which corresponds to the LMC metallicity and Z = 0.004 which corresponds to the SMC metallicity are shown in Fig. 1.3 and Fig. 1.4 respectively. From these figures we can see that the stars

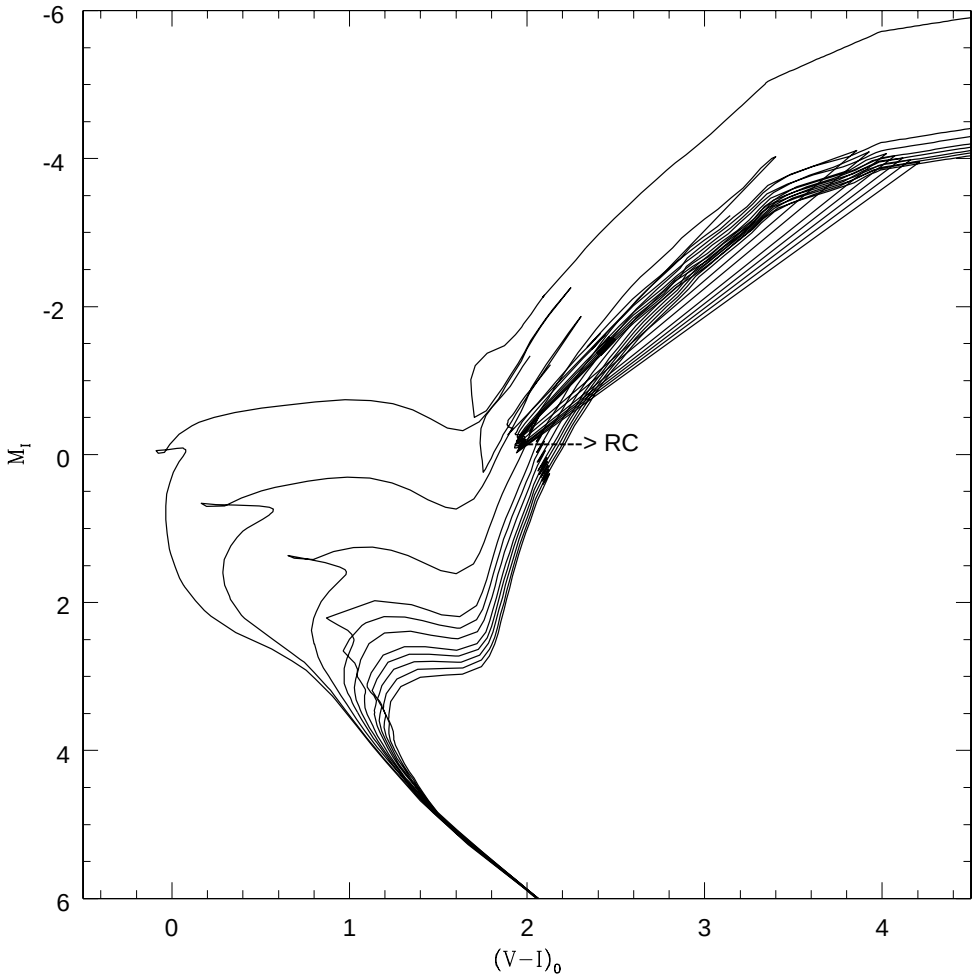

Figure 1.3: The isochrones obtained from the evolutionary tracks of Girardi et al. (2000) for the metallicity, Z = 0.008 and ages 0.5, 1, 2, 3, 4, 5, 6, 7, 8, 9 and 10 Gyr are shown.

with age older than 1 Gyr and younger than 10 Gyr, form the clump and have constant I band magnitude and $(V - I)_0$ colour. Thus the RC stars in the MCs have an age range of $\sim$ 2-9 Gyr and the luminosity and colour are relatively independent of the age. The above described properties of the RC stars make them standard candles. Large number of the RC stars are available in the MCs and have tightly defined colour and magnitude, which makes them an easily identifiable component in the CMDs. A sample CMD (of one region in the LMC) in which the RC stars are seen as a clump in the right side along with the giant branch is given in Fig. 1.5.

The RC stars were used as standard candles for distance determination by Stanek et al. (1998). Assuming a constant absolute I band magnitude for the RC stars, they determined

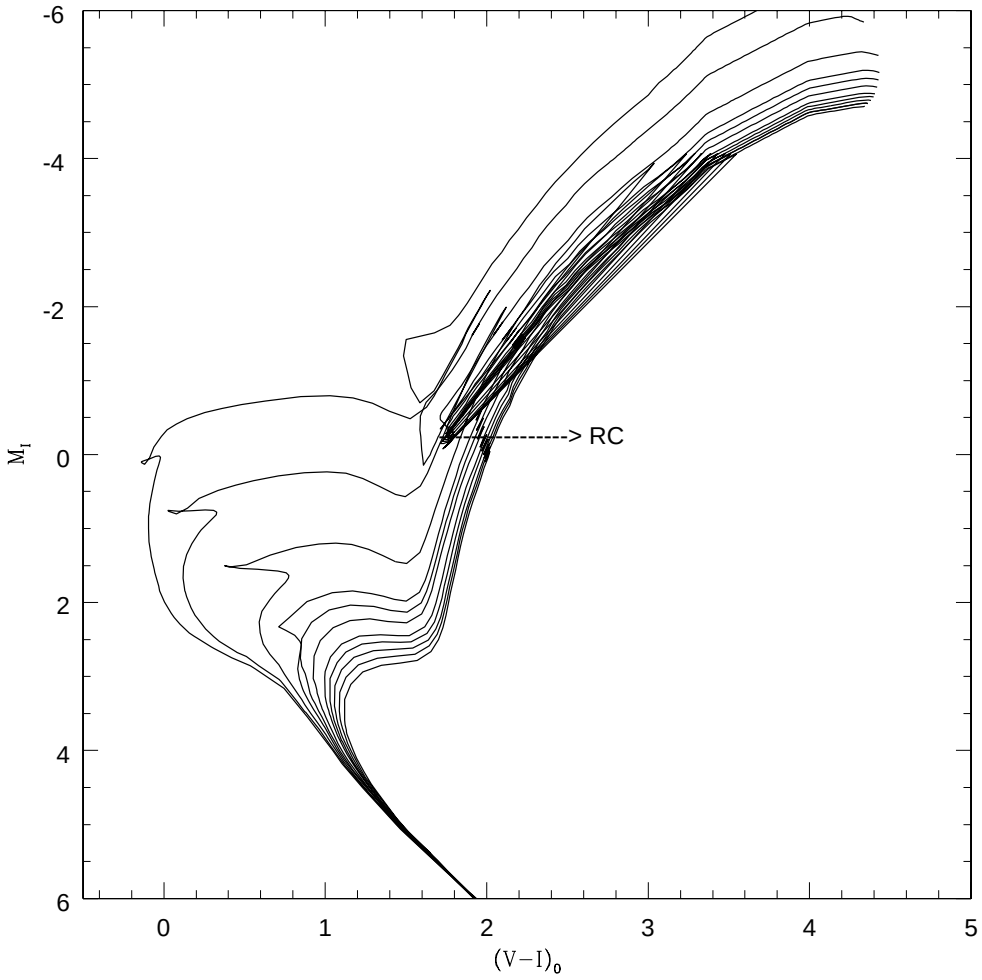

Figure 1.4: The isochrones obtained from the evolutionary tracks of Girardi et al. (2000) for the metallicity, Z = 0.004 and ages 0.5, 1, 2, 3, 4, 5, 6, 7, 8, 9 and 10 Gyr are shown.

the distance to the MCs as well as to the bulge of our Galaxy from the dereddened apparent magnitude of RC stars. Later Sarajedini (1999) and Cole (1998) claimed that the luminosity of the RC stars is highly influenced by the age and metallicity and must be accounted for in the determination of the distance. When the controversy regarding the use of RC stars as the absolute indicator continues, they can be used to estimate relative distances between regions within MCs by avoiding the disagreement over its zero point. Olsen & Salyk (2002) and Subramaniam (2003) used them as relative distance indicators to show that the southern LMC disk is warped and the LMC bar has some structures and warps respectively. Their characteristic colour was used by Subramaniam (2005) to estimate the reddening map towards the central region of the LMC.

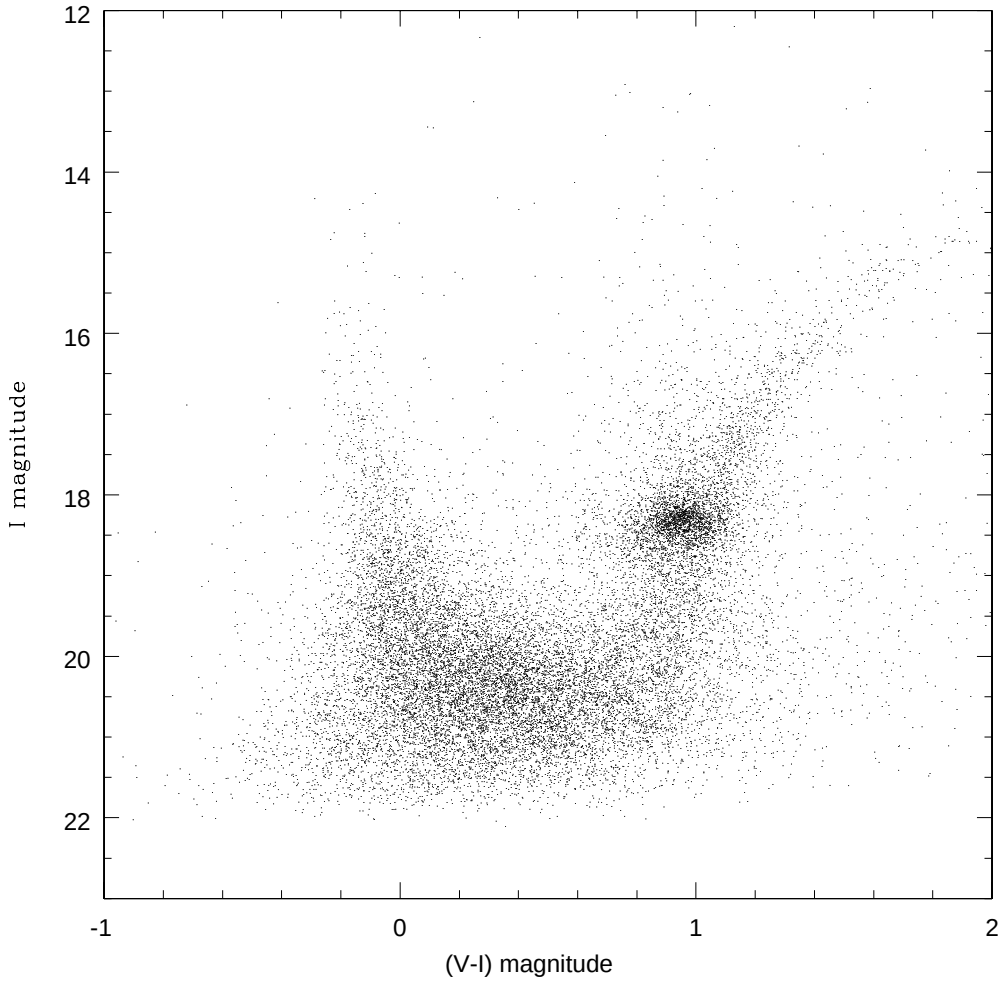

Figure 1.5: Colour magnitude diagram of a region in the LMC.

The RC stars in the MCs are a heterogeneous population and hence, they have a range in mass, age and metallicity. The density of stars in various locations will also vary with the local star formation rate as a function of time. These factors would contribute to the range of magnitude and colour of the net population of the RC stars in any given location of the MCs. These contributions also should be accounted for in the relative distance and line of sight depth estimations.

Recent studies show that the above parameters are more or less similar across the LMC (Subramaniam & Anupama 2002, Olsen & Salyk 2002 and van der Marel & Cioni 2001). Variation of star formation history and metallicity across the LMC has been studied by Cioni et al. (2006b) and Carrera et al. (2008). They have found small variations in the inner regions, but large variations in the outer regions. Cioni et al. (2006a) mapped

the variation of star formation history as well as metallicity using the AGB stars. They found that the south and south-western regions could be metal poor whereas, the north and north-eastern regions could be metal rich. Regions near the Shapley constellation III were found to have a younger population. Piatti et al. (1999) and Dolphin (2000) found that the RC population in the far northern regions is structured. Based on the studies of the LMC clusters, Grocholski et al. (2006) found that the LMC lacks the metallicity gradient typically seen in galaxies.

Cioni et al. (2006b) did not find any different population or metallcity gradient near the central regions of the SMC. Tosi et al. (2008) obtained deep CMDs of 6 SMC inner regions to study the star formation history. The interesting fact they found about the six CMDs is the apparent homogeneity of old stellar population, populating the subgiant branch and the clump. This suggested that no large differences in age and metallicity exist among old stars in these locations.

Girardi & Salaris (2001) simulated the RC stars in the LMC using the star formation rate estimated by Holtzman et al. (1999) and the age metallicity relation from Pagel & Tautvaisiene (1998). They also simulated the RC stars in SMC using star formation results and age metallicity relation from Pagel & Tautvaisiene (1998). The synthetic CMDs of the two systems were obtained and the distribution of RC stars is fitted using numerical analysis to obtain the mean and dispersion of the magnitude and colour distributions. The model predicted values are used in our study to account for the population effects of the RC stars. Detailed discussions on the impact of population effects of the RC stars in our results are included in the respective chapters.

1.6.2 Cepheids and RR Lyrae stars

Cepheids and RR Lyrae stars (RRLS) come under a category of variable stars known as intrinsic variable stars or pulsating stars. First, the properties and the mechanism responsible for the properties of the pulsating are discussed briefly. Then the studies of Cepheids and RRLS in the MCs are discussed.

Pulsating stars

Intrinsic variable stars or pulsating stars are stars, where a change in apparent brightness with time is caused by the physical changes occurring inside the star. In 1595, David Fabricius discovered the first pulsating star, O Ceti also known as the Mira variable. This is the prototype of the Long Period Variables (LPVs) with period 100-400 days. The

most important discovery was the observation of periodic light variation in the yellow supergiant δ Cephei in 1784 by John Goodricke. This is the prototype of a kind of pulsating stars called Classical Cepheids. Henrietta Swan Leavitt (1868-1921) discovered 2400 Classical Cepheids with periods between 1 to 50 days with most of them located in the Small Magellanic Cloud. The plot with apparent magnitude of these SMC stars against their pulsation periods demonstrated that the brightness and period are closely correlated. Since all the stars in the SMC are located roughly at same distance from us, the difference in their apparent magnitudes must be the same as the differences in their absolute magnitudes. Thus the observed differences in these stars' apparent brightness should reflect intrinsic differences in their luminosities. Thus, from the pulsation periods, the absolute magnitude of a Cepheid and hence the distance to the Cepheid can be estimated. Later, Sandage & Tammann (1968) calibrated the period-luminosity relation. Some of the other pulsating stars are the RRLS and δ Scuti variables. Out of several billion of stars only about million stars are pulsating stars. This implies that stellar pulsation is a transient phenomenon. The pulsating stars are located in a narrow (about 600-1100 K wide) and nearly vertical instability strip on the right hand side of the HR diagram. The location of different pulsating stars in the HR diagram is shown in Fig. 1.6.

In 1879, August Ritter proposed radial pulsations as the cause for the variability seen in the stars. Early ideas included dark patches on the surface of a rotating star, eclipses in the binary system. Later in 1914, Shapley also suggested that the variation in the temperature and brightness of Cepheid variables were caused by radial pulsations.

- **Pulsation Modes**: Stars are, to a first approximation, spherical. The simplest form of pulsation is radial - a simple spherically symmetric in and out expansion and contraction. The sound waves involved in the radial modes of stellar pulsation are essentially standing waves, similar to the standing waves that occur in an organ pipe that is open at one end. A star has an infinite number of modes of radial pulsation. The standing wave for each mode has a node at one end (the star's center), where the gas does not move, and an antinode at the other end (star's surface). The simplest is called the fundamental mode. In this mode, all parts of the star expand together and contract together, in unison. The gas moves in the same direction at every point in the star. There is a single node between the center and the surface for the first overtone mode, with the gas moving in opposite directions on either side of the node. Similarly, there are two nodes for the second overtone mode. For radial modes, the motion of the stellar material occurs primarily in the surface regions, but

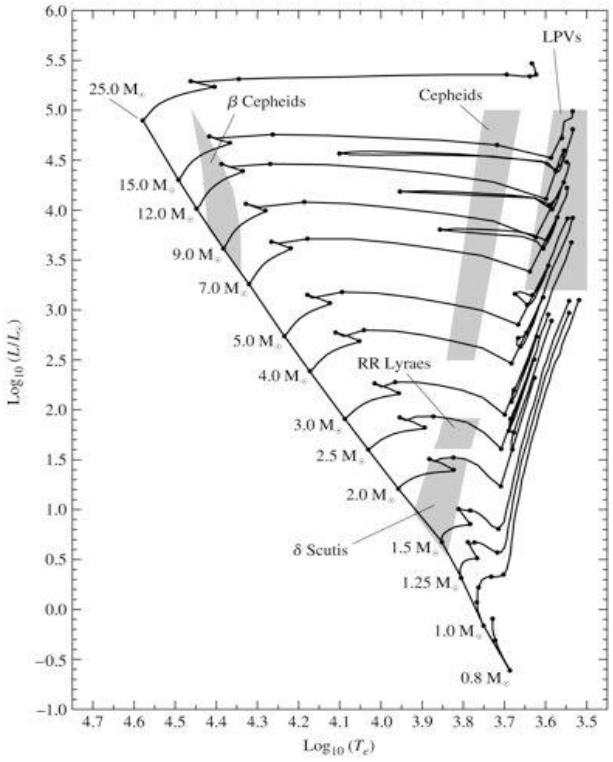

Figure 1.6: HR diagram with instability strip and locations of variable stars are shown.The figure is taken from Carroll & Ostlie: Modern Astrophysics, 2^{nd} edition.

there is some oscillation deep inside the star. The large amplitude pulsating stars like Cepheids, RRLS and Mira variables pulsate primarily in radial modes. The majority of classical Cepheids pulsate in the fundamental mode. The RRLS pulsate in fundamental or in the first overtone mode. The pulsating stars like δ Scuti pulsate in both radial as well as non radial modes. In non-radial pulsation, the star changes shape, not volume. There are two types of non-radial modes called the pressure modes and gravity modes. Non-radial pulsations tend to produce small amplitude variations than radial modes.

- **Pulsation Mechanism**: Eddington (1941) provided a theoretical frame work for the pulsation hypothesis proposed by Shapley (1914) & Ritter (1879). Eddington (1941) proposed that pulsating stars are thermodynamic heat engines. The gas comprising the layers of the stars do work as they expand and contract throughout the pulsation cycle. If the integral work done is positive then the layer contributes to driving the oscillations and if it is negative, the layer tends to dampen the oscillations. The net work done by each layer of star during one cycle is the difference between the heat flowing into the gas and heat leaving the gas. For driving the

oscillations, the heat must enter the layer during the high temperature part of the cycle and leave during the low temperature part. The driving layers of a pulsating star must absorb heat around the time of their maximum compression. In this case the maximum pressure will occur after maximum compression and the oscillations will be amplified.

First, Eddington considered the change in the nuclear generation in the core of a star as the driving mechanism. But this is not enough to drive the star's pulsation. Then he suggested an alternative called valve mechanism. If a layer of the star became more opaque on compression, it could dam up the energy flowing toward the surface and push the surface layers upward. Then, as this expanding layer became more transparent, the trapped heat could escape and the layer would fall back down to begin a new cycle. The condition is that the opacity must increase with compression. But according to Kramer's law of opacity, the opacity $\kappa \propto \rho/T^{3.5}$. As the layers of a star are compressed, both their density and temperature increases. But because the opacity is more sensitive to the temperature than to density, the opacity of the gas usually decreases upon compression.

The conditions responsible for exciting and maintaining the stellar oscillations were first identified by the Russian astronomer S.A.Zhevakin and then verified in detailed calculations by Rudolph Kippenhahn, Norman Baker and John P Cox. They found that the regions of a star where Eddington's valve mechanism can successfully operate are its partial ionization zones. In these layers of the star where the gases are partially ionized, part of the work done on the gases as they are compressed produces further ionization rather than raising the temperature of the gas. With a small temperature rise, the increase in density with compression produces a corresponding increase in opacity. Similarly, during expansion, the temperature does not decrease as much as expected since the ions now recombine with electrons and release energy. Again the density term dominates and the opacity decreases during the expansion. This layer of star can absorb heat during compression, be pushed outward to release the heat during expansion and fall back again to begin another cycle. This is known as the κ mechanism responsible for stellar pulsations. In a partial ionization zone the κ mechanism is reinforced by the tendency of heat to flow into the zone during compression simply because its temperature has increased less than the adjacent stellar layers. This effect is called the γ mechanism, after the smaller ratio of specific heats caused by the increased values of C_p and C_v. Thus, the partial ionization zones are the pistons that drive the oscillations of stars; they

modulate the flow of energy through the layers of the star and are the direct cause of stellar pulsation.

In most stars there are two main partial ionization zones. The hydrogen partial ionization zone is a broad region with a characteristic temperature of 1 to 1.5 x 10^4 K, in which both the ionization of neutral hydrogen (H I –> H II) and the first ionization of helium (He I –> He II) occur. The He II partial ionization zone is a region deeper in the stellar interior with a characteristic temperature of 4 x 10^4 K, where further ionization of Helium takes place. The location of these zones within the star determines its pulsation properties and the location of these zones is determined by the temperature of the star. For stars hotter than $T_{eff} \sim 7500$ K, the partial ionization zones are located too close to the surface of the star, where there is not enough mass to drive the oscillations effectively. This accounts for the hot blue edge of the instability strip on the HR diagram. For stars cooler than $T_{eff} \sim 5500$ K, on the other hand, the partial ionization zones are deep in the stellar interior. However at low temperatures, energy transport via convection becomes quite efficient in the stellar interior, preventing the build-up of heat and pressure beneath the driving pulsation layer. This results in the red edge of the instability strip. The numerical simulations of the pulsation models show that the He II partial ionization zone is primarily responsible for the pulsation of the stars in the instability strip. The hydrogen ionization zone , however, still plays an important role, producing an observable phase lag between the maximum brightness of the star and its minimum radius.

Cepheids

The Cepheids are yellow supergiant pulsating variable stars which lie in a narrow instability strip (Fig. 1.6) in the middle of the HR diagram. As explained in the previous section, the Cepehids come in the category of the intrinsic variables for which the variation in the apparent brightness is due to the physical changes occurring inside the star. Their temperatures are 6000-8000k, and their periods are 1-100 days or more. There are two classes of Cepheids - one the classical Cepheids which are young (age $\sim$ 100 Myr) and massive than the Sun and the other the Population II Cepheids which are old and less massive than the Sun. The classical Cepheids are probably the best-known and most important of all pulsating variable stars. They are bright and generally have large amplitudes. There is an important relation between their period and their luminosity which

makes them standard candles for distance estimation. As they are relatively young, they are expected to be found in the disk of a galaxy. The structural parameters of the LMC and SMC disks are estimated using Cepheids by Nikolaev et al. (2004) and Groenewegen (2000) respectively.

RR Lyrae stars

The RRLS are metal poor, low mass, core helium burning stars which undergo radial pulsations. Their period of pulsation range from 0.2-1 day and their spectral types are between A5 to F5. These are horizontal branch stars (Fig. 1.6) with a temperature range between 6000-7500 K, where they are unstable against pulsation. As they are horizontal branch stars they have a very narrow range in luminosities. The RRLS are excellent tracers of the oldest observable population (age $\sim$ 10-13 Gyr) of stars in a galaxy. The RRLS can be divided into several types based on their light curves. Type *a* have moderately long periods, large ranges and highly asymmetrical light curves. Type *b* have longer periods, somewhat small ranges and less asymmetrical light curves. There is a fairly a smooth transition between type *a* and *b*, so there may not be any significant difference between them. Both these types pulsate in the radial fundamental mode. These two types are together known as type *ab*. Type *c* have shorter periods, small ranges and sinusoidal light curves. They pulsate in first radial overtone mode.

The type RRab stars have similar properties and have the same time-averaged luminosity (because they lie on the horizontal branch). So they are used for distance estimation (Borissova et al. 2009). Clementini et al. (2003) and Subramaniam (2006) used the dispersion of the RRab stars to estimate the line of sight depth of the LMC. Their dispersion from the mean magnitude is a measure of the depth of the host galaxy. As the RRLS are metal poor and represent the old population of the host galaxy, they are good tracers of the halo of a galaxy. Pejcha & Stanek (2009) studied the structure of the LMC stellar halo using the RRLS in the LMC.

The RRab stars have a range in metallicity and age. There are intrinsic variations in their luminosities due to evolutionary effects. For using the RRab stars as standard candles the mean magnitude should be corrected for metallicity and evolutionary effects. Like the RC stars these can also be used as indicators of relative distances of different regions in the MCs. Their range in metallicity, age and their intrinsic variations in luminosities also contribute to the dispersion in their mean magnitude. After correcting for these contributions the dispersion can be used as a measure of line of sight depth.

1.7 Overview of the Thesis

- **Chapter 1** : An introduction to the Magellanic system as well as to the tracers we studied are presented.
- **Chapter 2**: The optical and near infrared data of the tracers which we use in our study are described. Then the methodology we apply in different tracers are discussed in detail.
- **Chapter 3**: The estimation of the line of sight depth of different regions in the LMC using the V and I bands photometric data of the RC stars is presented. The variation of the line of sight depth across the LMC disk as well as the bar are analyzed in detail. Finally, the implications of the results are discussed.
- **Chapter 4**: The location of the bar of the LMC as well as the structures in it are studied. The V and I bands photometric data of the RC stars are used for this analysis.
- **Chapter 5**: The estimation of structural parameters (inclination, i and the position of the line of nodes, ϕ of the LMC disk) using the RC stars is described. This chapter is divided into two parts.
  - **Optical Study**: In the first part of the Chapter 5, the structure of the LMC disk is studied using the optical V and I bands photometric data. The effect of coverage, adopted center, reddening and the complicated inner structure of the LMC in the estimated parameters are discussed in detail in this section.
  - **Near Infrared study**: Reddening plays a major role in the estimation of the structural parameters of the LMC disk. As the effect of reddening is less in longer wavelengths the study using near infrared data is important. In the second part of Chapter 5, near infrared (J and H bands) data is used for the estimation of the structural parameters of the LMC disk. The results from the optical and near infrared studies are compared.
- **Chapter 6**: The RRLS in the LMC are studied in search of the real metal poor halo. The results from this study and its implications are discussed. The I band photometric data is used for this study.

- **Chapter 7**: The line of sight depth of different regions in the SMC are estimated using the RC stars. The results of this study are presented in this chapter.
- **Chapter 8**: The 3D structure of the older component of the SMC is investigated using the RC stars and RRLS. Data from the V and I bands are used for this study. The line of sight distances to different regions are estimated using both the RC stars and RRLS. The line of sight depth to different regions in the SMC, estimated from both these populations, and the density distributions are compared. Finally the structural parameters of the system in which these two populations are distributed are estimated.
- **Chapter 9**: The structural parameters of the SMC disk are estimated using the V and I bands data of Cepheids. The structures in the SMC disk are also studied.
- **Chapter 10**: The summary and conclusions of the thesis work are presented in this chapter. The possible future projects are discussed.

CHAPTER 2

DATA & METHODOLOGY

2.1 Data

The photometric data obtained from the Optical Gravitational Lensing Experiment (OGLE) survey, Magellanic Cloud Photometric Survey (MCPS) and the Infrared Survey Facility (IRSF) Magellanic Cloud survey are used for our study. The details of each data set are given below.

2.1.1 Optical Gravitational Lensing Experiment Survey

The Optical Gravitational Lensing Experiment (OGLE) project is a long term project with the main goal of searching for the dark matter with microlensing phenomena. The first phase (OGLE I 1992-1995) was dedicated to detect statistically significant number of microlensing events towards the Galactic bulge. OGLE I observations were taken from the 1m Swope telescope of the Las Campanas Observatory, operated by the Carnegie Institution of Washington. The second phase (OGLE II, from 1997-2000) of the OGLE survey observed the bar regions of both the LMC and the SMC. The third phase (OGLE III, from 2001-2009) observed the bar as well as the surrounding central regions of the MCs. The observations of OGLE II and OGLE III were taken using the 1.3 m Warsaw telescope located at Las Campanas Observatory, Chile, which is operated by the Carnegie Institution of Washington. The IVth phase has started and covers a larger area of the LMC and the SMC in the sky compared to OGLE III coverage. One of the major outcomes of the OGLE II and OGLE III surveys is a large photometric database of stars in the MCs. We have utilised these catalogs in our study of the MCs.

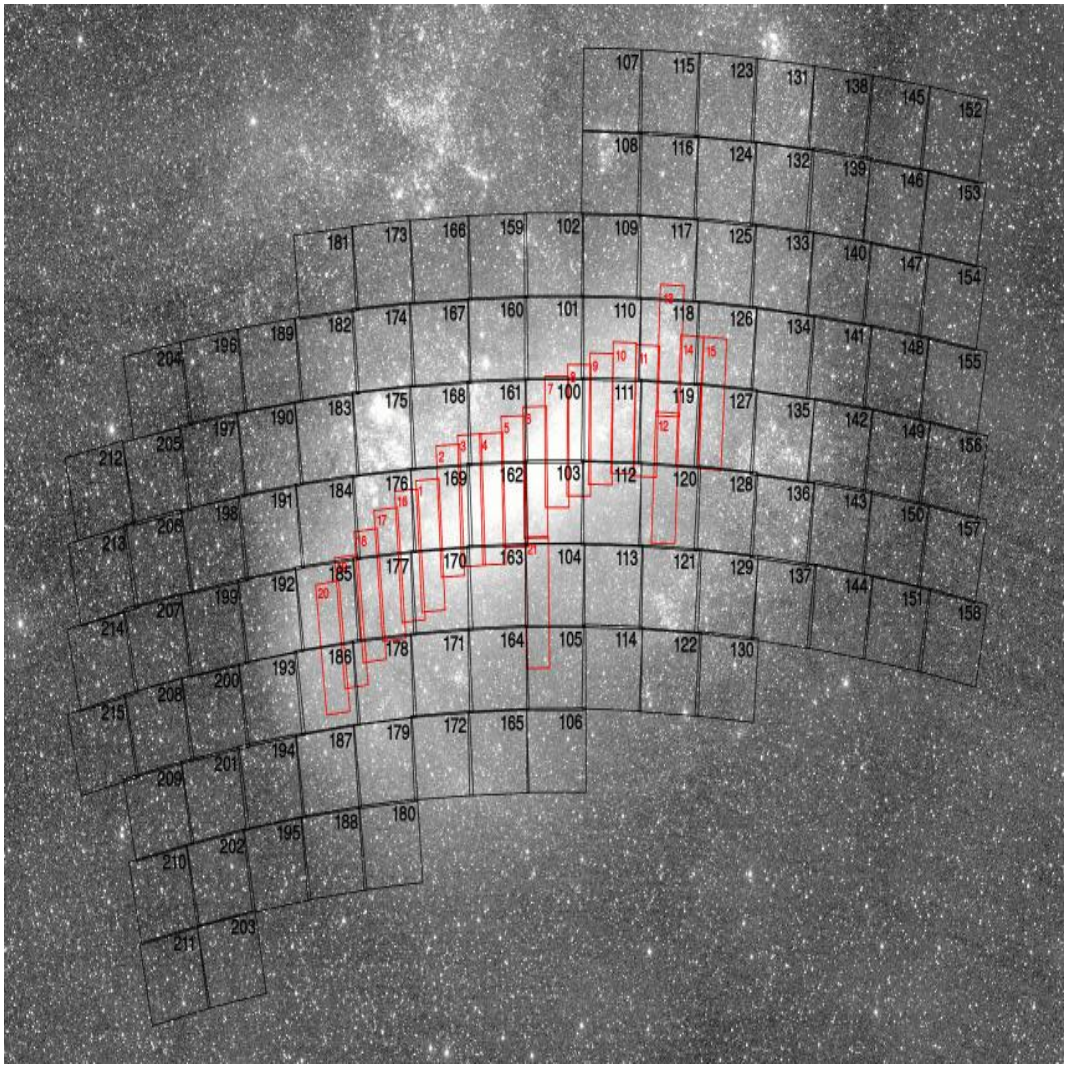

Figure 2.1: The red and black boxes are the OGLE II and OGLE III observed regions of the LMC.

During the second phase, OGLE II, the telescope was equipped with the first generation camera with a SITe 2048 x 2048 CCD detector working in drift scan mode. The pixel size was 24 μm which corresponds to 0.417 arcsec/pixel. For details of the instrumental setup refer to Udalski et al. (1997). The OGLE II survey scanned the central 5.7 square degrees of the LMC and presented a catalog (Udalski et al. 2000) of stars consisting of photometric data of 7 million stars in the B,V and I pass bands. The observed fields practically covered the entire bar of the LMC (21 fields), which covered 4.5 square degrees in the sky. Five additional fields in the North-West region of the LMC disk were also observed. The OGLE II survey of central region of the SMC contains photometric data of 2 million stars in the B,V and I pass bands. The catalog of the SMC (Udalski et al. 1998)

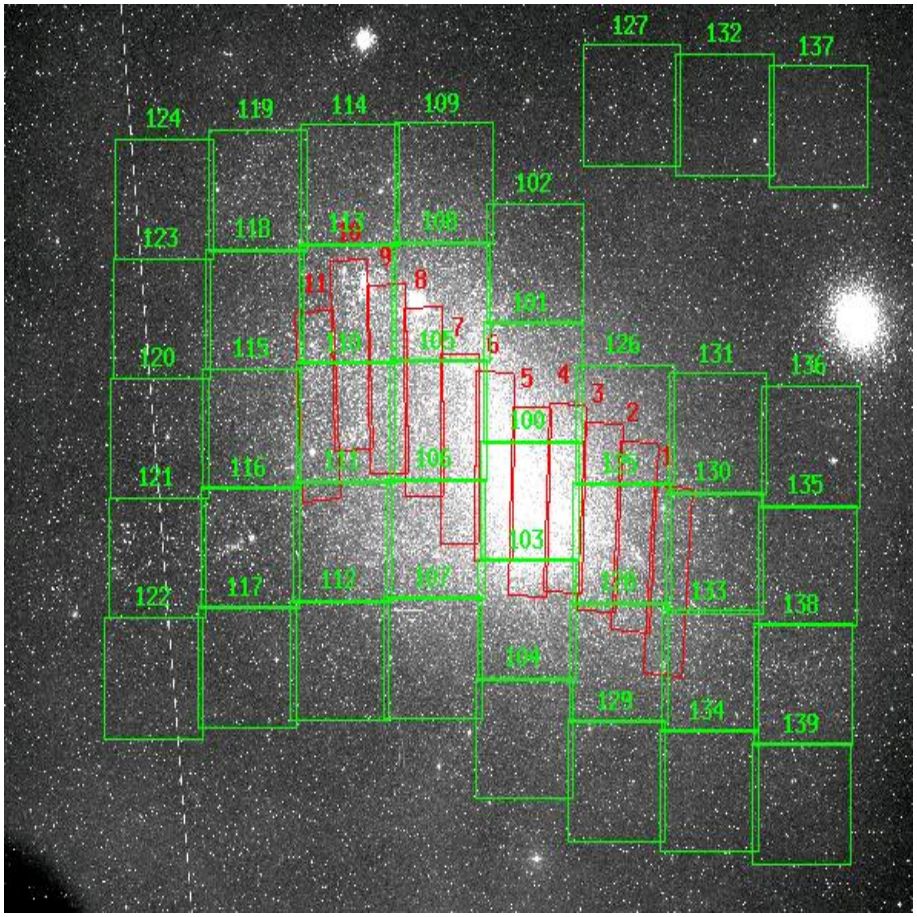

Figure 2.2: The red and green boxes are the OGLE II and OGLE III observed regions of the SMC.

presented data of 11 fields which cover the central 2.5 square degrees of the SMC in the sky.

During the third phase, OGLE III, the telescope was equipped with the second generation camera consisting of eight SITe 2048 x 4096 CCD detectors with 15 μm pixels which corresponds to 0.26 arcsec/pixel scale. Details of the instrumental setup can be found in Udalski (2003). The OGLE III survey observed the central 39.7 and 14 square degrees of the LMC and the SMC, which cover the central bar as well as the surrounding regions, in V and I bands. Udalski et al. (2008a) presented the *VI* photometric data of 35 million stars in the 116 LMC fields and Udalski et al. (2008b) presented the data of 6.2 million stars in the 40 SMC fields from this survey. The V and I band photometric data of the MCs obtained during the OGLE survey are used to identify and study the RC stars in the MCs. Along with the photometric maps, the OGLE survey identified and cataloged the variable stars (Cepheids, RRLS etc) in the MCs. The classical Cepheids and RR Lyrae

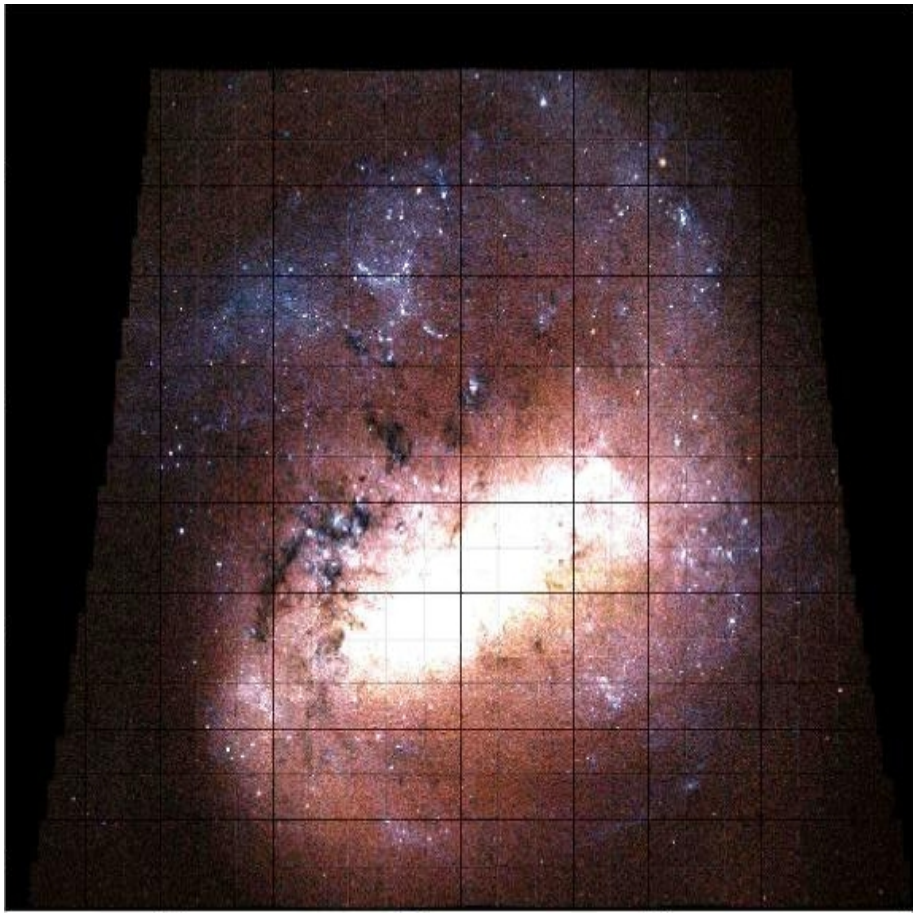

Figure 2.3: The MCPS observed region of the LMC.

stars identified in the MCs during the OGLE III survey are used in our study. Soszynski et al. (2008) and Soszyñski et al. (2010a) published the catalog of 3361 and 4630 classical Cepheids identified in the LMC and the SMC respectively during the OGLE III survey. The catalog of 24906 RRLS in the LMC and 2475 RR Lyrae stars in the SMC are given in Soszyński et al. (2009) and Soszyñski et al. (2010b) respectively. Th observed regions of the LMC and the SMC by this survey are shown in Fig. 2.1 and Fig. 2.2 respectively.

2.1.2 Magellanic Cloud Photometric Survey

The Magellanic Cloud Photometric Survey (MCPS) (Zaritsky et al. 1997) obtained the UBVI photometry of virtually all stars brighter than V= 21 mag in the MCs. The five year survey was conducted at the Las Campanas Observatory's 1 m Swope telescope and the images were obtained using the Great Circle Camera (GCC, Zaritsky et al. 1996). The

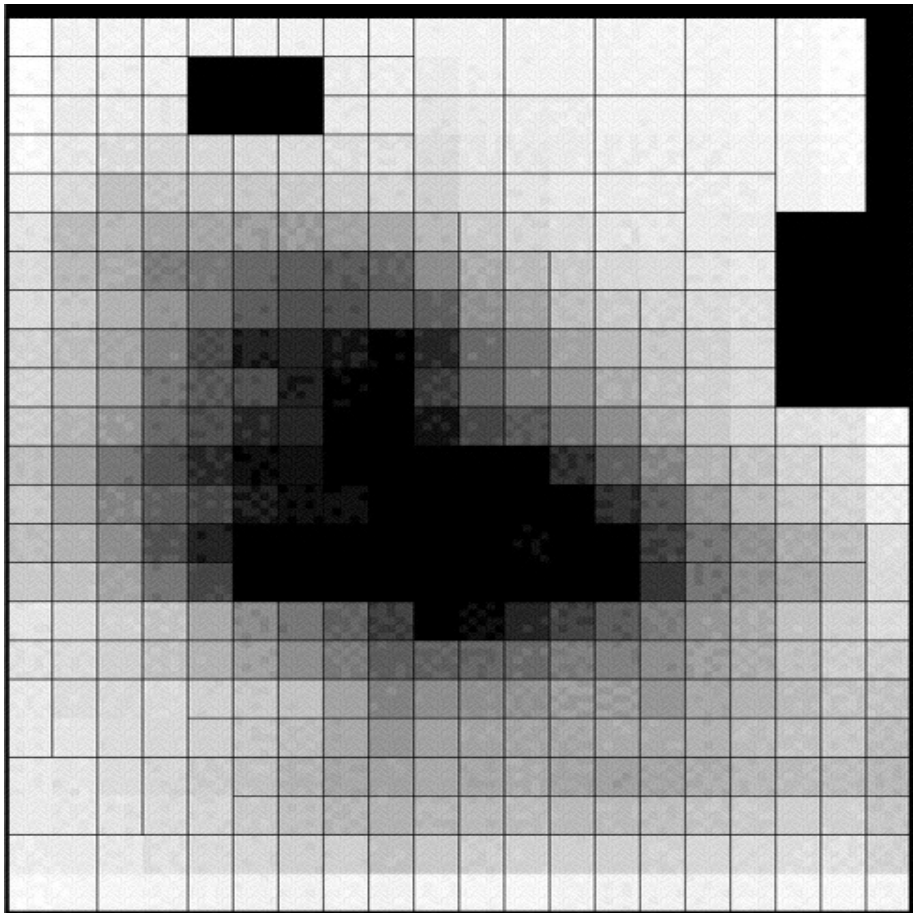

Figure 2.4: The MCPS observed region of the SMC.

thinned 2048 x 2048 CCD has 0.7 arcsec/pixel scale. The survey scanned 64 deg^2 of the LMC and 16 deg^2 of the SMC. The MCPS observed regions of the LMC and the SMC are shown in Fig. 2.3 and Fig. 2.4 respectively. Zaritsky et al. (2002) presented the UBVI photometric catalog of the SMC MCPS survey and Zaritsky et al. (2004) presented the data of the LMC MCPS survey. The RC stars in the MCs are identified and studied using this catalog also.

2.1.3 IRSF Magellanic Cloud Point Source Catalog

The IRSF Magellanic Cloud Point Source Catalog (IRSF-MCPSC) (Kato et al. 2007) is an outcome of an imaging survey of the MCs in the Near Infrared (NIR) bands J (1.25 μm), H (1.63 μm) and K_s (2.14 μm) during the period October 2001 to March 2006. The observations were made with the SIRIUS camera (Simultaneous three colour InfraRed Imager for Unbiased Survey) on the InfaRed Survey Facility (IRSF) 1.4 m tele-

scope at Sutherland, the South African Astronomical Observatory. The SIRIUS camera is equipped with three 1024 x 1024 HAWAII arrays to enable simultaneous observations in the three bands (Nagashima et al. 1999, Nagayama et al. 2003). The IRSF/SIRIUS pixel scale is 0.45 arcsec/pixel, yielding a field of view of 7.7 x 7.7 arcmin^2. The photometric catalog (Kato et al. 2007) includes 14811185 point sources for a 40 deg^2 area of the LMC and 2769682 sources for an 11 deg^2 area of the SMC. The LMC catalog is used for the study of the RC stars in the NIR bands.

2.2 Methodology

The relative distance of different regions of the MCs with respect to the mean distance to the galaxy and the extent along the line of sight are two important quantities which are required to understand the structure of the MCs. The basic methodology is to estimate the relative distances between regions in the MCs from the observed magnitudes, after correcting for extinction. All the tracers used in our study are standard candles. In the case of Cepheids, period-luminosity (PL) relation is used to estimate the individual distances to Cepheids and hence the relative distance of each Cepheid from the center of the galaxy. For the RC stars and RRLS their mean dereddened observed magnitude is a measure of the distances and the dispersion in their mean magnitude is an estimate of the line of sight depth. The R.A, Dec and relative distance between different regions are used to obtain a cartesian coordinate system. The structural parameters of different components of the MCs are obtained by applying appropriate methods, such as plane fitting procedure and inertia tensor analysis, on the cartesian coordinates.

2.2.1 Relative distances

- **Cepheids**: The methodology described below is similar to that used by Nikolaev et al. (2004) for the analysis of Cepheids. The analysis is based on the PL relation which is is given by

  $\overline{M_\lambda} = \alpha_\lambda \log P + \beta_\lambda$ .....(1)

  where λ denotes the photometric bands in which Cepheids are observed, $\overline{M_\lambda}$ is the mean intrinsic magnitude, α and β are the PL coefficients and P the pulsation period. The $\overline{M_\lambda}$ can be converted into observed mean magnitude, $\overline{m_\lambda}$ using the equation

$$\overline{m_\lambda} = \mu + \mathrm{A}_\lambda + \alpha_\lambda \mathrm{logP} + \beta_\lambda \text{ .....(2)}$$

where μ and A_λ are the distance modulus and extinction, in the photometric band denoted by λ, respectively. $\mathrm{A}_\lambda = \mathrm{R}_\lambda \mathrm{E}(B-V)$, where R_λ is the ratio of total to selective extinction and $\mathrm{E}(B-V)$ is the reddening. The quantities μ and $\mathrm{E}(B-V)$ can be divided into two parts, one mean quantity corresponding to the entire galaxy and the other which varies from star to star. The index i in the below equations denotes individual star.

$$\mu_i = \overline{\mu}_{galaxy} + \delta\mu_i \text{ .....(3)}$$

$$\mathrm{E}(B-V)_i = \overline{E(B-V)}_{galaxy} + \delta\mathrm{E}(B-V)_i \text{ .....(4)}$$

The mean quantities can be incorporated in the quantity β and the equation for each star connecting the mean observed magnitude, relative distance and reddening is given as

$$\overline{m_{\lambda,i}} = \delta\mu_i + \mathrm{R}_\lambda \delta\mathrm{E}(B-V)_i + \alpha_\lambda \mathrm{logP}_i + \beta'_\lambda \text{.....(5)}$$

The above equation can be solved using linear least square method, to obtain the individual distances and reddenings. As we are interested in the relative distance (ΔD) and relative reddening between different regions in the galaxy, the mean values of distance and reddening we take are not going to affect the determination of the structural parameters of the galaxy.

- **Red Clump stars**: The observed region of the MCs from different data sets are divided into several sub-regions. A sub-region of 1 arcmin^2 area on the sky corresponds to an area of 14.5 pc^2 and 17.5 pc^2 in the LMC and the SMC respectively. For each sub-region $(V-I)$ vs I colour magnitude diagram (CMD) is plotted and the RC stars are identified. A sample CMD of both the LMC and the SMC are shown in Fig. 2.5 and Fig. 2.6 respectively. For all the regions in the MCs, the RC stars are found to be located well within the box shown in the CMD, with boundaries 0.65 - 1.35 mag in $(V-I)$ colour and 17.5 - 19.5 mag in I magnitude.

  The RC stars occupy a compact region in the CMD and they have a constant characteristic I band magnitude and $(V-I)$ colour. A spread in magnitude and colour

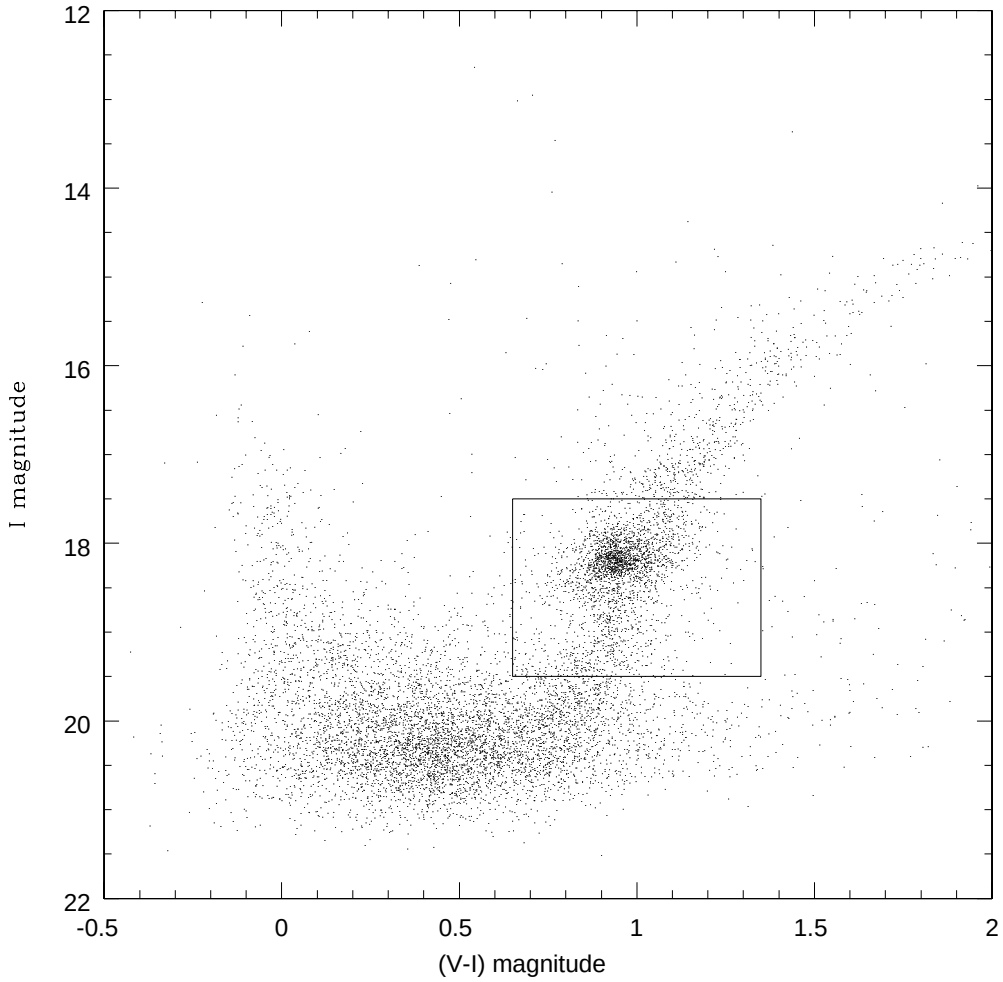

Figure 2.5: A sample CMD of a sub-region in the LMC. The box used to identify the RC stars is also shown.

of red clump stars is observed in the CMDs of both the LMC and the SMC. Their number distribution profiles resemble a Gaussian. The peak values of their color and magnitude distributions are used to obtain the dereddened RC magnitude.

To obtain the number distribution of the RC stars in each region, the data are binned in colour and magnitude. The obtained distributions in colour and magnitude are fitted with a function, Gaussian + quadratic polynomial. The Gaussian represents the RC stars and the other terms represent the red giants in the region. A non linear least square method is used for fitting and the parameters are obtained. In Fig. 2.7, Fig. 2.8, Fig. 2.9 and Fig. 2.10 the colour and magnitude distributions of the RC stars in the LMC and the SMC are shown respectively. The best fit profile is also

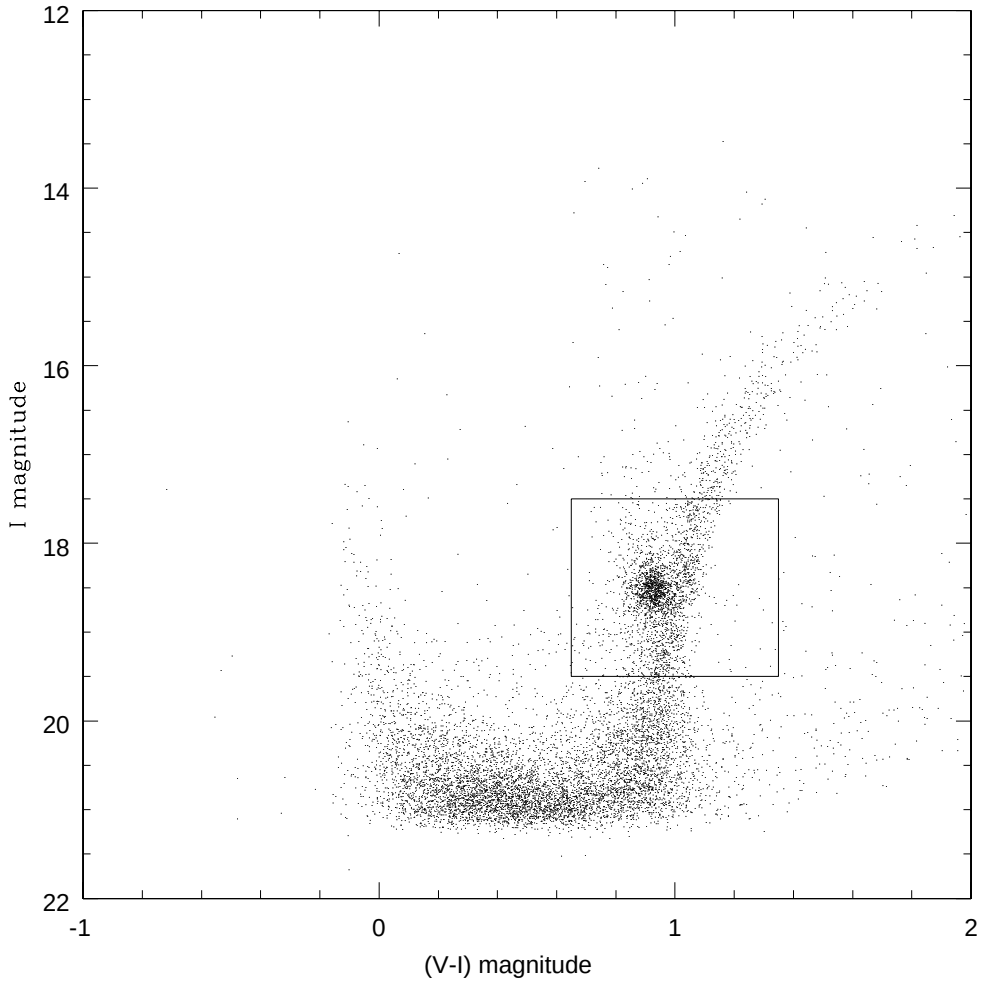

Figure 2.6: A sample CMD of a sub-region in the SMC. The box used to identify the RC stars is also shown

shown in all the plots. The parameters obtained are the coefficients of each term in the function used to fit the profile, error in the estimation of each parameter and reduced χ^2 value. The errors in the estimated parameters are calculated using the covariance matrix. The parameters that we are interested in the estimation of the dereddened I_0 magnitude are the peak I mag and $(V - I)$ colour.

The peak values of colour, $(V - I)$ mag in each location is used to estimate the reddening. The reddening is estimated using the formula

$$E(V - I) = (V - I)_{observed} - (V - I)_{intrinsic} \quad \text{.....(6)}$$

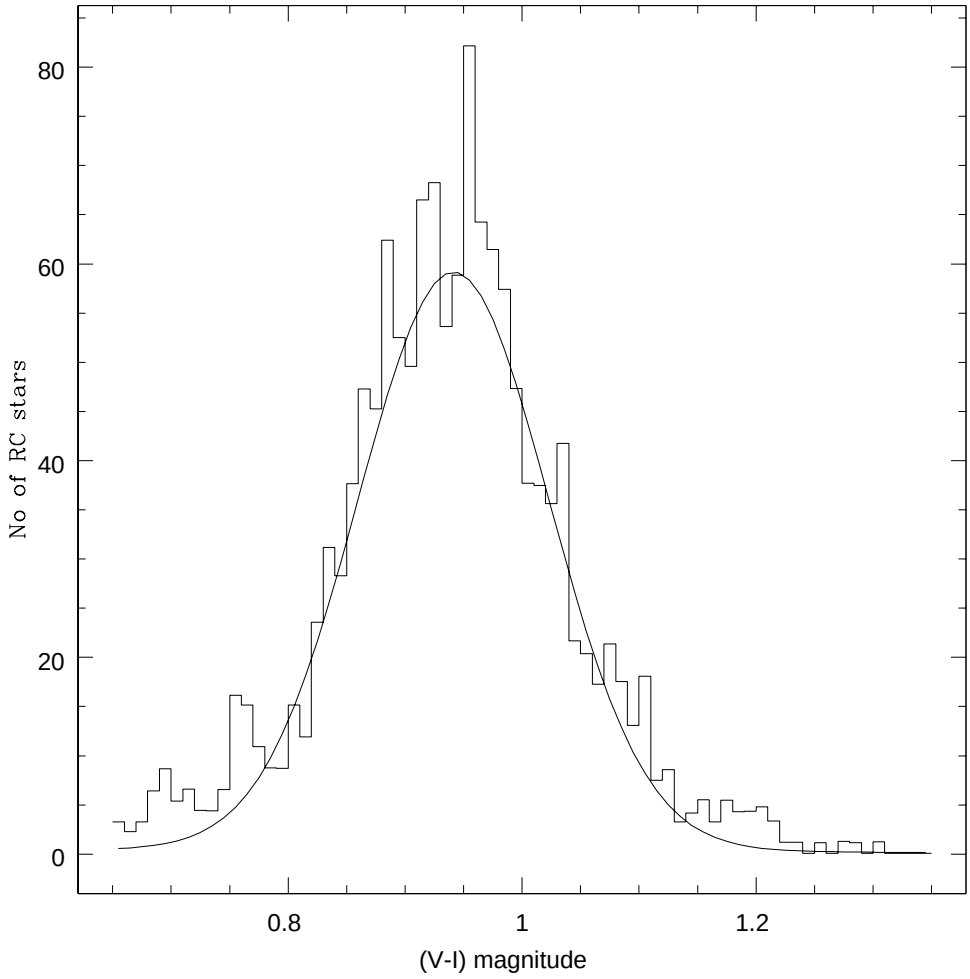

Figure 2.7: A typical colour distribution of the RC stars in the LMC. The best fit to the distribution is also shown.

where $(V-I)_{intrinsic}$ is the intrinsic colour of the RC stars in the MCs. The $(V-I)_{intrinsic}$ for the LMC is taken as 0.92 mag (Olsen & Salyk 2002). The intrinsic colour of the RC stars in the SMC is chosen as 0.89 mag to produce a median reddening equal to that measured by Schlegel et al. (1998) towards the SMC. The interstellar extinction is estimated using the formula, A_I = 1.4 x E($V-I$) (Subramaniam 2005).

After correcting the mean I mag for interstellar extinction, I_0 mag for each region is estimated using the relation

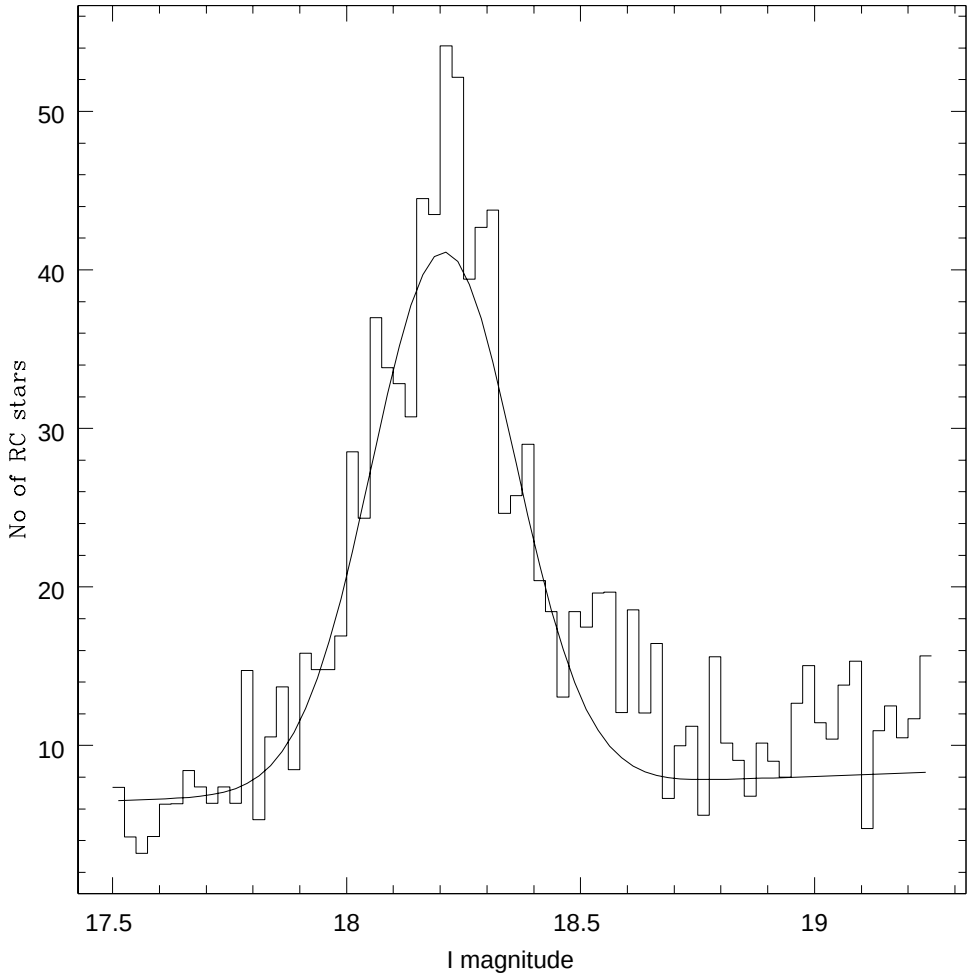

Figure 2.8: A typical magnitude distribution of the RC stars in the LMC. The best fit to the distribution is also shown.

$I_0 = I_{peak}$ - A_I .....(7)

The error in I_0 is estimated as

δI_0^2 = (avg error in peak I)^2 + (1.4 x avg error in peak $(V - I)$)^2 .....(8)

The variation in the I_0 mag between the sub-regions is assumed only due to the difference in the relative distances. Thus the difference in I_0 between the sub-regions

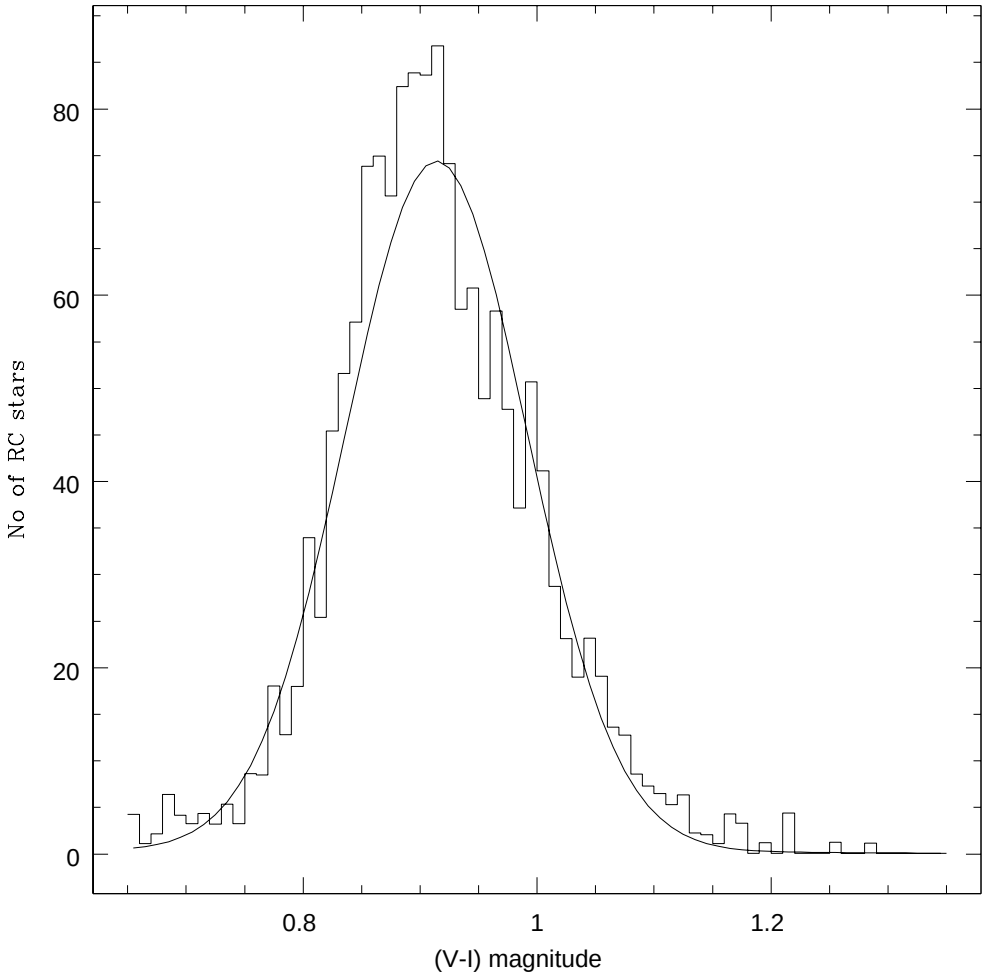

Figure 2.9: A typical colour distribution of the RC stars in the SMC. The best fit to the distribution is also shown.

is a measure of the relative distance (ΔD), using the distance modulus formula given below

(I_0 mean − I_0 of each region) = $5\log_{10}(D_0/(D_0 \pm \Delta D))$.....(9)

where D_0 is the mean distance to the galaxy.

- **RR Lyrae stars**: The ab type stars among the RRLS could be considered to belong to a similar class and hence assumed to have similar properties. The mean magnitude of these stars in the I band, after correcting for the metallicity and extinction effects, can be used for the estimation of distance. The reddening obtained using

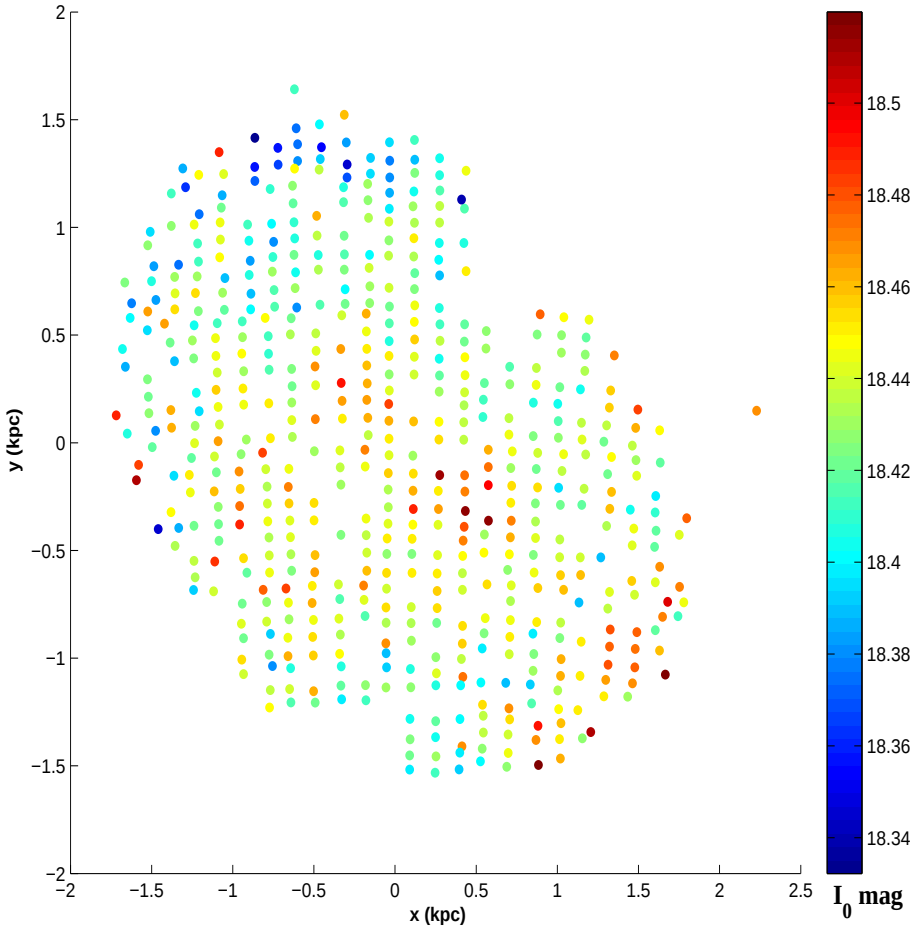

Figure 2.10: A typical magnitude distribution of the RC stars in the SMC. The best fit to the distribution is also shown.

the RC stars (described in the previous sub-section) is used to correct the extinction to individual RRLS. Stars within each bin of the reddening map are assigned a single reddening and it is assumed that reddening does not vary much within the bin. Thus the extinction corrected I_0 magnitude for all the RRLS are estimated.

2.2.2 Line of sight depth

- **Red Clump stars**: The spread in the distribution of the RC stars in the CMD includes the information of the line of sight depth of the region. The width in the colour and magnitude distributions of the RC stars can be used to estimate the line

of sight depth. The width of the Gaussian in the distribution of colour (σ_{colour}) is due to the internal reddening ($\sigma_{internalreddening}$), apart from observational error (σ_{error}) and population effects ($\sigma_{intrinsic}$). The width in the distribution of magnitude (σ_{mag}) is due to population effects ($\sigma_{intrinsic}$), observational error (σ_{error}), internal extinction ($\sigma_{internalextinction}$) and depth ($\sigma_{depth}$). By deconvolving the effects of observational error, extinction and population effects from the dispersion in magnitude, an estimate of depth can be obtained. By applying an non linear least square fit, the observed colour and magnitude distributions (as explained in section 2.2.1 on the RC stars) are fitted with a Gaussian + quadratic polynomial term and parameters are obtained. The parameters required for the estimation of the line of sight depth are σ_{mag} and σ_{colour}. The errors associated with both the parameters are also estimated.

The following relations are used to estimate the resultant dispersion due to depth.

$$\sigma^2_{col} = \sigma^2_{internalreddening} + \sigma^2{}_{intrinsic} + \sigma^2{}_{error} \quad \text{.....(10)}$$

$$\sigma^2{}_{mag} = \sigma^2{}_{depth} + \sigma^2{}_{internalextinction} + \sigma^2{}_{intrinsic} + \sigma^2{}_{error} \quad \text{.....(11)}$$

The average photometric errors in I and V band magnitudes were calculated for each region and the error in I magnitude and $(V - I)$ colour were estimated. These were subtracted from the observed width of magnitude and colour distribution respectively, thus accounting for the photometric errors (last term in the above equations). The contribution from the heterogeneous population of the RC stars which we discussed in section 1.6.2, $\sigma_{intrinsic}$ for both colour and magnitude are also subtracted from the observed dispersions. The $\sigma_{intrinsic}$ values in colour and magnitude taken for the LMC are 0.025 mag and 0.01 mag respectively. In the case of the SMC, 0.03 mag and 0.075 mag are taken as the $\sigma_{intrinsic}$ in colour and magnitude respectively. These values are taken from Girardi & Salaris (2001). After correcting for the population effects and the observational error in colour, the remaining spread in colour distribution (first equation) is taken as due to the internal reddening, E$(V - I)$. This is converted into extinction in I band, A_I. This is used to deconvolve the effect of internal extinction from the spread in magnitude. The resultant width in magnitude is converted into depth in kpc using distance modulus formula.

The error in the estimation of the dispersion corresponding to depth is obtained from the errors involved in the estimation of width of colour and magnitude dis-

tribution. The random error associated with the width corresponding to depth is $\Delta\text{depth}^2 = \Delta I^2_{width} + \Delta(V-I)^2_{width}$. Thus the associated error in the estimation of depth can be calculated for all the locations. This error will also translate as the minimum depth that can be estimated.

- **RR Lyrae stars**: Using the dereddened I_0 magnitude of each RR Lyrae star, the dispersion in the surveyed region of the MCs can be found. The data are binned to estimate dispersion. For each bin the mean magnitude and the dispersion can be estimated. The dispersion after correcting for age and evolutionary effects is a measure of the depth of the MCs. The corrections applied for the metallicity and evolutionary effects in the dispersion while estimating the line of sight depth are explained in detail in the respective chapters.

2.2.3 Conversion to Cartesian coordinate system

The relative distance of each region of the MCs is obtained from the variation in the I_0 magnitude. Here, the variation in I_0 is considered only due to the line of sight distance variation within the galaxy. The error in magnitude is also converted into error in distance.

Then the x,y, and z coordinates are obtained using the transformation equations given below (van der Marel & Cioni 2001, see also Appendix A of Weinberg & Nikolaev 2001).

$x = -D\sin(\alpha - \alpha_0)\cos\delta$,.....(12)

$y = D\sin\delta\cos\delta_0 - D\sin\delta_0\cos(\alpha - \alpha_0)\cos\delta$,.....(13)

$z = D_0 - D\sin\delta\sin\delta_0 - D\cos\delta_0\cos(\alpha - \alpha_0)\cos\delta$,.....(14)

where D_0 is the distance to the center of the MCs and D, the distance to the each sub-region is given by $D = D_0 + \Delta D$. The (α, δ) and (α_0, δ_0) represents the R.A and Dec of the region and the center of the MCs respectively.

The equation of the plane used is given by

$Ax+By+Cz+D=0$

From the coefficients of the plane A,B & C, i and ϕ can be calculated using the formula given below.

Inclination, i = arccos(C/ $\sqrt{A^2 + B^2 + C^2}$) .....(15)

PA_{lon}, ϕ = arctan(-A/B)-sign(B)π/2.....(16)

2.2.4 Inertia tensor analysis

The parameters of the spheroidal/ellipsoidal component of the SMC, like the axes ratio, inclination of the longest axis with the line of sight axis, i and the position angle of the projection of the ellipsoid, ϕ are estimated using the inertia tensor analysis. A detailed description of the tensor analysis is given below.

Moment of inertia of a body characterizes the mass distribution within the body. For any rotating three dimensional system, we can compute the moment of inertia about the axis of rotation, which passes through the origin of a local reference (XYZ) frame, using the inertia tensor. The origin of the system is the center of mass of the body. Consider a system made up of i number of particles, each particle with a mass m. For each particle the (x, y and z) coordinates with respect to the center of mass is known. Then, the moment of inertia tensor, I of the system is given by

$$\mathrm{I} = \begin{pmatrix} I_{xx} & I_{xy} & I_{xz} \\ I_{yx} & I_{yy} & I_{yz} \\ I_{zx} & I_{zy} & I_{zz} \end{pmatrix}$$

where

$I_{xx} = \Sigma_i\ m_i(y_i^2 + z_i^2)$

$I_{yy} = \Sigma_i\ m_i(x_i^2 + z_i^2)$

$I_{zz} = \Sigma_i\ m_i(x_i^2 + y_i^2)$

$I_{xy} = I_{yx} = \Sigma_i\ m_i(x_i + y_i)$

$I_{yz} = I_{zy} = \Sigma_i\ m_i(y_i + z_i)$

$I_{xz} = I_{zx} = \Sigma_i\ m_i(x_i + z_i)$

The components, I_{xx}, I_{yy} and I_{zz} are called the moments of inertia while I_{xy}, I_{yx}, I_{xz}, I_{zx}, I_{yz} and I_{zy} are the products of inertia. These components given above are basically specific to the local reference frame and reflect the mass distribution within the system in relation to the local reference frame. If we align the axes of the local reference frame in such a

way that the mass of the system is evenly distributed around the axes then the product of inertia terms vanish. This aligning the axes of local reference frame in such a way that the product of inertia terms vanish, would mean the transformation of the local reference frame (XYZ) to a system (X'Y'Z') . In the new frame of reference, inertia tensor, I' is given by

$$\mathrm{I'} = \begin{pmatrix} I_{x'x'} & 0 & 0 \\ 0 & I_{y'y'} & 0 \\ 0 & 0 & I_{z'z'} \end{pmatrix}$$

The terms $I_{x'x'}$, $I_{y'y'}$ and $I_{z'z'}$ are the non zero diagonal terms of the inertia tensor in the new reference frame (X'Y'Z') and are called the principal moments of inertia of the body. The three axes in the new reference frame are called the principal axes of the body.

To determine the principal axes of the system we have to diagonalize the inertia tensor I, which is obtained with respect to the local reference frame. The diagonalization of the inertia tensor provides three eigen values (λ_1, λ_2 and λ_3) which correspond to the moments of inertia ($I_{x'x'}$, $I_{y'y'}$ and $I_{z'z'}$) about the principal axes. For each eigen value we can compute the corresponding eigen vector. The eigen vectors corresponding to each eigen values are given as $e_{\lambda_1} = e_{11}$ i' + e_{12} j' + e_{13} k', $e_{\lambda_2} = e_{21}$ i' + e_{22} j' + e_{23} k' & $e_{\lambda_3} = e_{31}$ i' + e_{32} j' + e_{33} k' where i', j' and k' are unit vectors along the X', Y' and Z' axes respectively. The transformation of the XYZ system to X'Y'Z' can be obtained using the transformation matrix, T which is made up of the 9 components of the 3 eigen vectors. The transformation matrix, T is given by

$$\mathrm{T} = \begin{pmatrix} e_{11} & e_{21} & e_{31} \\ e_{12} & e_{22} & e_{32} \\ e_{13} & e_{23} & e_{33} \end{pmatrix}$$

From the eigen values and the transformation matrix, the axes ratio and the orientation of the characteristic ellipsoid that best describes the spatial distribution of the particles in the system can be obtained. As the moment of inertia of a system characterizes the resistance of the system to rotation, the component of moment of inertia along the major axis of the system will be least and maximum along the minor axis. Thus the three eigen values which represent the moments of inertia of the three axes (such that $I_{x'x'} > I_{y'y'} > I_{z'z'}$) of the ellipsoid can be written as

$I_{x'x'} = M(a^2 + b^2)$

$I_{y'y'} = M(a^2 + c^2)$

$I_{z'z'} = M(b^2 + c^2)$

where a,b & c are the semi-axes of the ellipsoid such that a>b>c and M the total mass of the system. Using the above relations we can estimate the axes ratio of the ellipsoid which best describes the spatial distribution of the particles in the system. The transformation matrix, T describes the spatial directions or the orientation of the ellipsoid with respect to the local reference frame.

CHAPTER 3

LINE OF SIGHT DEPTH ESTIMATION OF THE LARGE MAGELLANIC CLOUD USING THE RED CLUMP STARS *

3.1 Introduction

The line of sight depth of the MCs could vary as a function of radial distance from the center due to tidal effects. The presence of variation in depth across the LMC is likely to give valuable clues to the interactions it has experienced in the past. The N-body simulations by Weinberg (2000) predicted that the LMC's evolution is significantly affected by its interactions with the Milky Way, and the tidal forces will thicken and warp the LMC disk. Alves & Nelson (2000) studied the carbon star kinematics and found that the scale height, h, increased from 0.3 to 1.6 kpc over the range of radial distance, R, 0.5 to 5.6 kpc and hence concluded that the LMC disk is flared. Using an expanded sample of carbon stars, van der Marel et al. (2002) also found that the thickness of the LMC disk increases with the radius. There has not been any direct estimate of the thickness or the line of sight depth of the bar and disk of the LMC so far.

In this study, we used the dispersion in the colour and magnitude distribution of the RC stars for the line of sight depth estimation. The dispersion in colour is due to a combination of observational error, internal reddening (reddening within the disk of the LMC) and population effects. The dispersion in magnitude is due to internal disk extinction,

*Part of the results presented here are published in Subramanian, S., & Subramaniam, A., 2009, A&A, 496, 399

depth of the distribution, population effects and photometric errors associated with the observations. By deconvolving other effects from the dispersion of magnitude, we estimated the dispersion only due to the depth of the disk. The advantage of choosing the RC stars as a proxy is that a large number of these stars are available to determine the dispersions in their distributions with good statistics, throughout the LMC disk. The depth estimated here would corresponds to the depth of the intermediate age LMC disk. The depth of the intermediate age disk of the LMC may give clues to the formation and evolution, and thus in turn would give clues to the interaction of the LMC with the SMC. This could also place some constraints on their interaction with our Galaxy. Measurements of line of sight depth in the central regions of the LMC is of strong interest to understand the observed microlensing towards this galaxy.

3.2 Data & Analysis

The V and I bands photometric data from the OGLE II, OGLE III and MCPS catalog are used for this study. The OGLE II , OGLE III and the MCPS observed fields are divided into 1664 sub-regions (each sub-region having an area of 3.56×3.56 arcmin^2), 7416 sub-regions (each having an area of 4.44×4.44 arcmin^2) and 1512 sub-regions (each having an area of $\sim$ 10.53×15 arcmin^2) respectively. The data in the central regions may suffer from incompleteness due to crowding effects. The incompleteness in the OGLE II data is corrected using the values given in Udalski et al. (2000). The effect of crowding in the MCPS and OGLE III data is discussed in section 3.5. As explained in section 2.2.1, the RC stars are identified from the $(V - I)$ vs I CMD of each sub-region. Out of 1512 sub-regions of the MCPS field, only 1374 regions have a reasonable number of RC stars to do the analysis. In the case of OGLE III, 6826 regions with reasonable number of the RC stars are found. The number of RC stars in each region depends on the stellar density. The number is large in the central regions, whereas it decreases in the disk. The number of RC stars ranges between 500 - 2000 in the bar region, whereas the range is 100 - 1500 in the disk. For all the data sets, only data with errors less than 0.15 mag are taken for the analysis.

As discussed in chapter 2 the width corresponding to the line of sight depth can be obtained from the colour and magnitude distributions of the RC stars. To obtain the number distribution of the RC stars in each region, the data are binned with a bin size of 0.01 and 0.025 mag in colour and magnitude respectively. The width in colour and magnitude distributions are obtained using non-linear least square fits. Along with the

width of the distributions, the error in the estimation of each parameter and the goodness of the fit, which is the same as the reduced χ^2 value are obtained. Regions with reduced χ^2 values greater than 2.6 are omitted from the analysis. As the important parameter for our calculations is the width associated with the two distributions, we also omitted regions with fit error of width greater than 0.1 mag from our analysis. After these omissions, the number of regions useful for analysis in OGLE II, OGLE III and MCPS data sets became 1528, 5869 and 1301 respectively. Thus, the total observed dispersion in (V−I) colour and I magnitude are estimated for the RC stars in all these regions.

From the observed dispersions in the colour and magnitude distributions of the RC stars, width corresponding to the line of sight depth and the error associated with it are obtained using the equations (10) and (11) given in section 2.2.2. To convert the internal reddening to internal extinction we used the Rieke & Lebofsky (1985) interstellar extinction curve of our Galaxy. The relation is given by A_I = 0.934 x E($V - I$). The interstellar extinction law of our Galaxy is adopted for the calculations of Magellanic Clouds based on the results of the studies by Nandy & Morgan (1978), Lequeux et al. (1982) and Misselt et al. (1999), which showed that the LMC has extinction curves similar to that found in our Galaxy. The error associated with the line of sight depth will translate as the minimum depth that can be estimated. The minimal depth that can be estimated is $\sim$ 360 pc in the central regions and $\sim$ 650 pc in the outer regions.

3.3 Internal reddening in the LMC

One of the by products of this study is the estimation of internal reddening in the LMC. The shift of the peak of the (V−I) colour distribution from the expected value was used by Subramaniam (2005) to estimate the line of sight reddening map to the OGLE II region of the LMC. The above study estimated the reddening between the observer and the observed region in the LMC. In this study, we use the width of the (V−I) colour distribution to estimate an internal reddening map across the LMC. This estimates the front to back reddening of a given region in the LMC, which we call as the internal reddening (E(V−I)), and does not estimate the reddening between the front end of the region and the observer. Thus, this estimate traces the reddening within the bar/disk of the LMC and hence the location of the dust.

The colour coded figures of the internal reddening estimates in the LMC from OGLE II and OGLE III are presented in Fig. 3.1. A similar colour coded plot for the estimates from the MCPS data is shown in Fig. 3.2. It can be seen that the internal reddening is high only in some specific regions in the LMC. Most of the regions have very negligible

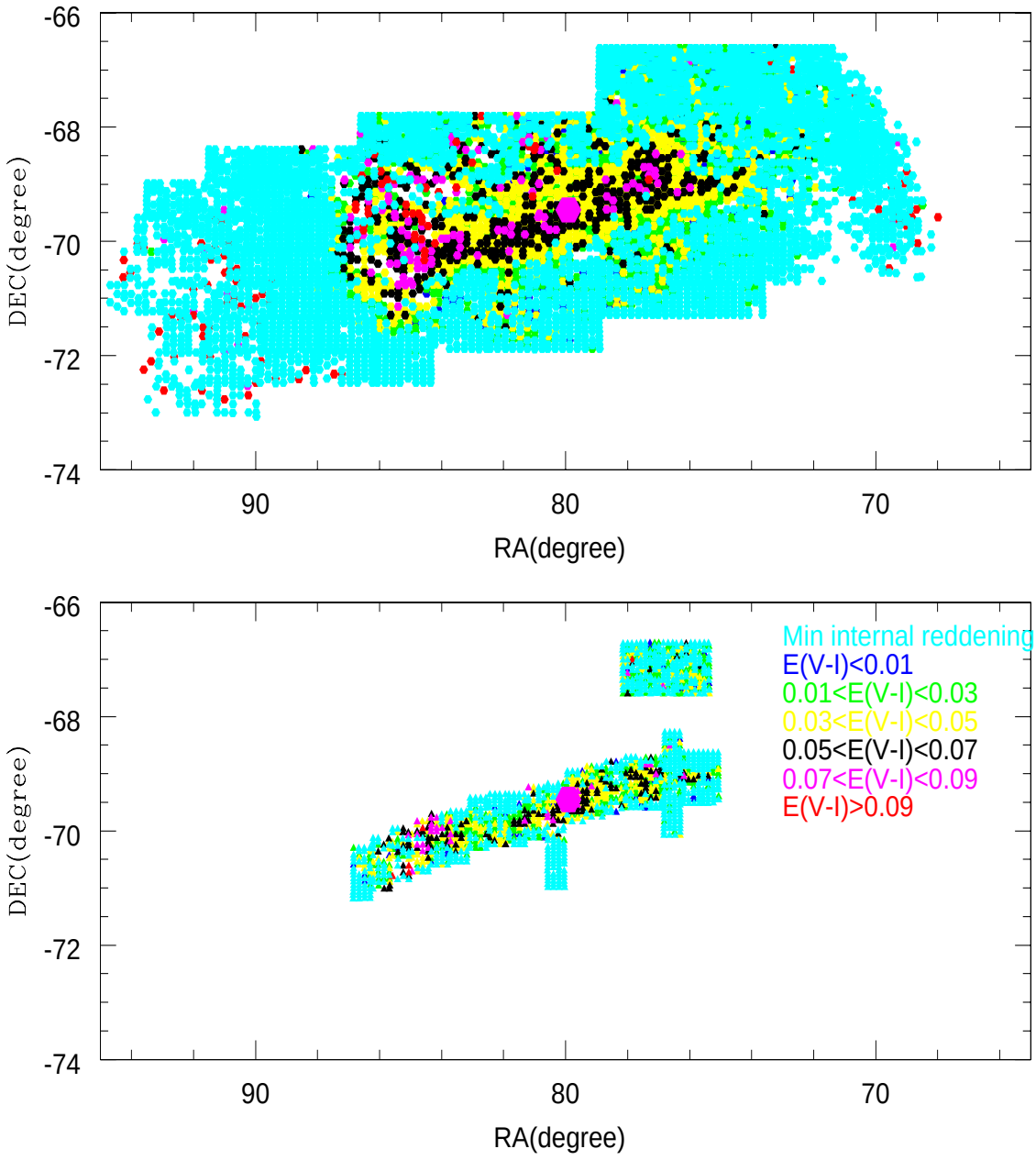

Figure 3.1: Two dimensional plot of the internal reddening in the LMC. The colour code is given in the figure. The magenta dot represents the optical center of the LMC. The upper plot is derived from the OGLE III data, whereas the lower plot is derived from the OGLE II data.

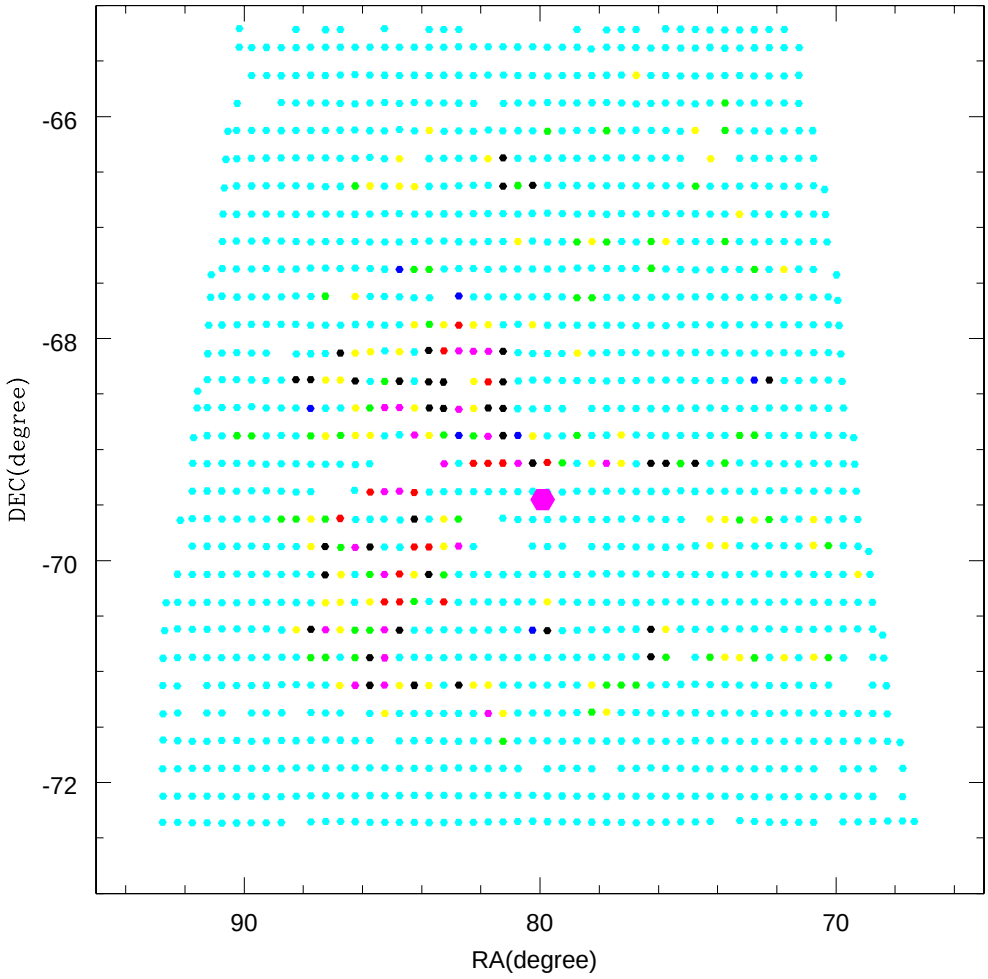

Figure 3.2: Two dimensional plot of the internal reddening in the LMC derived from the MCPS data. The colour code is same as that of Fig. 3.1. Magenta dot represents the optical center.

internal reddening suggesting that most of the regions in the LMC are optically thin. The regions of high internal reddening are located near the eastern end of the bar and the 30 Dor star forming region. The highest internal reddening estimated is E(V−I) = 0.13 mag in the OGLE II region, which is the bar region and 0.16 mag in the MCPS region, close to the 30 Dor location. In the case of OGLE III observed region the highest value of E($V - I$) is 0.14 mag. The regions in OGLE III field with this highest value of internal reddening are seen in the bar as well in the western edge of the disk. It is noteworthy that the highest internal reddening value estimated from all these data sets are not very high. The OGLE II and OGLE III internal reddening maps show that, apart from the

eastern end of the bar, some regions near the center also have large internal reddening. The MCPS data shows that the internal reddening across the LMC disk as seen by the RC stars is very small. But from OGLE III data we can see some regions in the western and eastern ends of the disk have larger internal reddening. The error associated with the width of colour distribution is translated as the minimum internal reddening that can be estimated. The minimum internal reddening that can be estimated in the central regions as well as in the disk of the LMC is ~ 0.003 mag. It is interesting to see low internal reddening across the LMC, as seen by the RC stars. This is in contradiction to the large extinction expected near the star forming regions, especially near 30 Dor. The reddening is estimated here using the same type of stars that are used to estimate the depth. Thus, we maintain the consistency of the same tracer for estimating the above two quantities. The higher values for the foreground reddening estimates were obtained by Harris et al. (1997) using the MCPS data for OB stars, whereas lower values were obtained using RC stars for the same regions by Subramaniam (2005) using OGLE II data. Thus, the reddening values estimated varies with respect to the tracer used. This variation of reddening as a function of the population is suggestive of population segregation across the LMC. The above results might suggest that the star forming regions in the LMC are likely to be behind the RC disk.

3.4 Results

The line of sight depth in the LMC has been derived using three data sets. The OGLE II data cover the central region and this is basically the bar region of the LMC. OGLE II data also cover a small detached disk region in the north-western direction. The OGLE III fields cover the bar as well as the surrounding regions of the disk. MCPS data cover a slightly more area of the disk compared to OGLE III. As the resolution of OGLE III data is higher than that of the MCPS data, we have finer area binning for the OGLE III data. Thus the OGLE II data is suitable to derive the depth of the bar region alone, whereas the MCPS and OGLE III data are suitable to derive the depth of the bar as well as the disk regions. The three data sets can be used for consistency checks and the results derived will be compared.

The depth of 1528 regions of the LMC (OGLE II data) are calculated. Out of 1528 regions, 1214 are in the central bar region and the remaining 314 regions are in the north western disk region. In the north western disk region there are regions with minimal thickness. The depth of 1301 regions of the LMC (MCPS data) are also calculated. A higher resolution two dimensional map of the depth of the bar and the disk is also ob-

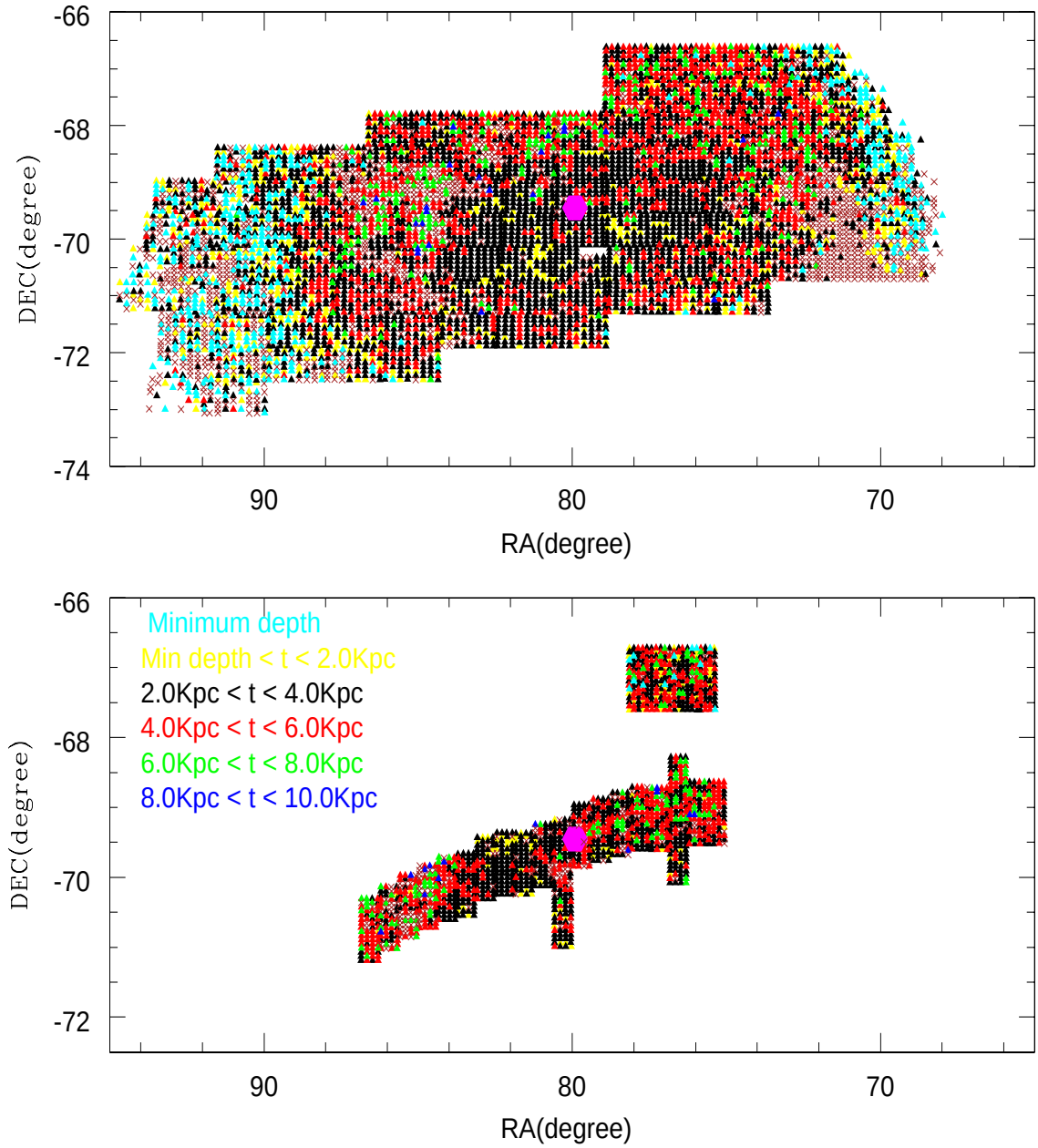

Figure 3.3: Two dimensional plot of depth (t) in the LMC. The colour code is given in the figure. The magenta dot represents the optical center of the LMC. The crosses represent the omitted regions due to poor fit.

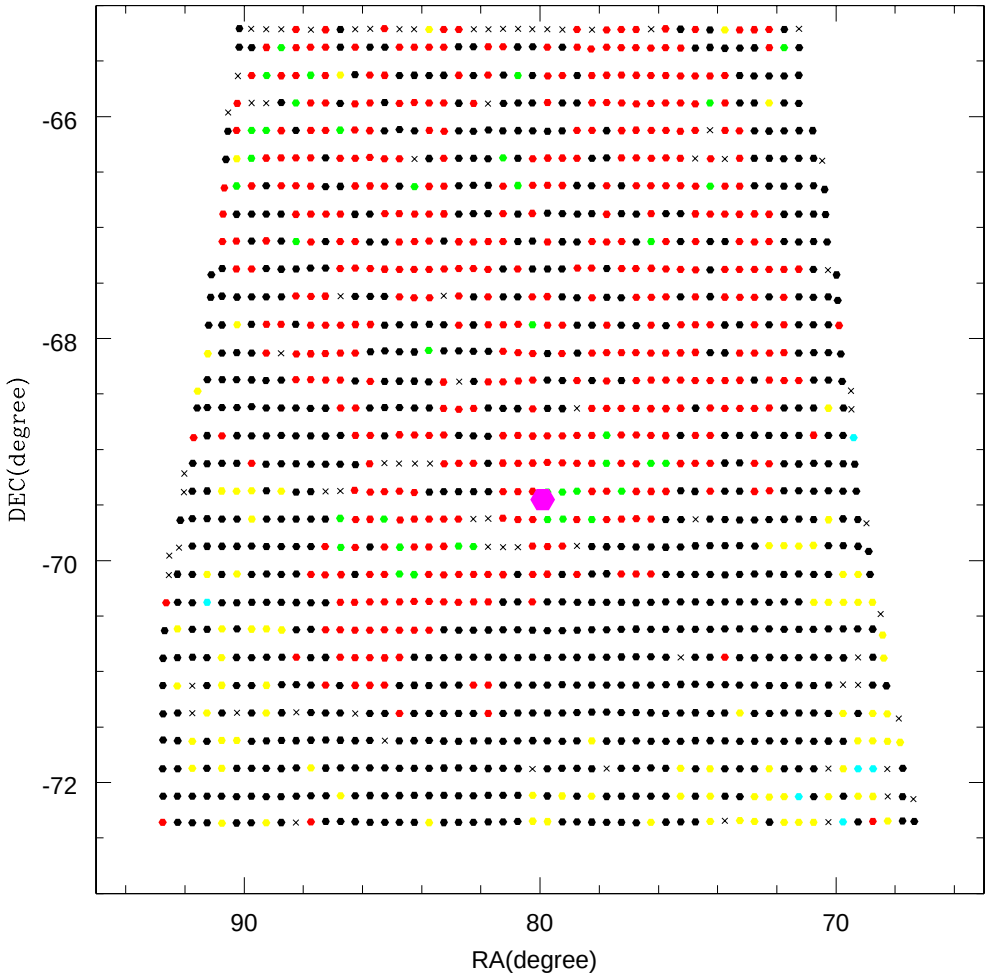

Figure 3.4: Two dimensional plot of depth (t) in the LMC. The colour code is the same as that in Fig. 3.3. The magenta dot represents the optical center of the LMC. The brown crosses represent the omitted regions due to poor fit.

tained from the 5869 sub-regions of the OGLE III observed field. Regions with minimal thickness are seen in the disk of the LMC.

A two dimensional plot of the depth for the 1528 OGLE II regions is shown in the lower panel of Fig. 3.3. This plot is colour coded as explained in the figure. The optical center of the LMC is taken to be R.A = 05^h 19^m 38^s, Dec = -69^0 27' 5".2 (de Vaucouleurs & Freeman 1972). The OGLE II data show a range of dispersion values from 0.03 to 0.46 mag (a depth of of 690 pc to 10.5 kpc; avg: 3.95 ± 1.42 kpc) for the LMC central bar region. For the N-W disk region, the dispersion estimated ranges from 0.023 mag to 0.33 mag (a depth of 500 pc to 7.7 kpc; avg: 3.56 ± 1.04 kpc).The minimum value in the

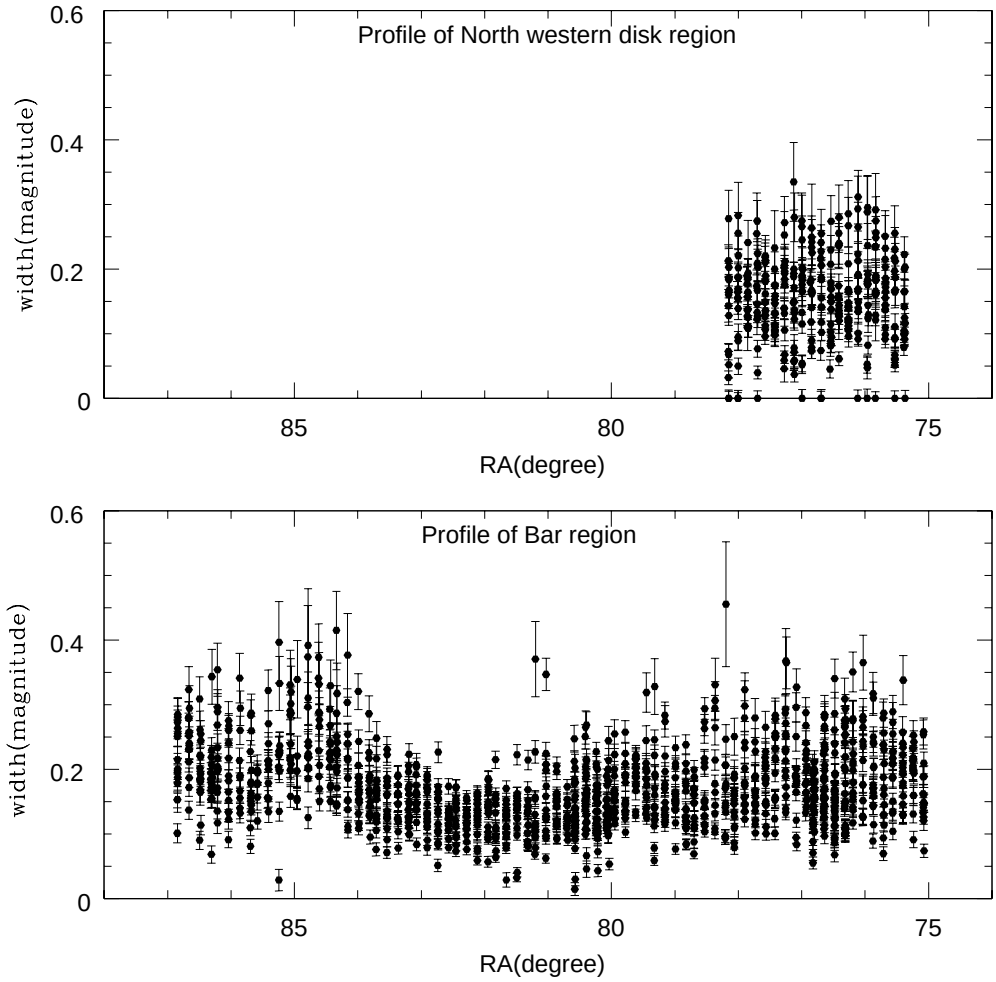

Figure 3.5: Width corresponding to depth with error bars plotted against RA for both the central bar region and north western disk region of the LMC.

N-W disk region is limited by errors. The fraction of such regions, where the minimum value is limited by errors, is 4.06%. Regions in the bar between RA 80 - 84 degrees show a reduced depth (0.5 - 4 kpc, as indicated by yellow and black points). The regions to the east and west of the above region are found to have larger depth (2.0 - 8.0 kpc, black, red and green points). Thus, the depth of the bar at its ends is greater than that near its center. Since the center of the bar does not coincide with the optical center, the thinner central bar region is located to the east of the optical center. The average values of these three regions of the bar are 3.21± 1.03 kpc for the central minimum, 4.13±1.35 kpc for the western region and 4.95±1.49 kpc for the eastern region. This is better brought out in Fig. 3.5, where the depth is shown as a function of R.A (the Dec range in OGLE II

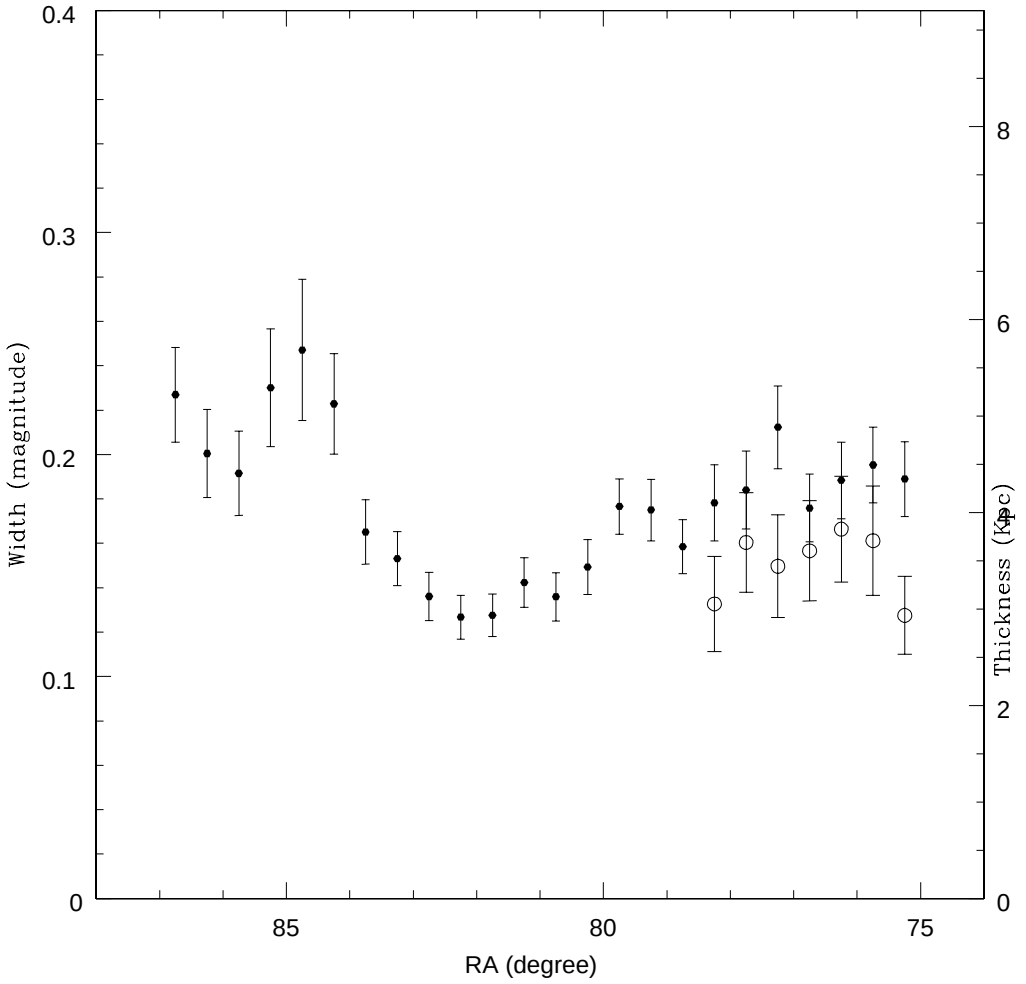

Figure 3.6: Width corresponding to depth averaged along the declination plotted against RA for both the central bar region (closed circles) and north western disk region (open circles)of the LMC.

data is less when compared to the R.A range). The lower panel shows the bar region and the upper panel shows the N-W disk region. An indication of flaring is seen here. In this figure, the depth of all the regions are shown and the error bar on each point denotes the error in the estimation of depth at each location. The depth averaged along the Dec of each R.A is shown in Fig. 3.6. This plot clearly suggests that the bar is flared at its ends. The open circles indicate the N-W disk points. Thus the N-W region has a depth similar to the central region of the bar. The plot also suggests that the eastern end of the bar is more flared than the western end. The errors shown are the standard deviation of the average, thus a large error indicates a large range in the depth values.

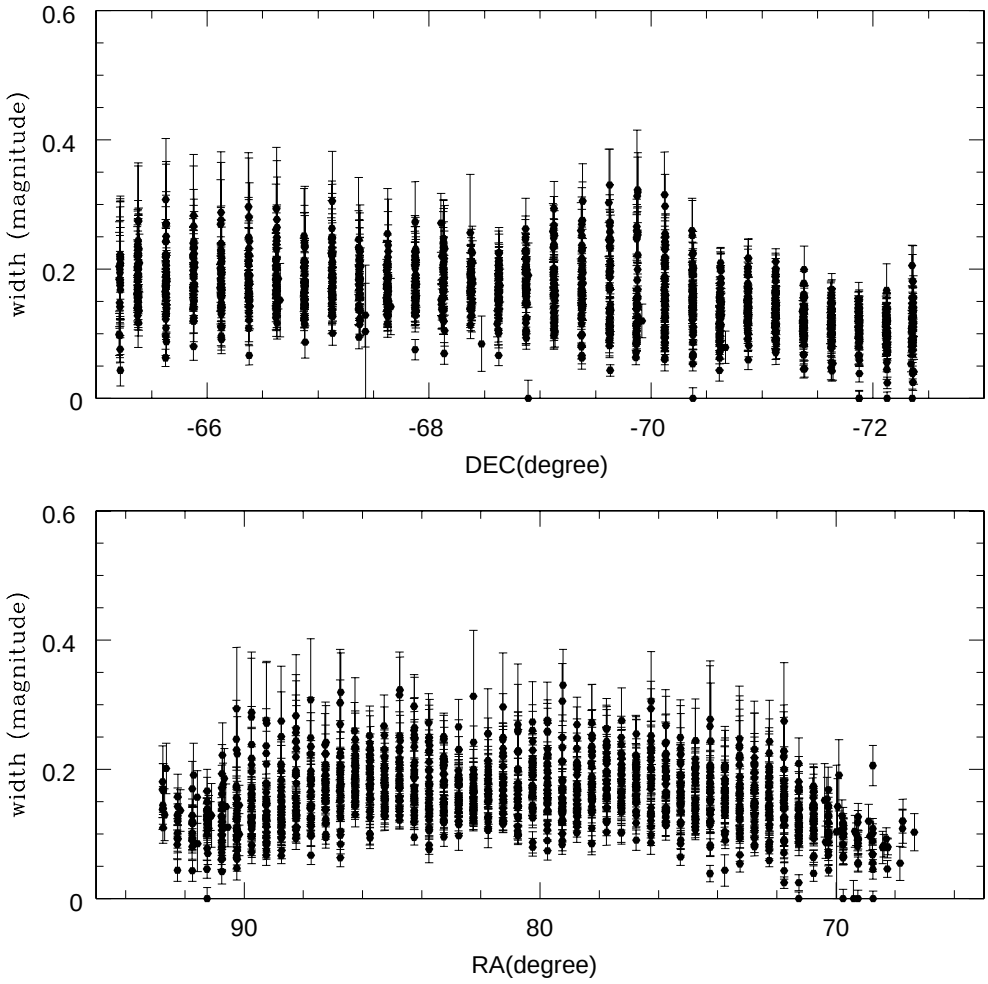

Figure 3.7: Width corresponding to depth with error bars plotted against RA and Dec for the MCPS data.

We also used the MCPS and OGLE III data to estimate the depth in the bar region. These data set could not be corrected for data incompleteness and thus might underestimate the RC stars, especially in the crowded bar region. As the resolution of OGLE III data is higher than that of the MCPS, the effect of incompleteness is expected to be less than that in MCPS. We used larger area bins for the OGLE III (4.44 arcmin^2) and MCPS (10.53 x 15 arcmin^2) data sets compared to OGLE II (3.56 x 3.56 arcmin^2) for the estimation of depth. The colour-coded figure for the OGLE III observed field of the LMC (bar and the disk) is shown in the upper panel of Fig. 3.3. A similar plot for the MCPS data set is shown in Fig. 3.4. The colour code of this figure is same as that of Fig. 3.3. A prominent feature of these two plots is the asymmetrical distribution of the red dots

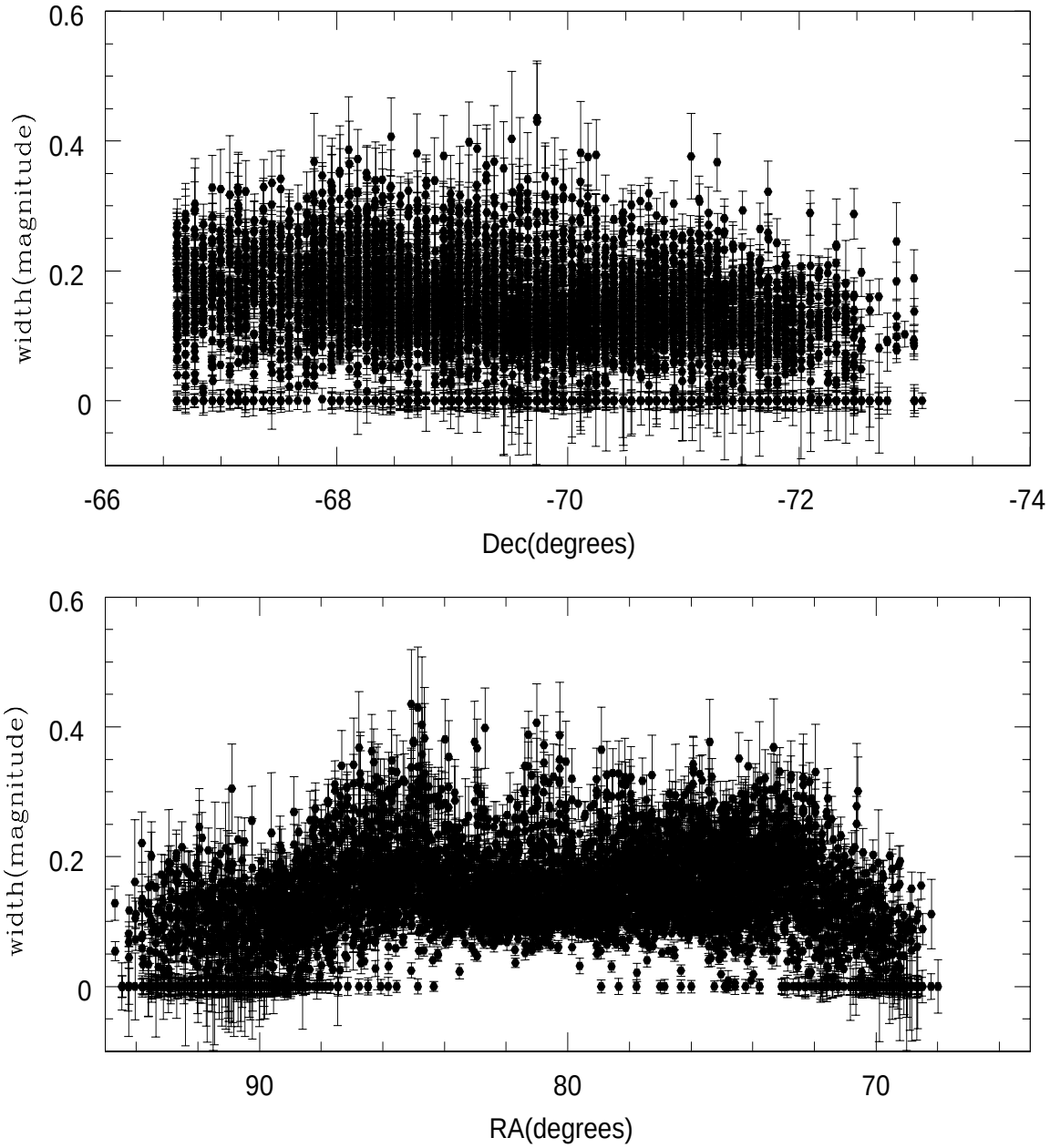

Figure 3.8: Width corresponding to depth with error bars plotted against RA and Dec for the OGLE III data.

(greater depth) when compared to the black dots (lesser depth). Thus, this plot reveals that there is a variation in depth across the disk of the LMC. The average depth for the bar estimated based on 320 regions (from MCPS) is 4.3 ± 1.0 kpc, and from 2509 regions (from OGLE III) is 3.65 ± 1.39 kpc which are very similar to the value estimated from the OGLE II data. As both the OGLE II and OGLE III give high resolution map of depth because of the smaller area bins, the depth estimates in the bar region observed in OGLE II is very well reproduced in the OGLE III depth plot than that of the MCPS. The large dispersion is not due to errors in the estimation of the depth of individual regions, but is due to the presence of regions with varying depths in the bar region.

We used the MCPS and OGLE III data to estimate the depth of the disk. We considered regions outside the location of the bar as disk regions. The estimated depth ranges from 650 pc to 7.01 kpc in the case of MCPS data and for OGLE III the range is from 460 pc to 8.64 kpc. The minimum value of depth is limited by errors. The fraction of such regions, where the minimum value is limited by errors, is 0.44% in the case of MCPS data. But for the OGLE III sub-regions this fraction is higher with a value of $\sim$ 14%. These regions are seen in the ends of the disk. Along with these minimum depth regions there are regions in the ends of the disk with considerable depth which are shown as yellow, black and red points in the upper panel of Fig. 3.3. These locations match well with the MCPS results. The average of the disk alone is estimated to be 3.44±1.16 kpc. The average values of the depth for different disk regions are estimated using both the MCPS and OGLE III data sets and are tabulated in Table 3.1, along with the values for the bar for comparison. The results from the MCPS data show that average depth of the northern disk is greater than the southern disk by more than 2 σ (of the southern disk). The depth of the northern disk is similar to the depth estimated for the bar. Thus the bar and the northern disk of the LMC have greater line of sight depth, whereas the east, west and the southern disk have reduced depth. The variation of depth as a function of R.A (bottom panel) and Dec (top panel) is shown in Fig. 3.7 for the MCPS regions. A similar plot for the OGLE III regions are shown in Fig. 3.8. The depth variation as a function of R.A indicates that the east and the west ends have a depth less than the bar, whereas the depth variation as a function of Dec indicates that the depth reduces from north to the south disk, with increased depth in the bar regions. The fact that the northern disk of the LMC has a greater depth compared to the other regions seems to be a surprising result. Though the results from OGLE III also show an increased depth in the northern disk compared to that of the southern disk, the average estimated is less than that estimated from MCPS data. This may be due to the fact that MCPS has covered more regions to the north when

Table 3.1: Depths of different regions in the LMC These are line of sight depths and need to be corrected for inclination, to estimate the actual depth.

Region	Range (kpc)	Average(kpc)	Std.dev(kpc)
OGLE II data			
LMC eastern bar (R.A > 84^o.0)	0.69-9.10	4.95	1.49
LMC western bar (R.A < 80^o.0)	1.26-10.44	4.14	1.35
LMC central bar (80^o.0 < R.A < 84^o.0)	0.69-8.50	3.21	1.03
LMC bar average	0.69-10.44	3.95	1.42
MCPS data			
LMC eastern disk (R.A > 88^o.0, -68^o.0 > Dec > -71^o.0)	0.65-5.89	2.80	0.92
LMC western disk (R.A < 74^o.0, -68^o.0 > Dec > -71^o.0)	0.65-5.58	3.08	0.99
LMC northern disk (Dec > -68^o.0)	1.00-7.01	4.17	0.97
LMC southern disk (Dec < -71^o.0)	0.65-4.58	2.63	0.79
LMC disk average	0.65-7.01	3.44	1.16
OGLE III data			
LMC eastern disk (R.A > 88^o.0, -68^o.0 > Dec > -71^o.0)	0.46-7.0	1.99	1.56
LMC western disk (R.A < 74^o.0, -68^o.0 > Dec > -71^o.0)	0.46-7.61	2.88	1.84
LMC northern disk (Dec > -68^o.0)	0.46 -8.46	3.79	1.71
LMC southern disk (Dec < -71^o.0)	0.46-8.6	2.65	1.56
LMC disk average	0.65-8.6	2.88	1.78

compared to OGLE III coverage. It will be interesting to study the line of sight depth of regions located further north, to find out how far this trend continues in the disk. Fig. 3.4 and Fig. 3.5 also give a mild suggestion that the depth of the disk gradually reduces towards the south, especially on the south-western side. This is indicated by the increase of yellow points and the appearance of cyan points. The plots mildly suggest that the maximum gradient in the depth is seen from the north-east to the south west of the LMC disk. This is similar to the position angle of the minor axis of the LMC (major axis $\sim 120^o$, van der Marel et al. 2002). Within the radius of the disk studied here, there is no evidence for flaring of the disk. An estimation of depth of outer disk at large radii is essential to confirm the above indicated trends.

3.5 Discussion

The line of sight depth of the LMC is estimated using the RC stars as tracers. They are intermediate age stars with ages greater than 1 Gyr, hence, the depth estimates are relevant to the intermediate age disk. The depth of the intermediate age disk may give clues to its evolution, as a thin disk is indicative of an undisturbed disk, whereas a thick disk would indicate a heated up and hence disturbed disk. Thus the depth of the disk as well as the bar regions of the LMC give insight about its evolution. The analysis presented here estimates the dispersion in the RC magnitude distribution due to depth, after correcting for dispersion due to other effects. The corrections due to the internal reddening and observational error were estimated for each region and were corrected accordingly. The correction for the presence of an age and metallicity range in the RC population, along with star formation history is done using the dispersion estimated by Girardi & Salaris (2001). Thus the values estimated here have a bearing on the assumptions made during the correction of the above effect.

For the estimation of the internal extinction from internal reddening we used the relation, A_I = 0.934 x E($V - I$) (Rieke & Lebofsky 1985). The above interstellar extinction relation is appropriate for the broad Johnson I filter. The OGLE II, OGLE-III and MCPS photometry was measured with CCDs, which independent of the actual I filter transmission curve would likely have a red cutoff at significantly shorter wavelengths than the Johnson I-band, making the observed pass band closer to the Kron-Cousins I-band. Then the appropriate conversion factor between A_I and E($V - I$) is $\sim$ 1.4. In order to check the effect of the choice of this conversion factor in our results, we repeated the whole analysis using the relation A_I = 1.4 x E($V - I$). The Table 3.2 gives the depth estimates obtained using this relation for the internal extinction. The table shows that these values are very

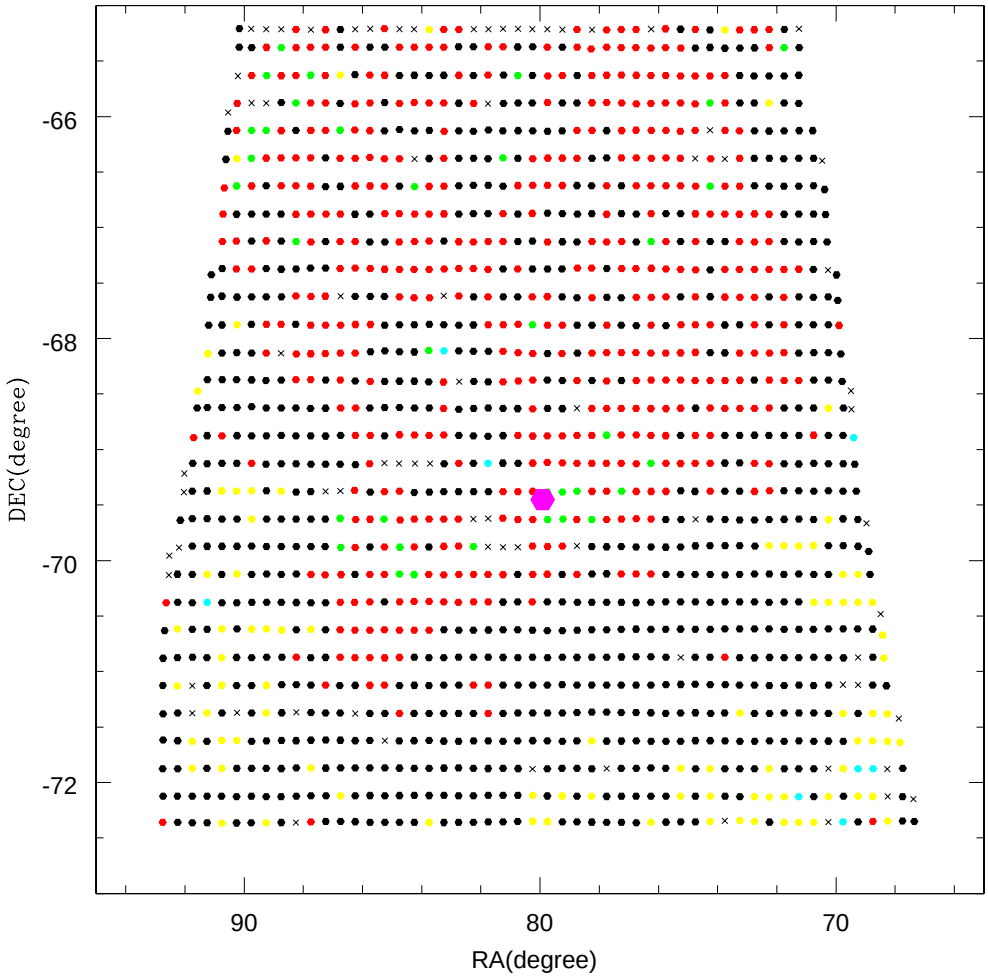

Figure 3.9: Two dimensional plot of depth (t) in the LMC (MCPS data set) when the relation A_I = 1.4 x E($V - I$) is used for internal extinction correction. The colour code is the same as that in Fig. 3.3. The magenta dot represents the optical center of the LMC.The crosses represent the omitted regions with poor fit.

similar to that shown in Table 3.1. In order to check the effect spatially, we plotted the two dimensional depth plot for the MCPS sub-regions using the depth values obtained when the modified relation is used. The plot is shown in Fig. 3.9. The colour code is same as in Fig. 3.3 and Fig. 3.4. The Fig. 3.4 and Fig. 3.9 look very similar suggesting that the choice of E($V - I$) to A_I conversion factor has not much effect in our present analysis. This may be due to the the low values of internal reddening as seen from the Fig. 3.1 and Fig. 3.2.

The variation in the estimated dispersion (after all the corrections) is assumed to be

Table 3.2: Depths of different regions in the LMC estimated using the interstellar extinction relation A_I = 1.4 x E($V - I$). These are line of sight depths and need to be corrected for inclination, to estimate the actual depth.

Region	Range (kpc)	Average(kpc)	Std.dev(kpc)
OGLE II data			
LMC eastern bar (R.A > $84^o.0$)	0.69-9.10	4.87	1.49
LMC western bar (R.A < $80^o.0$)	1.26-10.44	4.07	1.35
LMC central bar ($80^o.0$ < R.A < $84^o.0$)	0.69-8.50	3.15	1.01
LMC bar average	0.69-10.44	3.87	1.41
MCPS data			
LMC eastern disk (R.A > $88^o.0$, $-68^o.0$ > Dec > $-71^o.0$)	0.65-5.89	2.80	0.91
LMC western disk (R.A < $74^o.0$, $-68^o.0$ > Dec > $-71^o.0$)	0.65-5.58	3.07	0.99
LMC northern disk (Dec > $-68^o.0$)	1.00-7.01	4.16	0.97
LMC southern disk (Dec < $-71^o.0$)	0.65-4.58	2.62	0.78
LMC disk average	0.65-7.01	3.43	1.16
OGLE III data			
LMC eastern disk (R.A > $88^o.0$, $-68^o.0$ > Dec > $-71^o.0$)	0.46-7.0	1.97	1.56
LMC western disk (R.A < $74^o.0$, $-68^o.0$ > Dec > $-71^o.0$)	0.46-7.61	2.87	1.84
LMC northern disk (Dec > $-68^o.0$)	0.46 -8.46	3.77	1.71
LMC southern disk (Dec < $-71^o.0$)	0.46-8.6	2.63	1.57
LMC disk average	0.65-8.6	2.86	1.78

due to variations in depth across the galaxy. If this is actually due to the differences in RC population, as a result of variation in age, metallicity and star formation history, then the results indicate that the RC population and their properties are significantly different in the bar, north and south of the disk. Recent studies show that the above parameters are more or less similar across the LMC (Subramaniam & Anupama 2002, Olsen & Salyk 2002, van der Marel & Cioni 2001). Variation of star formation history and metallicity across the LMC has been studied by Cioni et al. (2006a), Carrera et al. (2008). They found small variations in the inner regions, but large variations in the outer regions. Cioni et al. (2006b) mapped the variation of star formation history as well as metallicity using the AGB stars. They found that the south and south-western regions could be metal poor whereas the north and north-eastern regions could be metal rich. Regions near the Shapley constellation III were found to have a younger population. This region is close to the northern limit studied here. Piatti et al. (1999) and Dolphin (2000) found that the RC population in the far northern regions is structured. All the above regions with varying RC population are outside the regions studied here. The results presented in this study suggest that the northern regions and the bar have large dispersion, probably due to depth when compared to the east, west and the southern regions. If this is not due to increased depth in these regions, then it would mean that the stellar populations in these regions are significantly different. In either case, the northern disk and the bar seem to be different from the rest of the LMC disk.

As incompleteness correction is done in one data set (OGLE II) and not in the other data sets (MCPS & OGLE III) we compared the depth estimates before and after adopting the completeness correction. We found that the change is within the bin sizes adopted here. Thus, incorporating the incompleteness correction has not changed the results presented here. The incompleteness correction is large in the central regions of the LMC bar, where the correction is between 30-40 percent. The outer regions of the bar (6-15%) as well as the NW region (5-9%) have less correction. The outer regions are thus less affected by the incompleteness. Thus the incompleteness problem is unlikely to affect the MCPS and OGLE III RC distribution in the LMC disk, whereas it may be unreliable in the central regions of the LMC bar.

We have removed regions with poor fit as explained in section 3.2. These regions are likely to have different RC structures suggesting a large variation in metallicity and/or population. The fraction of such region is $\sim$ 8-9% in the LMC. Such regions are indicated in Fig. 3.3 and Fig. 3.4. Thus to a certain extent, the above procedure has eliminated regions with significantly different metallicity and star formation history. Apart from

the above, the remaining regions studied here might have some variation in the the RC population contributing to the depth estimated. The results presented in this study might include include some contribution from the population effect.

The estimated depth for various regions in the LMC is given in Table 3.1. These values correspond to the 1-sigma depth. The line of sight depth estimated here is for the inclined disk. To estimate the actual depth of the disk, one needs to correct for the inclination. Assuming the inclination to be 35 degrees (van der Marel & Cioni 2001), the actual depth of the bar is $4.0 \times \cos(i) = 3.3 \pm 1.0$ kpc. Similarly, the southern disk has an actual depth of about 2.2 ± 1.0 kpc, whereas the northern disk is similar to the bar. Note that, after correcting for inclination, the depths in the northern and the souther regions are within the errors. This is because the difference in depth reduces due to correction for inclination, but the error does not. These values should be used when one compares the depth of the LMC with that of other galaxies. Thus, the LMC bar and the disk are thicker than the thin disk of our Galaxy ($\sim$ 100 pc). The scale height of the bar could be taken as half of its depth, assuming that the bar is optically thin. The z-extent of the bar, which is the scale height (1.65 kpc), is found to be similar to its scale length (1.3 - 1.5 kpc, van der Marel & Cioni (2001)). Hence the bar has a depth similar to its width. Thus the bar continues to be an unexplained structure/component of the LMC.

The LMC bar is found to be fairly thick (line of sight depth = 4.0 ± 1.4 kpc). We also find evidence for flaring and a disturbed structure at the ends of the bar region. The thick and flared bar of the LMC indicates that this region of the LMC is perturbed. The structure of the LMC bar as delineated by the RC stars showed warps (Subramaniam 2003), which is also clear indication of disturbance. The depth estimates also suggest that the LMC disk is fairly thick (2.4 - 4.0 kpc), with a decrease in depth/thickness and/or varying stellar population from the north to the south. The tidal effects due to LMC-Galaxy interactions (if they were interacting) are unlikely to cause this, as the tidal effects are stronger near the outer regions and weaker towards the inner regions. Flaring of the disk is expected if tidal interactions are present. On the other hand, except for the thicker northern region, flaring of the disk is not seen, at least up to the radii studied here. Hence we do not see any evidence for tidal interactions, at least in the inner disk. The recent results on the proper motion of the LMC and SMC (Kallivayalil et al. 2006a) suggested that the Clouds are approaching our Galaxy for the first time. This would suggest that the LMC has not interacted with our Galaxy before. Our results are in good agreement with this scenario.

In general, thicker and heated up disks are considered as signatures of minor mergers

(Quinn & Goodman 1986; Velazquez & White 1999). Thus, the LMC is likely to have experienced minor mergers in its history. The presence of warps in the bar (Subramaniam 2003) and evidence of counter rotation in the central regions (Subramaniam & Prabhu 2005) also support the minor merger scenario. Thus, it is possible that the LMC has experienced minor mergers during its evolution. These mergers have affected the northern disk and the bar. The variation in depth observed across the LMC disk could constrain the way in which these mergers could have happened.

3.6 Conclusions

• The LMC is found to have large line of sight depths (1-sigma) for the bar (4.0±1.4 kpc) and the disk (3.44± 1.16 kpc and 2.88 ± 1.78 kpc from the MCPS and OGLE III data sets respectively).

• The LMC bar and the northern disk have similar, but large depth. The eastern, western and the southern disk have similar, but reduced depth. This may also be interpreted as due to different stellar populations.

• The depth profile indicates flaring of the LMC bar.

• The large depth of the LMC suggest that it has experienced heating, probably due to minor mergers.

CHAPTER 4

THE MYSTERIOUS BAR OF THE LARGE MAGELLANIC CLOUD *

4.1 Introduction

The off-centered stellar bar is one of the most striking features of the LMC. On the other hand, this is one of the least studied and understood features of the LMC (van der Marel 2006). Bars are a common phenomenon in late-type spirals and Magellanic irregulars (de Vaucouleurs & Freeman 1972). The asymmetric bar is used to explain the recent star formation history as well as the one-armed spiral feature in the LMC (Gardiner et al. 1998, Dottori et al. 1996). Subramaniam (2003) studied the relative distance within the LMC bar using the RC stars and found that the bar is warped and also found structures in the bar. Lah et al. (2005) and Koerwer (2009) also found similar structures within the LMC bar. Zaritsky (2004) suggested that the bar of the LMC is a levitating bar and it is the result of viewing a triaxial stellar bulge that is embedded in a highly obscuring thick disk. The author also mentioned that there are surprisingly few direct constraints on the three-dimensional structure of this entity. Zhao & Evans (2000) proposed that this off-centerd bar is unvirialised structure slightly misaligned with, and offset from, the plane of the LMC disk. The small displacement and misalignment are consequences of recent tidal interactions with the SMC and the Galaxy. Many considered this as the possible reason for the microlensing events observed towards the LMC. Nikolaev et al. (2004) suggested that the bar is infront of the disk by 0.5 kpc based on the distance estimations of Cepheids. Thus, the location of the bar with respect to the disk is still debated. The

*Results presented here are published in Subramaniam, A., & Subramanian, S., 2009, ApJ, 703, L37

near-IR star count maps presented by van der Marel & Cioni (2001) found the bar to be a smooth structure. On the other hand, the bar is not visible in the HI distribution or in the HI velocity maps (Staveley-Smith et al. 2003). Thus, when the bar is a prominent feature in the optical and near -IR, such a feature is not visible in the gas and recent star formation. Thus, the striking difference between these two distributions in the LMC has been an unsolved mystery.

In this chapter, we map the vertical structure (derived from the relative magnitude variation of the RC distribution) in the inner LMC using the OGLE III catalog (Udalski et al. 2008a). Reddening corrected mean magnitude of the RC distribution is assumed to reflect the variation in distance along the line of sight, such that, regions with brighter peak magnitudes are assumed to be located closer. This method was used by Subramaniam (2003), who found a warped bar using the OGLE II data, and by Olsen & Salyk (2002), who found a warp in the southwestern disk. Since the OGLE III scans cover the bar as well as the disk region surrounding the bar, it is probably one of the best sets of data for studying the relative location of the bar with respect to the inner disk. This high resolution map (64.5 pc^2) is expected to bring out any difference in location between the disk and bar, since the bar and the disk are sampled. A difference in I_0 could arise due to differences in the RC population between regions or due to variation in star formation history, metallicity, etc. Thus any difference, or variation, seen in the I_0 is interpreted as due to a vertical structure and/or change in the RC population.

The present analysis is expected to reveal the properties of the bar and the disk as delineated by the RC stars, which are older than 1 Gyr. Thus the properties derived here pertain to the disk of intermediate-age in the LMC. Since the bar of the LMC is believed to be about 4 Gyr old (Smecker-Hane et al. 2002), the RC stars are one of the best tracers to differentiate the bar from the disk.

4.2 Data and Analysis

The V and I band data from the OGLE III catalog (Udalski et al. 2008a) are used for this study. The observed OGLE III region is divided into 7416 sub-regions with an area of 4.44 x 4.44 $arcmin^2$. As explained in section 2.2.2, the RC stars are identified from the (V-I) vs I colour magnitude diagram (CMD) of each sub-region and the peak colour and magnitude of the RC distribution in each sub-region are obtained. The reduced χ^2 value and the errors associated with the peak values of the distribution are also obtained. Regions with peak errors greater than 0.1 mag and those with reduced χ^2 value greater

than 2 are omitted from the analysis. This rejection is similar to that adopted by Subramaniam (2003). The number of regions shortlisted to map the structure reduced to 5754. The dereddened I_0 magnitude of the RC stars in these sub-regions are obtained using the equations (6) and (7) given in section 2.2.2.

In this analysis, we have not incorporated the incompleteness due to crowding, especially in the central regions where the effect is expected to be prominent. In order to estimate the effect due to crowding and the incompleteness, we compared the estimated parameters with and without incompleteness correction (refer chapter 3). We used the OGLE II data, for which the data for incompleteness correction are given. Also, we compared the I_0 values obtained from OGLE II data Udalski et al. (2000) incorporating incompleteness correction with the present estimates in the next section. We did not find any significant difference between the parameters, suggesting that the incompleteness/crowding does not affect the results presented here.

4.3 Results: The structure of the inner LMC

The difference in I_0 magnitude of the sub-regions is a measure of the relative distance. The estimated high resolution structure map of the LMC is shown in Fig. 4.1. This shows the variation in structure, which is basically the variation in relative distance in the line of sight, and/or variation in the RC population. The center of the LMC is taken to be $05^h19^m38^s.0$ $-69^o27'5".2$ (2000.0) (de Vaucouleurs & Freeman 1972). Only regions with total error in I_0 less than 0.03 mag are used for the analysis and a difference of 0.1 mag corresponds to a statistical significance of 3 σ. We have also shown the approximate location of the bar, using two parallel lines. This is the region covered by OGLE II scans. Since same technique was used by Olsen & Salyk (2002) for regions located mostly in the disk, we compared our estimates with their reddening corrected mean RC magnitudes. These are shown in red in Fig. 4.1. The points are shown such that bigger dots correspond to regions located closer (since they appear brighter) and smaller dots correspond to regions located farther away (since they appear fainter).

The absence of any definite feature correlated to the location of the optical bar in the plot is striking. This suggests that the bar is not located in front or back of the disk, at least in the tracer adopted. Thus, the bar is likely to be very much part of the LMC disk. This result also suggests that the RC population in the disk and the bar are very similar. In order to compare the location of the disk studied by Olsen & Salyk (2002), we have shown their locations in red, and the size of the dots follow the same convention. OGLE

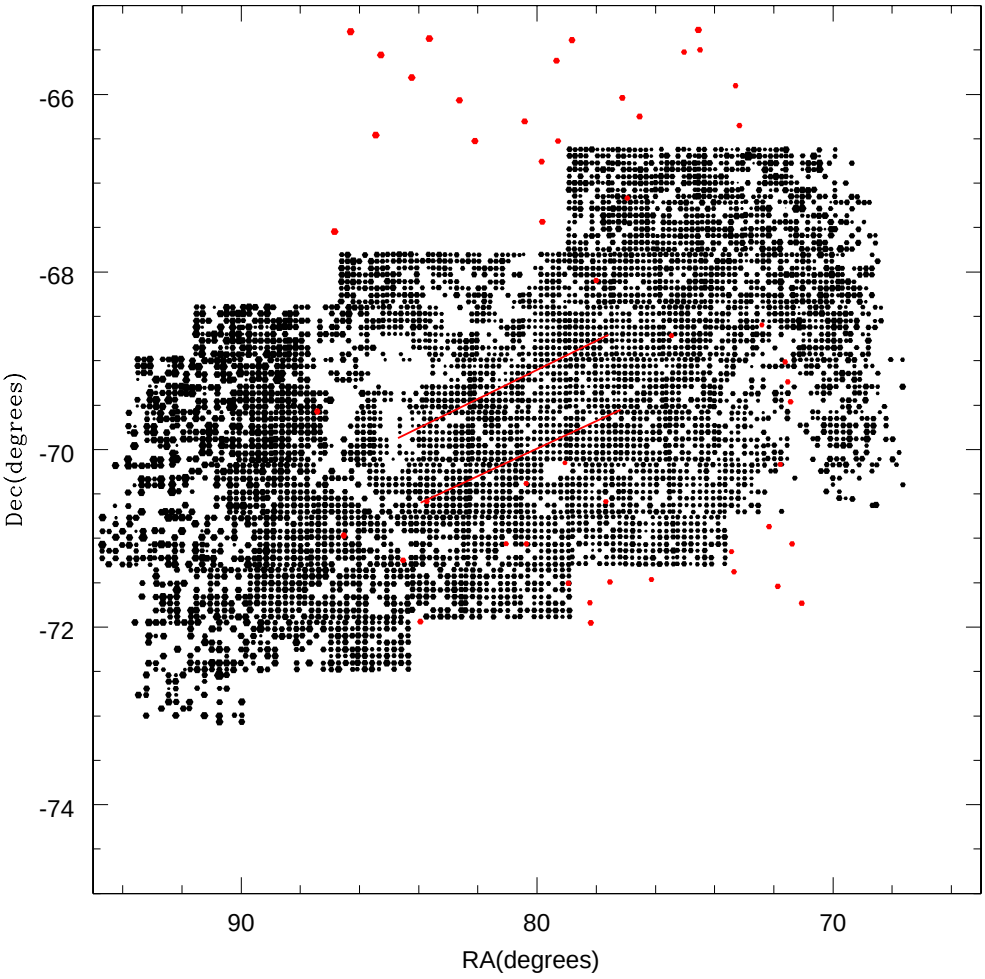

Figure 4.1: The reddening corrected mean magnitude (I_0) of RC stars estimated from OGLE III data. The sizes of dots are scaled such that the bigger points are brighter and smaller points are fainter. The range of I_0 shown here is from 17.9 to 18.3 mag (see Fig. 4.3). The red parallel lines indicate the approximate location of the bar. The red points correspond to data taken from Olsen & Salyk (2002).

III fields span a wider range in RA, but smaller range in Declination, whereas the regions studied by Olsen & Salyk (2002) cover the Declination more, especially the northern disk regions. It is should noted that this study has a continuous sampling of the central LMC, unlike Olsen & Salyk (2002). Their data match with the present estimations very well in the overlapping regions. This is better verified in Fig. 4.3.

Another striking feature is the brightening of the RC stars towards the eastern end of the bar. This region is outside the bar and located in the disk. The major axis of the LMC

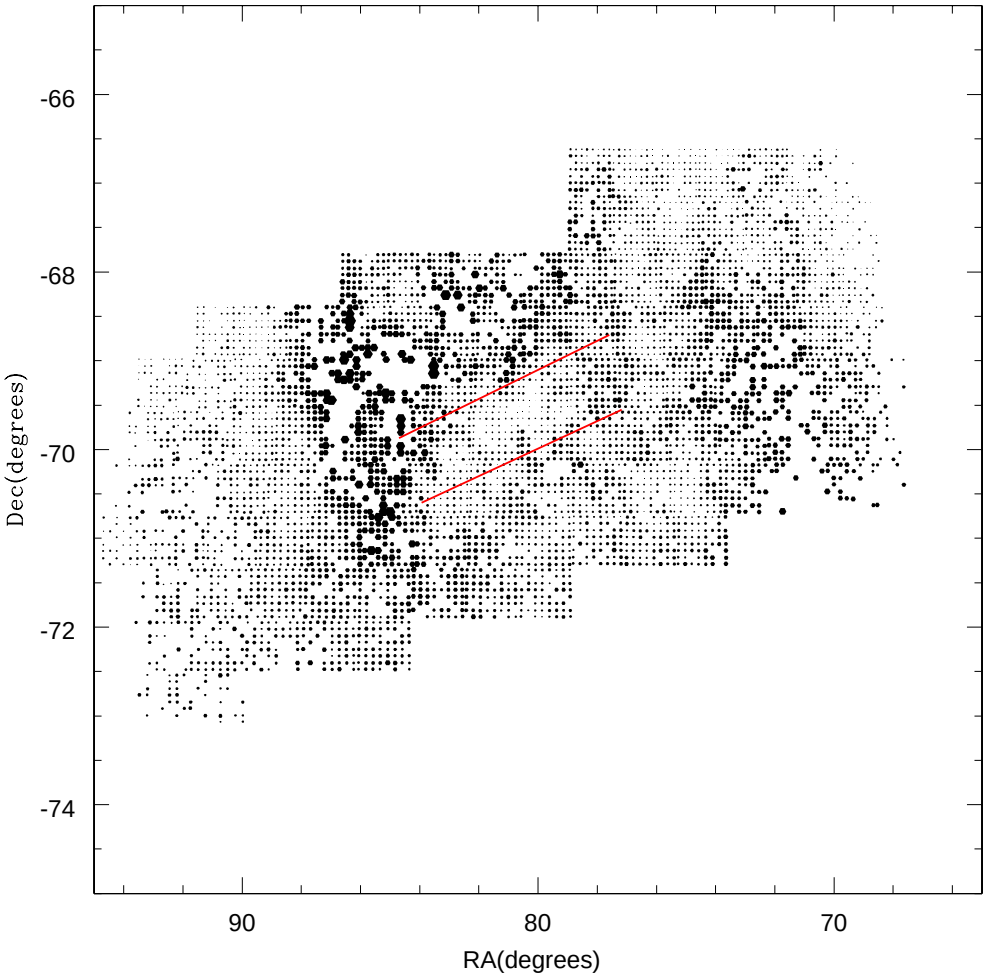

Figure 4.2: The mean reddening E(V-I) across the OGLE III field as estimated from the RC stars are shown. The size of the dots scale with the reddening value such that regions with large reddening (0.2-0.3) mag appear as bigger dots. The approximate location of the bar is shown as red parallel lines.

is along the bar, therefore the magnitude variation due to the effect of inclination is not expected along the bar. On the other hand, the figure shows that regions located to the east of the bar along the same position angle, are brighter. Along the major axis, a mild warp in the western end is also suggestive. These features could also be due to a different RC population, perhaps due to a gradual change in the star formation history or metallicity with radial distance. The warp found by Olsen & Salyk (2002) is in the regions which are located to the south-west of the OGLE III region.

In order to see the effect of the reddening in the results arrived at, the E(V−I) mean

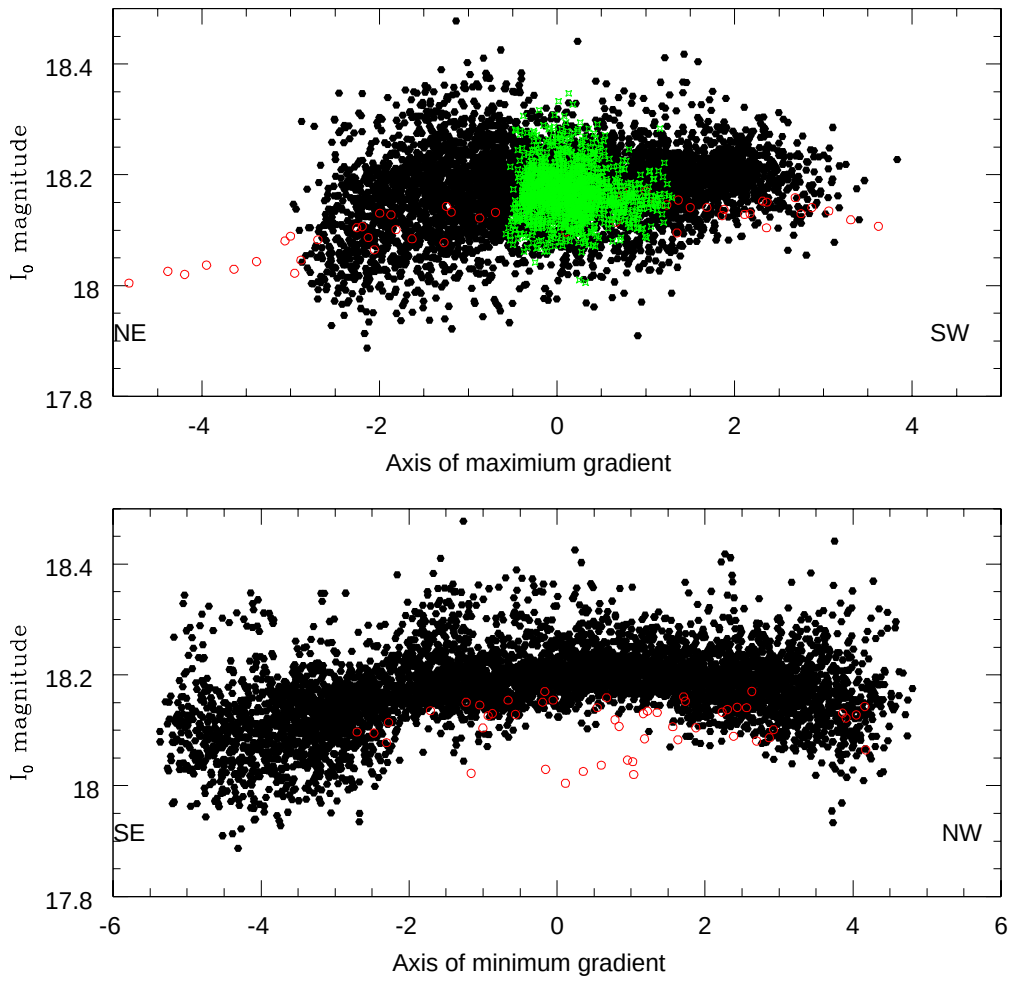

Figure 4.3: The I_0 values are plotted along the axis of minimum gradient (line of nodes, P.A = $121^o.5$,lower panel) and along the axis of maximum gradient (perpendicular to the line of nodes, upper panel). The red open circles correspond to the data taken from Olsen & Salyk (2002) and green points correspond to the data taken from Subramaniam (2003).

reddening map is shown in Fig. 4.2. The minimum and maximum reddening values are 0.02 - 0.3 mag respectively, where most of the regions show reddening less than 0.15 mag. By comparing Fig. 4.1 and Fig. 4.2, it can be seen that the vertical structure, if any, as seen in Fig. 4.1 does not correlate with the pattern of mean reddening. Thus, the reddening correction does not have any bearing on the structure map derived in Fig. 4.1.

The edge-on view of the LMC along the axes of minimum and maximum gradient are shown in Fig. 4.3. The line of nodes is taken as P.A. = $121^o.5$ (van der Marel & Cioni 2001). The lower plot shows the edge-on view, along the line of nodes and is

not expected to show any gradient in magnitude across the disk. The upper plot shows the magnitude variation along the perpendicular axis, and this is the axis which shows maximum variation in magnitude. The directions of the plotted axes are indicated. The data from Olsen & Salyk (2002) are shown as red open circles. We have also compared the I_0 estimates obtained by Subramaniam (2003) for the OGLE II region, after incorporating incompleteness correction, shown as green points. These are shown only in the upper plot so that the lower plot is not crowded to hide any features suggesting a non-planar bar with respect to the disk. The OGLE II data agree very well with the OGLE III data. The data from Olsen & Salyk (2002) also match well. The brighter points seen in the lower plot are from their northeastern region, which are outside the OGLE III region. The bar is located between X = 2^o and $+2^o$, along with the disk in this edge-on view. In this central region, we see a single and relatively thin structure, suggestive of the bar located within the disk and in the plane of the disk. Some regions located to the eastern and western ends show signatures of warp, as suggested by the brighter points. The upper panel is suggestive of gradient in I_0 , which is basically the inclination of the disk. We also find that the northeastern regions show relatively large range in I_0 , when compared to the southwestern regions. The regions observed by Olsen & Salyk (2002) in the northeastern side are located outside our field and are brighter, though regions within OGLE III are comparable. Both the plots suggest that some regions located away from the center have brighter RC magnitudes, suggesting that there are extra-planar features/warps or variation in RC population, with radial distance.

In order to prove the co-planarity quantitatively, we have averaged I_0 values in a bin of $1^o.5$ in R.A. and $0^o.5$ in Dec. The number of regions averaged varies between 25 and 55. The bar and the nearby regions are shown in Fig. 4.4. The averages shown for the bar are very similar to the result from OGLE II analysis (Subramaniam 2003). We also confirm their result of the eastern part of the bar located closer than the western end. The average I_0 values in the bar region range between 18.12 and 18.18 mag (east to west), similar to the adjoining disk. The southern disk is brighter than the bar by 0.02 mag and the eastern regions are brighter by 0.02 mag, suggesting that the bar is behind the eastern and the southern disk by 0.02 mag. The western and the northern disk have similar average I_0 as the bar, within 0.02 mag. There is one location in the northern region, where it is fainter than the bar by 0.02 mag. The eastern regions are in general brighter. These regions have I_0 values similar to the adjoining bar region. Koerwer (2009) found a probable brightening of RC stars in the bar region by 0.04 mag. We do find the one localized region, near the center of the bar to show a similar brightening. To summarize, there is

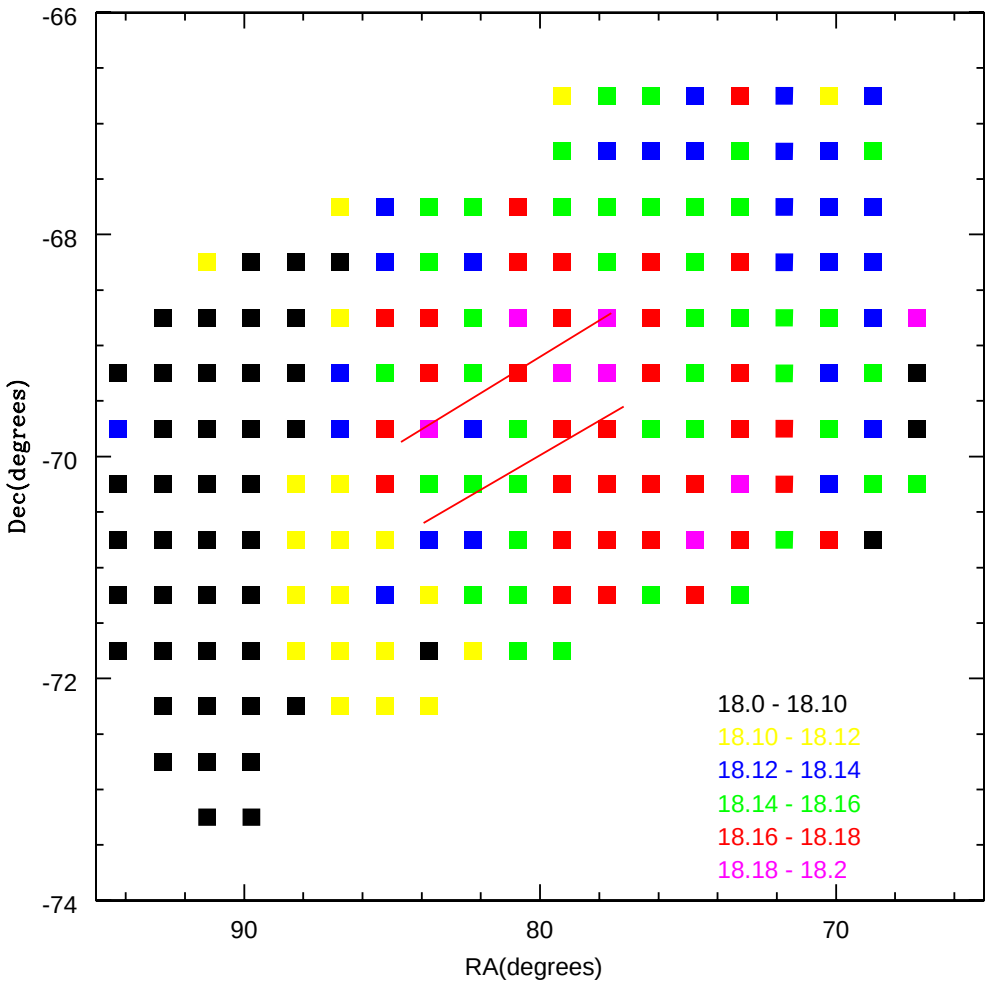

Figure 4.4: The average I_0 values across the LMC is shown. The colour code and the location of the bar are shown in the figure.

significant variation in the average value of I_0 , along the bar as well as in the adjoining disk. The bar and the disk are found to be coplanar within 0.02 mag.

4.4 Discussion

The results derived here rules out the possibility that the bar may be located in front of the disk. The reddening in the LMC has been found to vary with the tracer, (Subramaniam 2005) and hence same tracer is used for reddening estimation. Also, the data presented here agree very well with the previous estimations by (Subramaniam 2003 and Olsen & Salyk 2002). The analysis of Olsen & Salyk (2002) had points which are widely separated

and Subramaniam (2003) used only the bar region. Thus a comparative study of the bar and the disk with homogeneous data was not possible so far. The effect of crowding on the parameter estimation while studying the bar and the outer disk regions was considered in the study given in chapter 3. There we found marginal difference when one included incompleteness correction for the bar region. Thus the study presented here uses a method which was used earlier and uses a homogeneous data which cover the bar and the inner disk.

The structure map clearly shows that the LMC bar is very much part of the LMC disk and cannot be differentiated from the disk as a separate entity. The estimated value of I_0 shows similar range in the bar as well as in the disk region, making it difficult to differentiate the bar from the disk. The observed range of I_0 values (18.12 - 18.18 mag) in the in the bar region, tally very well with the surrounding disk. Zhao & Evans (2000) suggested that the bar could be a misaligned and off-set along the line of sight direction by about 2 kpc. This study indicates that there is no difference between the mean distance to the bar and disk, though both the entities have large dispersion about the mean, indicating a not so thin disk and the bar.

The range of estimated I_0 value decreases for regions located at eastern and western end of the observed region. The figures also suggest a warp in the eastern and the western end of the observed region along the major axis. This is in addition to the warp found by (Olsen & Salyk 2002) in the south-western part of the LMC disk. The gradual brightening of the RC stars with increasing radial distance from the center could also be due to change in the RC population. A detailed analysis of the star formation history along with metallicity is required to identify whether these are real warps or just different RC population.

4.5 Conclusions

• This suggests that the bar is coplanar with the disk, within $\sim$ 460 pc. Thus, this study confirms that the bar is very much a part of the intermediate age disk of the LMC and not a separate component located in front of the disk.

• The gradual brightening of the RC stars with increasing radial distance from the center could also be due to change in the RC population.

CHAPTER 5

ESTIMATION OF THE STRUCTURAL PARAMETERS OF THE LARGE MAGELLANIC CLOUD *

5.1 Introduction

The LMC is believed to be a disk galaxy with a planar geometry. The orientation measurements of the LMC disk plane have been done previously by various authors using different tracers. By assuming the LMC disk to be circular when viewed face-on, de Vaucouleurs & Freeman (1972) found a disk inclination of $i = 27^o \pm 2^o$and a position angle of the line of nodes (PA_{lon}), $\phi = 170^o \pm 5^o$ from the elliptical outer isophotes in red exposures. Based on the analysis of spatial variations in the apparent magnitude of AGB stars in the near-IR colour-magnitude diagrams extracted from the Deep Near-Infrared Southern Sky Survey (DENIS) and Two Micron All-Sky Survey (2MASS), van der Marel & Cioni (2001) estimated an $i = 34^o.7 \pm 6^o.2$ and $\phi = 122^o.5 \pm 8^o.3$ for the LMC disk between $2^o.5$ to $6^o.7$ from the LMC center. Olsen & Salyk (2002) derived an $i = 35^o.8 \pm 2^o.4$ and $\phi = 145^o \pm 4^o$ by studying the RC magnitudes in the inner LMC, excluding the bar region. They also showed that the southwestern part of the LMC disk is warped. Recently, Koerwer (2009) derived an $i = 23^o.5 \pm 0^o.4$ and $\phi = 154^o.6 \pm 1^o.2$, using the *JH* photometric data of RC stars from the IRSF MCPSC. Cepheids are also used to obtain the orientation measurements of the LMC disk. Caldwell & Coulson (1986) analyzed a sample of 73

*Part of the results presented here are published in Subramanian, S., & Subramaniam, A., 2010, A&A, 520, 24

cepheids and obtained $i = 28^o.6 \pm 5^o.9$ and $\phi = 142^o.4 \pm 7^o.7$. Based on a sample of 2000 cepheids identified in the MACHO survey, Nikolaev et al. (2004) obtained an $i = 30^o.7 \pm 1^o.1$ and $\phi = 151^o \pm 2^o.4$. Persson et al. (2004) obtained an $i = 27^o \pm 6^o$ and $\phi = 127^o \pm 10^o$ from the analysis of 92 near infrared light curves of Cepheids. The structural parameters of the HI disk of the LMC are also estimated by various H I studies. Feitzinger et al. (1977) derived an inclination of $33^o \pm 3^o$ and PA_{lon} of $168^o \pm 4^o$ by geometrical means. The H I velocity studies by Luks & Rohlfs (1992) revealed two kinematic components, the L (lower velocity) component and the D (disk) component. The PA_{lon} of around 162^o was estimated for the disk component. Kim et al. (1998) estimated the PA_{lon} of H I disk to be around 168^o and an inclination of $22^o \pm 6^o$.

5.2 Optical Study

In the optical study we use the photometric data of the RC stars in the V and I pass bands from the MCPS and the OGLE III data sets to estimate the structural parameters of the LMC disk plane. These catalogs have homogeneous and continuous sampling of stars spread over the inner LMC up to a radius of about 6 degrees. Olsen & Salyk (2002) studied the structure of the LMC using RC stars in discrete and widely separated pointings located away from the bar region. Compared to the above study, we use a homogeneous and continuous sample of RC stars.

5.2.1 Data & Ananlysis

The V and I band photometric data from the OGLE III and MCPS catalogs are used in this study. The OGLE III and the MCPS observed regions are divided into 1854 sub-regions (each with an area of 8.88 x 8.88 arcmin^2) and 1512 sub-regions (each with an area of 10.53 x 15 arcmin^2) respectively. For each sub-region a (V-I) vs I CMD is plotted and the RC stars are identified as explained in section 2.2.1. The OGLE III sub-regions have a range of 500-9000 in the number of the RC stars identified. The eastern and western ends of the disk, which are less dense have $\sim$ 500-700 RC stars. But the dense regions in the center of the data set contains up to 9000 RC stars. Out of 1512 regions in the MCPS data, only 1377 regions have a resonable number (100-2000) of RC stars to do the analysis.

To estimate the structural parameters of the LMC, the dereddened peak I_0 magnitude of the RC stars is to be obtained for all the sub-regions. The analysis is similar to that

done by Olsen & Salyk (2002). The RC stars in each sub-region of OGLE III data are binned in colour and magnitude with a bin size of 0.01 mag and 0.025 magnitude respectively. From these distributions the peak I magnitude, peak (V-I) colour, the associated errors and the reduced χ^2 values are obtained using the numerical analysis explained in section 2.2.1. Regions with peak errors greater than 0.1 mag and those with reduced χ^2 value greater than 2.0 are omitted from the analysis. Thus the final analysis contains 1262 regions of OGLE III data and 1231 regions of MCPS data.

The peak values of the color, (V−I) mag at each location is used to estimate the reddening. The reddening is calculated using the relation E(V−I) = $(\mathrm{V-I})_{obs}$ − 0.92 mag. The intrinsic color of the RC stars is taken to be 0.92 mag (Olsen & Salyk (2002). The reddening values were found to be negative for 451 locations in the MCPS data set. These regions were mostly located near the center. Zaritsky et al. (2004) found many regions with negative A_v values while estimating the extinction towards the LMC using the MCPS data and assigned an extinction of zero for those regions. They suggested that the negative extinction values are due to observational uncertainties. Reddening plays an important role in the estimation of peak magnitude and hence the estimated structure, thus regions which showed negative values for reddening estimates are omitted from our analysis. Hence the number of regions used for final analysis became 780 for the MCPS data. Assigning a zero reddening to those regions with negative reddening estimates and its impact on the estimates of the LMC disk parameters are discussed in 5.1.5. The selection of the intrinsic (V−I) color of the RC stars may also be the reason for obtaining negative reddening values. For the MCPS data, the intrinsic (V−I) color of the RC stars can be set to produce the median reddening obtained by Schlegel et al. (1998) towards the LMC. Implications of resetting the intrinsic (V−I) color of RC stars for the MCPS data are discussed in detail in 5.1.5. Negative reddening was not found for any regions in the OGLE III data.

The interstellar extinction is estimated by A_I=1.4xE(V−I) (Olsen & Salyk (2002)). After correcting the mean I mag for interstellar extinction, I_0 for each region is estimated using the equation (7) given in section 2.2.1. The difference in I_0 between regions is a measure of the relative distances such that 0.1 mag in ΔI at a distance of 50 kpc corresponds to 2.3 kpc in distance. The variation in I_0 mag is converted into relative distances. The relative distance is

ΔD = (I_0 mean − I_0 of each region)x23 kpc.

The error in I_0 is estimated as

$\delta {I_0}^2$ = (avg error in peak I)^2 + (avg err in peak (V-I))^2 .

Here, the variation in I_0 is considered only due to the line of sight distance variation within the galaxy. The error in magnitude is also converted into error in distance.

In this analysis, we have not incorporated the incompleteness due to crowding, especially in the central regions where the effect is expected to be prominent. In order to estimate the effect due to crowding and the incompleteness, we compared the I_0 values with and without incompleteness correction (refer chapter 3). We used used the OGLE II data for the analysis. We did not find any significant difference between the parameters, suggesting that the incompleteness/crowding does not affect the results presented here.

For each sub-region we have R.A, Dec and relative distance with respect to the LMC center. Then the x,y,z cartesian coordinates corresponding to each region are obtained using the equations (12), (13) and (14) given in chapter 2. In this analysis, the optical center of the LMC, $05^h19^m38^s.0$ $-69^o27'5".2$ (J2000) (de Vaucouleurs & Freeman (1972)) is taken as the center of the LMC. A least-square plane fit (refer chapter 2) is applied to the x,y, and z data of the MCPS & OGLE III data sets. The inclination, i and the PA_{lon} of the LMC disk are estimated from the relations (15) and (16) given in 2.2.3.

We calculated the deviations of the LMC disk from the plane defined by the estimated coefficients. The expected z for a plane is calculated using the equation of the plane, Ax+By+Cz+D =0. The difference in the expected and calculated z values is taken as the deviation of the LMC disk from the plane. Thus the extra-planar features of the LMC disk are identified and quantified. Once the deviations are estimated, the regions with deviations above three times the error in z are omitted and the plane-fitting procedure is applied to the remaining regions to re-estimate the structural parameters of the LMC disk plane.

The error in the estimate of the LMC disk parameters is calculated from the error associated with the z values. The plane-fitting procedure is applied to the (x, y, z+δz) and (x, y, z−δz) systems instead of (x, y, z). From the coefficients obtained the LMC disk parameters are re-calculated. Thus the deviations of the structural parameters from the

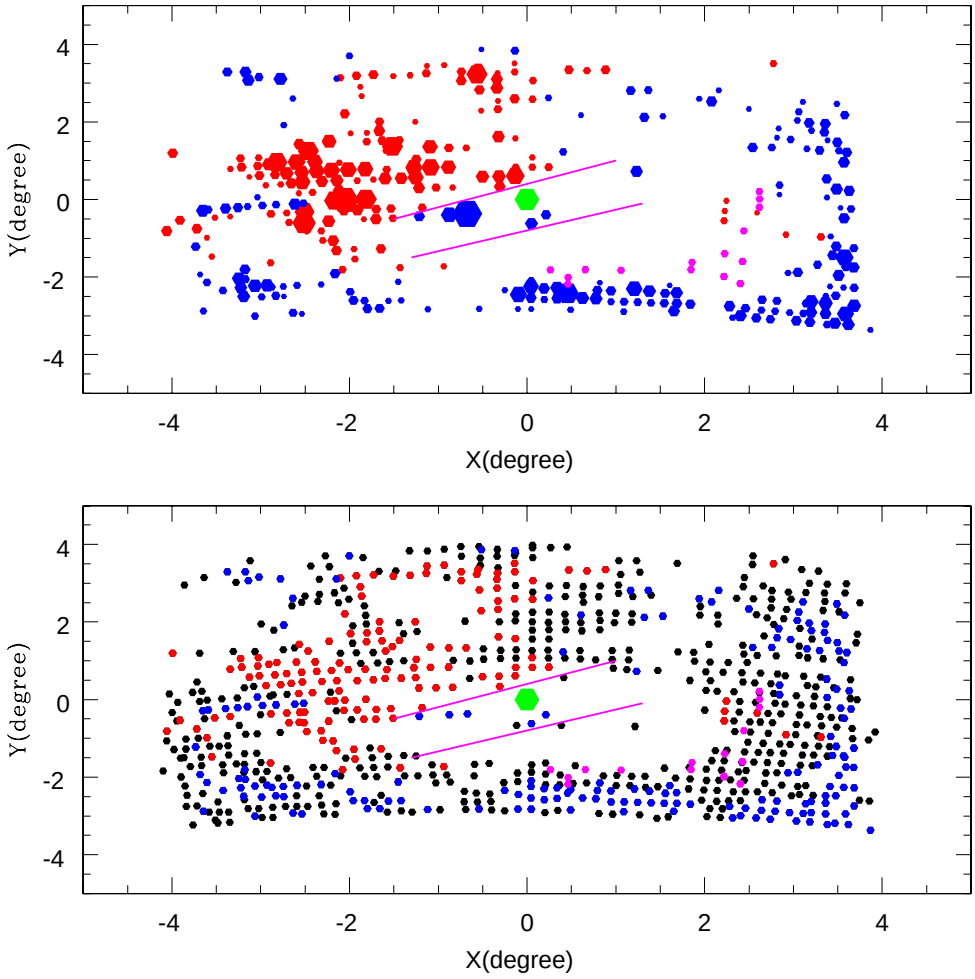

Figure 5.1: The MCPS regions which are on the fitted plane and those which are deviated from the plane are shown. In the lower panel, black dots represent the regions on the fitted plane, red dots represent the regions behind the fitted plane and the blue dots represent the regions which are in front of the fitted plane. The upper panel shows only the regions with deviations greater than 3 sigma from the LMC disk plane. The size of the points are proportional to the amplitude of the deviations. Magenta dots in both panels are the regions which are suggested as warps by Olsen & Salyk (2002). The green hexagon in both plots represents the optical center of the LMC.

fitted plane to the (x ,y, z) are estimated and are converted as the error in the estimate of

the parameters.

5.2.2 Results

The structural parameters of the LMC disk are estimated using the dereddened mean magnitude of RC stars. A plane-fitting procedure applied to 780 regions of the MCPS data set gives an inclination of i= $38^o.2 \pm 5^o.0$ & PA_{lon}, ϕ = $141^o.5 \pm 9^0.8$ for the LMC disk. The deviation of the LMC disk regions from the estimated plane are calculated as explained in the previous section. The average error in the estimate of I_0 mag is converted into distance and its around 500 pc for the MCPS data. Deviations above 3 sigma are considered as significant deviations from the fitted plane. Fig.5.1 shows the deviation of the MCPS regions from the plane. In the bottom panel, all the regions used for the analysis are plotted. The black points are those which are on the fitted plane, red points are disk regions which are behind the plane and blue points are the disk regions which are in front of the plane. In the upper panel only the regions with deviations above 3 sigma are plotted and the size of the points are proportional to the amplitude of the deviation. Here also, red points are regions behind the fitted plane and blue are in front of the fitted plane. From the plots we can see that there are many regions which deviate from the planar structure of the LMC disk. The plot shows that the RC stars in the regions southeast, southwest and northwest of the LMC disk are brighter than what is expected from the plane fit. Also, some regions northeast to the LMC bar are dimmer than expected.

The RC stars in the LMC disk are a heterogeneous population, and therefore they would have a range in mass, age, and metallicity. The density of stars in various locations will also vary with the local star-formation rate as a function of time. These factors result in a range of magnitude and color of the net population of RC stars in any given location and would contribute to the observed peaks in magnitude and color distributions. Therefore, the deviations found in some regions may also be due to these population differences of RC stars. Then the brightening of RC stars in the southeast, southwest and northwest of the LMC disk indicates either a different RC population and/or these regions are warped. Similarly, the dimming of RC stars in the north east of the LMC bar indicates a difference in RC population and/or these regions are behind the fitted plane. Based on the studies of the LMC clusters, Grocholski et al. (2006) found that the LMC lacks the metallicity gradient typically seen in the galaxies. Studies by Subramaniam & Anupama (2002), Olsen & Salyk (2002) and van der Marel & Cioni (2001) found no noticeable change in age and metallicity of the RC population in the central region of the

LMC. As the regions we study are located in the central region of the LMC, the effects of population difference of RC stars in these regions are likely to be negligible. Hence we can see from these plots that the southeast, southwest and the northwestern regions of the LMC disk may be warped and the regions northeast to the bar of the LMC are behind the fitted plane. In figure 5.1, the regions suggested by Olsen & Salyk (2002) as warps are over plotted as magenta points. Their points in the southwestern regions are near the warped regions suggested by us, though they do not coincide.

The extra-planar features seen in the LMC disk would have affected the estimate of the planar parameters of the LMC disk. The reduced χ^2 value for the estimate of planar parameters using the MCPS data set is 2.0. The higher value of reduced χ^2 value can be due to the presence of structures in the LMC disk. So we omitted the regions with deviations above 3 sigma and the planar parameters are estimated again. Around 320 regions out of 780 regions showed deviations above 3 sigma and the remaining 460 regions are used for the re-estimate. Thus the structural parameters obtained for the LMC disk plane after removing the extra planar features are inclination, $i = 37^o.2 \pm 2^o.3$ and PA_{lon}, $\phi = 141^o.4 \pm 3^o.7$. The reduced χ^2 value for the plane fitting in this case is 0.4.

The plane-fitting procedure applied to 1262 regions of the OGLE III data gives an $i = 21^o.0 \pm 2^o.2$ & $\phi = 171^o.1 \pm 8^o.8$ for the LMC disk. As done for the MCPS data, deviations from the LMC disk plane with the above planar parameters are estimated. The average error in the estimate of z distance for the OGLE III data set is around 300 pc. The regions which show deviations above 3 sigma are considered as real deviations. Fig.5.2 shows the deviation plot for the OGLE III data. The bottom panel shows all the 1262 regions used for plane fitting and the upper panel shows only those regions which show deviations above 3 sigma. In the upper panel the size of the points are proportional to the amplitude of the deviations. The color code in the figure is the same as in Fig.5.1. As in the MCPS data, the OGLE III also shows, similar brightening in the southeast, northwest and southwestern regions of the LMC disk. The northeastern part adjacent to the LMC bar is also dimmer in this plot similar to the MCPS plot. So either the northwestern, south western and southeastern parts of the LMC disk regions are in front of the fitted plane and/or the RC population in these regions is different. Again the northeastern part north of the LMC bar is either behind and/or the RC population in this region is different. As done for the MCPS data set, the extra-planar features are removed and the parameters are estimated again for the OGLE III data set. Out of 1262 regions, 397 regions showed deviations above 3 sigma, and these regions are removed from the plane-fitting procedure. Thus the structural parameters obtained for the LMC disk plane after removing the extra

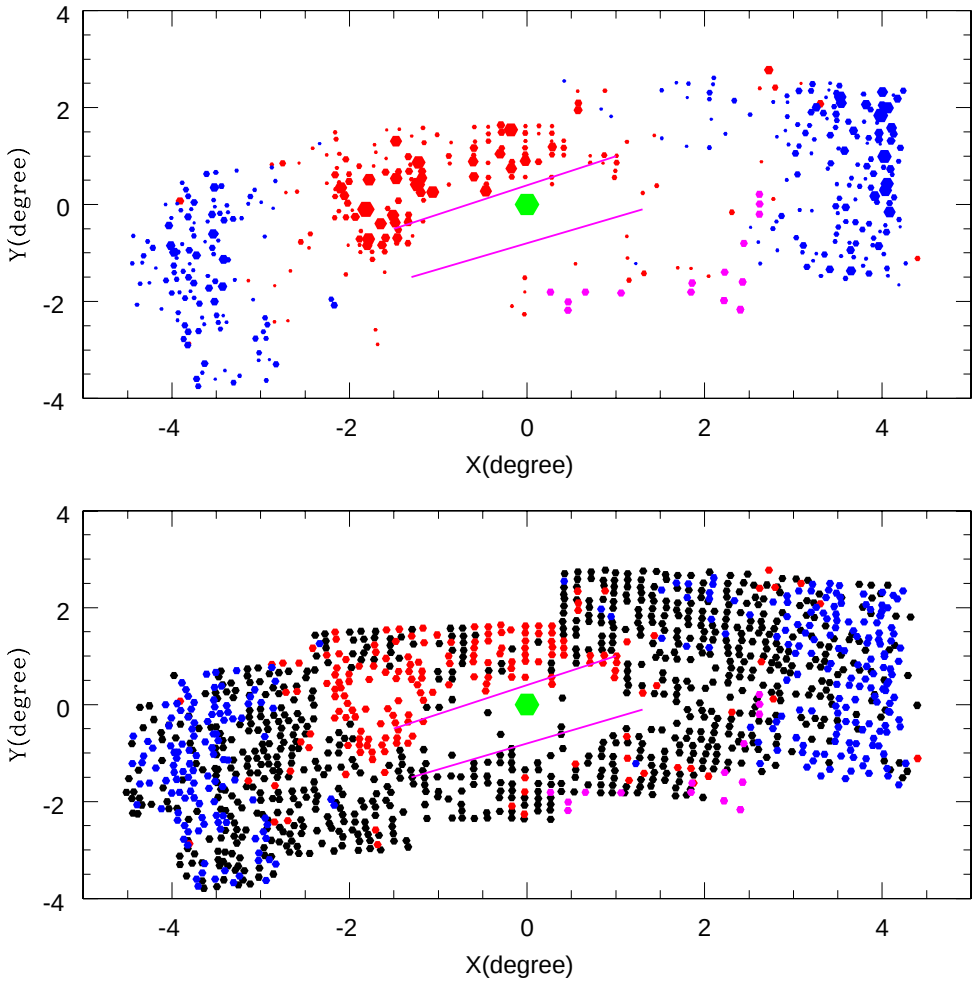

Figure 5.2: The OGLE III regions which are on the fitted plane and those which are deviated are shown. In the lower panel, black dots represent the regions on the fitted LMC plane, red dots represent the regions behind the fitted plane and the blue dots represent the regions which are in front of the fitted plane. The upper panel shows only the regions with deviations, greater than 3 sigma, from the LMC disk plane. The size of the points are proportional to the amplitude of the deviations. Magenta dots in both panels are the regions which are suggested as warps by Olsen & Salyk (2002). The green hexagon in both plots represents the optical center of the LMC.

planar features are inclination, $i = 23^o \pm 0^o.8$ and $\phi = 163^o.7 \pm 1^o.5$. The reduced χ^2 value of the plane-fitting procedure with all the 1262 regions was 1.0 and, when the region with large deviations are removed, the reduced χ^2 became 0.3.

The dereddened RC magnitude is plotted against the axis perpendicular to the line of nodes, axis of maximum gradient and its shown in Fig.5.3. The upper panel shows the

plot for the MCPS data and the lower panel shows the plot for the OGLE III data. From both plots we can clearly see the effect of inclination. The slopes estimated for both data sets excluding the regions with deviations above 3 sigma are 0.0254 mag/degree, and the y-intercept is 18.18 mag for the MCPS data and a slope of 0.0152 mag/degree and the y-intercept of 18.13 mag for the OGLE III. The inclination estimated for the MCPS data is 33.3 degrees and 21.5 degrees for the OGLE III. The inclinations estimated from the plots for both data sets match well with the inclination values estimated from the plane-fitting procedure for the same data set.

The y-intercepts obtained from Fig.5.3 for both data sets are the mean I_0 value of RC stars. As RC stars are standard candles, this value is a measure of the distance to the center of the LMC. The y-intercepts obtained for the OGLE III and the MCPS data sets from Fig.5.3 are 18.13±0.01mag and 18.18±0.01 mag respectively. The distance modulus, μ_0 to the LMC center can be estimated using the formula

$$\mu_0 = I_{0mean} - M_{I(LMC)}.$$

In the above equation, $M_{I(LMC)}$ is the I-band absolute magnitude of RC stars in the LMC. Stanek et al (1998) used the absolute I-band magnitude of RC stars in the Hipparcos sample as the zero point for distance estimation to the LMC. Later Girardi & Salaris (2001) found from their simulations of local clump and those found in the LMC that there is a systematic magnitude difference between them. This systematic magnitude difference is due to the differences in the age, metallicity, and star-formation history of the RC stars in the Galaxy and the LMC. Girardi & Salaris (2001) simulated the RC stars in the LMC bar as well as in the outer fields using the star-formation rate estimated by Holtzman et al. (1999) and the age-metallicity relation from Pagel & Tautvaisiene (1998). From their simulations, they estimated a $M_{I(LMC)}$ of -0.371 for the central region of the LMC bar. Thus the distance moduli, μ_0 to the LMC center estimated from the OGLE III and the MCPS data are 18.50±0.01 and 18.55±0.01 respectively after correcting for population effects. These values agrees well with the previous estimates of 18.5 ± 0.02 (Alves 2004) and 18.53 ± 0.07 (Salaris & Girardi 2002) toward the LMC.

5.2.3 Discussion

The dereddened peak I magnitude of RC stars from the OGLE III and the MCPS data sets are used to estimate the structural parameters of the LMC disk and hence the deviations of the LMC regions from the plane. The planar parameters of the LMC disk

Table 5.1: Summary of orientation measurements of the LMC disk plane

Reference	Inclination, i	PA$_{lon}$, ϕ	Tracer used for the estimate
de Vaucouleurs & Freeman (1972)	$27^o \pm 2^o$	$170^o \pm 5$	Isophotes
Feitzinger et al. (1977)	$33^o.0 \pm 3^o$	$168^o \pm 4^o$	HI
Caldwell & Coulson (1986)	$28^o.0 \pm 5^o.9$	$142^o.4 \pm 7^o.7$	Cepheids
Luks & Rohlfs (1992)	–	$162^o.0$	HI
Kim et al. (1998)	$22^o.0 \pm 6^o$	$168^o.0$	HI
van der Marel & Cioni (2001)	$34^o.7 \pm 6^o.2$	$122^o.5 \pm 8^o.3$	AGB stars
Olsen & Salyk (2002)	$35^o.8 \pm 2^o.4$	$145^o \pm 4^o$	Red clump stars
Nikolaev et al. (2004)	$30^o.7 \pm 1^o.1$	$151^o \pm 2^o.4$	Cepheids
Persson et al. (2004)	$27^o.0 \pm 6^o.0$	$127^o \pm 10^o.0$	Cepheids
Koerwer (2009)	$23^o.5 \pm 0^o.4$	$154^o.6 \pm 1^o.2$	Red clump stars
Our estimates			
OGLE III	$23^o \pm 0^o.8$	$163^o.7 \pm 1^o.5$	Red clump stars
MCPS	$37^o.4 \pm 2^o.3$	$141^o.2 \pm 3^o.7$	Red clump stars

obtained from the analysis of 1262 regions of the OGLE III data turned out to be an inclination of i=$23^o \pm 0^o.9$ and PA_{lon}, ϕ = $163\ ^o.7 \pm 1^o.6$. From the analysis of 780 regions of the MCPS data, an inclination, i=$37^o.4 \pm 2^o.5$ and PA_{lon} ϕ = $141^o.2 \pm 3^o.7$ are obtained. Previously many studies have estimated the planar parameters of the LMC disk using various tracers. The values obtained from those studies along with our estimates are summarised in Table 5.1. Tracers used in those studies are also mentioned in the table. Our estimates based on the analysis of the MCPS data is matching well within the error bars with the estimates of Olsen & Salyk (2002). Various studies of the LMC disk and bar regions (Fig.6 given in Koerwer 2009 and Fig.4 in Subramaniam 2003) have shown that it is a highly structured galaxy. The estimate of the planar parameters are likely to be severely affected by these structures. The difference in the regions, coverage of the LMC, and the tracer used for the estimate of the planar parameters may be the reason for the differences in the estimated parameters of various studies. Also, Nikolaev et al. (2004) showed that the analysis based on the photometric data from the concentric rings in the inner LMC is strongly dependent on the adopted LMC center, which can cause a variation of about 35 degrees in the values of PA_{lon}.

Choice of the LMC center

The adopted center of the LMC for the analysis may have an effect on the estimated parameters. We used the plane fitting method, rather than the ring analysis, which is probably less affected by the choice of the center. For our analysis, we have taken the optical center, $05^h19^m38^s.0\ -69^o27'5".2$ (J2000) (de Vaucouleurs & Freeman (1972)), as the center of the LMC. To see the effect of the adopted center on the estimated parameters, we did the analysis with the HI rotation center (Kim et al. (1998)), geometric center of the sample Cepheids used in the analysis of Nikolaev et al. (2004) and also the carbon stars isopleths center (van der Marel & Cioni (2001)) as the center of the LMC. We find that the choice of center causes only marginal changes in the estimated parameters, and the changes are within the error. The estimated parameters with different centers are given in Table 5.2.

Choice of area of the regions

In order to check the effect of area of the bins used in our analysis, the OGLE III region is divided into sub regions with area, 8.88 x 16.76 $arcmin^2$, comparable to the area of sub-region of the MCPS data. The whole analysis is repeated and the structural parameters of the LMC disk are estimated. The parameters, inclination and PA_{lon} obtained

Table 5.2: Summary of orientation measurements of the LMC disk plane with choice of the center

Reference	Inclination, i	PA_{lon}, ϕ
MCPS data		
Optical center (de Vaucouleurs & Freeman 1972)	$37^o.4\pm2^o.3$	$141^o.2\pm3^o.7$
HI rotation center (Kim et al. 1998)	$37^o.2\pm2^o.2$	$142^o.7\pm3^o.4$
Geometric center of Cepheids used in (Nikolaev et al. 2004)	$36^o.8\pm2^o.2$	$141^o.4\pm3^o.8$
Center of carbon stars outer isopleths (van der Marel & Cioni 2001)	$36^o.9\pm2^o.5$	$137^o.4\pm4^o.0$
OGLE III data		
Optical center de Vaucouleurs & Freeman (1972)	$23^o.0\pm0^o.8$	$163^o.7\pm1^o.5$
HI rotation center (Kim et al. (1998))	$23^o.1\pm0^o.8$	$164^o.9\pm1^o.7$
Geometric center of Cepheids used in Nikolaev et al. (2004)	$22^o.7\pm0^o.8$	$164^o.0\pm1^o.6$
Center of carbon stars outer isopleths (van der Marel & Cioni (2001))	$22^o.0\pm0^o.8$	$161^o.9\pm1^o.6$

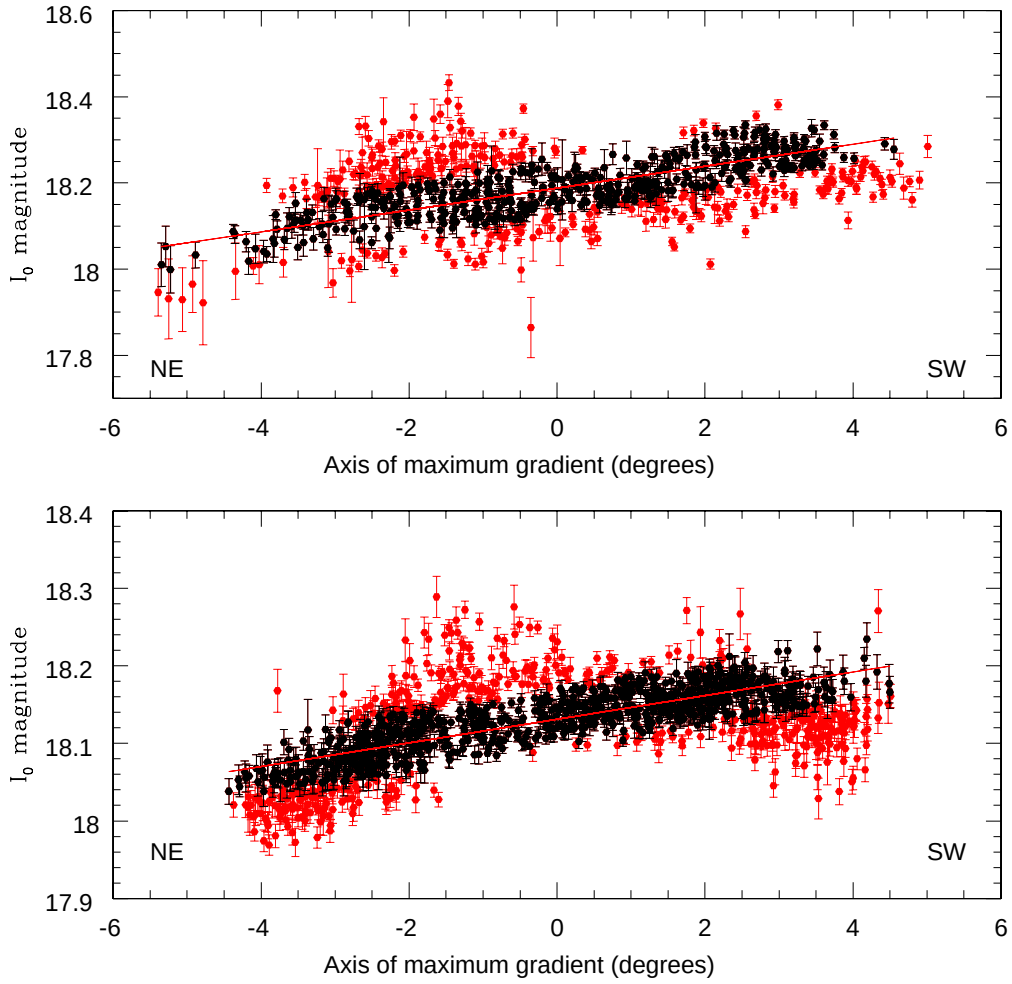

Figure 5.3: Dereddened RC magnitude plotted against the axis of maximum gradient. The red points are regions which show deviation larger than 3 sigma. The direction of inclination is shown as red line. The upper panel is for the MCPS data and the lower panel is for the OGLE III.

are $24.5^o \pm 0^o.5$ & $166^o \pm 1^o$ respectively. These values are comparable with our results obtained from the analysis of the OGLE III data with smaller area (8.88 x 8.88 arcmin^2) sub-regions. This means that extending the area of sub-regions is unlikely to change the estimated parameters. But when the area of the OGLE III sub-region is made 4.44 x 4.44 arcmin^2, smaller than 8.88 x 8.88 arcmin^2 used for our analysis, there was problem in the plane-fitting procedure due to the large number of points. This can be due to the finer structures present in the inner LMC.

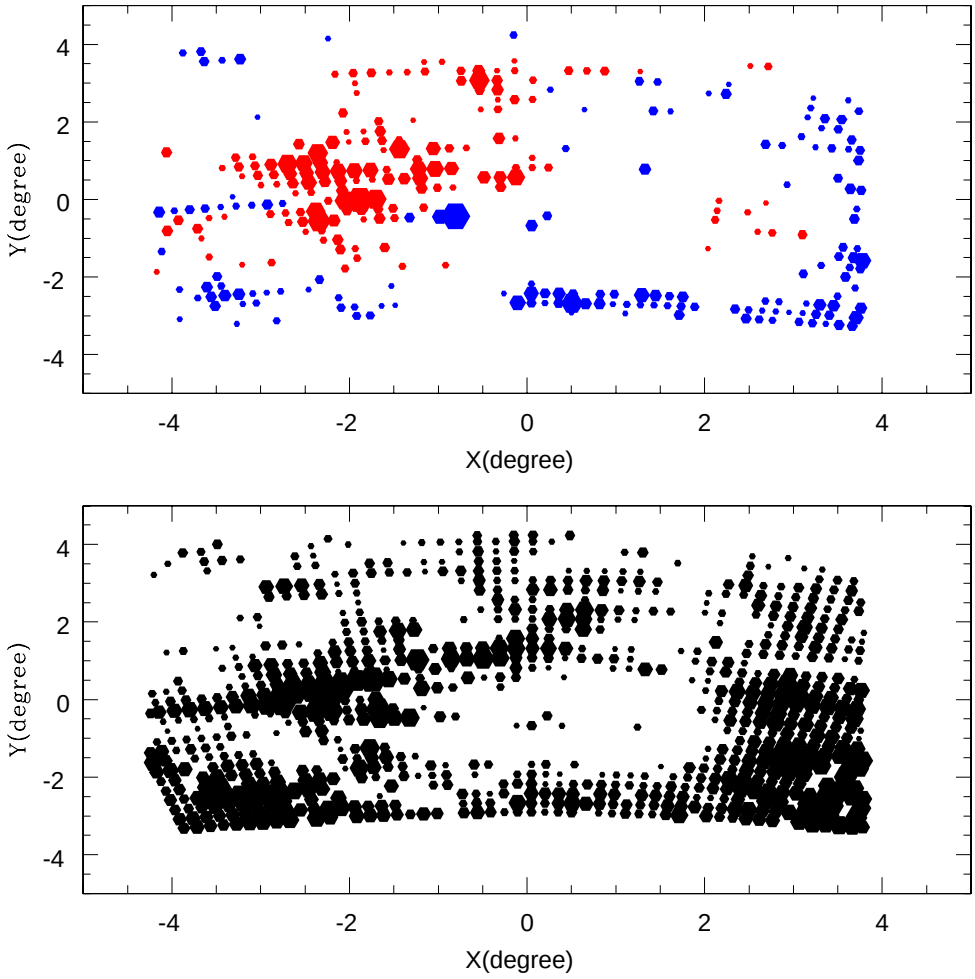

Figure 5.4: Two-dimensional plot of the extinction, A_I for the MCPS data is shown in the lower panel and a two-dimensional plot of deviation is shown in the upper panel. In the lower and upper panels the size of the points are proportional to the amplitude of the extinction and deviation of the regions from the plane of the LMC disk respectively. The blue and red points in the upper panel are the regions which are in front and behind the fitted plane respectively.

Effect of reddening

The other important point to be discussed is the role of reddening in the estimated structure of the LMC disk. The extra-planar features which are found both behind the disk and in front of the disk could be in the plane of the LMC disk itself if there were an over-estimate or under-estimate of the reddening. It has been demonstrated by Zaritsky et al. (1997) that the extinction in the LMC varies both spatially and as a function of

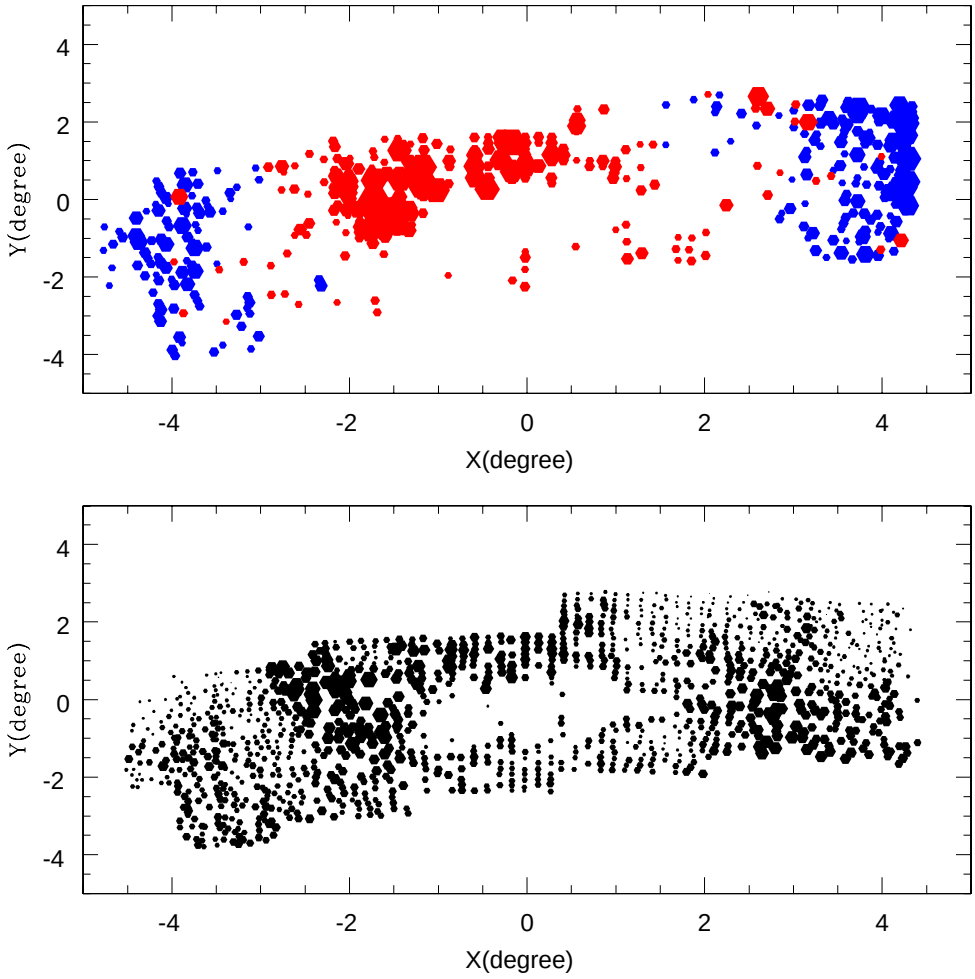

Figure 5.5: Two-dimensional plot of the extinction, A_I for the OGLE III data is shown in the lower panel and a two-dimensional plot of deviation is shown in the upper panel. In the lower and upper panels the size of the points are proportional to the amplitude of the extinction and deviation of the regions from the plane of the LMC disk respectively. The blue and red points in the upper panel are the regions which are in front and behind the fitted plane respectively.

stellar population. In our study, the dereddening of RC stars is done using the reddening values estimated from the RC stars itself.

To understand the effect of reddening on the detected extra-planar features, we compared a two dimensional plot of reddening with the deviations. The plots for the MCPS and the OGLE III data are shown in Figs.5.4 and 5.5 respectively. In both the plots the lower panel shows the reddening distribution and the upper panel shows the distribution of the deviations. In the lower panel, the size of the point is proportional to the redden-

ing value and in the upper plot the size of the point is proportional to the amplitude of the deviation. The red points in the upper panel of the plot represents the regions behind the plane and blue points represent the regions in front of the plane. We can see that in the MCPS plot (Fig.5.4) the regions in the southwestern part of the LMC disk around our suggested warps show more reddening. Hence it is possible that these warps are due to an over-estimate of reddening in these regions. Olsen & Salyk (2002) also found that the reddening near the southwestern part of the disk near the regions of their suggested warp is higher. They correlated the large reddening in the southwestern LMC regions to the diffuse extinction due to the high Galactic foreground dust, having A_I of approximately 0.3 mag, given in the COBE-DIRBE-IRAS/ISSA dust map (Schlegel et al. (1998)). Olsen & Salyk (2002) measured an A_I of approximately 0.25 mag at the LMC's southwest edge. We measured an A_I ranging from 0.1 to 0.2 with an average of 0.16 mag at the LMC southwest edge. The plot which shows the amplitude of the deviation against the extinction values for the MCPS region is shown in Fig.5.6. The magenta dots are the regions in the southwestern region of LMC, which are brighter than the surrounding regions. The reddening is high in these regions compared to the surrounding regions. There are also regions which are in front of the plane, like the southeastern disk, which do not show large reddening. Again, regions in the northeastern part with respect to the LMC bar show large reddening and these regions are shown in the deviation plot as behind the fitted plane. Once again, it could be argued that the reddening has not been accounted for properly here. There are also some nearby regions behind the fitted plane, which do not show large reddening. Thus some regions which are in the front or behind show a range of reddening as seen in Fig.5.6. On the other hand, we do not see a strong correlation between reddening and the deviation, because both positive and negative deviations are observed for regions with large reddening. That is, the reddening could not have been both under and over-estimated. Thus, reddening is not strongly correlated with the estimated structures, but the extend of the deviation from the LMC plane may still be affected by the reddening that is present.

As mentioned in the analysis section, while estimating the reddening values for the MCPS regions, 451 regions out of 1231 regions showed a negative value for the reddening. We removed those regions from our analysis. Zaritsky et al. (2004) estimated the extinction map for the LMC by comparing the stellar atmospheric models and observed colors using the MCPS data. They also found that many regions show negative extinction values. They suggested that large observational uncertainties scatters the extinction

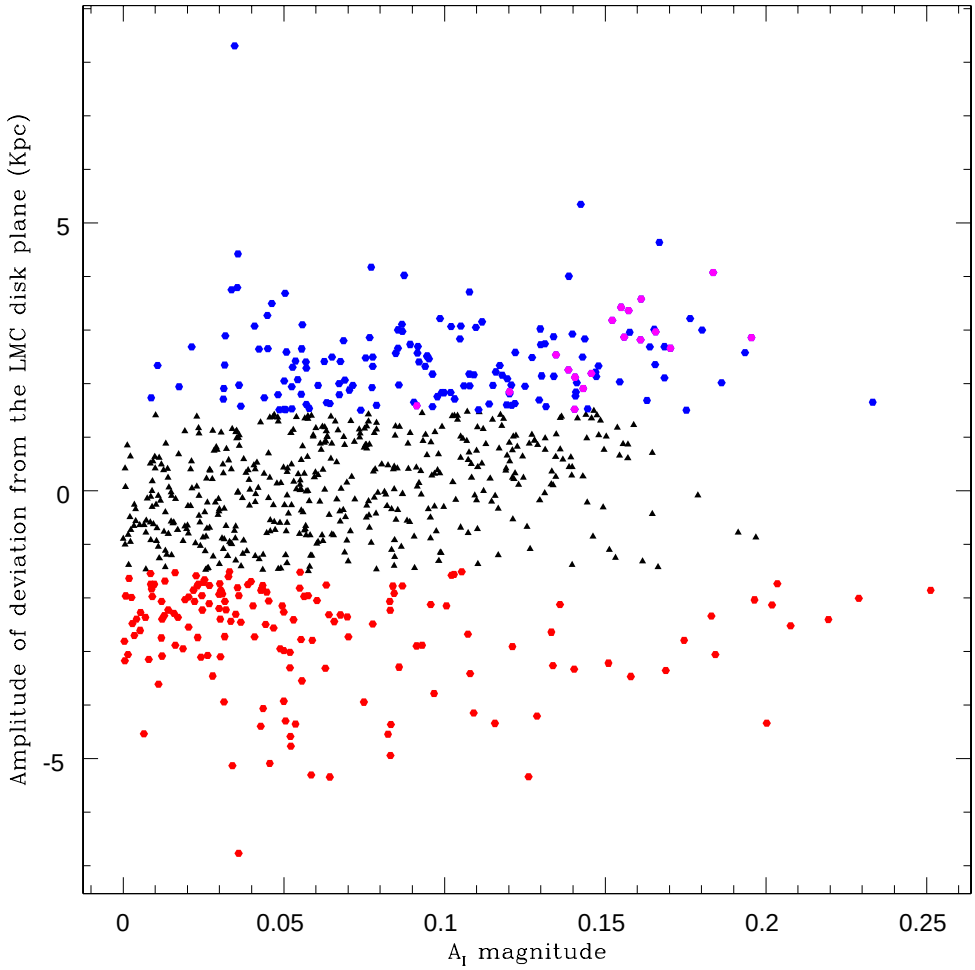

Figure 5.6: Amplitude of the deviations of the regions from the fitted plane are plotted against the A_I mag for the MCPS data. Black points are those with deviations less than 3 sigma, and red and blue are those with deviations more than 3 sigma and are behind the plane and in front of the plane respectively. Magenta dots are regions which are in front of the fitted plane in the southwestern part of the LMC disk.

to negative values, and they set those negative values as zero extinction values. We estimated the structural parameters of the LMC disk using all the 1231 regions of the MCPS data after assigning zero reddening value for those regions which show negative value for the reddening. A weighted plane-fitting procedure was applied to the 1231 regions of the MCPS data and deviations were estimated. Deviations above 3 sigma were considered as deviations, and after removing those regions, planar parameters of the LMC disk plane was re-estimated. An inclination, $i = 39^o.3 \pm 3^o.2$ and PA_{lon} $\phi = 139^o.0 \pm 4$ was obtained.

The planar parameters are matching well with the parameters we estimated without considering the regions which showed negative values for reddening. To find where these regions are located with respect to the plane of the LMC disk, we plotted the reddening E(V-I) mag vs amplitude of the deviation calculated. This plot is shown in Fig.5.7. We can clearly see that most of the regions which are assigned zero reddening values show large deviation from the plane. These regions are found both in front and behind the fitted plane. These deviations may be real. Because the reddening has an important role in the estimation of the structural parameters of the disk and the amplitude of the deviations, we prefer the analysis without considering regions with negative reddening. The agreement in the estimated parameters could just be a coincidence because the deviations estimated are both in front and behind the plane and thus the net effect on the parameters of the LMC plane is minimum.

For the MCPS data, the color of the RC stars is bluer in general when compared to the OGLE III RC stars. This can be due to the difference in the filter systems used and/or calibrations. The choice of intrinsic (V−I) color of RC stars can be another reason for obtaining negative reddening values for a large number of regions in the MCPS data. The intrinsic color of RC stars for calculating reddening is taken to be 0.92 mag (Olsen & Salyk (2002)). Olsen & Salyk (2002) selected this value to produce the median reddening obtained toward the LMC by Schlegel et al. (1998). For the OGLE III data set we calculated the intrinsic (V−I) color of RC stars to produce the median reddening obtained by Schlegel et al. (1998). The value turned out to be 0.915 mag, which is similar to the value given by Olsen & Salyk (2002). So we did the analysis of the OGLE III data with intrinsic color value, 0.92 mag. Also, there are no locations in the OGLE III data, where the value of estimated reddening goes negative. We calculated the intrinsic (V−I) color of RC stars in the MCPS data set in a similar way. The value obtained is 0.84 mag. Using this value we repeated the analysis explained in Sect.3 to estimate the LMC disk parameters. Now, out of 1231 locations, only 64 regions showed negative value for reddening. A plane fitting procedure is applied to 1167 regions and deviations from the plane are also estimated. Regions with deviations above 3 sigma are removed and the plane fitting procedure is applied to the remaining regions. The values obtained are i= $38^o.7\pm2^o.4$ and ϕ = $150^o.9\pm3^o.8$. The inclination value is comparable and within errors with the analysis done with intrinsic (V−I) color of RC stars as 0.92 mag. But the PA_{lon} value is higher than those obtained in the earlier analysis. Thus by including more regions in the inner LMC, the PA_{lon} increased significantly, whereas the inclination did not change.

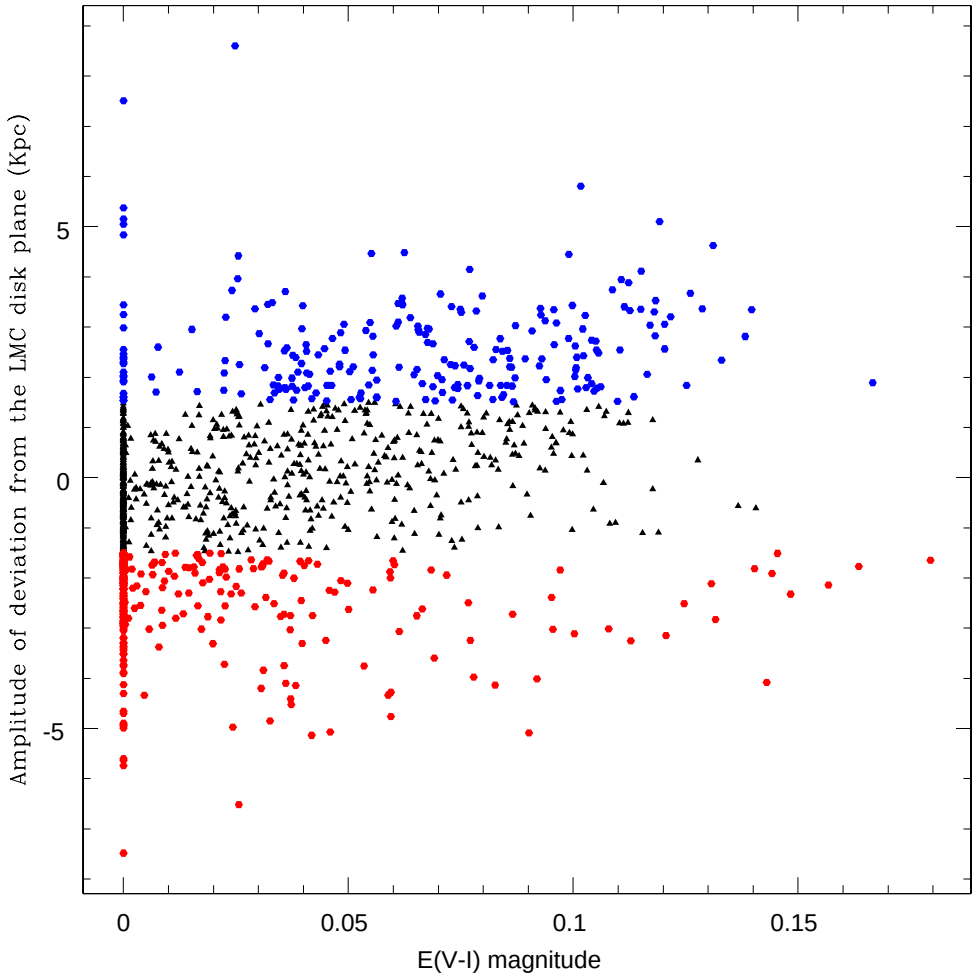

Figure 5.7: Amplitude of the deviations of the regions from the plane of the LMC disk plane are plotted against the reddening, E(V−I) values for the MCPS data after assigning zero reddening for the regions which show negative values for the reddening. (see Fig.5.6 for details)

Effect of coverage and inner structure of the LMC disk

The estimated planar parameters of the LMC may vary depending on the difference in the coverage of the LMC studied to estimate these parameters. We also obtained significantly different results from the MCPS and the OGLE III data. In order to understand the effect due to coverage, we estimated the planar parameters of the LMC disk excluding the inner LMC data at different radii from the LMC center. Thus the planar parameters are estimated using the data above the radius of 1, 2, 3, and 4 degrees from the LMC center. The results are summarised in Table.5.3. One of the important results of this analysis is

Table 5.3: Summary of orientation measurements of the LMC disk plane at different radii

Region	Inclination, i	PA_{lon}, ϕ
MCPS data		
r > 1	$36^o.1 \pm 2^o.2$	$141^o.8 \pm 3^o.9$
r > 2	$34^o.2 \pm 1^o.7$	$143^o.3 \pm 4^o.3$
r > 3	$29^o.8 \pm 1^o.1$	$151^o.7 \pm 5^o.0$
r > 4	$39^o.4 \pm 2^o.4$	$147^o.8 \pm 1^o.5$
OGLE III data		
r > 1	$23^o.5 \pm 0^o.8$	$162^o.0 \pm 1^o.6$
r > 2	$23^o.2 \pm 0^o.5$	$160^o.6 \pm 1^o.3$
r > 3	$28^o.4 \pm 0^o.2$	$146^o.9 \pm 1^o.9$
r > 4	$35^o.6 \pm 1^o.7$	$137^o.8 \pm 2^o.0$
r ≤ 3	$16^o.5 \pm 0^o.9$	$161^o \pm 4^o.5$

that the parameters estimated excluding the data within the radius of 3 degrees from the LMC center in both the MCPS and the OGLE III sets are similar, as shown in Table.5.2. From Table.1 we can see that there is a significant difference in the estimates of the planar parameters, from the analysis of full data set of the OGLE III and the MCPS data. When the inner data are excluded from the analysis, the results are matching within the error bars. This indicates that the inner structure of the LMC disk affects the estimate of the LMC disk parameters. Even though both the MCPS and the OGLE III contain data within 3 degrees of the radius from the LMC center, the OGLE III data are more affected by the inner structures. This is because the OGLE III contains a highest number of inner regions compared to the MCPS data. As mentioned before, several central regions had to be removed from the analysis of the MCPS data because they showed negative reddening. That probably is the reason for a high PA_{lon} and low inclination obtained from the OGLE III analysis.

To understand the inner structure of the LMC, we tried fitting a plane to the data within 3 degrees from the LMC center. For the MCPS data the fitting was a problem because of fewer points and also because of the deviations present within the 3 degree region from the center. For the OGLE III data the parameters obtained are $i = 16^o.5 \pm 0^o.9$ and $PA_{lon} = 161^o \pm 4^o.5$. This indicates that the inner and outer structures of the LMC

Table 5.4: Summary of orientation measurements of the LMC disk plane at different radial rings

Region	Inclination, i	PA_{lon}, ϕ
MCPS data		
2.5<r<3.5	$38^o.9 \pm 0^o.3$	$161^o.9 \pm 3^o.5$
3.5<r<4.5	$25^o.2 \pm 1^o.4$	$151^o.4 \pm 7^o.5$
4.5<r<5.5	$37^o.7 \pm 1^o.4$	$134^o.2 \pm 0^o.7$
OGLE III data		
2.5<r<3.5	$21^o.4 \pm 0^o.3$	$157^o.6 \pm 2^o.6$
3.5<r<4.5	$31^o.4 \pm 0^o.4$	$139^o.5 \pm 1^o.4$
4.5<r<5.5	$39^o.1 \pm 1^o.6$	$134^o.6 \pm 0^o.9$

disk are different. Regions within the 3 degree radius fit to a plane with significantly less inclination and large PA_{lon}, whereas regions outside 3 degrees have a large inclination and less PA_{lon}.

A similar analysis was performed by van der Marel & Cioni (2001), for AGB stars, where they estimated the variation of i and PA_{lon} as a function of radius. They used rings, whereas we used concentric regions progressively excluding the inner regions. To compare our results with theirs, we also obtained parameters of the LMC disk in different rings, and the results are given in Table.5.4. They found that the i and PA_{lon} decrease with radius, whereas we find only the PA_{lon} to decrease with radius. Thus both analyses agree that the PA_{lon} decreases with increasing radius. The differences in the trend seen for the inclination may be due to the difference in the tracer and the method used. The inclination i is found to be increasing with radius for the OGLE III data. For the MCPS data, we find that the outer two rings show an increasing i, whereas the innermost ring does not follow the trend. Therefore a definite pattern is not seen for the MCPS data set. Combining the result obtained in the last paragraph, we suggest that there is a difference in the structure of the LMC inside and outside a radius of around 3 degrees. Our results suggest that the outer disk is inclined more than the inner disk with a reduced PA_{lon}. Subramaniam & Prabhu (2005) proposed the existence of two disks in the inner 3^o of the LMC, with one counter rotating. May be the existence of two disks in the inner LMC is the reason that it

is different from the outer structure.

Deviations and warps

After fitting the LMC plane, the deviations of the disk with respect to the fitted plane seen in the overlapping regions of the OGLE III and the MCPS data sets are similar. The extra-planar feature, which is seen as behind the LMC plane in the northeast of the LMC bar is interesting. This feature is seen in both the MCPS and the OGLE III deviation plots. Some of the star-forming regions (Kim et al. (2000)) are lying around this feature. Brightening of the RC stars in the western and eastern ends of the disk are seen in the OGLE III deviation plot. The brightening in the northwestern part of the LMC disk is more clearly seen with larger amplitude. The deviation of the the MCPS data shows a similar brightening in the northwestern, southwestern, and southeastern regions of the LMC disk. The warps suggested by Olsen & Salyk (2002) in the southwestern region of the LMC are overplotted in our deviation plots, and not many regions which they suggest as warps are coinciding with our deviations, though they are located near the regions where we see deviations in the southwestern disk. Thus the brightening of the RC stars in the southwestern part of the LMC disk and the dimming of RC stars in the northeastern part near the LMC bar are suggestive of a symmetric warp in the LMC disk. Nikolaev et al. (2004) suggested a symmetric warp in the LMC disk similar to our results. Along with the symmetric warp, the brightening of RC stars in the northwestern part of the LMC disk is also very clearly seen in both the MCPS and the OGLE III deviation plots. The southeastern part of the LMC disk is also comparatively brighter than other regions, which makes the warp asymmetric. In the MCPS deviation plot, brightening of RC stars is seen near the optical center, in the bar region of the LMC. This kind of RC brightening is seen near the optical center in the bar region of the LMC shown in chapter 4 and also by Koerwer (2009).

The edge-on view of the LMC as seen from the minor-axis (Fig.5.3) also suggests that the inner LMC might have a different inclination with respect to the outer regions. Apart from this, the symmetric warp can also be noticed in this plot. It can also be noticed that the warp is not centered at the LMC center, but shifted towards the southwest by about a degree. Thus, our results suggest an off-centered symmetric warp. It is quite clear from the analysis that the inner structure of the LMC is quite complicated. In order to get a 3-D picture of the region studied here, we have shown the R.A, Dec, and Z plot of the OGLE III region in Fig.5.8. The surface plot shown here is obtained with a standard surface plot algorithm and thus involves interpolation and averaging. Therefore, this plot can be used

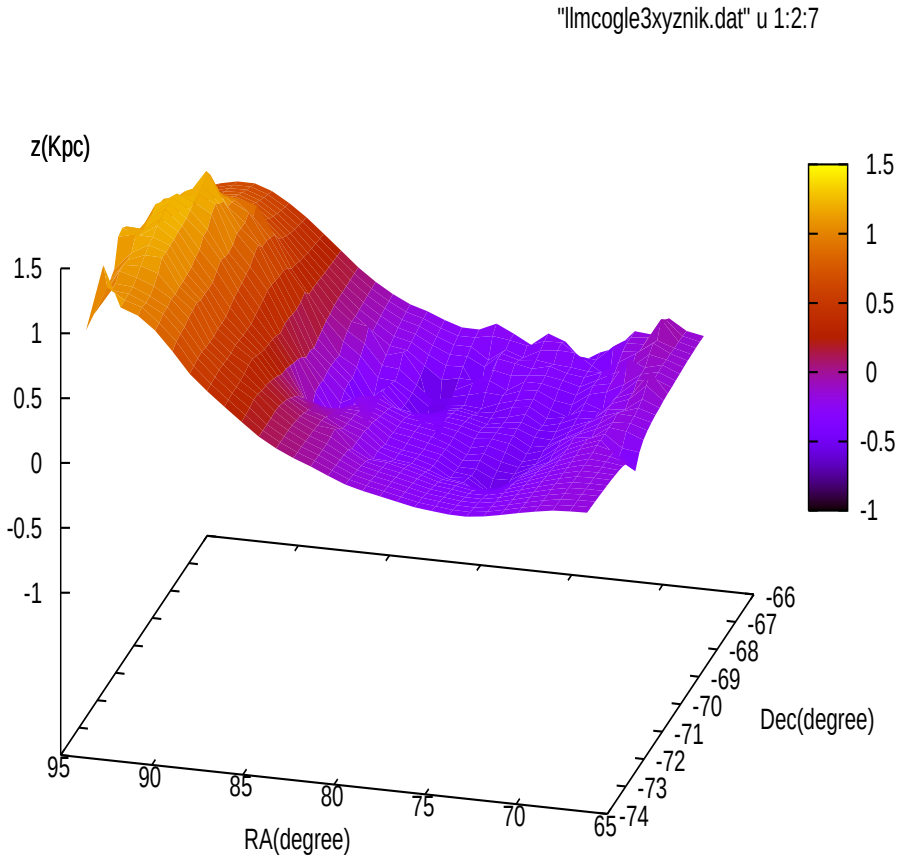

Figure 5.8: 3D plot of the LMC disk obtained from the OGLE III RC stars.

to obtain a qualitative understanding of the structure, but cannot be used for any quantitative analysis. The figure clearly shows that the inner regions have a smaller inclination and the outer regions have large inclination. The increase in the inclination seems to start at a closer radius in the northeast, when compared to the southwest, which makes it off-centered. It is clear from this figure that the LMC disk shows a lot of structures, and it is difficult to define a plane. By fitting a plane, a large number of regions are likely to show deviation from the plane suggesting warps. It is also clear that depending on the coverage of the data, the plane fitted and the parameters obtained are likely to change, which in turn will identify different regions to have deviations/warps. Also, defining a warp gets complicated due to contribution from reddening and population effects. In general, we notice that the inclination increases with radius. The northeast of the LMC is closer to us, and

we find that it gets even closer with radius, with an increase in inclination. The southwest part, instead of getting more distant, also seems to get slightly closer. This is also seen as a warp by Olsen & Salyk (2002). Thus, the plot suggests that studies which ignored the inner regions and considered only the outer regions are likely to derive a highly inclined plane with a smaller PA_{lon}. Studies that did not consider the outer regions would derive a less inclined plane with a large PA_{lon}. Because the change in the inclination is off-centered, methods which use ring-analysis are likely to be more affected by the inner structure and choice of center.

Warps and structural changes seen in the LMC disk could be due to tidal interactions. The SMC is unlikely to be the cause because it is smaller compared to the LMC. This effect may be due to the gravitational attraction of our Galaxy on the LMC. Thus, our results point in the direction that the increased inclination and the warps identified in the outer regions may be due to the interaction with our Galaxy. It is important to study more distant regions to understand the change in the disk structure with radius. A detailed study of the outer structure may throw light on the details of the tidal effects on the LMC disk and its origin.

Comparison with the structure of the H I gas disk

It is interesting to compare the structure of the H I gas disk of the LMC with that of the stellar disk. Various HI studies have estimated the PA_{lon} and the inclination of the H I disk by kinematical as well as by geometrical methods. These studies also suggested the presence of extra-planar features in the H I disk. Feitzinger et al. (1977) derived an inclination of $33^o \pm 3^o$ and PA_{lon}, $168^o \pm 4^o$ by geometrical means. The H I velocity studies by Luks & Rohlfs (1992) revealed two kinematic components, the L (lower velocity) component and the D (disk) componenet. The D component was found to be extended in the whole LMC, and the L component, with two deformed lobes, was found to the north of 30 Dor and south of 30 Dor region. The L component was found to be around 50-500 pc above the D component. The PA_{lon} of around 162^o was estimated for the disk component by kinematical method (line of maximum velocity gradient). The above values are not very different from the PA_{lon} of the stellar disk estimated from the OGLE III data. Kim et al. (1998) estimated the PA_{lon} of H I disk to be around 168^o by kinematical method. They suggested that the H I disk is inclined in a way that PA=78^o is closer to us. This value is agrees well with our result, which gives the PA of the closest part to be around $71^o \pm 4^o.5$ for the inner stellar disk from the OGLE III data. Kim et al. (1998) also estimated the inclination of the H I disk from the outer isophotes of HI brightness temperature to

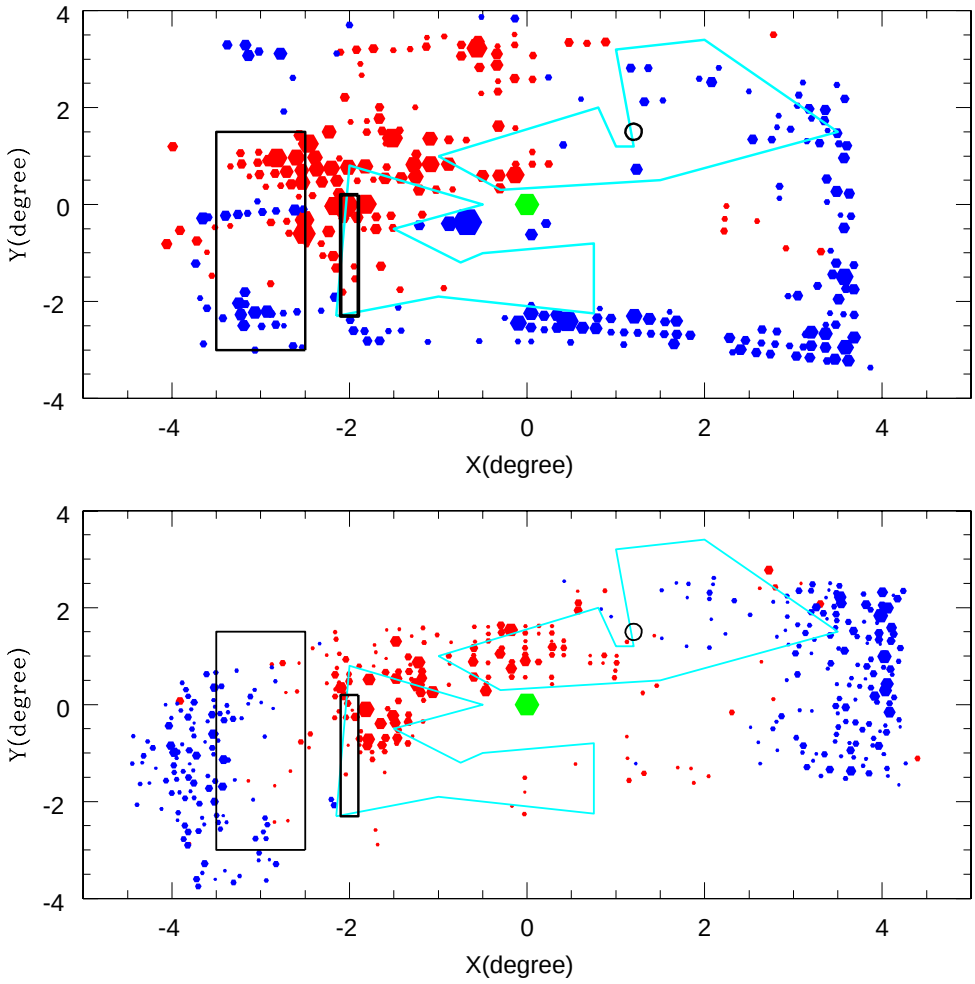

Figure 5.9: Deviations found in the stellar disk of the LMC using the OGLE III and the MCPS data are plotted in the lower and upper panels respectively. The color code is the same as in Fig.5.1 and Fig.5.2. The two cyan lobes in both the panels are the L component identified in H I disk by Luks & Rohlfs (1992). The black features in both the panels are the kinematical warps suggested by Luks & Rohlfs (1992) in the L and D components.

be around 22^o. As this value was poorly determined and highly correlated with other parameters, they adopted the canonical value of 33^o (Westerlund 1997).

In order to compare the H I and stellar disk structures, we plotted the deviations found in the stellar disk from the OGLE III and the MCPS data sets along with the structures found in the H I disk. In Fig.5.9 the lower panel shows the deviations found in the OGLE III data and the upper panel shows the deviations found in the MCPS data set for the stellar disk. As in the previous plots, red points denote the regions behind the fitted plane and

blue points denote the regions in front of the fitted plane, with sizes proportional to the amplitude of the deviations. The approximate location of the L component identified by Luks & Rohlfs (1992) is shown as two irregular structures in cyan color. Luks & Rohlfs (1992) suggested the presence of kinematical warps in some regions of the D component as well as in some regions of the L component. These regions are shown as black features. The kinematical warps identified in the D component are in the big rectangular box in the east. The regions where kinematical warps are identified in the L component are shown as black circle and small black rectangular box. Most of the kinematical warps identified in the H I disk are more or less near the extra-planar features found in the stellar disk.

The PA_{lon} estimated for the H I disk is similar to the PA_{lon} of the stellar disk in the inner regions of the LMC, particularly the estimates from the OGLE III data. The effect of inclination of the LMC, which makes the northeastern part appear to be closer, is seen both in stellar as well as in the H I disk of inner LMC. The inclinations are also similar. The kinematic warp seen in the D component coincides with the eastern stellar warp. There is a mild indication that the L component coincides with regions which are located behind the disk. On the whole, the L component and the kinematical warps identified in both components of H I, more or less coincide with the warps in the stellar disk. There is no H I counter part for the southwestern warp found in the stellar disk. These results suggest that the inner stellar and H I disk structures of the LMC are similar.

5.3 Near Infrared Study

Reddening plays an important role in the estimation of the strucutral parameters of a galaxy. As the effect of reddening is less in longer wavelengths, the LMC structure estimated using NIR data of RC stars is likely to have reduced effect due to reddening. Recently, Koerwer (2009) derived an i = 23^o .5 ± 0^o.4 and ϕ = 154^o.6 ± 1^o.2, using the JH photometric data of RC stars from the IRSF MCPSC. He was unable to identify the warps in the south western end of the disk, which is evident in the optical studies (Olsen & Salyk 2002 and the results in previous section). In this study, a constant reddening was assumed for all the regions of the LMC. The extinction maps of the LMC estimated from the optical bands, given in the lower panels of fig 5.4 and 5.5 show variation in different sub-regions. Especially a large reddening in the south-western disk is seen in the map where warps are identified. The sample of RC stars used in the study by Koerwer (2009) have contamination from AGB stars. Also there is an overlap of sub-regions in the ends of the disk which can cause some structural information to be averaged out. The above

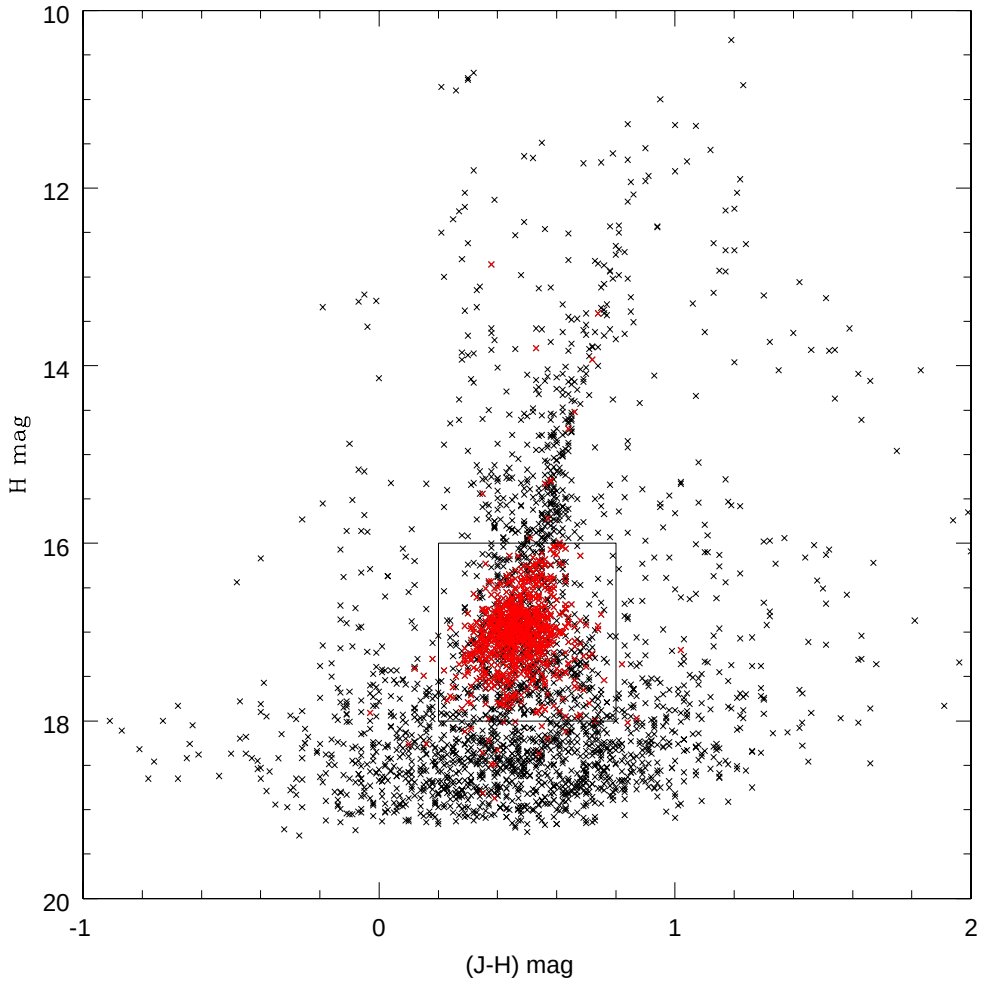

Figure 5.10: A sample IR CMD of a sub-region in the LMC is shown. The red points are the RC stars identified from the optical CMD of the sub-region. The box within which the RC stars in the IR CMD are distributed is also shown.

mentioned points motivated us to study the LMC structure using the same NIR data of the RC stars used by Koerwer (2009). In this paper we use the photometric data of the RC stars in the J and H pass bands IRSF MCPSC (Kato et al. 2007). The K_s band magnitude limits of the survey is too shallow to reliably detect the RC stars.

5.3.1 Data & Analysis

We divided the IRSF MCPSC region into 928 regions with a bin size of 10.53 x 15 arcmin^2 . The average photometric error of RC stars in J and H bands are around 0.1 mag. Photometric data with error less than 0.3 mag are considered for the analysis. The IRSF

observed region of the LMC covers ~ 40 deg^2 in the sky. These regions come within the MCPS observed region of the LMC. A sample $(J-H)$ vs H CMD is shown in figure 5.10. To isolate the approximate RC location in the infrared CMD, we used the optical CMD of the corresponding sub-region from the MCPS data. We cross-correlated the optical and infrared data and obtained the infrared (J,H) magnitudes of the RC stars identified within the box of the optical CMD (Fig 2.1). Those points are over-plotted as red points in fig 5.10. Most of the RC stars are well within the box of infrared CMD, with boundaries 0.2 - 0.8 mag in $(J-H)$ colour and 16.0 - 18.0 mag in H magnitude. Stars outside the box are not considered for the analysis. Thus the RC stars are identified for all the 928 sub-regions. Out of 928 regions only 890 regions have reasonable number (400-3000) of RC stars to do the analysis. The number distribution of the RC stars in H mag and $(J-H)$ mag are obtained with a bin size of 0.15 and 0.05 mag respectively. The peak H mag, peak $(J-H)$ mag, the associated errors and the reduced χ^2 values are obtained from the distributions using numerical analysis (refer Chapter 2). The H magnitude and $(J-H)$ colour distributions are shown in figure 5.11 and 5.12 respectively. Regions with peak errors greater than 0.1 mag and those with reduced χ^2 value greater than 2.5 are omitted from the analysis. Thus the regions used for final analysis became 635 out of 890. Most of the central regions are removed from the analysis due to poor fit.

The peak values of the colour, $(J-H)$ mag at each location is used to estimate the reddening. The reddening is calculated using the relation E$(J-H) = (J-H)_{obs}$ - 0.44 mag. The intrinsic colour of the RC stars is taken to be 0.44 mag. We selected the intrinsic colour to produce a median reddening obtained by Schlegel et al. (1998) towards the LMC. The interstellar extinction is estimated by A_I =1.6xE$(J-H)$. After correcting the mean H mag for interstellar extinction, H_0 for each region is estimated. The difference in H_0 mag between regions is a measure of the relative distances and is converted into relative distances. The R.A, Dec and relative distance from the center of a sub-region are used to convert the system into a cartesian coordinate system as given in equations (12), (13) and (14) in chapter 2. Then a plane fitting procedure (section 2.2.3) is applied to the x,y,z system and the structural parameters of the LMC disk are obtained along with the errors in the parameters (refer section 5.1.2).

5.3.2 Results & Discussion

The structural parameters of the LMC disk are estimated using the dereddened mean H_0 magnitude of the RC stars. The study gives an inclination of i= $26^o \pm 0^o.6$ & PA_{lon} = $150^o.9 \pm 0^o.5$ for the LMC disk. The deviation of the LMC disk regions from the estimated

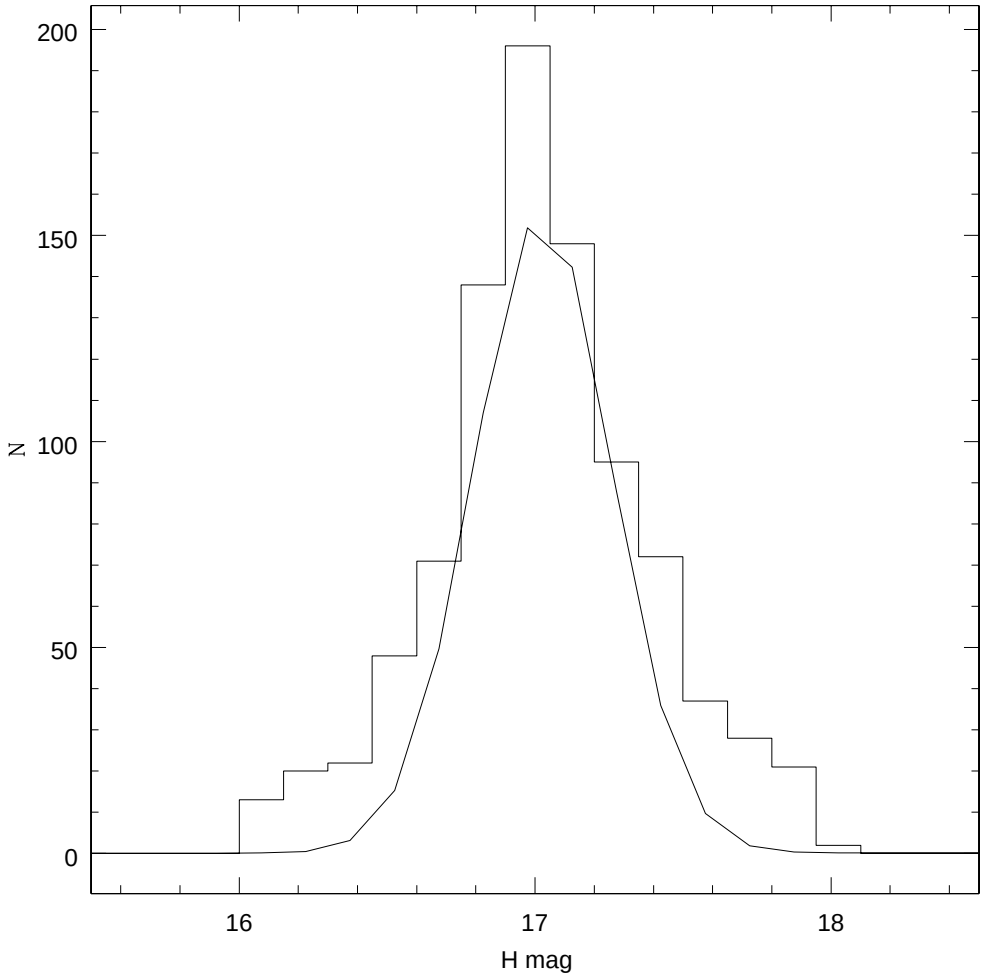

Figure 5.11: A typical H magnitude distribution of a sub-region in the LMC. The best fit profile to the distribution is also shown.

plane are calculated as explained in the section 5.1.2. The average error in the estimation of H_0 mag is converted into distance and its around 300 pc. Deviations above 3-sigma are considered as significant deviations from the fitted plane. Fig 5.13 shows the deviation of the LMC regions from the plane. In the bottom panel, all the regions used for the analysis are plotted. The black points are those which are on the fitted plane, red points are disk regions which are behind the plane and blue points are the disk regions which are in front of the plane. In the upper panel only the regions with deviations above 3 sigma are plotted and the size of the points are proportional to the amplitude of the deviation. Here also, red points are regions behind the fitted plane and blue are in front of the fitted plane. From the plots we can see that there are many regions which are deviated from the planar structure

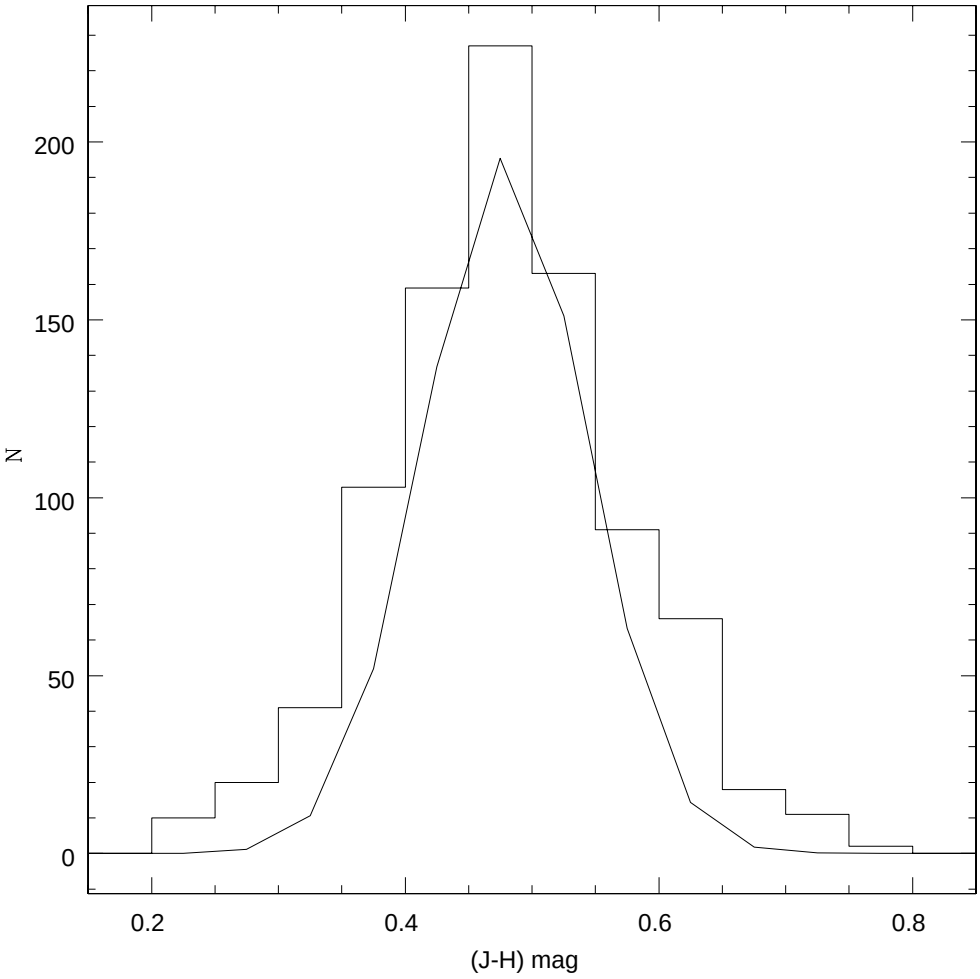

Figure 5.12: A typical $(J - H)$ colour distribution of a sub-region in the LMC. The best fit profile to the distribution is also shown.

of the LMC disk. The plot shows that the RC stars in the regions, south east, south west & north west of the LMC disk are brighter than what is expected from the plane fit. Also, some regions north east to the LMC bar are dimmer than expected. Most of the regions in the central bar are omitted from our analysis due to poor fit of the RC distributions. The remaining few regions in the center of the bar show a brightening with respect to the fitted plane. This matches with the one localized region in the bar which showed a similar brightening in the optical analysis of the bar region (section 4.3).

In order to understand the effect of reddening, we plotted a two dimensional plot of reddening as well as the deviations. The lower panel of figure 5.14 shows the reddening distribution and the upper panel shows the distribution of the deviations. In the lower

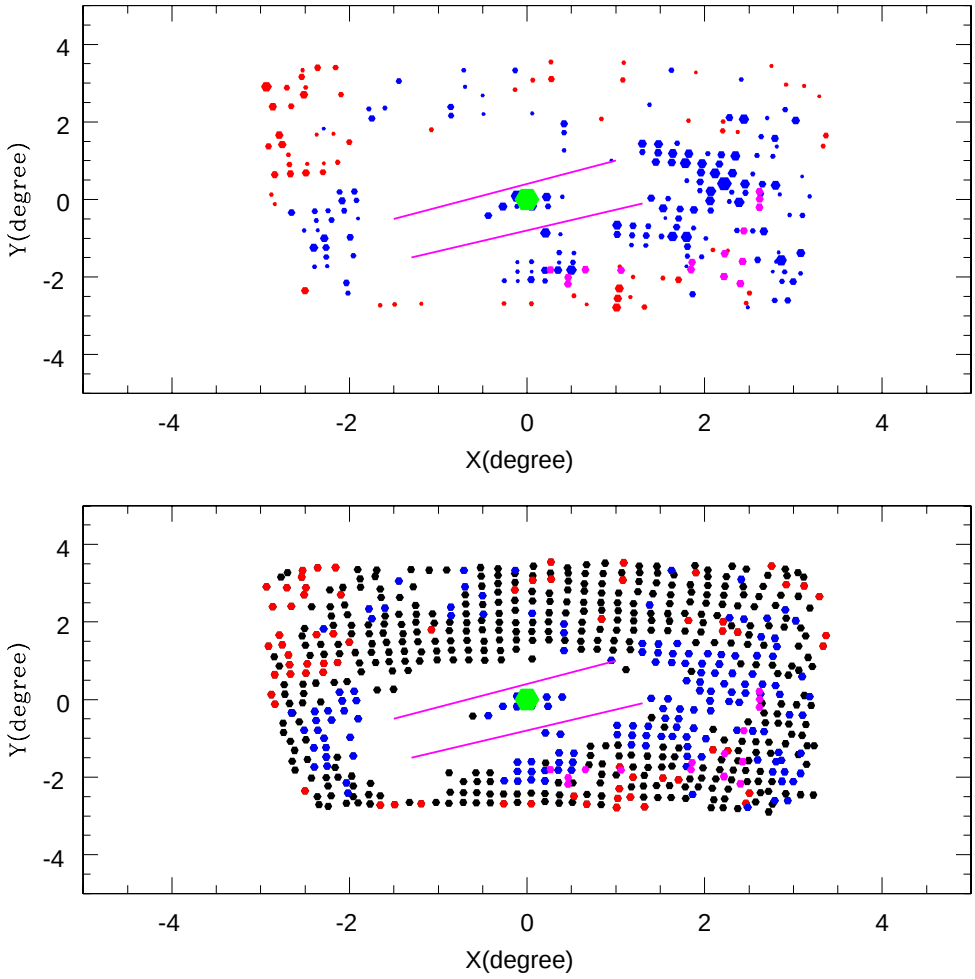

Figure 5.13: The IRSF regions which are fitted on the plane and those which are deviated are shown. In the lower panel, black dots represent the regions on the fitted LMC plane, red dots represent the regions behind the fitted plane and the blue dots represent the regions which are in front of the fitted plane. The upper panel shows only the regions with deviations, greater than 3 sigma, from the LMC disk plane. The size of the points are proportional to the amplitude of the deviations. Magenta dots in both panels are the regions which are suggested as warps by Olsen & Salyk (2002). The green hexagon in both plots represents the optical center of the LMC.

panel the size of the point is proportional to the reddening value and in the upper plot the size of the point is proportional to the amplitude of the deviation. The red points in the upper panel of the plot represents the regions behind the plane and blue points represent the regions in front of the plane. As we see in the lower panel of the figure, the reddening varies across the LMC. The regions in the southwestern part of the LMC disk around

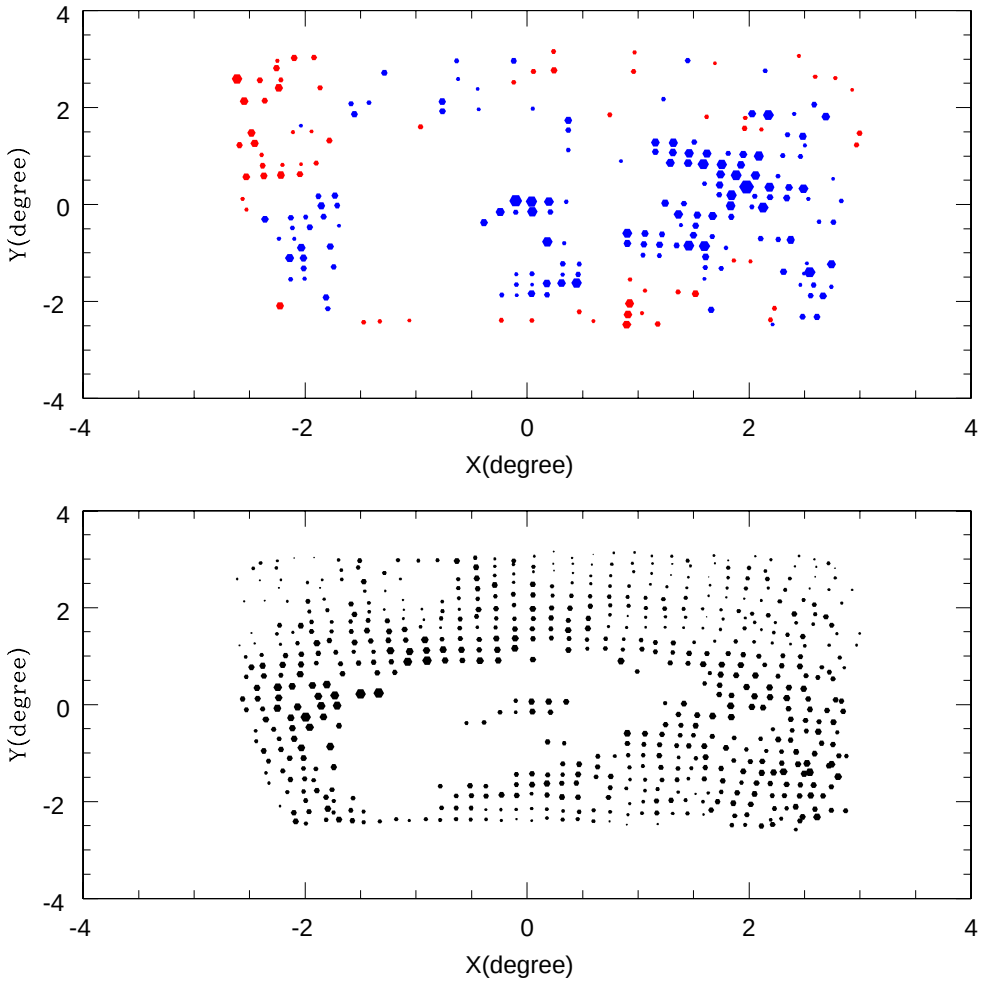

Figure 5.14: The lower panel shows the distribution of reddening across the LMC, estimated using the IRSF data. The size of the points is proportional to the amplitude of the reddening. The upper panel shows the distribution of deviations from the plane. The blue points are the regions which are infront of the plane and the red points are those which are behind the plane.

our suggested warps show more reddening. Thus if we assume a constant reddening across the LMC we will not be able to identify these warps. At the same time, we do not see a strong correlation between reddening and the deviation, because both positive and negative deviations are observed for regions with large reddening. That is, the reddening could not have been both under and over-estimated.

5.4 Conclusions

We used the RC stars identified from the OGLE III, MCPS and IRSF MCPSC data to estimate the structural parameters of the LMC. The results can be summarised as follows:

•We estimated the structural parameters of the LMC disk such as the inclination, i, and the position angle of the line of nodes (PA_{lon}), ϕ using a least-square plane-fitting procedure.

•We find an inclination of i =$23^o.0\pm0^o.8$ and PA_{lon}, ϕ = $163^o.7\pm1^o.5$ using the OGLE III data and an inclination of i=$37^o.4\pm2^o.3$ and PA_{lon} ϕ = $141^o.2\pm3^o.7$ using the MCPS data. Extra-planar features, which are in front as well as behind the fitted plane, are seen in both the data sets.

• We find an inclination, i = 26^o ± $0^o.6$ and PA_{lon} = $150^o.9$ from the IRSF MCPSC data. Extraplanar features in the southeast,southwest and northeast regions of the LMC which are seen in the analysis of optical data are confirmed.

• We find that the choice of center has a negligible effect on the estimated parameters.

•The reddening is found to be large in some regions located in front and also in regions located behind the fitted plane. Deviations are also found in regions without large reddening. These suggest that the reddening is only mildly correlated with the deviations of the disk from the fitted plane. Reddening varies across the LMC and it plays a major role in the identification of the extraplanar features.

•We find that the disk within a 3 degree radius has lower inclination and higher PA_{lon}, and differs from the outer disk. The change of structure in the outer LMC could be due to tidal effects.

• The edge-on view of the LMC disk along the minor axis suggests an off-centered symmetric warp.

• We suggest that the complicated structure of the inner LMC causes variation in the

estimated planar parameters depending on the area covered for each study, including the two data sets used here.

- In the inner LMC, the stellar as well as the H I disk have similar properties.

CHAPTER 6

TRACING THE METAL POOR HALO OF THE LARGE MAGELLANIC CLOUD USING THE RR LYRAE STARS *

6.1 Introduction

The LMC is known to be a disk galaxy with or without a halo. There have been many efforts to find evidence for the presence of a halo in the LMC. Such evidence is looked for in the old stellar population such as globular clusters (GCs) and field RRLS. The oldest GCs appear to lie in a flat rotating disk whose velocity dispersion is 24 kms^{-1} (Kinman et al. 1991 and Schommer et al. 1992). van den Bergh (2004) re-estimated the velocity dispersion of the GCs and concluded that they could still have formed in the halo. Since the number of GCs in the LMC is small (13 clusters), it is difficult to infer the signature of the halo from this sample. Another tracer is the RRLS, which are almost as old as the oldest GCs. Recent surveys of the LMC such as OGLE and MACHO have identified a large number of RRLS. Among the follow up studies, Minniti et al. (2003) found kinematic evidence for the LMC halo, by estimating the velocity dispersion in the population of RRLS. Alves (2004a) estimated the mass of the LMC based on RRLS surface density and remarked that their exponential scale length is very similar to that of the young LMC disk. Freeman (1999) remarked that the similarity of their scale length to the scale length of the young stellar disk suggested that the RRLS in the LMC are disk objects, like old clusters, and supported the view that the LMC may not have a metal-poor

*Results presented here are published in Subramaniam. A., & Subramanian. S., 2009, A&A, 503, L9

halo.

Subramaniam (2006) studied the density distribution of RRLS and found that it is elongated as the LMC bar. Since these stars were found to have a disk-like distribution and halo-like location, she speculated that these stars might have formed in the disk and its present location could be due to later mergers. The OGLE III catalogue of RRLS Soszyński et al. (2009), confirmed this bar-like elongation. In this study, we used the RRLS catalogue of Soszyński et al. (2009) in the LMC, consisting of 17693 ab type RRLS to obtain their number density and scale height distribution. The method used by Subramaniam (2006) is followed here. The density distribution is clearly found to be elongated and the PA estimate matches that of the RC stars. The scale height found by Subramaniam (2006) was larger than the scale height for the disk as delineated by the RC stars. Thus it was suggested that the puffed up distribution of the RRLS could be due to mergers and the RRLS might have initially formed in the disk. In this study, the scale-height distribution of the OGLE III RRLS is estimated and is compared with that obtained from the RC stars (refer Chapter 3). The comparison identifies two populations, where one population is found to follow the disk population. We have explored whether another property of the LMC disk, i.e., inclination, is present in the RRLS.

6.2 Estimation of the number density distribution of RRLS

Soszyński et al. (2009) presented a catalogue of RRLS discovered in the inner parts of the LMC, consisting of 17693 objects. The center of the LMC was taken as R.A = 05^h 19^m 38^s ; Dec = -69^o275.2 de Vaucouleurs & Freeman (1972). The R.A and Dec of the RRLS were converted to the projected X and Y coordinates. The data are binned in 0.2 degree bins on both the axes and the number of RRLS in each box is counted to obtain the number density in square degrees. A plot of their density is shown in Fig. 6.1, where the variation in the number density is clearly seen. On the whole, the smooth spatial variation in the density is found to have an elongated distribution. The direction of elongation is found to be similar to the elongation of the bar of the LMC. The position angle (PA) of the elongation is estimated to be PA = 125^o ± 17^o, for the eastern side and this value is within the errors of the value found by Subramaniam (2006) using OGLE II RRLS (PA = $112^o.5$ ± $15^o.3$) and by Pejcha & Stanek (2009) (PA = $112^o.4$). A clear value for the PA emerges on the eastern side, but a clear value does not emerge on the western side. The above value is very similar to the PA_{maj} as estimated from RC stars, $114^o.4$ ± 22^o .5, Subramaniam (2004) and also the PA_{maj} from the red giants $122^o.5$ ± $8^o.3$ (van der

Marel & Cioni 2001). All the above values are the same within the errors. Subramaniam (2006) also found that the density distribution of RRLS is similar to the RC and red giant stars along the major axis. The density distribution of the RRLS is found to be located slightly away from the adopted optical center of the LMC. Their center was was found to be at R.A = 05^h 20^m $40^s.4$ and Dec = -69^o48'5" by Subramaniam (2006). We also find the center of the RRLS to be same as above, within errors. This is also similar to the value estimated by Alves (2004a). This center is denoted in Fig. 6.1, as blue cross and is slightly shifted with respect to the optical center.

Thus, the bar-like elongation seen in the RRLS is signicant. It is not possible for the RRLS to have formed in the halo and still have a bar-like elongation. A probable scenario is that most of the RRLS are formed in the disk. To summarise, the RRLS in the inner LMC are likely to have formed in the disk and are unlikely to trace the halo.

6.3 Estimation of dispersion in the mean magnitude of ab type RRLS

The ab type stars among the RRLS could be considered to belong to a similar sub class and hence assumed to have similar properties. The mean magnitude of these stars in the I pass band, after correcting for the metallicity and extinction effects, can be used for the estimation of distance. On the other hand, the observed dispersion in their mean magnitude is a measure of the depth in their distribution. A high resolution reddening map of the region observed by the OGLE III survey is presented in Fig. 4.2, estimated using the RC stars. This data is used to estimate the extinction to individual RRLS. Stars within each bin of the reddening map are assigned a single reddening and it is assumed that the reddening does not vary much within the bin (4.44 X 4.44 arcmin^2). The contribution to the dispersion from the variable extinction is minimised, though there may still be a non-zero contribution to the estimated dispersion.

The observed distribution of ab type stars in the X and Y direction are binned such that there are more than 10 stars in most of the locations and a maximum of $\sim$ 300 stars in some locations. We used a bin size of $0^o.5$ in X and $0^o.5$ in Y. We estimated mean magnitudes and dispersions for 231 locations. This value of the dispersion can be used to estimate the scale-height, but has contributions from (1) photometric errors, (2) range in the metallicity of stars, (3) intrinsic variation in the luminosity due to evolutionary effects within the sample and (4) the actual depth in the distribution of the stars (Clementini et al. 2003). We need to remove the contribution of the first three terms (σ_{int}) so that

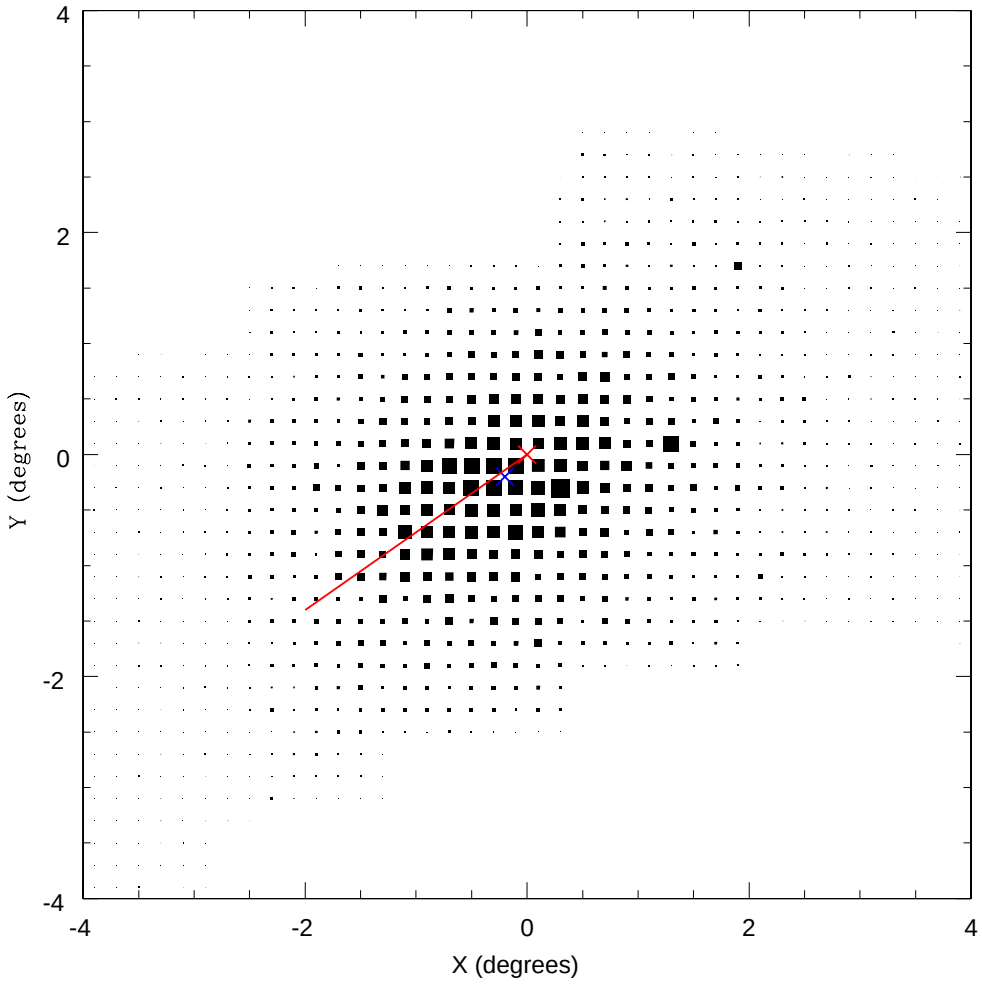

Figure 6.1: Number density distribution of RR Lyrae stars in the LMC. The optical center is shown as black cross, the center of the RRLS density is shown in blue cross.

the value of the last term (σ_{dep}) can be evaluated. Clementini et al. (2003) estimated the value of σ_{int} as 0.1 mag for their sample. Subramaniam (2006) estimated a value of 0.15 mag for a similar analysis based on OGLE II data of RRLS. When we tried to subtract a value of 0.15 mag, we found that many regions have a dispersion less than this value, especially at locations away from the center. Hence we decided to ignore this reduction and use the total value of dispersion to estimate the scale height, very well aware that values estimated will be upper limits. Thus we do not derive any quantitative estimates on scale height. We have plotted the observed dispersion in magnitude (bins with less than 10 stars are excluded), converted into Z distance in an edge-on view along the X-axis shown in Fig. 6.2. The scale height displayed is the Gaussian dispersion of z-heights

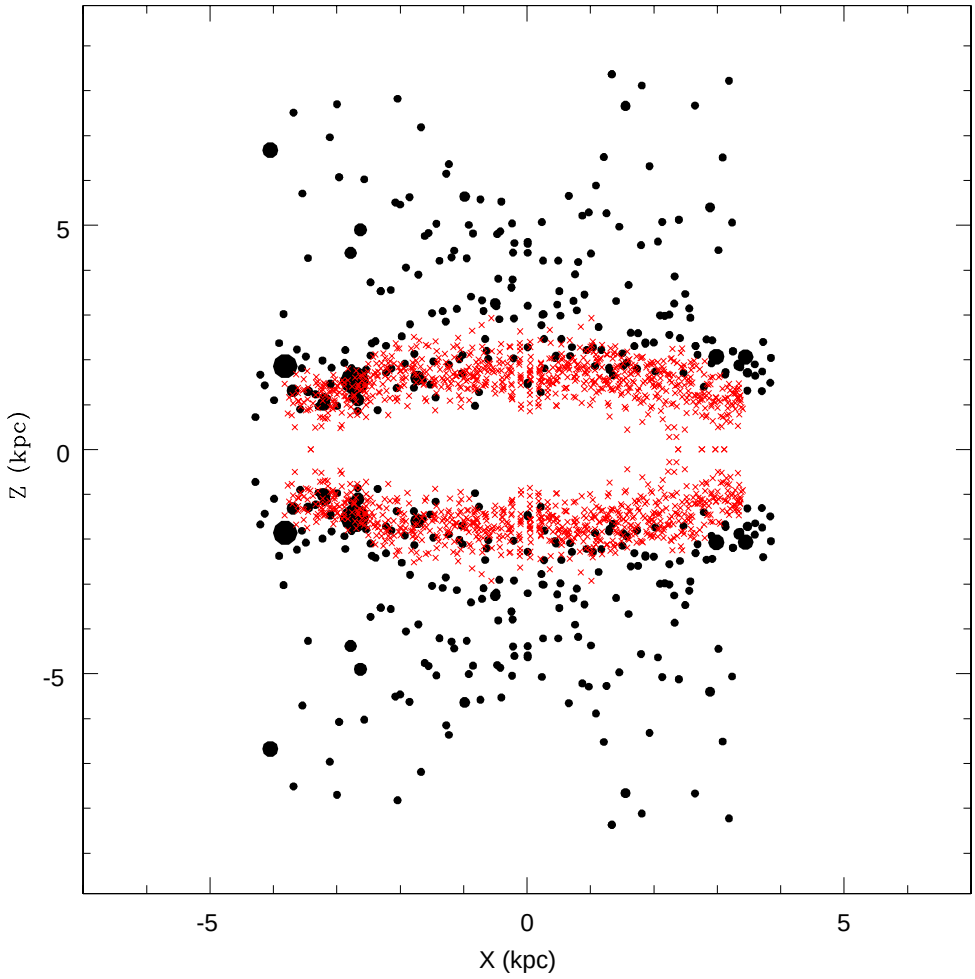

Figure 6.2: The distribution of scale-height of RRLS (black) compared with that of RC stars (red).

in each bin, rather than the conventional scale height of an exponential distribution. The distance is obtained from the relation 0.1 mag = 2.3 kpc. In order to give a complete edge-on view, the estimated depth in magnitude is halved and shown along the +ve and -ve Z-axis. In order to compare this depth with the disk population, we have shown the RC depth (halved for the edge-on view) estimated in chapter 3. Their result also points to a thicker LMC disk, even after correcting for inclination, as shown by the red points. The figure clearly shows two population of RRLS, one population being very much like the RC stars in depth distribution and the other showing an inflated distribution. The number of regions identified with the disk-like RC stars increases away from the center. The inflated regions are located more or less in the bar region. The figure also suggests an

X-shaped distribution in the edge-on view. An X-Y view of the dispersion is also shown as an inset in Fig. 6.3, where the size of the points is proportional to the dispersion. This might give clues to the formation of this distribution, if the RRLS are actually formed in the bar/disk and then became inflated later.

In order to estimate the fraction of locations of each population, the histogram of σI_0 is shown in Fig. 6.3. The histogram has a peak in the 0.1 - 0.2 mag bin, where 43% (100 regions out of 231) of the locations show a dispersion of less than 0.2 mag. This explains why we could not subtract the estimated contribution of σ_{int} . These regions are located all over, with increasing number away from the bar. 47% of regions show dispersions between 0.2 - 0.5 mag, and most of them are located within the bar region. About 10% of regions show dispersions of more than 0.5 mag. This clearly shows out that majority of the RRLS are in two types of distribution, one disk-like and the other with a larger scale-height. This analysis might suggest that not more than 10% of the RRLS in the inner LMC are likely to have formed in the extended halo.

6.4 Inclination of the distribution of the RRLS

Having estimated the major axis of the elongation, we shifted the coordinate system from X-Y to X'-Y' such that the new X' and Y' are along the major and minor axes respectively. In order to see the disk+bar of the RRLS in the edge on view, along the major and minor axes, we have shown the binned I_0 mag (binned between 18.0 - 19.0) against the two axes in Fig. 6.4. The almost horizontal distribution along the major axis confirms that the estimated PA is close to the line of nodes. The bar region was excluded (X' = Y' = 2 degrees), and the remaining 57 data points were fitted to estimate the slope as 0.0099±0.0028 mag/degree, the mean I_0 mag (y-intercept) as 18.654, with a correlation coefficient of 0.43. The low correlation coefficient is due to the extra planar features seen beyond 3 degrees from the center. The estimated fit is shown in the figure, it fits the inner regions as well. The edge-on view along the minor axis shows a variation in I_0 magnitude, which suggests inclination of the plane containing the RRLS. We excluded the regions between 0 and $2^o.0$ of the minor axis, where significant deviation is noticed. We fitted the rest of the regions and the inclination was estimated. The values estimated using 46 points are inclination (slope) = -0.0265±0.0036 mag/degree, mean magnitude (y-intercept) = 18.637 mag and the correlation coefficient was found to be 0.74. The fit as shown in the figure reveals that the fit is satisfactory, except for the extra-planar feature towards the north eastern part. The inclination estimated here, i = $31^o.3 \pm 3^o.5$, is very similar to the

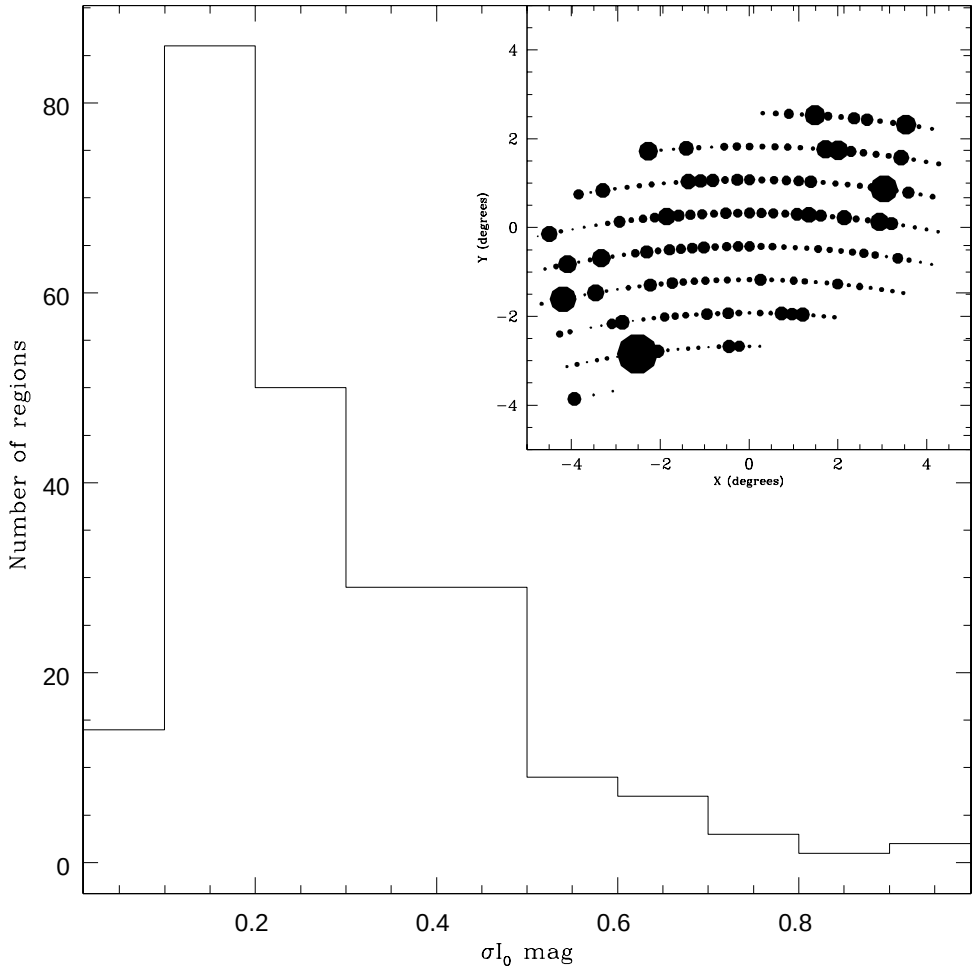

Figure 6.3: The histogram of the dispersion in RRLS (σI_0).

previous estimates of inclination for the disk (i = $30^o.7 \pm 1^o.1$ Nikolaev et al. (2004), i = $34^o.7 \pm 6^o.2$ van der Marel & Cioni (2001)). If we consider all the points, including the extra-planer features, the inclination becomes i = $20.8 \pm 3^o.5$, using 66 points. The extra-planer feature, suggestive of an extension behind the disk, is located close to the 30 Doradus star forming region. In this analysis, we have considered reddening estimated using RC stars. This feature could arise because of uncorrected reddening for at least part of the RRLS in this region. The colour of the dereddened RRLS were found to be relatively redder in these locations, supporting the above idea. To summarise, we establish the significant result that the RRLS distribution has a line of nodes as well as an inclination similar to that of the LMC disk, which confirms the idea that a major fraction

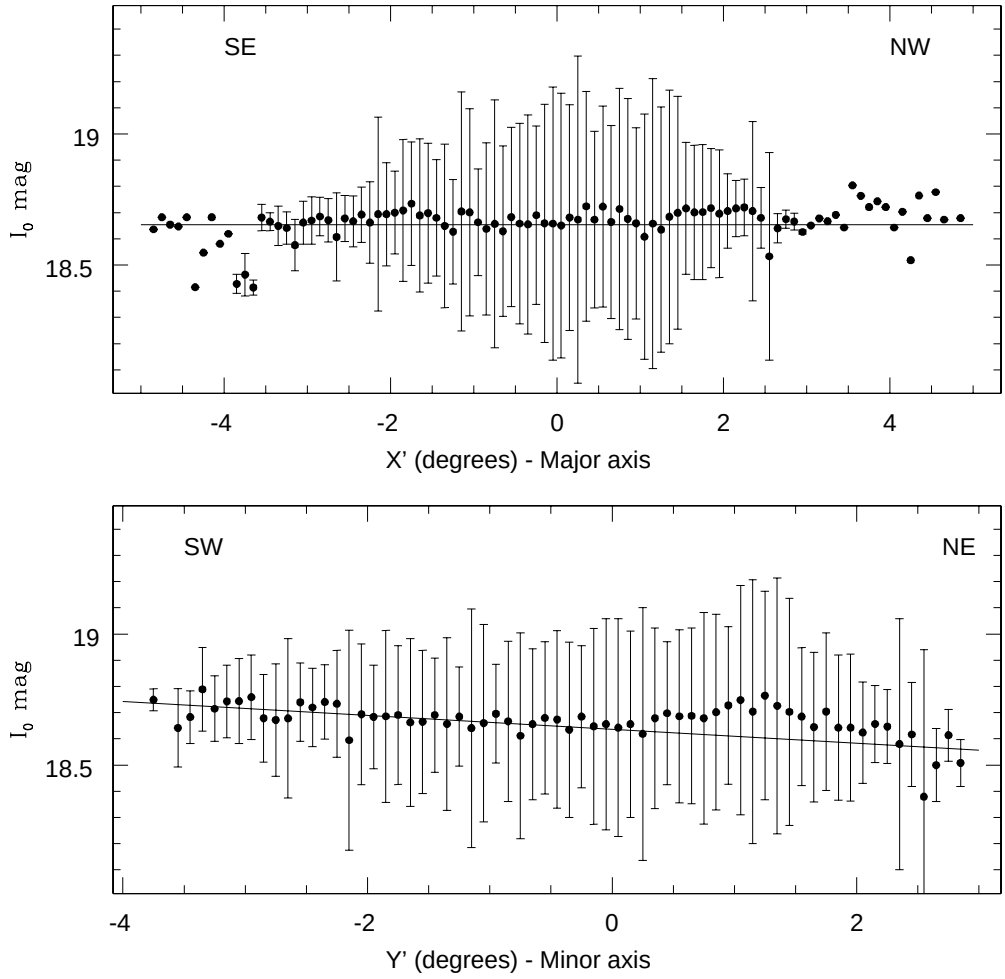

Figure 6.4: The edge on view of the binned I_0 magnitudes along the major and minor axes. The direction of the inclination is shown in the lower figure.

of RRLS is in a non-spheroidal distribution.

6.5 Discussion: Clues to the early formation of the LMC disk

The distribution of RRLS in the inner LMC is found to have a major axis, line of nodes and inclination similar to the disk. These three properties suggest that the RRLS are not in a spheroidal system, but on an equatorial plane, similar to that of the LMC disk. Also, this is the oldest tracer that shows disk properties. Therefore, turning the argument

around, we suggest that RRLS trace the early formation of the disk in the LMC. The bar feature in the RRLS could be either due to them forming in the bar or being trapped by the bar, after they formed. The oldest disk as traced by the RRLS and the youngest disk traced by the Cepheid (Nikolaev et al. 2004) have similar inclinations. With respect to the scale-height, we estimate that less than half of the stars follow the disk scale-height, whereas a similar fraction follow an inflated distribution. Only a small fraction (10%) is likely to trace the extended halo of the LMC. We suggest the following model for the formation of RRLS and the early evolution of the LMC.

The LMC showed a prominent star formation event at the time of the formation of RRLS, which mimics the LMC disk. The enhanced density of RRLS near the central region is suggestive of a prominent star formation event. This probably is the oldest and most significant star forming event, with the result of the formation of the LMC disk. A merger event with a gas rich galaxy at about 10 - 12 Gyr could have caused this major event. The low star formation rate of the LMC halo must have kept the chemical enrichment low enough for the RRLS to form during the merger. This also points to a very low stellar density halo for the LMC. If the RRLS shows the bar feature because that they formed in the bar, then the bar was also formed during this merger event, along with the disk. It might be possible that the globular clusters in the LMC were also formed in this merger event. The globular clusters in the LMC show disk like kinematics (Freeman et al. 1983, Schommer et al. 1992, van den Bergh 2004). Increased gas material due to the merger could have triggered the formation of the globular clusters. We also identified that when one component of RRLS shows disk-like scale height, another component appeared to be inflated. These two population could also indicate the early formation of the LMC. The inflated distribution could have formed in the early part of the merger, where, the disk is not completely formed, giving it an inflated location. If this coincides with globular cluster formation, then the RRLS in the inflated component are formed just before the formation of the disk. The star formation must have proceeded along with the formation of the disk. In summary, we suggest that the major star formation event in the LMC happened at $\geq$ 9 Gyr, probably with a gas rich merger. This merger resulted in the formation of most of the inner RRLS, probably the globular clusters and the disk of the LMC.

We also explore the possibility that all the RRLS formed in the disk and one fraction got inflated. One scenario is where another gas-rich merger dislocated some stars to the halo, resulting in a distribution with increased scale-height. Another mechanism for distributing stars vertically above the plane is bar instabilities. After the bar is formed, it

thickens, its scale-height increases and it forms a peanut/boxy bar, due to various instabilities (Combes et al. 1990, Pfenniger & Friedli 1991). Once the RRLS are trapped in the bar potential, they might experience various bar instabilities resulting in a vertical distribution. The fact that the observed inflated distribution in the RRLS is located in the region of the bar could suggest a bar-related phenomenon. If this is a viable mechanism, then the RRLS can be used to understand the evolution of the LMC bar. The survival and the evolution of the bar could also be a pointer to the dark matter halo (Martinez-Valpuesta et al. 2006).

6.6 Conclusions

- The distribution of RRLS in the inner LMC is found to have a major axis (= $125^o \pm 17^o$) and inclination (= $31^o.3 \pm 3^o.5$) similar to that of the disk. These suggest that the RRLS are not in a spheroidal system, but on an equatorial plane, similar to that of the disk.

- From the scale height estimates we found that 43% of stars in the sample follow disk like scale height. There is another fraction (47%) of RRLS which has puffed up distribution which probably traces the inner halo. Only a small fraction (10%) is likely to trace the extended halo of the LMC.

- We suggest a major star formation event happened at 10-12 Gyr ago in the LMC, probably with a gas rich merger to explain the disk-like distribution of the major fraction of the RRLS.

CHAPTER 7

ESTIMATION OF THE LINE OF SIGHT DEPTH OF THE SMALL MAGELLANIC CLOUD USING THE RED CLUMP STARS *

7.1 Introduction

The studies of Mathewson et al. (1986) and Mathewson et al. (1988) found that the SMC cepheids extend from 43 to 75 kpc with most cepheids found in the neighbourhood of 59 kpc. Later, Welch et al. (1987) estimated the line of sight depth of the SMC by investigating the line of sight distribution and period - luminosity relation of cepheids. They accounted for various factors which could contribute to the larger depth estimated by Mathewson et al. (1986) & Mathewson et al. (1988), and found the line of sight depth of the SMC to be $\sim$ 3.3 kpc. Hatzidimitriou & Hawkins (1989), estimated the line of sight depth in the outer regions of the SMC to be around 10-20 kpc.

In this study, we used the dispersions in the colour and magnitude distribution of RC stars for depth estimation. The dispersion in colour is due to a combination of observational error, internal reddening (reddening within the SMC) and population effects. The dispersion in magnitude is due to internal extinction, depth of the distribution, population effects and photometric errors associated with the observations. By deconvolving other effects from the dispersion of magnitude, we estimated the dispersion only due to the

*Results presented here are published in Subramanian, S., & Subramaniam, A., 2009, A&A, 496, 399

depth of the SMC. The advantage of choosing RC stars as a proxy is that there are large numbers of these stars available to determine the dispersions in their distributions with good statistics, throughout the SMC. The depth of the intermediate age component of the SMC may give clues to the formation and evolution of the SMC, and thus in turn would give clues to the interactions between the LMC and SMC.

7.2 Data & Analysis

The V and I band photometric data from the OGLE II and MCPS catalog are used for this study. The OGLE II and the MCPS fields are divided into 176 sub-regions (each sub-region having an area of 7.12×7.12 square arcmin), and 876 sub-regions (each having an area of ∼ 8.9×10 square arcmin) respectively. The data in the central regions may suffer from incompleteness due to crowding effects. The incompleteness in the OGLE II data is corrected using the values given in Udalski et al. (2000). The effect of crowding in the MCPS data is discussed in section 7.5. As explained in section 2.2.1, the RC stars are identified from the $(V - I)$ vs I CMD of each sub-region. Out of 876 sub-regions of the MCPS field, only 755 regions have a reasonable number of RC stars to do the analysis. The number of RC stars in each region depends on the stellar density. The number is large in the central regions, whereas it decreases in the disk. The number of RC stars ranges between 1000 - 3000 in the bar region, whereas the range is 100 - 1500 in the disk. For both the data sets, only data with errors less than 0.15 mag are taken for the analysis.

As discussed in section 2.2.2 the width corresponding to the line of sight depth can be obtained from the colour and magnitude distributions of the RC stars. To obtain the number distribution of the RC stars in each region, the data are binned with a bin size of 0.01 and 0.025 mag in colour and magnitude respectively. The width in colour and magnitude distributions are obtained using non-linear least square fits. Along with the width of the distributions, the error in the estimation of each parameter and the goodness of the fit, which is the same as the reduced χ^2 value are obtained. Regions with reduced χ^2 values greater than 2.6 are omitted from the analysis. As the important parameter for our calculations is the width associated with the two distributions, we also omitted regions with fit error of width greater than 0.1 mag from our analysis. After these omissions, the number of regions useful for analysis in OGLE II and MCPS data sets are 150 and 600 respectively. Thus, the total observed dispersion in (V−I) colour and I magnitude are estimated for the RC stars in all these regions.

From the observed dispersions in the colour and magnitude distributions of the RC

stars, width corresponding to the line of sight depth are obtained using the relations (10) and (11) given in section 2.2.2. The error associated with the deptha is also obatined. To convert the internal reddening to internal extinction we used the Rieke & Lebofsky (1985) interstellar extinction relation of our Galaxy. The relation is given by A_I = 0.934 x E($V - I$). The interstellar extinction law of our Galaxy is adopted for the calculations of Magellanic Clouds based on the results of the studies by Nandy & Morgan (1978), Lequeux et al. (1982) and Misselt et al. (1999), which showed that the SMC has extinction curve similar to that found in our Galaxy. The error associated with the line of sight depth will translate as the minimum depth that can be estimated. The minimal depth that can be estimated is $\sim$ 350 pc in the central regions and $\sim$ 670 pc in the outer regions.

7.3 Internal reddening in the SMC

One of the by product of this study is the estimation of internal reddening in the SMC. In this study, we used the width of the (V−I) colour distribution to estimate the internal reddening map across the MCs. This estimates the front to back reddening of a given region in the SMC, which we call as the internal reddening (in E(V−I)), and does not estimate the reddening between the front end of the region and the observer. Thus, this estimate traces the reddening within the SMC and hence the location of the dust. The estimates and figures given below thus gives the internal reddening within the SMC.

The colour coded figure of the internal reddening in the SMC is presented in Fig. 7.1. It can be seen that the internal reddening is high only in some specific regions. Most of the regions have very negligible internal reddening suggesting that most of the regions in the SMC are optically thin. A region of high internal reddening is found to the west of the optical center. Also, the bar region is found to have some internal reddening, whereas the outer regions have very little internal reddening (within the area studied). The highest reddening estimated is E(V−I) = 0.08 mag in the OGLE II regions and 0.12 mag in the MCPS region. These regions are located close to the optical center. The rest of regions have very little internal reddening. Thus, our results indicate small internal extinction across the SMC, as seen by the RC stars. The minimum internal reddening that can be estimated is 0.002 mag in the central regions and 0.005 mag in the outer regions.

7.4 Results

We used OGLE II and MCPS data sets for this study. The area covered by OGLE II

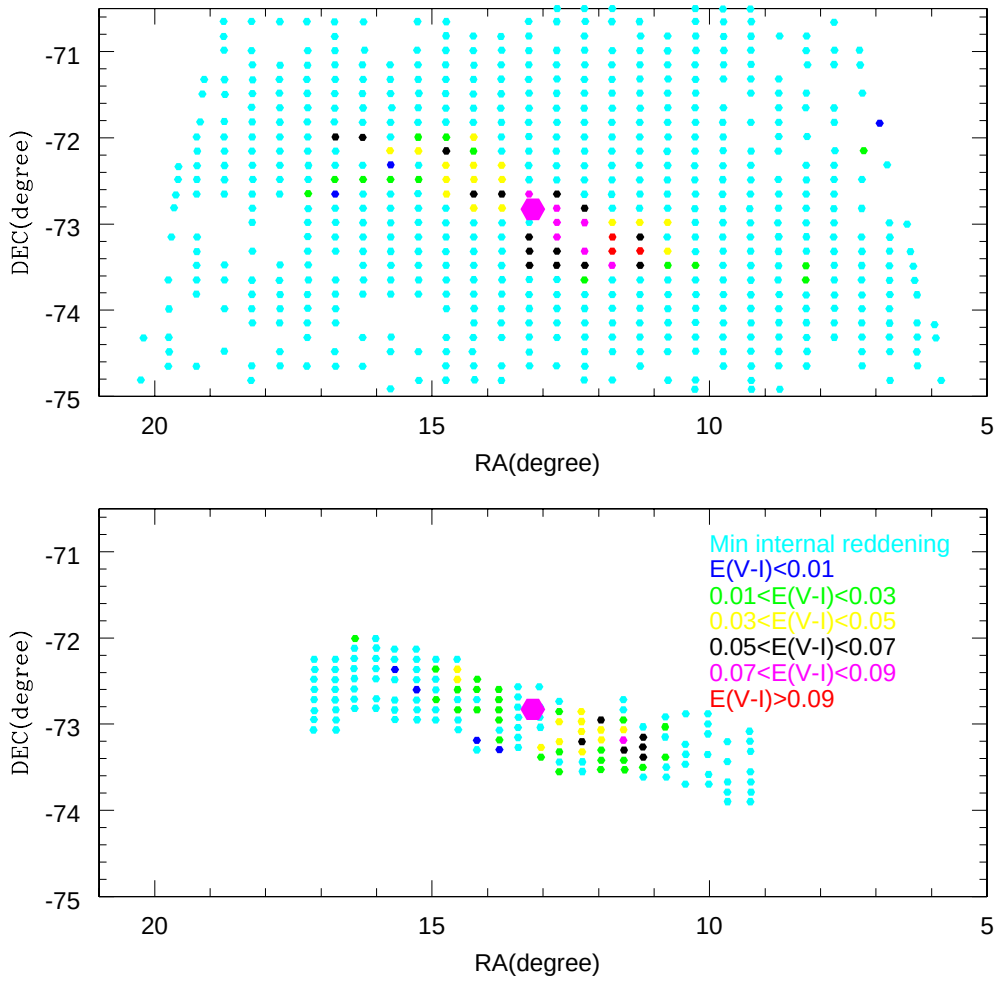

Figure 7.1: Two dimensional plot of the internal reddening in the SMC. The colour code is given in the figure. The magenta dot represents the optical center of the SMC. The upper plot is derived from the MCPS data, whereas the lower plot is derived from the OGLE II data.

is mainly the bar region, whereas the bar and the surrounding regions are covered by the MCPS data.The depth of 150 regions (OGLE II data) and 600 regions (MCPS data) of the SMC were calculated.

A colour coded, two dimensional plot of depth for these two data sets are shown in Fig. 7.2. OGLE II data is shown in the lower panel and MCPS data in the upper panel. The optical center of the SMC is taken to be R.A = 00^h 52^m 12.5^s , Dec = -72^0 49' 43" (J2000, de Vaucouleurs & Freeman 1972). There is no indication of a variation of depth across the SMC as indicated by the uniform distribution of the red and black dots. The

prominent feature in both the plots is the presence of blue and green points indicating increased depth, for regions located near the SMC optical center. The OGLE II data cover only the bar region and it can be seen that this data is not adequate to identify the extension of the central feature, whereas the MCPS data clearly delineates this feature.

The net dispersions range from 0.10 to 0.35 mag (a depth of 2.8 kpc to 9.6 kpc) in the OGLE II data set and from 0.025 mag to 0.34 mag (a depth of 670 pc to 9.47 kpc) in the MCPS data set. The minimum depth estimated in the MCPS data is limited by errors. The fraction of such regions where the minimum value is limited by errors is 2.83%. The average value of the SMC thickness estimated using the OGLE II data set in the central bar region is 4.9± 1.2 kpc and the average thickness estimated using MCPS data set, which covers a larger area than OGLE II data, is 4.42 ± 1.46 kpc. The average depth obtained for the bar region alone is 4.97 ±1.28 kpc, which is very similar to the value obtained from OGLE II data. The depth estimated for the region excluding the bar is 4.23±1.47 kpc. Thus the bar and the surrouning regions of the SMC do not show any significant difference in the depth. The marginal difference in the depth values between the bar and the surrounding regions is due to the presence of higher depth regions near the center. Thus, except for the central feature, the depth across the SMC appears uniform. Our estimate is in good agreement with the depth estimate of the SMC using eclipsing binary stars by North et al. (2009). They estimated a 2-sigma depth of 10.6 kpc, which corresponds to a 1-sigma depth of 5.3 kpc.

In order to study the variation of depth of the SMC (OGLE II data) along the R.A, dispersion corresponding to the depth is plotted against R.A in Fig. 7.3. The lower panel shows all the regions along with the error in depth estimation for each location. The upper panel shows the depth averaged along Dec and the error indicates the standard deviation of the average. Both the panels clearly show the increased depth near the SMC center. There is no significant variation of depth along the bar.

For the MCPS data, the dispersion corresponding to depth is plotted against R.A as well as DEC in figure 7.4. There is an indication of increased depth near the center. The plot also indicates that there is no significant variation in depth between the bar and the surrounding regions. In Fig. 7.5, the depth averaged over R.A and Dec are shown in the upper and lower panel respectively. These are plotted for a small range of Dec (-72.0 to -73.8 degrees) and R.A (10 - 15 degrees), in order to identify the increased depth in the central region.The increased depth near the center is clearly indicated. Thus, the depth near the center is about 9.6 kpc, which is twice the average depth of the bar region (4.9 kpc). Thus, the SMC has a more or less uniform depth of 4.9 ±1.2kpc over bar as well as

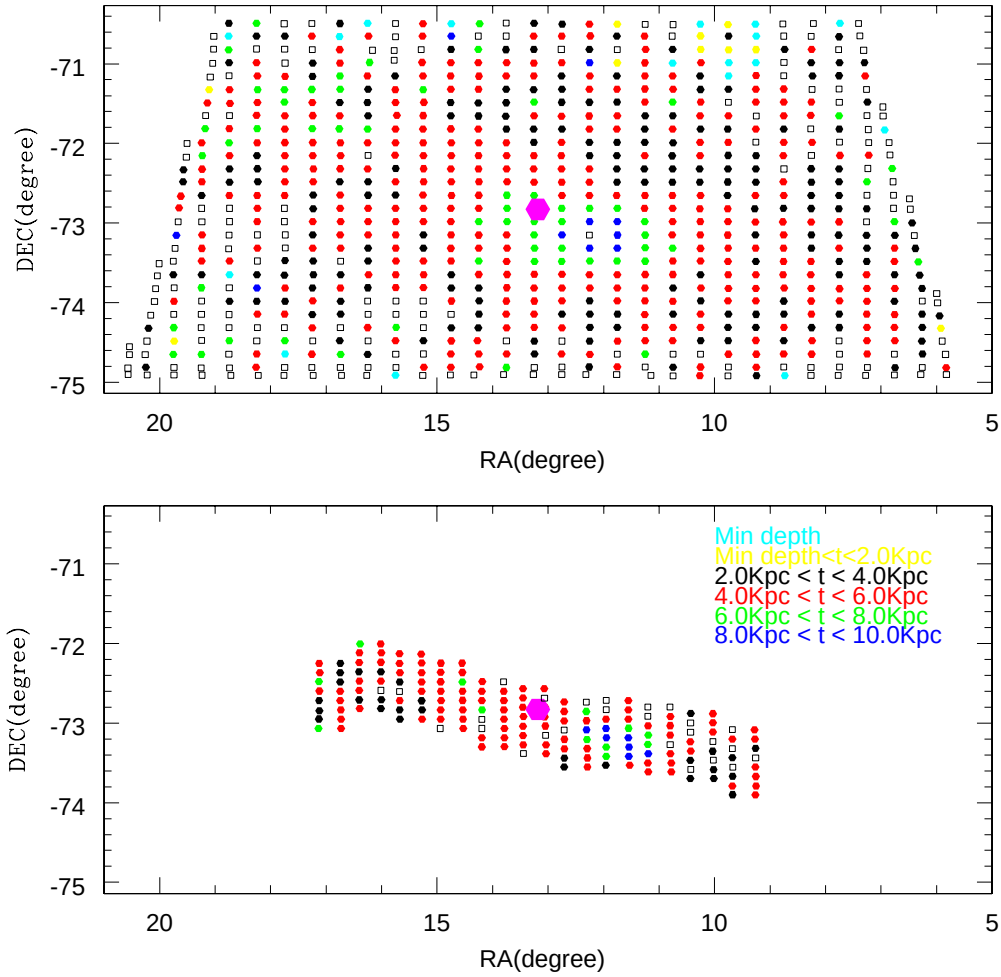

Figure 7.2: Two dimensional plot of depth (t) in the SMC. Upper panel is for the MCPS data and lower panel is for OGLE II data.The colour code is same for both the panels. The magenta dot represents the optical center of the SMC. The empty squares represent the omitted regions with poor fit.

the surrounding regions, with double the depth near the center.

7.5 Discussion

As incompleteness correction is done in one data set (OGLE II) and not in the other (MCPS), we compared the depth estimates before and after adopting the completeness correction. We found that the change is within the bin sizes adopted here. Thus, incorporating the incompleteness correction has not changed the results presented here. The

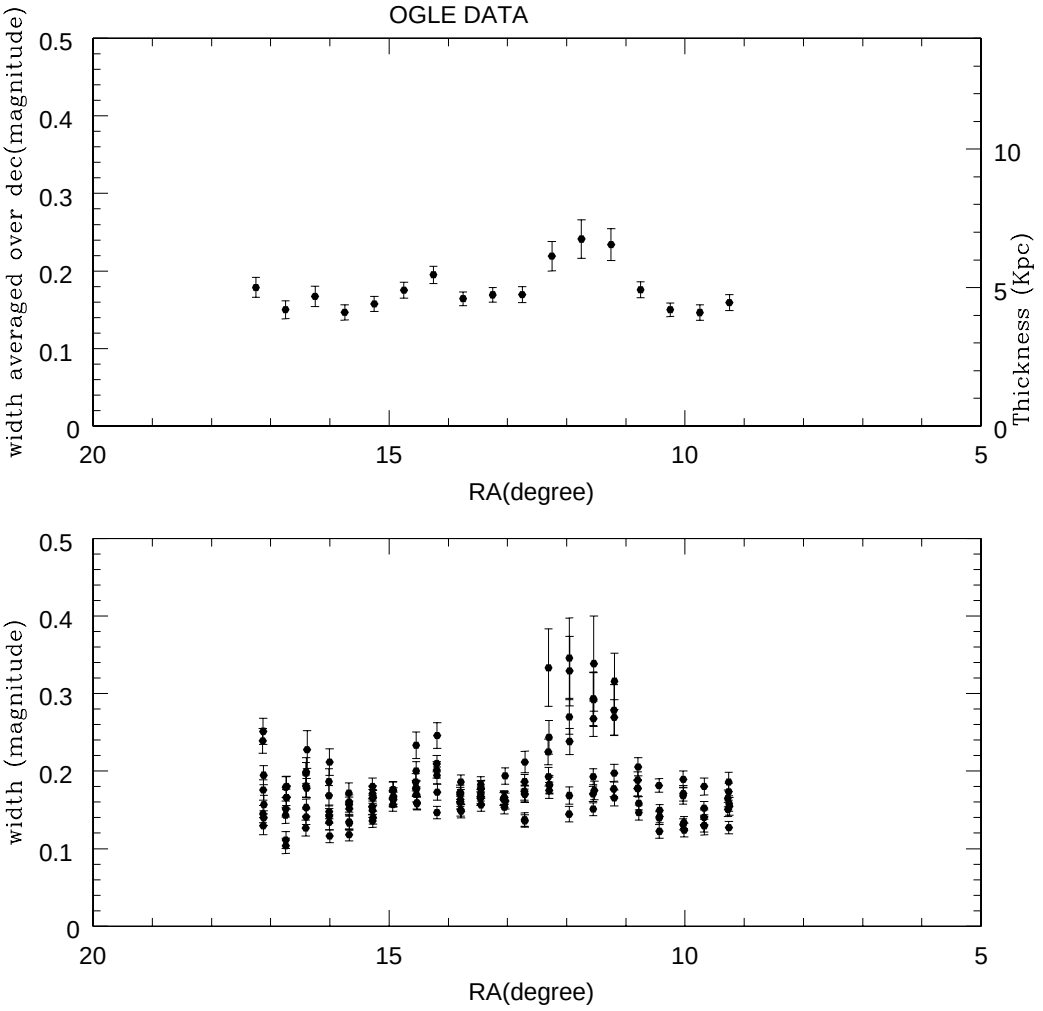

Figure 7.3: Lower panel: Width corresponding to depth against R.A for bar region of the SMC (OGLE II data). Upper panel: Average of depth along the declination against R.A in the bar region of the SMC (OGLE II data).

Table 7.1: Depths of different regions in the SMC. These are line of sight depths and need to be corrected for inclination, to estimate the actual depth.

Region	Range of depth (kpc)	Avg.depth (kpc)	Std.deviation (kpc)
SMC bar	3.07-9.53	4.90	1.23
SMC region excluding the bar	0.67-9.16	4.23	1.48

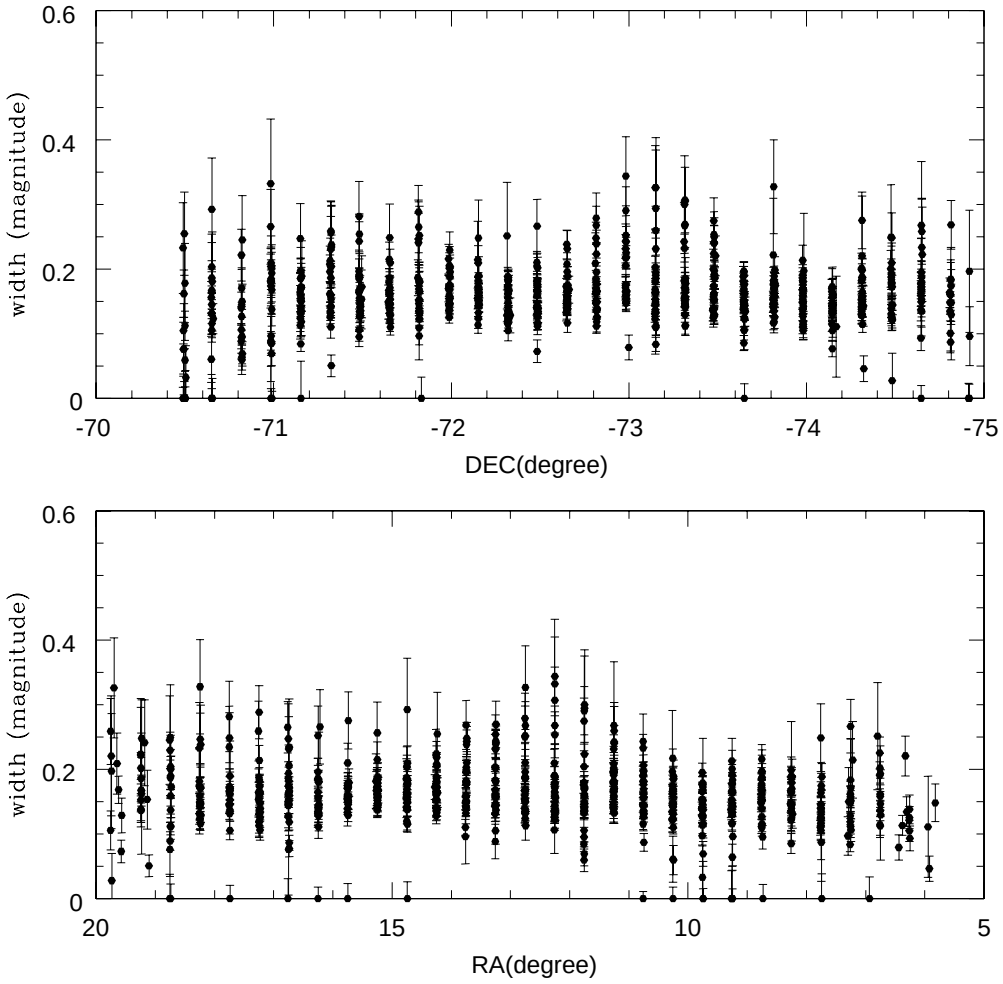

Figure 7.4: Width corresponding to depth against R.A in the lower panel and against Dec in the upper panel for the SMC (MCPS data).

incompleteness correction in the central regions is about 12% and that in the outer region is about 5%. The incompleteness in the MCPS data does not affect the results presented here.

We have removed regions in the MCs with poor fit as explained in section 7.2. These regions are likely to have different RC structures suggesting a large variation in metallicity and/or population. The fraction of such region is about 5.3%. Such regions are indicated in Fig. 7.2. Thus to a certain extent, the above procedure has eliminated the regions with very different metallicity and star formation history that are seen in most of the regions. Apart from the above, the remaining regions studied here might have some variation in the the RC population contributing to the depth estimated. The results presented in this

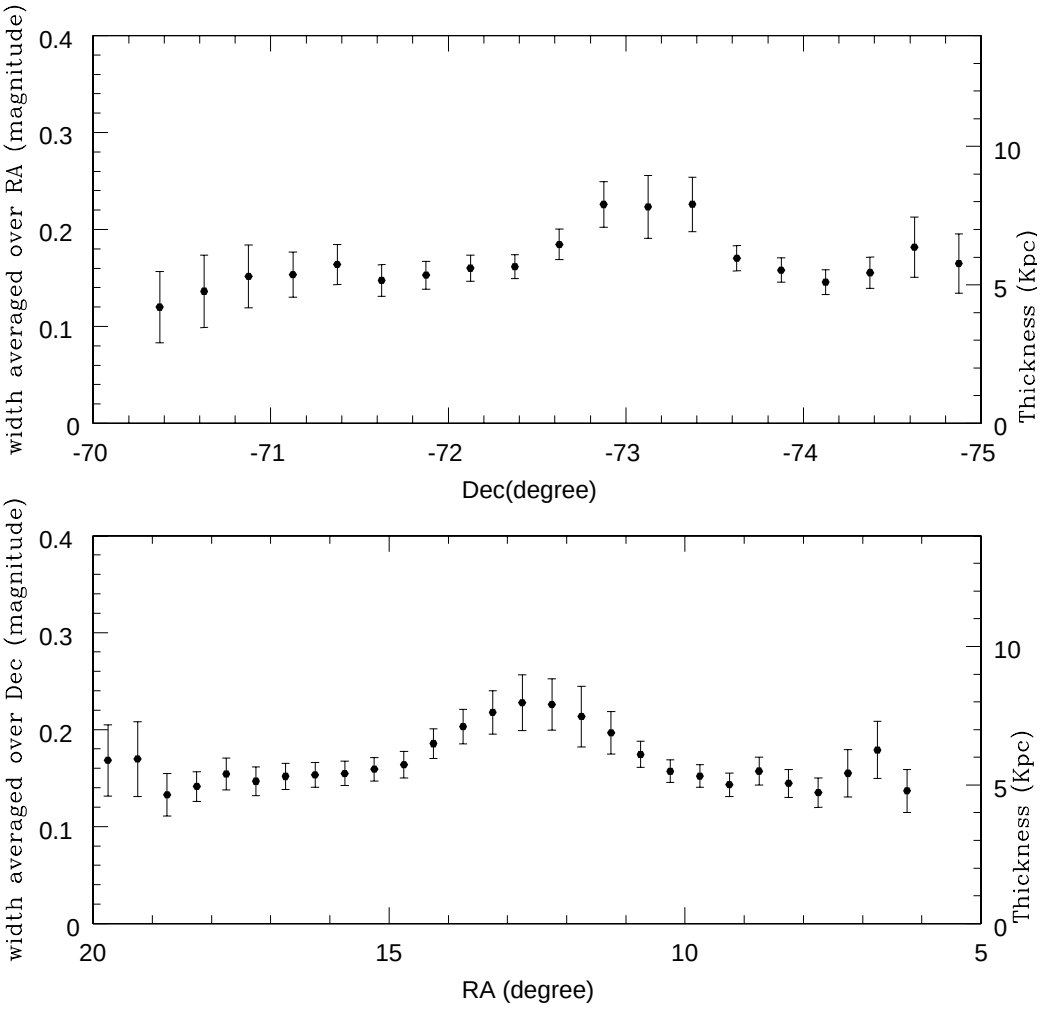

Figure 7.5: Lower panel: Width corresponding to depth averaged over Dec and plottedagainst R.A for a small range of Dec in the central region of the SMC (MCPS data). Upper panel: Width corresponding to depth averaged over R.A and plotted against Dec for a small range of R.A in the central region of the SMC (MCPS data).

study will include some contribution from the population effect.

For the estimation of the internal extinction from internal reddening we used the relation, A_I = 0.934 x E($V - I$) (Rieke & Lebofsky 1985). As explained in section 3.5 ,the above interstellar extinction relation is appropriate for the broad Johnson I filter and the appropriate conversion factor between A_I and E($V - I$) for OGLE and MCPS bands is $\sim$ 1.4. In order to check the effect of the choice of this conversion factor in our results, we repeated the whole analysis using the relation A_I = 1.4 x E($V - I$). From this analysis we obtained mean values of 4.90 $\pm$ 1.24 kpc and 4.23 $\pm$ 1.47 kpc for the bar and for the

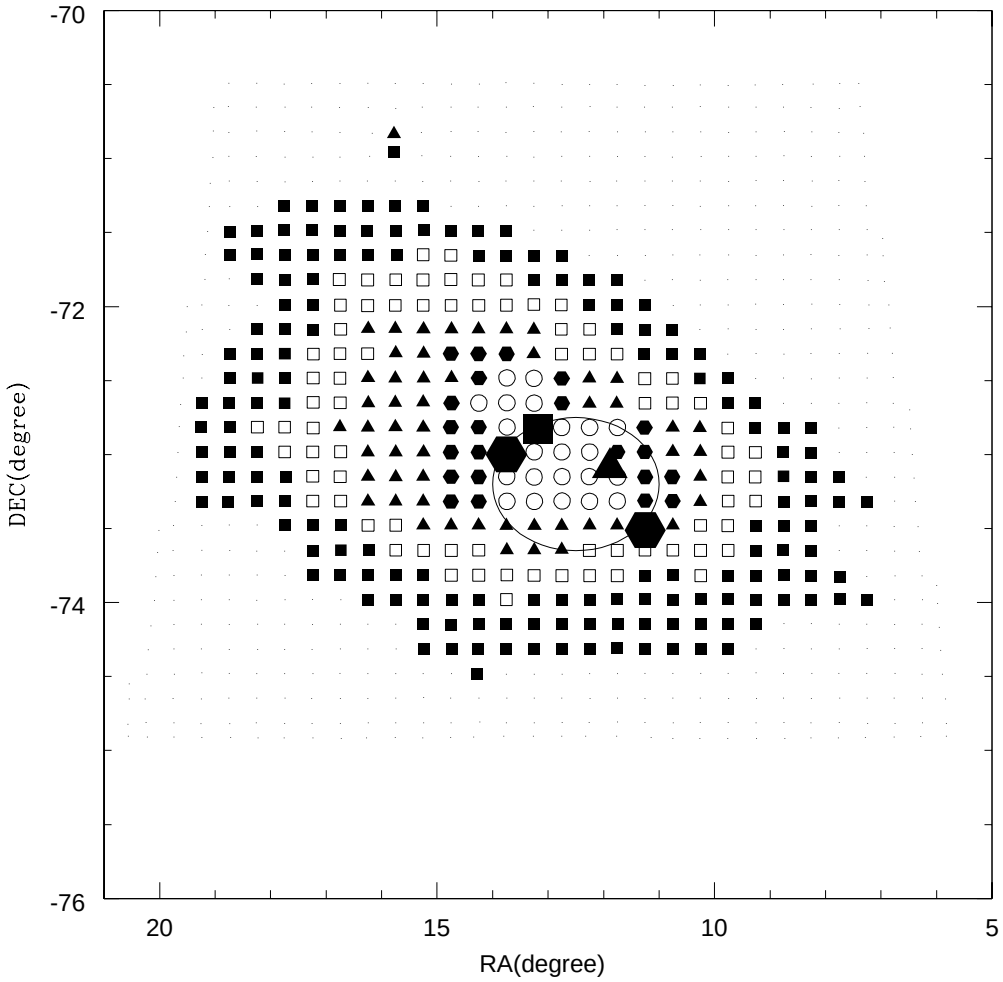

Figure 7.6: Two dimensional plot of density distribution estimated from MCPS data. The small symbols like the open circles, hexagons, triangles, open squares, filled squares and dots represent the density of the regions in the decreasing order such that the small open circles in the central region indicate the high density regions and the dots represent the lowest density regions. The ellipse shows the boundary of regions with large depth, the large hexagons indicate the stellar peaks found by Cioni et al. (2000a), the large triangle indicate the HI peak (Stanimirović et al. 2004) and the large square denotes the optical center.

regions excluding the bar respectively. These values are very similar to those given in table 7.1. This suggests that the choice of E($V - I$) to A_I conversion factor has not much effect in our present analysis. This may be due to the the low values of internal reddening as seen from the Fig. 7.1.

The SMC is found to have a depth greater than the LMC. The bar and the surrounding

regions do not show much difference in depth. The profile of the depth near the center (Fig. 7.5) looks very similar to a typical luminosity profile of a bulge. This could suggest the presence of a bulge near the optical center of the SMC. If a bulge is present, then a density/luminosity enhancement in this region is also expected. We plotted the observed stellar density in each region from the MCPS data to see whether there is any such central enhancement. This is shown in Fig. 7.6. The regions with high density are shown as open circles, located close to the optical center. The regions with large depth are found to be within the ellipse shown in the figure. It can be seen that regions with highest stellar density lie more or less within this ellipse. Cioni et al. (2000a) studied the morphology of the SMC using the DENIS catalogue. They found that the distribution of AGB and RGB stars show two central concentrations, near the optical center, which match with the carbon stars by Hardy et al. (1989). They also found that the western concentration is dominated by old stars. The approximate locations of these two concentrations found by Cioni et al. (2000a) are shown as hexagons in Fig. 7.6. Also, the strongest H I concentration in the SMC map by Stanimirovic et al. (1999) falls between these two concentrations. The maximum H I column density, 1.43×10^{22} atoms cm^{-2} is located at R.A = 00^h 47^m 33^s, Dec = -73^0 05' 26" (J2000.0) (Stanimirović et al. 2004). This location is shown as a large triangle in Fig. 7.6. The optical center of the SMC is shown as a large square. All these peaks as well as the optical center are located on or within the boundary of the ellipse. Thus, the peaks of stellar as well as the H I are found within the central region with large depth. This supports the idea that a bulge may be present in the central SMC. This bulge is not very luminous, but clearly shows enhanced density. It is also the central region of the triangular shaped bar.

The increased dispersion near the SMC center, which is interpreted as due to large depth, could be partially due to the presence of RC population which is different. Cioni et al. (2006b) did not find any different population or metallcity gradient near the central regions. Tosi et al. (2008) obtained deep CMDs of 6 SMC regions to study the star formation history. Three of their regions are located close to the bar and three are outside the bar. They found an apparent homogeinty of the old stellar population populating the sub giant branch and the clump. This suggested that there is no large differences in age and metallicity among old stars in these locations. Their SF1 region is located close to the region of large depth identified here. The RC population in this region is found to be very rich and the spread in magnitude is greater than those found in the other CMDs. This spread is also suggestive of increased depth near this location. It will be worthwhile to study the star formation history of regions near the SMC center to understand how

different the stellar population is in this suggested bulge.

It may be worthwhile to see whether this bar is actually an extended/deformed bulge. It is interesting that the so-called triangular shaped bar of the SMC is also an unexplained component, which does not show the signatures of a typical bar. This could naturally explain the formation of the odd shaped bar in the SMC. Thus, we propose that the central SMC has a bulge. The elongation and the rather non-spherical appearance of the bulge could be due to tidal effects or minor mergers (Bekki & Chiba 2008).

7.6 Conclusions

• The SMC bar and the disk have similar depth, with no significant depth variation across the disk. The estimated depth for the bar and the disk regions are 4.9±1.23 kpc and 4.23±1.48 kpc respectively.

• Increased depth (~ 8-10 kpc) is found near the optical center of the SMC.

• The increased depth and the enhancement in the stellar & H I density near the center, suggest that the SMC possibly has a bulge. The central bar may be this deformed/extended bulge.

CHAPTER 8

THE 3D STRUCTURE OF THE SMALL MAGELLANIC CLOUD

8.1 Introduction

In an extensive survey of variable stars in the SMC, Graham (1975) discovered 76 RR Lyrae stars (RRLS) in the field centered on the globular cluster, NGC 121. He found that the period distribution of the RRLS in the SMC is unlike that found anywhere in the Galaxy and closely resembles the distribution of variable stars in the Leo II dwarf galaxy. His studies also showed that these stars are distributed rather evenly and concentrate neither towards the bar nor towards the center of the SMC. He mentioned that the lack of strong stellar concentration is another property in common with the stellar populations in the dwarf spheroidal galaxies. Smith et al. (1992) and Soszynski et al. (2002) also found an even and smooth distribution of RRLS in the northeastern regions and the central 2.4 square degree regions of the SMC respectively. Soszyñski et al. (2010b) presented a catalog of the RRLS in the SMC from Optical Gravitational Lensing Experiment (OGLE) III survey. From the spatial distribution of the RRLS they suggested that the halo of the SMC is roughly circular in the sky. However their density map of the RRLS revealed two maxima near the center of the SMC.

Zaritsky et al. (2000) showed that the older stellar populations (age > 1 Gyr) in the SMC are distributed in a regular, smooth ellipsoid. Similar conclusions were drawn by Cioni et al. (2000a) from the DENIS near infrared survey. Maragoudaki et al. (2001) further investigated the dynamical origin of the bar using isodensity contour maps of stars with different ages. They found similar results for old stellar populations. A sample of

12 populous SMC clusters which possess RC stars are studied by Crowl et al. (2001) to determine the distances to these clusters. The line of sight depth of the SMC is estimated as the standard deviation (sigma) of these distances. They found a 1-sigma depth of ≈ 6-12 kpc for the SMC. Viewing the SMC as a triaxial ellipsoid with RA, DEC and the line of sight depth as the three axes, they found an axes ratio of 1:2:4. From a spectroscopic study of 2046 red giant stars Harris & Zaritsky (2006) found that the older stellar components of the SMC have a velocity dispersion of 27.5 kms^{-1} and a maximum possible rotation of 17 kms^{-1}. Their result is consistent with other kinematical studies based on the radial velocities of the PNe and carbon stars, which represent the old and intermediate-age stellar populations (Dopita et al. (1985), Suntzeff et al. (1986) & Hatzidimitriou et al. (1997)). This implies that the structure of the older stellar component of the SMC is a spheroidal/ellipsoidal, that is supported by its velocity dispersion.

From the analysis of young stars (age < 200 Myr) Zaritsky et al. (2000) suggested that the irregular appearance of the SMC is due to the recent star formation. As in the case of young stars, the large scale H I morphology of the SMC obtained from the high resolution H I observations (Stanimirović et al. (2004)) is also quite irregular and does not show symmetry. The most prominent features are the elongation from the northeast to the southwest and the V-shaped concentration in the east. The H I observations also show that the SMC has a significant amount of rotation with a circular velocity of approximately 60 kms^{-1} (Stanimirović et al. (2004)) and a large velocity gradient of 91 kms^{-1} in the southwest to 200 kms^{-1} in the north east. Evans & Howarth (2008) obtained velocities for 2045 young (O, B, A) stars in the SMC, and found a velocity gradient of similar slope as seen in the H I gas. Surprisingly though, they found a position angle ($\sim 126^o$) for the line of maximum velocity gradient that is quite different, and almost orthogonal to that seen in the H I . van der Marel et al. (2009) suggested that this difference in the position angles may be an artifact of the different spatial coverage of the two studies (Evans & Howarth (2008) did not observe in the North-East region where the H I velocities are the largest), since it would be difficult to find a physical explanation for a significant difference in kinematics between H I gas and young stars. The inclination of the SMC disk in which the young stars are believed to be distributed is estimated as $70^o \pm 3^o$ and $68^o \pm 2^o$ from the photometric studies of Cepheids by Caldwell & Coulson (1986) and Groenewegen (2000) respectively. The position angle of the line of nodes is estimated to be $\sim 148^o.0$.

Gardiner & Noguchi (1996) modelled the SMC as a two component system consisting of a nearly spherical halo and a rotationally supported disc. The tidal radius of the SMC is

estimated as 5 kpc according to their model. Their best fit to the distribution halo particles within 5 kpc radius was in good agreement with the observed distributions of the old (> 9 Gyr) and intermediate age (2−9 Gyr) stellar populations in the SMC. The distribution of disc particles could reproduce the observed irregular distribution of young stars in the SMC. Bekki & Chiba (2008) suggested that a major merger event in the early stage of the SMC formation caused the coexistence of a spheroidal stellar component and an extended rotating H I disk.

Both the observational and theoretical studies suggest that the old and the intermediate-age stellar populations in the SMC are distributed in a spheroidal/ellipsoidal component. Motivated with this result, here we study the RC stars and the RRLS in the inner SMC, which represent the intermediate-age and the old stellar populations respectively. This study aims to understand the structure of the inner SMC and hence to quantitatively estimate the structural parameters.

In this study we estimate the structural parameters of the older component of the SMC from the analysis of the RC stars and the RRLS in the inner SMC. Udalski et al. (2008b) presented the V and I bands photometric data of the 16 sq.degrees of the SMC from the OGLE III survey. The catalog of the SMC RRLS from the OGLE III survey is presented by Soszyñski et al. (2010b). Both these data sets are used in this study. The mean dereddened I_0 magnitude of the RC stars and the RRLS are used to estimate the relative locations of different regions in the SMC with respect to the mean SMC distance. The dispersion in the mean magnitude is used to obtain the line of sight depth across the SMC.

8.2 Data and Analysis

8.2.1 Red Clump Stars

We divided the OGLE III region into 1280 regions with a bin size of 8.88 x 4.44 square arcmin. As described in section 2.2.1, the RC stars are identified from the CMD. The number of the RC stars identified in each sub-region ranges from 100−3000. To obtain the number distribution of the RC stars, they are binned in colour and magnitude with a bin size of 0.01 and 0.025 mag respectively. These distributions are fitted with a Gaussian + Quadratic polynomial using a nonlinear least-square method and the parameters are obtained (refer 2.2.1). The parameters obtained are the coefficients of each term in the function used to fit the profile, error in the estimate of each parameter, and reduced

χ^2 value. For all the sub-regions we estimated the peaks and the widths in the I mag and (V−I) mag of the distributions, associated errors with the parameters, and reduced χ^2 values. The errors associated with the parameters are obtained using the covariance matrix, where the square root of the diagonal elements of the matrix gives the error values.

The number of the RC stars identified within the box in the CMD are less (100-400) for 602 sub-regions. These sub-regions are located towards the edge of the survey and in the three isolated fields in the north western region of the SMC. For these 602 sub-regions we carefully analyzed the magnitude and colour distributions. Because of the number of stars the peaks of the distributions were not very clear and unique. As our methodology depends very much on the statistical analysis of the sample we omitted these 602 sub-regions, with RC stars less than 400, for the remaining analysis. Thus the number of regions used for the study reduced to 678. The magnitude and colour distributions of most of these 678 regions were checked manually and found that the fits are satisfactory.

The sub-regions with reduced χ^2 values greater than 2.0 for both magnitude and colour distributions are omitted from the analysis. The regions with peak and width error greater than 0.05 mag in the magnitude distributions are also removed from the analysis. In the case of colour distribution, regions with peak and width error greater than 0.02 mag are not considered for the analysis. Thus we used only 553 sub-regions out of 678 sub-regions, for the final analysis.

The peak value of the colour, (V−I) mag at each location is used to estimate the reddening. The reddening is calculated using the relation E(V−I) = $(V-I)_{obs}$ - 0.89 mag. The intrinsic colour of the RC stars in the SMC is chosen as 0.89 mag to produce a median reddening equal to that measured by Schlegel et al. (1998) towards the SMC. The interstellar extinction is estimated by A_I = 1.4xE(V−I) (Subramaniam (2005)). After correcting the mean I mag for interstellar extinction, I_0 mag for each region is estimated using the equation (7) given in chapter 2.

The variation in the I_0 mag between the sub-regions is assumed only to be due to the difference in the relative distances. The difference in I_0 mag is converted into relative distance, ΔD using the distance modulus formula,

$$(I_0 \text{ mean} - I_0 \text{ of each region}) = 5\log_{10}(D_0/(D_0 \pm \Delta D))$$

where D_0 is the mean distance to the SMC which is taken as 60kpc. The average error in I_0 is calculated using the formula, $\delta {I_0}^2$ = (avg error in peak I)^2 + (1.4 x avg error in peak (V−I))^2, and the error is estimated as 0.013 mag which corresponds to ∼ 360 pc.

The cartesian coordinates corresponding to each subregion is obtained from the realtions (12), (13) and (14) given in Chapter 2.

The estimated dispersions of the colour and magnitude distributions are used to obtain the line of sight depth of each region in the SMC. We followed the the methodology given in section 2.2.2. Thus the width corresponding to the depth of the RC distribution in each sub-region of the SMC OGLE III data is estimated. The average error in the depth estimate is $\sim$ 400 pc.

8.2.2 RR Lyrae stars

The ab type RRLS could be considered to belong to a similar class and hence assumed to have similar properties. The mean magnitude of these stars in the I band, after correcting for extinction effects, can be used for the estimation of distance and the observed dispersion in their mean magnitude is a measure of the depth in their distribution. The reddening obtained using the RC stars (described in the previous sub-section) is used to estimate the extinction to individual RRLS. Stars within each bin of the reddening map are assigned a single reddening and it is assumed that reddening does not vary much within the bin. Thus the extinction corrected I_0 magnitude for all the RRLS are estimated. As in the case of the RC stars, the difference in I_0 between each RR Lyrae star is assumed to be only due to the variation in their distances and the relative distance, ΔD, corresponding to each star is estimated. The error in the relative distance estimation of individual RR Lyrae star is basically the error in the extinction correction of I_0 mag. The average error in the extinction estimation, obtained from the RC stars, converts to a distance of $\sim$ 110 pc. The location of each RR Lyrae star in the cartesian coordinate system is then calculated using the transformation equations given in 2.2.3.

Using the dereddened I_0 magnitude of each RR Lyrae star, the dispersion in the surveyed region of the SMC can be found. The dispersion is a measure of the depth of the SMC. The data are binned in 0.5 degree in both x & y axes to estimate dispersion. Thus the observed region is divided into bins with an area of 0.25 square degrees. The number of stars in each bin have a range of 10 - 50. The bins with stars less than 10 are removed from our analysis. For each location we estimated the mean magnitude and the dispersion. The estimated dispersion have contributions from photometric errors, range in the metallicity of stars, intrinsic variation in the luminosity due to evolutionary effects within the sample and the actual depth in the distribution of the stars (Clementini et al. (2003)). We need to remove the contribution from the first three terms ($\sigma_{intrinsic}$) so that the value of the last term can be evaluated. Clementini et al. (2003) estimated the value

of $\sigma_{intrinsic}$ as 0.1 mag for their sample of 100 RRLS in the LMC. Subramaniam (2006) used a larger sample of RRLS in the LMC from OGLE II catalog and estimated the value of $\sigma_{intrinsic}$ as 0.15 mag. Both these values are estimated using the globular cluster data in the observed field. In the case of the SMC, there is only one globular cluster and it is not in our observed field. So we used the intrinsic spread estimated for the RRLS in the LMC for the analysis of the RRLS in the SMC. Using both these values we estimated the corrected sigma values which correspond to only depth. The relation used is

$$\sigma^2{}_{I_0 mag} = \sigma^2{}_{depth} + \sigma^2{}_{intrinsic}$$

8.3 Reddening Map of the SMC

One of the by-product of this study is the estimation of reddening towards the SMC. The observed shift of the peak (V−I) colour of the RC stars in the LMC, from the expected value was used by Subramaniam (2005) to estimate the line of sight reddening map to the OGLE II regions of the LMC. Such a reddening map towards the SMC using the RC stars is obtained here. The intrinsic value of the (V−I) colour of the RC stars in the SMC is chosen as 0.89 mag to produce a median reddening equal to that measured by Schlegel et al. (1998) towards the SMC. Using this value the E(V−I) values are estimated. The colour coded figure of the reddening in the SMC is presented in Fig. 8.1. The colour code is given in the plot. The average value of E(V−I) obtained towards the SMC is 0.053 ± 0.017 mag. From the plot we can see that most of the regions in the SMC have E(V−I) less than 0.08 mag shown as blue and cyan points. The regions in the south western and north eastern sides of the center and the eastern wing regions have larger reddening compared to the other regions of the SMC. This reddening map estimated using the RC stars are used for dereddening the RC stars as well as the RRLS in this study.

The previous estimates of the reddening towards the SMC are compared with our estimates. Caldwell & Coulson (1985) found a mean E(B−V) of 0.054 mag from the analysis of 48 Cepheids. This value can be converted into an E(V−I) of 0.0756 mag using the relation E(V−I) = 1.4 * E(B−V) (Subramaniam (2005)). Udalski (1998) (using red clump stars) estimated a mean E(V−I) value of 0.1 mag. Massey et al. (1995) and Grieve & Madore (1986) estimated an E(B−V) of around 0.09 mag which converts to an E($V-I$) value of 0.126 mag. Haschke et al. (2011) provided the reddening maps towards the SMC from the study of the RC stars and RRLS. The intrinsic colour of the RC stars used by them is also 0.89 mag. The reddening map of the SMC estimated from the RC stars given

in Figure 4 of Haschke et al. (2011) is very similar to our reddening map given in Figure 8.1. The mean value of E(V−I) estimated by them towards the SMC using the RC stars is 0.04 mag and that estimated from RRLS is 0.07 mag. The reddening maps of the RC stars and RRLS given in Figure 4 and Figure 11 of Haschke et al. (2011) are very similar. This fact supports and validates our usage of the reddening map obtained from the RC stars for dereddening the RRLS. The previous estimates other than that of Haschke et al. (2011) are higher than our estimates. This could be due to the choice of our intrinsic (V−I) colour of the RC stars in the SMC. But such a change only will shift the reddening value in all regions in a similar way. As we are only interested in the relative positions of the regions in the SMC such a change in the intrinsic colour of the RC stars is not going to affect our final results.

In order to compare the adopted intrinsic colour of the RC stars in the SMC with theoretical values, we measured the peak colour of the RC stars from the synthetic CMD of the SMC given in Girardi & Salaris (2001). It turned out to be ∼ 0.89 mag. The table given in Girardi & Salaris (2001) provide $(V-I)_0$ colour for the LMC metallicity of z= 0.004 between 0.90 and 0.94 mag (age between 2-9 Gyr). For a lower metallicity of z = 0.001, their models lead to a colour between 0.8 mag and 0.84 mag (age between 2-9 Gyr). The mean metallicity found by Cole (1998) and Glatt et al. (2008) for the SMC is between 0.002 and 0.003. This value supports our adopted value of $(V-I)_0$ colour of the RC stars in the SMC, which is bluer than that of the LMC and redder than the colour obtained for a lower metallicity system.

8.4 Results

8.4.1 Relative distances

The mean dereddened I_0 magnitude of the RC stars for the 553 sub-regions of the SMC are estimated. The mean magnitudes of different sub-regions are shown as different colour points in the two dimensional plot of X vs Y in the Fig. 8.2. The colour code is given in the figure. The average dereddened magnitude, I_0 of 553 sub-regions is 18.43 ± 0.03 mag. The regions in the south (y< 0) are fainter compared to the regions in the north. The brighter regions (I_0 < 18.39) shown as blue points are located more in the northeastern side. This result indicates that the northeastern regions of the SMC are closer to us.

The relative distance to each RR Lyrae star with respect to the mean distance to the

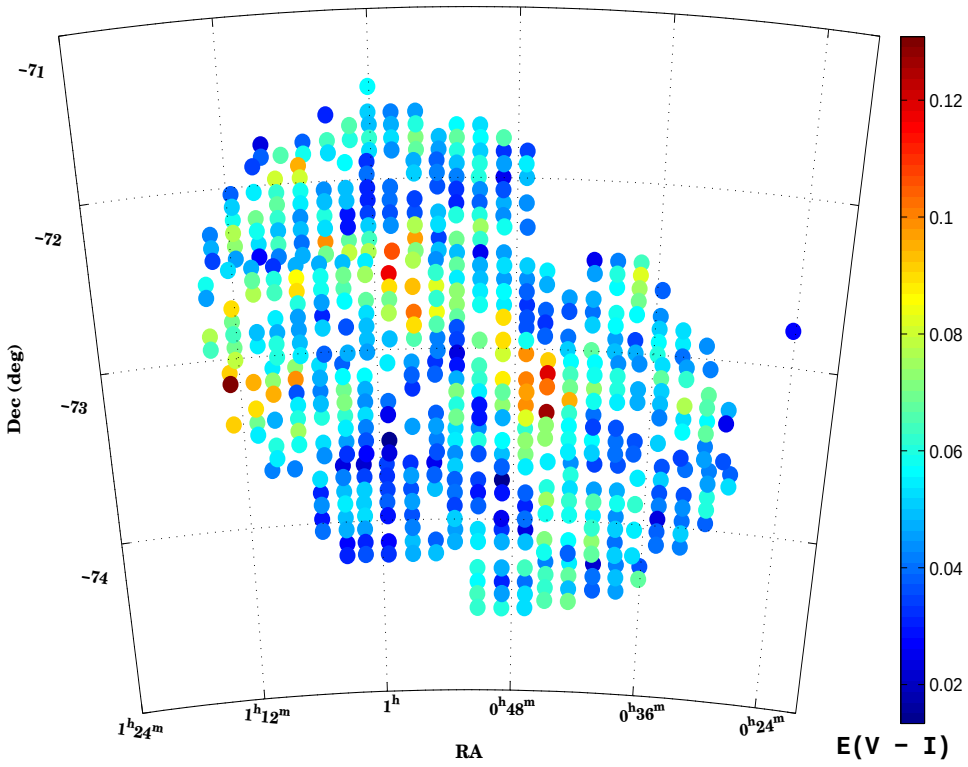

Figure 8.1: A two dimensional plot of the reddening in the sub-regions of the SMC.

SMC is estimated from the dereddened I_0 magnitude, assuming that the average distance to our sample of RRLS in the SMC is 60 kpc. The spatial distribution of RRLS in the XZ and YZ planes with over plotted density contours are shown in Fig. 8.3 and Fig. 8.4 respectively. The convention of the +ve and -ve Z axes are such that the +ve Z axis is towards us and -ve Z axis away from us. The distribution of RRLS in the SMC looks more or less symmetric and extends from -20 kpc to +20 kpc with respect to the mean. Most of the stars are located between ± 10 kpc. An extension to large distances can be seen at x ~0. The outer density contours shown in Fig. 8.3 indicate that the eastern side of the SMC is on an average closer to us than the western side. We calculated the average I_0 magnitude of RRLS in the eastern end (x<-1.5, 245 stars) and in the western end (x>1.5, 221 stars). It was found that the eastern side is 0.034 mag brighter than the western

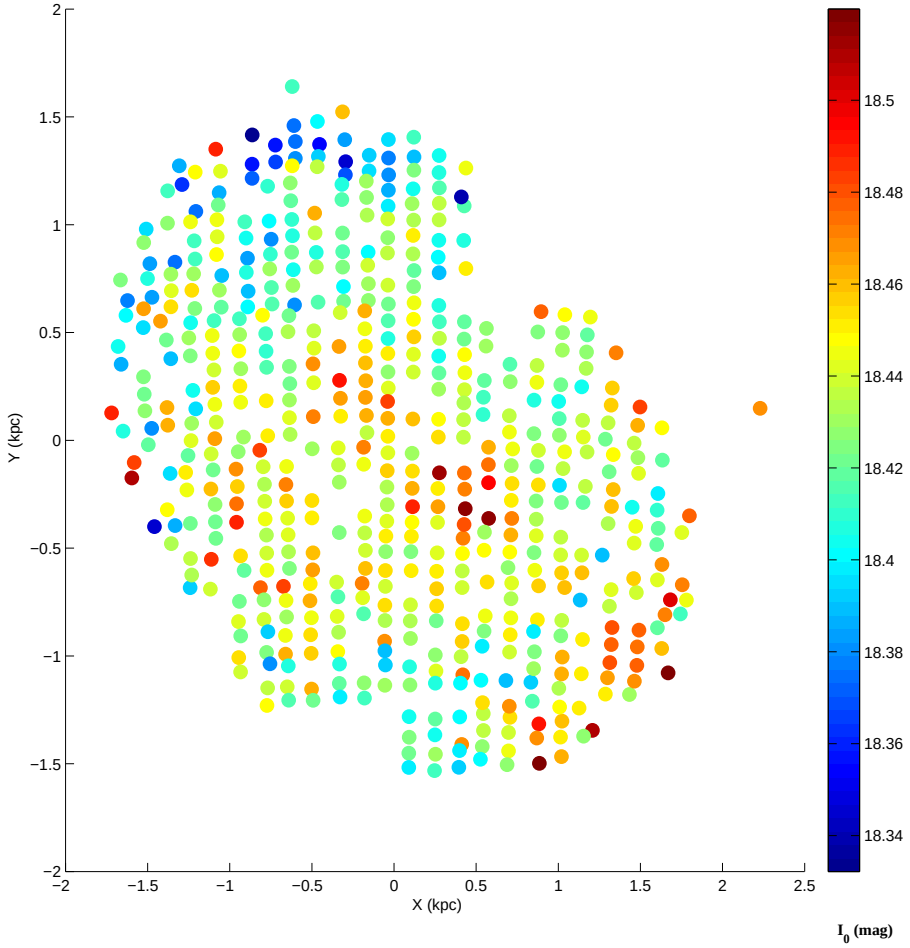

Figure 8.2: A two dimensional plot of the mean magnitudes of the RC stars in the sub-regions of the SMC.

side, which makes the eastern side on an average 950 pc closer to us than the western side. Similarly, the outer density contours shown in Fig. 8.4 suggest that the northern side is closer to us than the southern side. We calculated the average I_0 in the northern end (y>1.5, 133 stars) and in the southern end (y<-1.5,104 stars). It was found that the northern side is 0.019 mag brighter than the southern side, which makes the northern side on an average 520 pc closer to us than the southern side. Thus the outer density contours of figures 8.3 and 8.4 and the quantitative estimates mildly suggest that the north eastern part of the SMC is closer to us. This result is very similar to the result obtained from the RC stars. As this effect is significant in outer regions and our study is limited to inner regions, we need more data in the outer region to securely say that the northeastern part

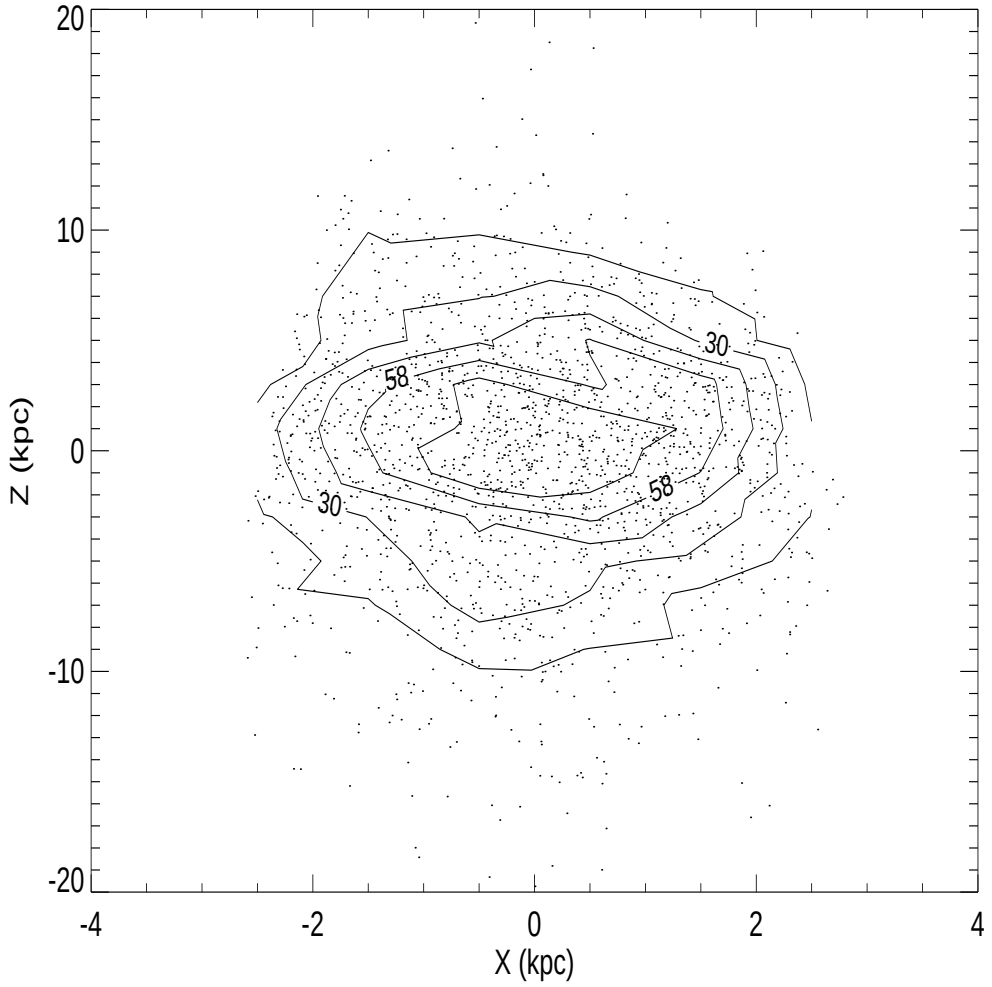

Figure 8.3: Relative distances to each RR Lyrae star in the SMC with respect to the mean distance are plotted against X axis and are shown as black dots. The density contours are over plotted. The east is in the direction of decreasing X axis.

of the SMC is closer to us. From the photometric study of stellar populations upto 11.1 kpc in the SMC, Nidever et al. (2011) found that the eastern part of the SMC is closer to us than the western side.

In the case of the RC stars as well as RRLS, the variation in the I_0 magnitude is assumed as only due to the difference in the distances. As discussed earlier in 1.6.2, there can be contributions in their mean magnitude from the population effects. Thus the line of sight distance estimates suggest that either the RC population and RRLS in the north eastern part of the SMC are different from those found in the other regions of the SMC and/or the northeastern regions of the SMC are closer to us. The previous studies (refer

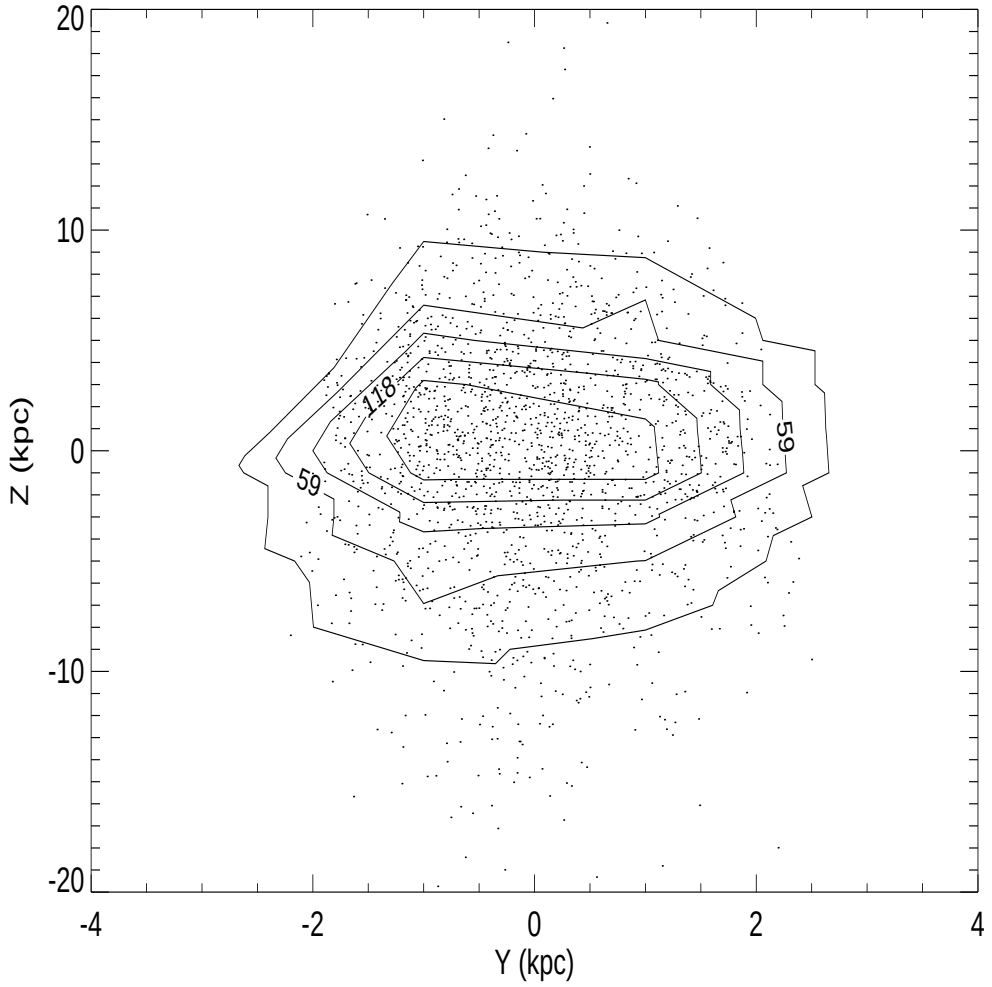

Figure 8.4: Relative distances to each RR Lyrae star in the SMC with respect to the mean distance are plotted against Y axis and are shown as black dots. The density contours are over plotted. The north is in the direction of increasing Y axis.

1.6.2) suggest that there is no large variation in the age and metallcity among old stars in the inner SMC. Thus the contribution to the I_0 magnitude from the population effects across the SMC is expected to be minimum. The exact contribution can be understood only from the detailed spectroscopic studies of the old stellar populations.

8.4.2 Line of sight depth of the SMC

The dispersions in the magnitude and colour distributions of the RC stars are used to obtain the depth corresponding to the width (1-sigma) of the 553 sub-regions in the

SMC. The width corresponding to depth is converted into depth in kpc using the distance modulus formula,

$$\sigma_{depth} = 5\log_{10}[(D_0 + d/2)/(D_0 - d/2)$$

where d is the line of sight depth in kiloparsec.

A colour coded, two dimensional plot of depth is shown in Fig. 8.5. The colour code is explained in the plot. From the plot we can see that the depth distribution in the SMC is more or less uniform. The prominent feature in the plot is the enhanced depth (depth > 8 kpc) seen near the central regions. An increased depth of around 6-8 kpc is seen near the north eastern regions also. The average depth obtained for the SMC observed region is 4.57 ± 1.03 kpc. These results are matching well with the depth estimates given in 7.4.

The dispersion in the mean magnitude of RRab stars is also used to estimate the depth (1-sigma) of the SMC. The dispersion in the mean magnitude for 70 sub-regions of the SMC is estimated and converted into depth in kpc. The average value of depth estimated when the intrinsic spread was taken as 0.1 mag is 4.07 ± 1.68 kpc and the average depth is 3.43 ± 1.82 kpc when 0.15 mag was taken as the intrinsic spread. These estimates match with the depth estimate obtained from the RC stars within the error bars.

The depth estimated using the RC stars and RRLS are plotted together in Fig. 8.6 against the X and Y axes. In both the lower panels, the depth values are plotted against the X-axis and in both the upper panels, they are plotted against the Y-axis. Basically the depth values correspond to the extent (front to back distance) over which these stars are distributed in the SMC. The measured 1-sigma depth (front to back distance) is halved and plotted along the +ve and -ve depth-axis, assuming that the depth is symmetric with respect to the SMC. The red crosses correspond to the depth estimated using the RC stars and the black points correspond to the depth estimated using the RRLS. The error bars for each point are not plotted to avoid crowding. In the left panels, the black dots correspond to the depth estimated using the RRLS when the $\sigma_{intrinsic}$ is taken as 0.1 mag. Similarly, in the right panels the black dots correspond to the depth estimated using the RRLS when the $\sigma_{intrinsic}$ is taken as 0.15 mag. The larger depth near the center (x∼0 and y∼0) is seen for both the populations. 18 regions in the right panels and the 3 regions in the left panels which are shown as open circles at zero depth are those for which the depth of the RRLS became less than zero when the correction for $\sigma_{intrinsic}$ were applied. For a large number of regions the depth value becomes less than zero when $\sigma_{intrinsic}$ is taken as 0.15 mag. Thus, it appears to be more appropriate to take $\sigma_{intrinsic}$ as 0.1 mag for the RRLS in the

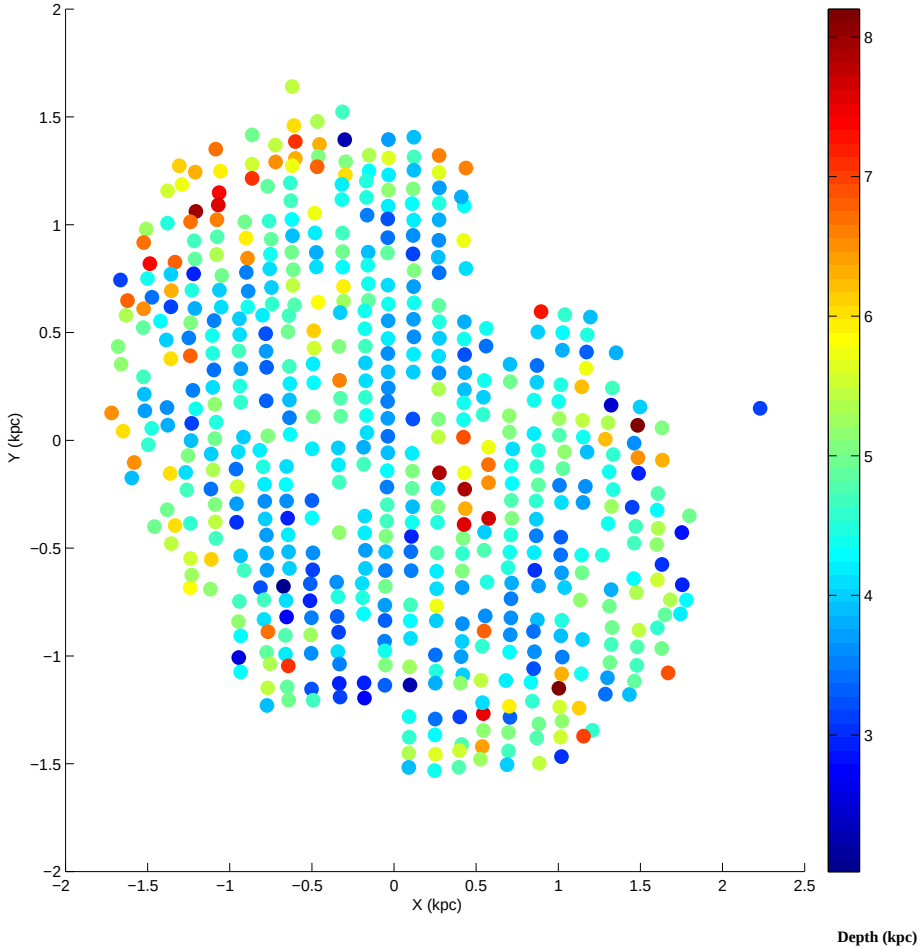

Figure 8.5: A two dimensional plot of the depth in the sub-regions of the SMC obtained from the analysis of the RC stars.

SMC. The depth profiles of both the populations are similar, suggesting that both the RC stars and RRLS occupy a similar volume in the SMC.

It is important to see how the dispersion in the distribution of the RRLS is related to the real RRLS distribution, obtained from the individual RRLS distances. This comparison will help us to estimate the actual depth from the dispersion of the RRLS in the SMC. We halved the 1-sigma depth (front to back distance estimated after correcting for $\sigma_{intrinsic}$ to be taken as 0.1 mag) obtained for each sub-region with respect to the mean distance and plotted in the -ve and +ve Z axis as filled circles against the X-axis in the left lower panel of Fig. 8.7. Similarly, 2-sigma depth, 3-sigma depth and 3.5-sigma depth are plotted in the lower right panel, upper-right panel and upper left panel of Fig. 8.7 respectively.

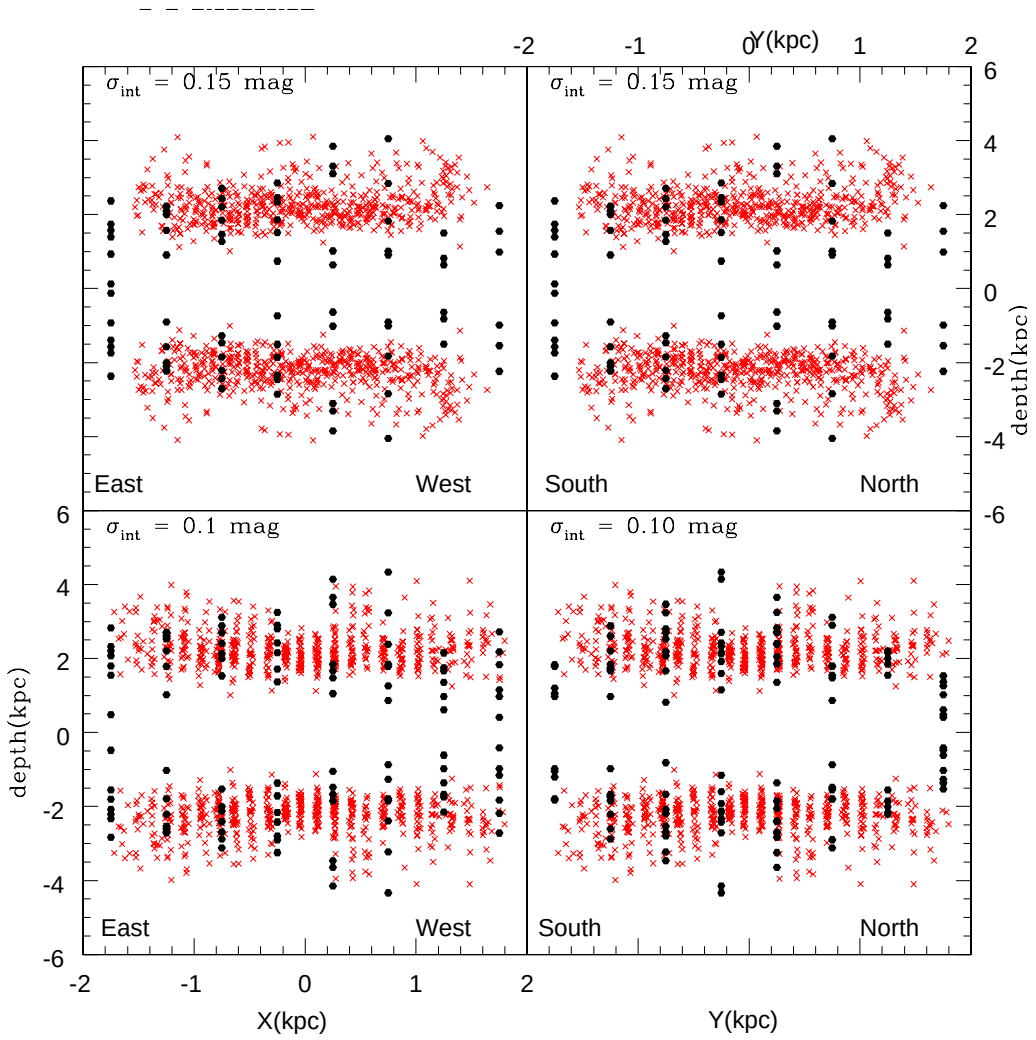

Figure 8.6: The line of sight depth (1-sigma) of both the RC stars (red crosses) and the RRLS (black dots) are plotted against the X and Y axes. In the left lower and right lower panels, the RRLS depth are estimated using $\sigma_{intrinsic}$ = 0.1 mag. In the right upper and left upper panels, the RRLS depth are estimated using $\sigma_{intrinsic}$ = 0.15 mag.

Individual RRLS distances with respect to the mean SMC distance are shown as black dots in all the panels of the figure. From the figure we can clearly see that the distribution of RRLS is atleast extended upto 3.5 sigma dispersion, if we take an intrinsic spread of 0.1 mag. This 3.5 sigma width (σ_{dep} = 0.146 mag) translates to a front to back distance of around 14.12 kpc. In Fig. 8.8, the depth estimated from RRLS after correcting for $\sigma_{intrinsic}$ = 0.15 mag are plotted over the individual RRLS distances. The left upper panel shows the 4 sigma depth plotted over the individual RRLS distances. From the figure we can clearly see that the distribution of RRLS is atleast extended to 4 sigma dispersion, if we

take an intrinsic spread of 0.15 mag. This 4 sigma width (σ_{dep} = 0.124 mag) translates into a front to back distance of around 13.7 kpc. Thus the RRLS in the SMC are distributed over a distance of $\sim$ 14 kpc along the line of sight. In the case of the RC stars, we have estimated only the mean distances to the sub-regions and the depth of the sub-regions. So we cannot compare the real RC distribution with the width of the distribution to define the depth. Since the depth profiles of the RC stars and the RRLS are similar, we expect these two populations to occupy a similar volume in the SMC and the RC stars also to be distributed in a depth of 14 kpc. The large depth suggests a spheroidal/ellipsoidal distribution for the above populations.

8.4.3 Density distributions of RC and RR Lyrae stars

From the above section we found that both the RC stars and RRLS have similar line of sight depth. The density distributions of both these populations will give a clue about the system in the XY plane. The surface density distribution, and the radial density profile are studied to understand the structure of the SMC. The surface density is calculated by dividing the observed region into different sub-regions and obtaining the number of objects per unit area in each sub-region. The radial density profiles are obtained by finding the projected radial number density of objects in concentric rings around the centroid of the SMC. These profiles can be compared with the theoretical models. The two theoretical models which can be used for the comparison of spatial distribution of different stellar populations in the SMC are the exponential disk profile and the King's profile. The exponential disk profile is give by

$$f(r) = f_{0d} e^{-r/h}$$

where f_{0d} and the h represent the central density of the objects and the scale length, respectively and r is the distance from the center of the distribution. The King's profile (King 1962), which is often used to describe the distribution of globular clusters, but also applies to dwarf spheroidal galaxies, is given by

$$f(r) = f_{0k}\{[1+(r/a)^2]^{-1/2} - [1+(r_t/a)^2]^{-1/2}\}^2$$

where r_t and a are the tidal and core radii respectively, f_{0K} is the central density of objects and r is the distance from the center. Both these profiles are used to fit the observed

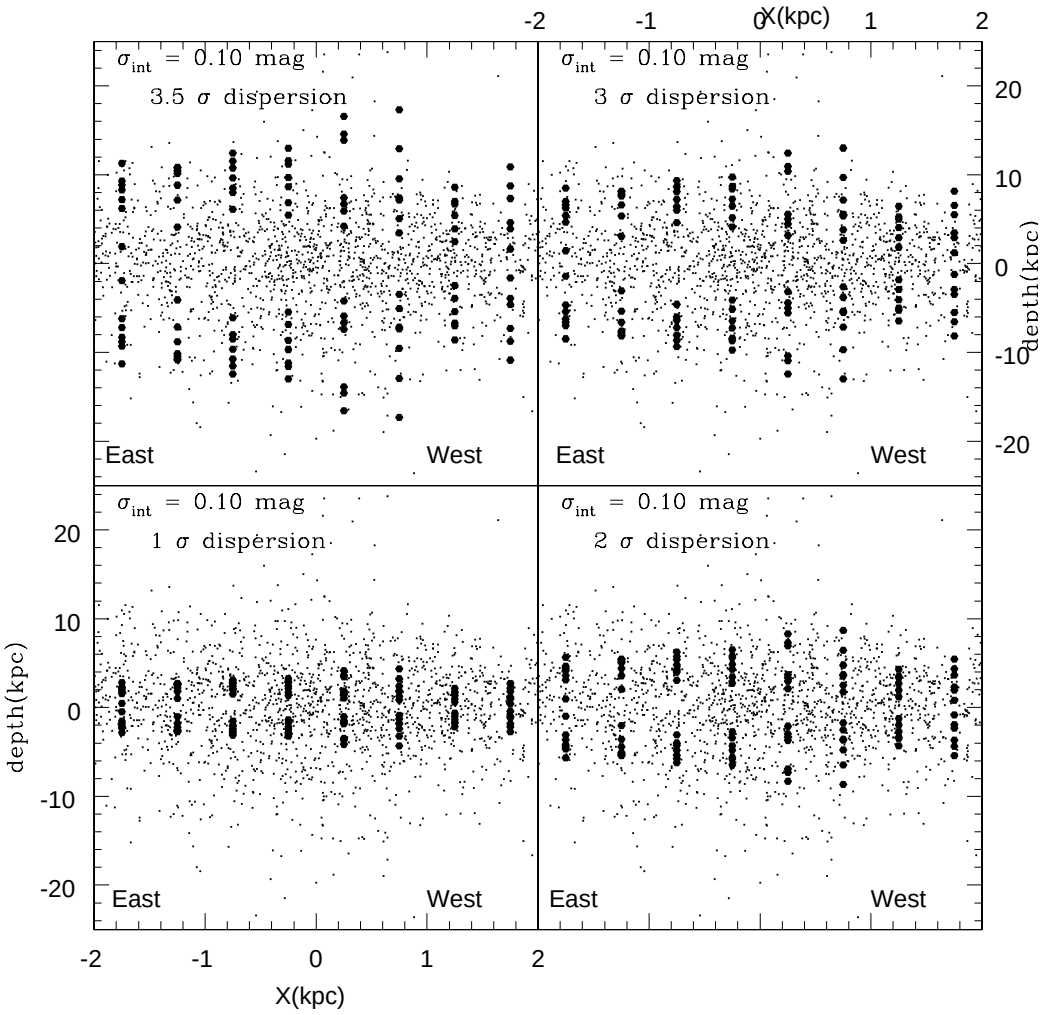

Figure 8.7: The distance to each RRLS with respect to the mean distance to the SMC is plotted as black dots in all the panels against the X-axis. The open circles in all the panels from lower right to upper left in the counter clockwise direction are the 1-sigma, 2-sigma, 3-sigma & 3.5-sigma depths. These are halved with respect to the mean distance to each sub-region and plotted in the -ve and +ve Z-axis against the X axis. The depth is calculated using an intrinsic spread of 0.1 mag.

distribution of the RC stars in the SMC.

The number of the RC stars, identified from the CMD, in each sub-region of the OGLE III region are estimated. We used all the 1280 sub-regions (each having an area of 32.6 square kpc) in the observed OGLE III region. We estimated the number density, number of the RC stars per unit area, for each sub-region. The number density distribution of the RC stars is shown in Fig. 8.9. The number density of RC stars in each sub-region ranges from 7500/kpc^2 - 200,000/kpc^2. In this figure, discrete points represent each sub-

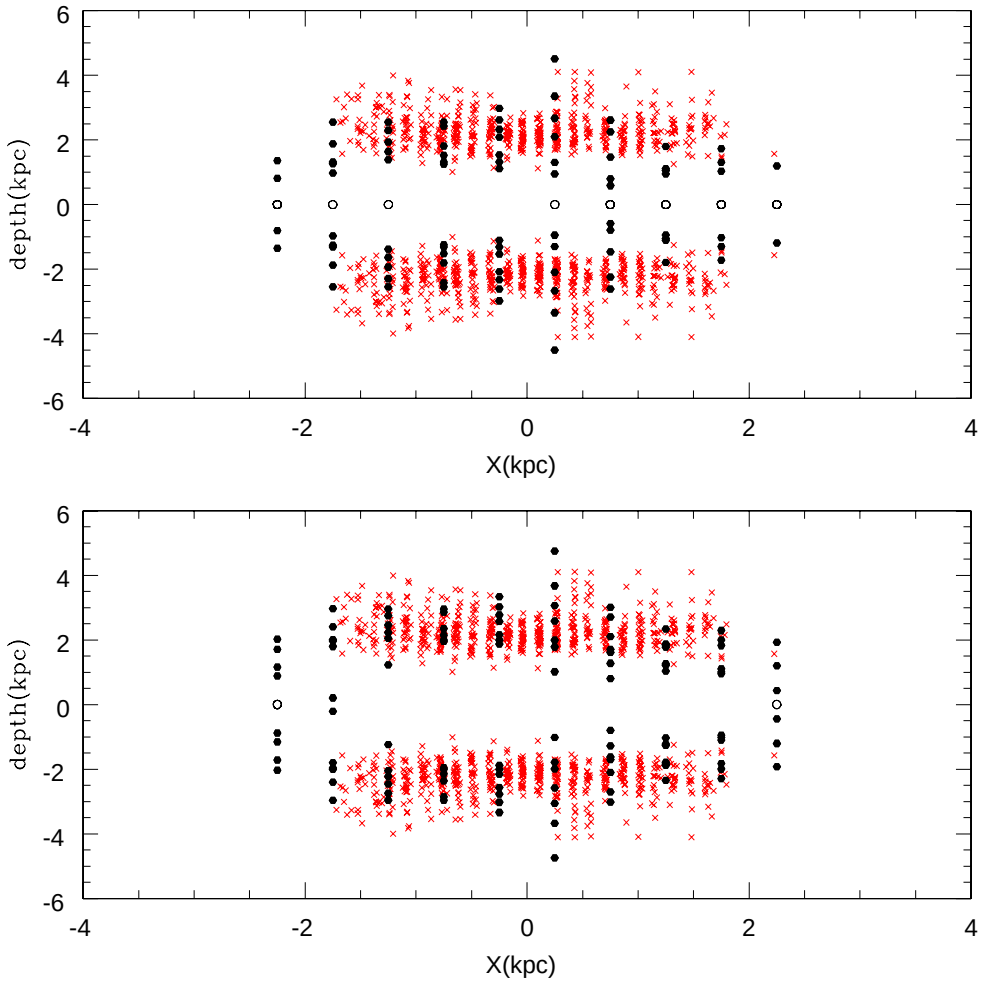

Figure 8.8: The distance to each RRLS with respect to the mean distance to the SMC is plotted as black dots in all the panels against the X-axis. The open circles in all the panels from lower right to upper left in the counter clockwise direction are the 1-sigma, 2-sigma, 3-sigma & 4-sigma depths. These are halved with respect to the mean distance to each sub-region and plotted in the -ve and +ve Z-axis against the X axis. The depth is calculated using an intrinsic spread of 0.15 mag.

region and the colour denotes the number density. The plot clearly shows the smooth RC distribution with an elongation in the north−east to south− west (NE-SW) direction. The colour code is given in the figure, where d denotes the red clump number density. The position angle of the elongation of the RC distribution is around 54^o for the eastern side. The plot also shows the shift in the RC density center, R.A = 0^h 52^m $34^s.2$, Dec = -73^o $2^{'}$ $48^{''}$ (shown as green hexagon in Fig. 8.12) from the optical center, R.A = 0^h 52^m 45^s, Dec = -72^o $49^{'}$ $43^{''}$ (shown as magenta hexagon in Fig. 8.12) of the SMC. The center of

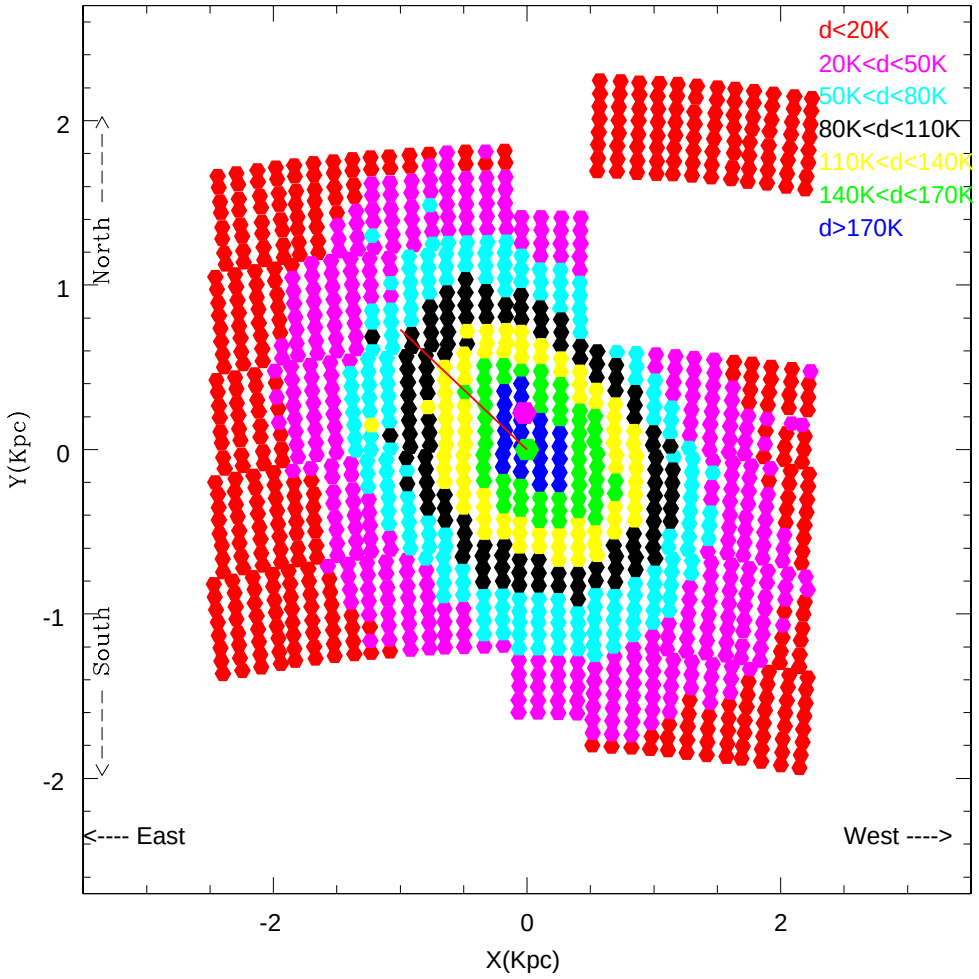

Figure 8.9: A two dimensional plot of the number density, d of the RC stars (d in the units of 1000(K)/square kpc) in the SMC. The green and magenta hexagons represent the centroid of the sample and the optical center respectively. The red line shows the direction of elongation.

the density distribution shown here is very similar to the centroid (given in section 2.1) of our RC sample in 553 sub-regions which are used for the estimation of dereddened magnitude and depth.

As the data coverage of the OGLE III is not symmetric with respect to the density center, the radial density distribution of the RC stars within a radius of 0.8^o is obtained. The region within 0.8^o radius from the density center are divided into 16 equal area (28.3 square arcmin) annuli. The number of RC stars in each annuli is obtained and it is divided by the area of the annuli to obtain the number density. Thus the radial density distribution

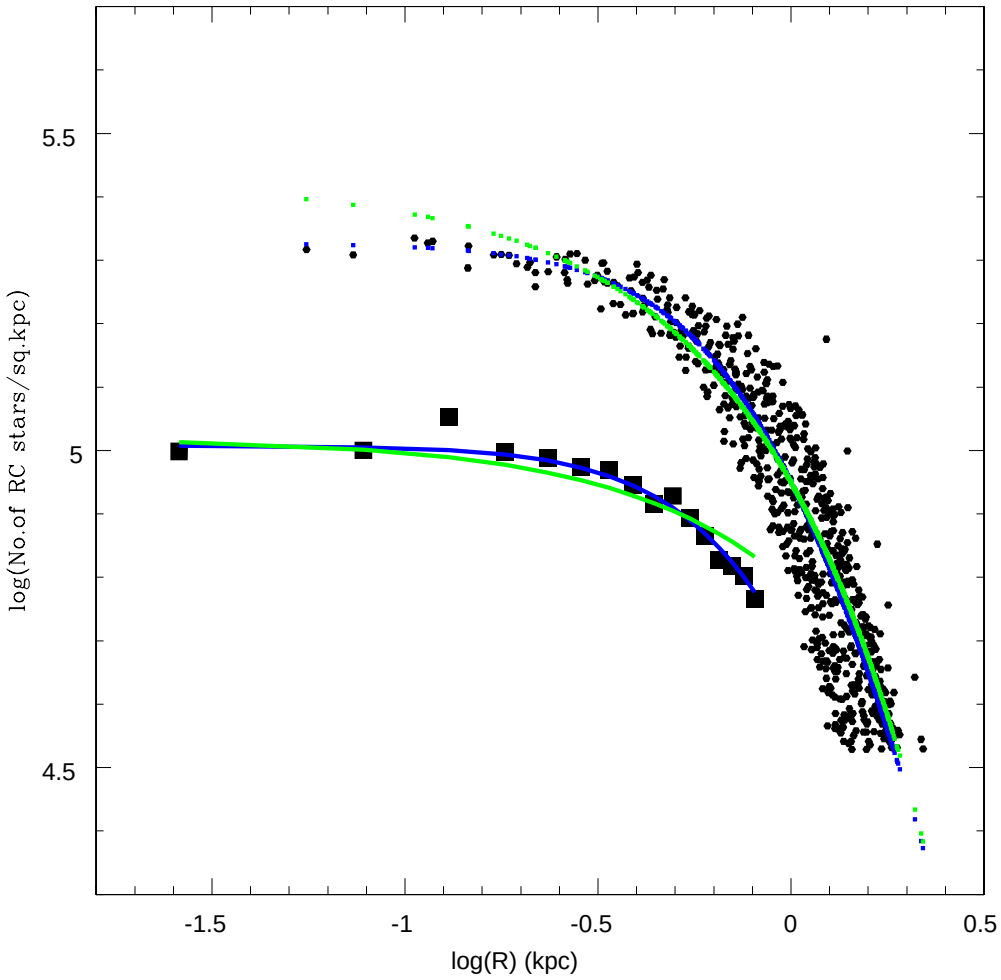

Figure 8.10: Radial density distribution of the RC stars within the radius of the 0.8^o in the SMC are shown as black squares. The best fitted King's profile and the exponential profile for the radial density distribution are shown as blue and green solid lines respectively. The surface density distribution of the RC stars for the whole observed region of the OGLE III are shown as black dots. The best fitted King's profile and the exponential profile for the surface density distribution are shown as blue and green dashed lines respectively.

Table 8.1: Parameters of the Exponential and King's profiles

Data	f_{0d}(no/sq.kpc)	h (kpc)	f_{0k} (no/sq.kpc)	r_c(kpc)	r_t (kpc)
Radial	(104±0.4)x10^3	1.87±0.1	(141±7)x10^3	1.08±0.02	7 ± 1
Surface	(264±0.1)x10^3	0.91±0.1	(248±1)x10^3	0.9±0.01	12.04± 0.01

of the RC stars within 0.8^o radius from the density center is obtained and are shown as black squares in Fig. 8.10. The best fitted exponential disk profile and the King's profile are shown in the figure as green and blue solid lines respectively. We can see that the radial density profile of the RC stars in the SMC is marginally better described by the King's profile than by the exponential profile. We obtained the surface density profile of the RC stars in the whole observed area of the SMC. The number density of the RC stars in the 1280 sub-regions of the SMC are plotted against the radial distance of each sub-region from the density center in Fig. 8.10. The black points in the figure denotes the surface density of the RC stars in each sub-region. The best fit exponential disk profile and the King's profile are shown as green and blue dashed lines in Fig. 8.10. Here we can see that the surface density profile of the RC stars in the SMC is best described by the King's profile. The parameters obtained by fitting the radial density and surface density distributions by exponential and King's profiles are given in table 8.1. The estimated tidal radius of the SMC system is $\sim$ 7-12 kpc. Thus the RC stars in the SMC are distributed in a spherical/ellipsoidal volume, which indicates that the SMC can be approximated as a spheroidal/ellipsoidal galaxy. But in the surface density profile we can see a spread in the points for each radii, which indicates that the volume in which the RC stars are distributed is not exactly spherical. Again from the map of the surface density distribution shown in Fig. 8.9, we can see the elongation in the NE-SW direction. Thus the RC stars in the SMC are distributed in an ellipsoidal system.

Our sample of RRLS which are pulsating in the fundamental mode consists 1904 stars. The density center of our sample is R.A = 0^h 53^m 31^s, Dec = -72^o $59^{'}$ $15^{''}$.7. The density center of our sample lies in between the two concentrations found by Soszyñski et al. (2010b). To study the density profiles a large number of sample is required. The surface density map of the RRLS identified from the OGLE III photometric maps is shown in the lower panel of figure 7 in Soszyñski et al. (2010b). They identified two concentrations in the RRLS spatial distribution and found that the RRLS in the SMC form a roughly circular strucutre in the sky which indicates that the RRLS in the SMC are distributed in a spheroidal/ellipsoidal volume.

8.5 Axes ratio and orientation of the SMC ellipsoid

We model the observed system of the SMC in which the RC stars and RRLS are distributed as a triaxial ellipsoid. The parameters of this ellipsoidal system, like the axes ratio and the orientation can be estimated using the inertia tensor analysis. The tensor

analysis used here is similar to the methods used by Pejcha & Stanek (2009) and Paz et al. (2006), but with some modification. The tensor analysis used here is given explained in 2.2.5.

8.5.1 RR Lyrae stars

The method described in the section 2.2.5 can be applied to our sample of the RRLS to estimate the parameters of the ellipsoidal component of the SMC. First we applied this method only to (x,y) system and found that the SMC RR Lyrae distribution is elongated with an axes ratio of 1:1.3 and the major axis has a position angle of 74^o (NE-SW). We repeated the procedure to the (x,y,z) coordinates of the RRLS. The axes ratio obtained is 1:1.3:6.47 and the longest axis is inclined with the line of sight direction with an angle (i) of $0^o.4$. The position angle of the projection of the ellipsoid (ϕ) on the plane of the sky is given by $74^o.4$. The data of the RRLS used here contain the RRLS in the isolated north western OGLE III fields. As they are discrete points in the density distribution, we removed the RRLS in those fields and repeated the procedure. When we removed the RRLS in those fields, the density center changed to R.A = 0^h 54^m $38^s.6$, Dec = -73^o $4'$ $52''.2$. The axes ratio obtained is 1:1.57:7.71 with $i = 0^o.4$ and $\phi = 66^o.0$. Here we can see that the coverage of the data plays an important role in the estimation of the structural parameters of the ellipsoid. This may also suggest that there may be a variation in the inner and outer structures of the SMC. Nidever et al (2011) found that the inner SMC ($R<3^o$) is more elliptical than the outer component ($3^o<R<7^o.5$).

In order to understand the radial variation of the inner structure we estimated the parameters using the data within different radii. At first, the analysis is done excluding the RRLS in the north western fields. The axes ratio, i and ϕ of the RRLS distribution are obtained for the data within different radii, starting from 0.75^o. The values obtained are given in table 8.2. The values show that the i is more or less constant with a value of around $0^o.5$. But the axes ratio and ϕ have a range. The axes ratio has a range from 1:1.05:19.84 to 1:1.57:7.7. The ϕ ranges from 60^o to 78^o. The data within 0.75^o of the density center is symmetric and the parameters obtained confirm that the RRLS distribution in the SMC is slightly elongated in the NE-SW direction. As the radius increases the data coverage is not symmetric and circular, and the axis ratio of x and y show an increasing trend. The surface density map of RRLS shown (in figure 7 of Soszyñski et al. 2010b) does not show large elongation, rather the map looks nearly circular with a mild elongation in the NE-SW direction. So the elongation obtained for the RRLS distribution in the plane of the sky, at larger radius where the data coverage is not even, may not be

real. We did a similar analysis to understand the radial variation including the fields in the north western regions. Here the concentric circles with different radii are centered on the density center (given in last paragraph) estimated including the RRLS in the north western fields. These values are also given in table 8.2. From this also it is evident that there is a mild elongation in the NE-SW direction in the distribution of the RRLS in the SMC. Here we have to also keep in mind that the density center estimation of the SMC RRLS is not accurate as there are two concentrations found in the density distribution shown in figure 7 of Soszyñski et al. (2010b). The variation in the density center also modifies the structural parameters of the distribution.

From the detailed analysis described in the last two paragraphs, it is clear that the quantitative estimates of the structural parameters of the SMC are very much dependent on the data coverage. Though there are differences in the values, we can say that the RR Lyrae distribution in the inner SMC is slightly elongated in the NE-SW direction. The longest axis Z', which is perpendicular to the X'Y' plane (a plane obtained by the counter clockwise rotation of the XY plane with an angle ϕ with respect to the Z axis) is aligned almost parallel to the line of sight, Z axis. The x, y and z values of the whole sample of the RRLS are plotted in Fig. 8.11 to get a 3D visualization of the SMC structure. The figure clearly shows the elongation in the Z' $\sim$ Z axis.

8.5.2 Red Clump stars

From the previous sections we found that the RC stars and RRLS occupy a similar volume of the SMC. Hence we can apply the method of inertia tensor to the RC stars for the estimation of the parameters of the ellipsoidal component of the SMC. First we apply this method to the (x,y) coordinates of the 553 sub-regions of the SMC. Here each (x,y) pair represents the coordinates of a sub-region. We weighted it using the number of the RC stars identified in that region to get the axes ratio. We find that the RC distribution in the SMC is elongated with an axes ratio of 1:1.48 and the position angle of the major axis is $55^o.3$. Now we applied the same procedure to the (x,y,z) system of the RC stars. In the case of RRLS, we took the distance of the individual RR Lyrae star with respect to the mean distance as the z coordinate. But in the case of RC stars we only have the mean magnitudes corresponding to the mean distances to the sub-regions. The mean magnitude of a region in the ellipsoidal or nearly spheroidal system is the average of the magnitude of symmetrically distributed RC stars. In order to get the real RC distribution we did the following. After subtracting the average extinction, we obtained the magnitude distribution of the RC stars for each sub-region. Using the method explained earlier in

Table 8.2: Orientation measurements of the ellipsoidal component of the SMC estimated using the RR Lyrae stars

Excluding the three north western fields
Center R.A = $0^h\ 54^m\ 38^s.6$, Dec = -$73^o\ 4'\ 52''.2$

Data	No of RRLS	Axes ratio	i	ϕ
r < 0.75	421	1:1.05:19.84	$0^o.4$	$78^o.83$
r < 1.00	676	1:1.03:14.59	$0^o.4$	$72^o.20$
r < 1.25	924	1:1.04:11.35	$0^o.2$	$75^o.68$
r < 1.50	1187	1:1.10:9.43	$0^o.1$	$63^o.41$
r < 1.75	1407	1:1.23:8.66	$0^o.1$	$61^o.68$
r < 2.00	1563	1:1.34:8.21	$0^o.1$	$66^o.00$
r < 2.25	1711	1:1.47:7.87	$0^o.3$	$67^o.62$
r < 2.50	1780	1:1.54:7.73	$0^o.4$	$67^o.48$
r < 2.75	1798	1:1.57:7.71	$0^o.4$	$66^o.30$
r < 3.00	1803	1:1.57:7.71	$0^o.4$	$65^o.96$

Including the north western fields
Center R.A = $0^h\ 53^m\ 31^s$, Dec = -$72^o\ 59'\ 15''.7$

Data	No of RRLS	Axes ratio	i	ϕ
r < $0^o.75$	428	1:1.07:20.01	$0^o.5$	$48^o.84$
r < $1^o.00$	671	1:1.03:14.01	$0^o.4$	$64^o.88$
r < $1^o.25$	927	1:1.03:11.19	$0^o.4$	$67^o.84$
r < $1^o.50$	1177	1:1.13:9.59	$0^o.2$	$59^o.54$
r < $1^o.75$	1399	1:1.23:8.70	$0^o.2$	$60^o.10$
r < $2^o.00$	1568	1:1.30:8.00	$0^o.1$	$64^o.87$
r < $2^o.25$	1755	1:1.34:7.22	$0^o.3$	$68^o.78$
r < $2^o.50$	1845	1:1.36:6.89	$0^o.4$	$70^o.80$
r < $2^o.75$	1892	1:1.34:6.57	$0^o.4$	$73^o.70$
r < $3^o.00$	1904	1:1.33:6.47	$0^o.3$	$74^o.40$

Table 8.3: Orientation measurements of the ellipsoidal component of the SMC using the RC stars

Data	Axes ratio	i	ϕ
RC stars within 1-sigma depth	1:1.49:3.08	$4^o.22$	$55^o.7$
RC stars within 2-sigma depth	1:1.48:5.26	$1^o.23$	$55^o.4$
RC stars within 3-sigma depth	1:1.48:7.10	$0^o.68$	$55^o.6$
RC stars within 3.5-sigma depth	1:1.48:7.88	$0^o.58$	$55.^o.5$
RC stars within 4-sigma depth	1:1.48:8.58	$0^o.49$	$55.^o.4$

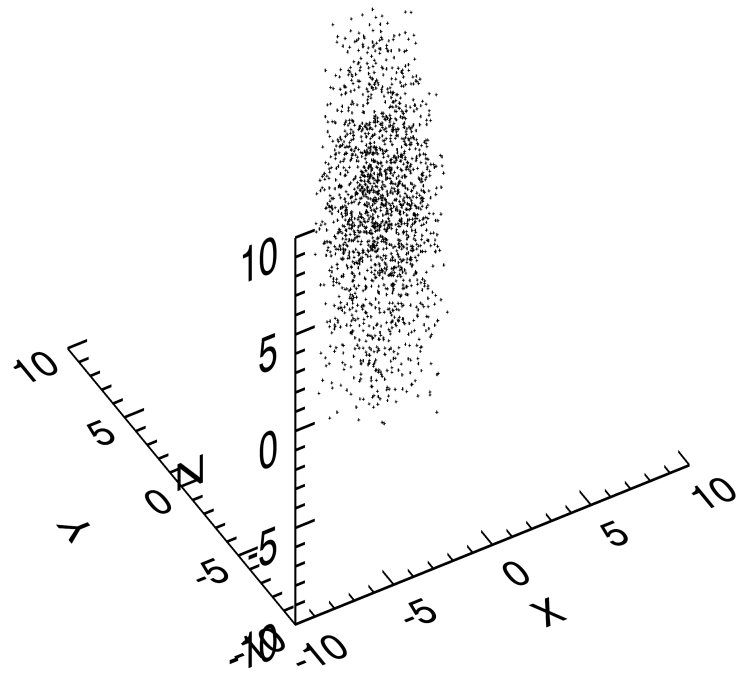

Figure 8.11: The x,y and z values of the whole sample of the RRLS are plotted.

section 2.1, we estimated the peak and the width of the magnitude distribution for each sub-region and eventually the width corresponding to depth. The depth (front to back distance) of the RC stars in a region is the measure of the extend up to which the RC stars in that region is distributed. Most of the RC stars in a sub-region are at the mean distance obtained for that sub-region and the remaining are distributed within the depth of the region. We assume the distribution to be symmetric with respect to the mean distance to that sub-region. Initially we took the I_0 values of the bins within 1-sigma width and converted them into z distances. As we have the number of stars in each bin we weighted and applied the inertia tensor analysis to the x,y and z coordinates.

Earlier we found that the RC and RR Lyrae depth distributions are similar. Also, from figures 10 and 11 we can see that the RR Lyrae distribution extends up to 3-4 sigma depth.

Table 8.4: Orientation measurements of the ellipsoidal component of the SMC using the RC stars and the RRLS in the same region. Excluding the north western fields and the edges of the data

Data	Axes ratio	i	ϕ
1654 RRLS	1:1.46:8.04	$0^o.50$	$58^o.3$
RC stars within 3.5-sigma depth	1:1.48:7.88	$0^o.58$	$55^o.5$

Hence we can take the z component to extend upto higher sigma levels (2-sigma, 3-sigma, 3.5-sigma, 4-sigma) to understand the real RC distribution in the SMC. We applied the inertia tensor analysis using z components which extend up to 2-sigma, 3-sigma, 3.5-sigma & 4-sigma. The parameters obtained are given in table 8.3. From the table we can see that the orientation measurements of the ellipsoidal component of the SMC using RC stars, where the z component extend up to 3.5 sigma is similar to the values obtained for the RR Lyrae distribution excluding the north western fields. As we removed the regions with RC stars less than 400, the north western fields are not included in the analysis. The axes ratio and the angle i are matching well with the ellipsoidal parameters of the SMC, estimated using the distribution of the RRLS. The position angle, ϕ estimated using the RC stars and RRLS are slightly different.

Based on the analysis described above we can say that the RC stars in the SMC are distributed in an ellipsoidal system with an axes ratio of 1:1.48:7.88. The position angle, ϕ is $55^o.5$. The longest axis Z' which is perpendicular to the X$'$Y$'$ plane (obtained by the counter clockwise rotation of the XY plane with an angle $55^o.5$ with respect to the Z axis) is inclined with the Z axis with an angle of $0^o.58^o$. The inclination of the Z$'$ axis with the line of sight is very small and we can assume the longest axis to be almost along the line of sight.

8.5.3 Comparison of the structural parameters obtained from both the populations

The quantities estimated in this analysis strongly depend on the data coverage. In order to compare the axes ratio and the orientation measurements obtained from both the populations, it is important to take the sample of both the population of stars from the same region. In the case of the RC stars regions which include the north western fields and also regions in the edges of the data set are omitted based on the selection criteria. Such

a truncation of the data is not done in the case of the RRLS. Only the RRLS which are possible Galactic objects are removed from the analysis. These stars are not concentrated on a particular region but are scattered. If we remove the RRLS in the north western fields and the edges of the data, then the sample of RRLS cover the nearly the same region as the RC stars sample. We used the RRLS within the box of size size -1.8−1.8 in both the X and Y axes. Thus the RRLS in the edges of the data set and in the north western fields are nearly removed. Then we estimated the parameters using this sample of the RRLS and the values are given in table 8.4. From the table we can see that when the sample of both the populations are taken from similar regions of the SMC the estimated parameters match well.

8.6 Discussion

We find the Z' ∼ Z axis is the longest axis in the analysis of both the RRLS and the RC stars. The reason for such a result is mainly the coverage of the SMC. The studied data covers only the central regions thus restricting the coverage in the XY plane. On the other hand the full Z direction is sampled. Hence the present view of the SMC based on our axes ratio is like viewing only the central part of a sphere along the Z axis. Such a perspective will give an elongated Z axis. This is clear from Fig. 8.11. In order to test whether the z'∼z axis is due to the viewing perspective, we have sampled the data similarly along the three axes. The extend of the sample along all the three axes can be made equal by taking the data only within a spherical radii (ρ) of 2, 2.5 and 3 degrees from the center. We took the RRLS stars within these different radii and estimated the structural parameters. The estimated parameters are given in table 8.5. An elongation in the NE-SW axis is seen suggesting that the elongation of the RRLS in the NE-SW is a real feature. The decrease in the relative length of the z' axis is expected as the selection mentioned above removes relatively more number of stars along the z' direction than in the x' and y' directions. From table 8.5 we can see that the inclination of the longest axis with the line of sight axis decreases from inner to outer radii. The finite XY coverage restricts further analysis of this trend. The very small value of i (given in tables 8.2, and 8.4) estimated from the analysis of all the RRLS, including those at larger z distances from the center, indicates that the decreasing trend of i is continued to outer radii also. In table 8.5 we can also see an increase in ϕ and the relative length of y' axis from inner to outer region. From section 8.4.1 and from table 8.2 we can understand that these two quantities are dependent on the choice of the centroid of the system. So we cannot definitely say anything more about

Table 8.5: Estimated structural parameters with equal extent in all the three axes

Data	Number of RRLS	Axes ratio	ϕ (degrees)	i (degrees)
$\rho < 2.0$	344	1:1.17:1.28	67.5	4.2
$\rho < 2.5$	540	1:1.24:1.39	69.5	3.3
$\rho < 3.0$	730	1:1.33:1.61	70.2	2.6

this trend. Another important result to be noticed from table 8.5 is that even though the z' axis is the longest of the three, the values of the longest and the second longest (y') axes are comparable. This suggests that when the coverage along all the three axes becomes comparable, the structure of the SMC is spheroidal or slightly ellipsoidal.

The above analysis indicates that the XY extent of the SMC upto which stellar populations are studied/detected plays an important role in understanding the actual structure of the SMC and hence the estimation of the structural parameters. The tidal radius estimates give the radial extent up to which the stellar populations are bound to the SMC or up to which they are expected to be found. Gardiner & Noguchi (1996) estimated the tidal radius of the SMC to be $\sim$ 5 kpc. Later Stanimirović et al. (2004) suggested the tidal radius of the SMC to be 4-9 kpc. The estimations obtained in our study from the radial density and surface density profiles of the RC stars, given in table 8.1, suggest the tidal radius to be 7-12 kpc. There are many recent studies which found old and intermediate stellar populations in the outer regions. Noël et al. (2007) found that up to 6.5 kpc from the SMC center, the galaxy is composed of both, intermediate-age and old population, without an extended halo. De Propris et al. (2010) estimated the SMC edge in the eastern direction to be around 6 kpc from the survey of red giant stars in 10 fields in the SMC. A very recent photometric survey of the stellar periphery of the SMC by Nidever et al. (2011) found the presence of old and intermediate age populations at least up to 9 kpc. The above mentioned observational studies and tidal radius estimates suggest that the full extent of the SMC in the XY plane (2*9 = 18 kpc) is of the order of the front to back distance estimated (14 kpc) along the Z axis. We found in earlier sections that the inner SMC is slightly elongated in the NE-SW direction. Thus we suggest, that the actual structure of the SMC is spheroidal or slightly ellipsoidal. Better estimates of the structural parameters can be obtained with a data set of larger sky coverage. In the following section, we combine previous studies and suggest an evolutionary model for the SMC.

Bekki & Chiba (2008) suggested that the SMC may be formed due to a dwarf-dwarf merger, resulting in a stellar spheroidal component and a gaseous disk component, hap-

pened before the formation of the MW-LMC-SMC system. They also suggest that since stellar populations formed before the merger event should have dynamically hot kinematics, the youngest age of stellar populations that show both spheroidal distributions and no or little rotation can correspond to the epoch when the merger occurred. As the merger event should evoke a large scale star formation event in the galaxy, the epoch of merger can also be traced from the enhancements seen in the star formation history of the SMC.

The most comprehensive study of the star formation history of the SMC is presented by Harris & Zaritsky (2004). They derived the global star formation history of the SMC. They found that there was a significant epoch of star formation up to 8.4 Gyr ago when 50% of the stars were formed, followed by a long quiescent period in the range 3 Gyr < age < 8.4 Gyr, and a more or less continuous period of star formation starting 3 Gyr ago and extending to the present. They also found three peaks in the SFR, at 2−3 Gyr, at 400 Myr, and 60 Myr ago. Their CMDs do not go deep enough to derive the full star formation history from the information on the main sequence. Obtaining CMDs reaching the oldest main sequence turnoff is essential in order to properly constrain the intermediate-age and old population (Gallart et al. (2005)). As we study the intermediate age and old stellar populations in the SMC, here we compare the star formation studies done based on the CMDs which reach the oldest main sequence turnoffs. These studies go deeper and hence have smaller field of views. Dolphin et al. (2001), Chiosi & Vallenari (2007), and Noël et al. (2009) have done such studies and obtained the star formation history of the SMC.

Dolphin et al. (2001) found a broad peak of star formation between 5 and 8 Gyr ago. Chiosi & Vallenari (2007) found two main episodes of star formation , at 300−400 Myr and between 3−6 Gyr. They also found that the star formation rate was low until $\approx$ 6 Gyr ago, when only a few stars were formed. Noël et al. (2009) found star formation enhancements at two intermediate ages, a conspicuous one peaked at 4−5 Gyr old in all fields and a less significant one peaked at 1.5−2.5 Gyr old in all fields. The enhancement at old ages, with the peak at 10 Gyr old is seen in all fields. But in the western fields, this old enhancement is split into two at 8 Gyr old and at 12 Gyr old. Their farthest field is at 4.5 kpc. All these studies show an enhancement in the star formation in the SMC around 4−5 Gyrs ago.

If the 4−5 Gyr global star formation in the SMC is assumed to be due to a dwarf-dwarf merger, then according to the merger model, the merged galaxy will settle down within 1-3 Gyr (Lotz et al. (2008)). This scenario will then demand a spheroidal component well mixed with stars older than 2 Gyr. Our results find that the old population (RR Lyrae stars, age > 9 Gyr) and the intermediate age component (Red clump stars, age = 2−9 Gyr)

seem to occupy similar volume, suggesting that stars older than 2 Gyr are in a well mixed ellipsoid.

Tsujimoto & Bekki (2009) proposed that the evidence of a major merger event in the SMC is imprinted in the age-metallicity relation as a dip in [Fe/H]. They predicted that the major merger with a mass ratio of 1:1 to 1:4 occurred at ∼ 7.5 Gyr ago in the SMC. Based on this model they could reproduce the abundance distribution function of the field stars in the SMC. As they could not correlate a peak in the star formation history of the SMC at the epoch of the merger they suggested that the major merger which occurred in the SMC at 7.5 Gyr ago did not trigger a major star burst due to some physical reasons but proceeded with a moderate star formation. Noël et al. (2009) did not find a dip in the age metallicity relation of the SMC, which Tsujimoto & Bekki (2009) claim to detect and suggested as the imprint of a major merger at 7.5 Gyr ago. Again if this merger event in the SMC at 7.5 Gyr old is the reason for the kinematical and morphological differences of the young and old stars then we cannot expect stars younger than 4-5 Gyr in the spheroidal/ellipsoidal distribution. As we see the RC stars which have an age range of 2-9 Gyr in the spheroidal/ellipsoidal distribution we propose a merger event which started around 4-5 Gyr ago as the reason for the observed distribution of stars in the SMC.

A wider and larger future photometric (OGLE IV) and spectroscopic surveys which cover both the inner and outer regions of the SMC will help to understand the complete structure and kinematics of the SMC.

8.7 Conclusions

• The dereddened I_0 magnitude of the RC stars and RRLS are used to determine the relative positions of the regions in the SMC with respect to the mean distance and it suggest that either the population of the RC stars and RRLS in the north eastern regions are different and/or the north eastern part of the SMC is closer to us.

• The line of sight depth of the SMC estimated using the RC stars and the RRLS is found to be ∼ 14 kpc. The depth profiles of both the population look similar indicating that these two populations are located in the similar volume of the SMC.

• The surface density distribution and the radial density profile of the RC stars suggest that they are distributed in a nearly spheroidal system. The tidal radius estimated for

the SMC system is ∼ 7-12 kpc. An elongation from NE -SW is also seen in the surface density map of the RC stars in the SMC.

• The observed SMC is approximated as a triaxial ellipsoid and the structural parameters, like the axes ratio, inclination, i of the longest axis with the line of sight and the position angle, ϕ of the projection of the ellipsoid on the plane of the sky are estimated using the inertia tensor analysis. The parameters are very much dependent on the coverage.

• An axes ratio of 1:1.5:8.04 , $i = 0^o.5$ and $\phi = 58^o.3$ are estimated from the analysis of RRLS. Similarly an axes ratio of 1:1.5:7.88 , $i = 0^o.6$ and $\phi = 55^o.5$ are estimated from the analysis of the RC stars assuming them to be also extended to a depth of 3.5-sigma.

• From the analysis of the RC stars and RRLS in the same region of the SMC the parameters estimated turned out to be very similar.

• The study of data only within concentric spheres of radii 2, 2.5 and 3 degrees from the center, where the extent in all the three axes becomes equal, shows that the relative lengths of the z' and y' axes are comparable. Our tidal radius estimates and various observational studies of the outer regions suggest that the full extent of the SMC in the XY plane is similar to the front to the back distance estimated along the line of sight. These results suggest that the actual structure of the SMC is spheroidal or slightly ellipsoidal.

• We propose that the SMC experienced a merger with another dwarf galaxy at about 4−5 Gyr ago, and the merger process was completed in another 2-3 Gyr. This resulted in a spheroidal distribution comprising of stars older than 2 Gyr.

CHAPTER 9

DISK OF THE SMC: ESTIMATION OF THE STRUCTURAL PARAMETERS USING CEPHEIDS

9.1 Introduction

The SMC is believed to be a two component system where the old and intermediate age stars are distributed in a spheroidal or slightly ellipsoidal component and the young stars and gas distributed in a disk. Young stars (age <200 Myr) and the H I gas are the good tracers of the SMC disk parameters. The analysis of young stars (age < 200 Myr) (Zaritsky et al. 2000) and the high resolution H I observations (Stanimirović et al. 2004) show that SMC disk is quite irregular and asymmetric. The H I observations also show that the SMC has a significant amount of rotation with a circular velocity of approximately 60 kms^{-1} (Stanimirović et al. (2004)) and a large velocity gradient of 91 kms^{-1} in the southwest to 200 kms^{-1} in the north east. Evans & Howarth (2008) obtained velocities for 2045 young (O, B, A) stars in the SMC, and found a velocity gradient of similar slope as seen in the H I gas. Surprisingly though, they found a position angle ($\sim 126^o$) for the line of maximum velocity gradient that is quite different, and almost orthogonal to that seen in the H I.

Cepheids (age < 100 Myr) are also used to investigate the structure of the SMC disk. Using H I velocity and cepheid data, Caldwell & Coulson (1986) found the SMC to consist of a central bar seen edge-on, a near arm in the northeast (NE), a far arm in the southwest (SW), and a mass of material pulled out of the center and seen infornt of the

SW arm. They obtained an inclination, i = 70°.0±3°.0 and position angle of the closest part to be 58°±10° from the study of 63 Cepheids. From the study of Cepheids in the bar region of the SMC, Groenewegen (2000) estimated an inclination of 68°.0±2°.0 and position angle of the line of nodes, ϕ to be 148°.0±7°.0.

Gardiner & Noguchi (1996) modelled the SMC as a two component system consisting of a nearly spherical halo and a rotationally supported disc. The tidal radius of the SMC is estimated as 5 kpc according to their model. The distribution of disc particles could reproduce the observed irregular distribution of young stars in the SMC. Bekki & Chiba (2008) suggested that a major merger event in the early stage of the SMC formation caused the coexistence of a spheroidal stellar component and an extended rotating H I disk.

In the present study we have studied the V and I band photometric data of the fundamental mode Cepheids in the SMC from the OGLE III catalog. The period luminosity relations are obtained and they are used to estimate the structural parameters of the SMC disk.

9.2 Data and Analysis

The seventh part of OGLE III catalog (Soszyñski et al. 2010a) of variable stars consists of 4630 classical Cepheids in the SMC. 2626 classical Cepheids in the catalog are fundamental mode Cepheids. Among these only 2603 stars have simultaneous detection in both the V and I bands and we considered only these 2603 stars for our analysis. A mean reddening, E($B-V$) of 0.054 mag (Caldwell & Coulson 1985) towards the SMC is considered and the V and I bands magnitudes are corrected for extinction using the following extinction relations,

A_V = 3.1 x E($B-V$)
A_I = 1.96 x E($B-V$)

The period luminosity relations of the sample using the extinction corrected V and I magnitudes are obtained. These coefficients are substituted in the PL relation given by equation (5) given in section 2.2.1. The variation in distance and reddening of each star from the mean value towards the SMC are estimated by solving the equations for V and I pass bands. The R.A, Dec and the variation in individual distance are converted into x,y,z coordinates using the relations (12), (13) and (14) given in section 2.2.2. On the cartesian

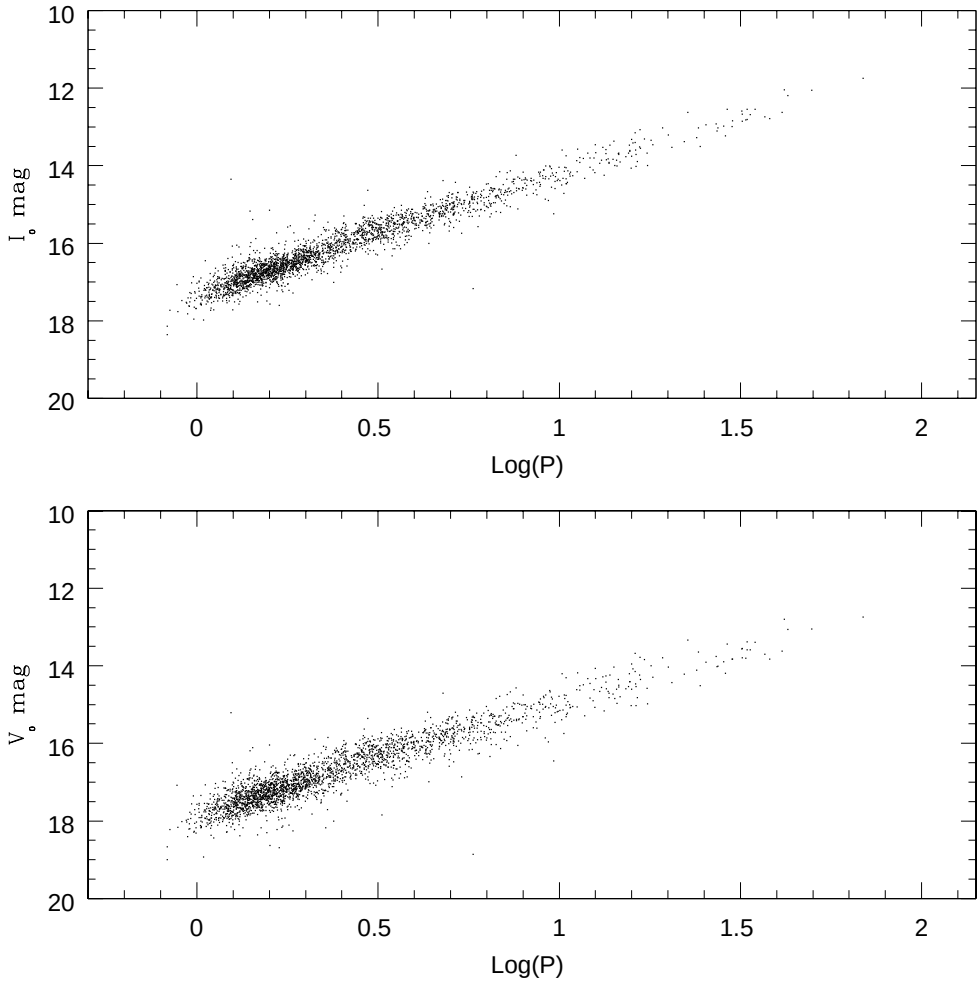

Figure 9.1: The Log(P)vs V_0 and Log(P) vs I_0 PL diagrams of fundamental mode Cepheids in the SMC are shown in lower and upper panels respectively.

coordinate system, the plane fitting procedure is applied to obtain the structural parameters (using the equations (15) and (16) given in section 2.2.3)of the disk of the SMC. We calculated the deviations of the SMC disk from the plane with estimated coefficients. The expected z value for a plane is calculated with the equation of a plane, Ax+By+Cz+D =0. The difference in the expected and calculated z value is taken as the deviation of the SMC disk from the plane. Thus the extra-planar features are identified and quantified. Once the deviations are estimated, the regions with deviations above three times the error in z are omitted and the plane-fitting procedure is applied to the remaining regions to re-estimate

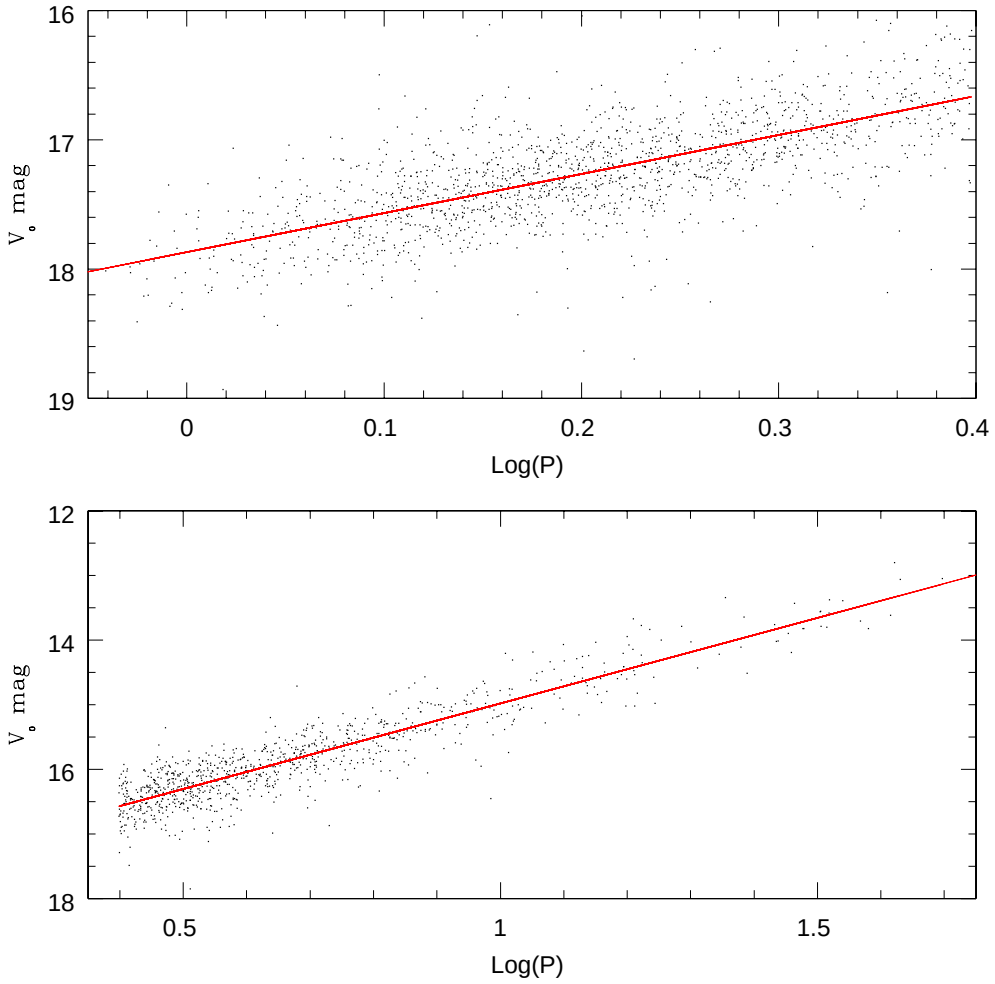

Figure 9.2: The Log(P) vs V_0 PL diagrams of longer (P > 2.5 days) and shorter (P < 2.5 days) period fundamental mode Cepheids are shown in lower and upper panels respectively.

the structural parameters of the SMC disk plane.

9.3 Results

9.3.1 PL relations

The logP vs I_0 and logP vs V_0 period-luminosity (PL) diagrams are shown in the upper and lower panels of Fig. 9.1 repectively. A non-linearity in the relations are seen

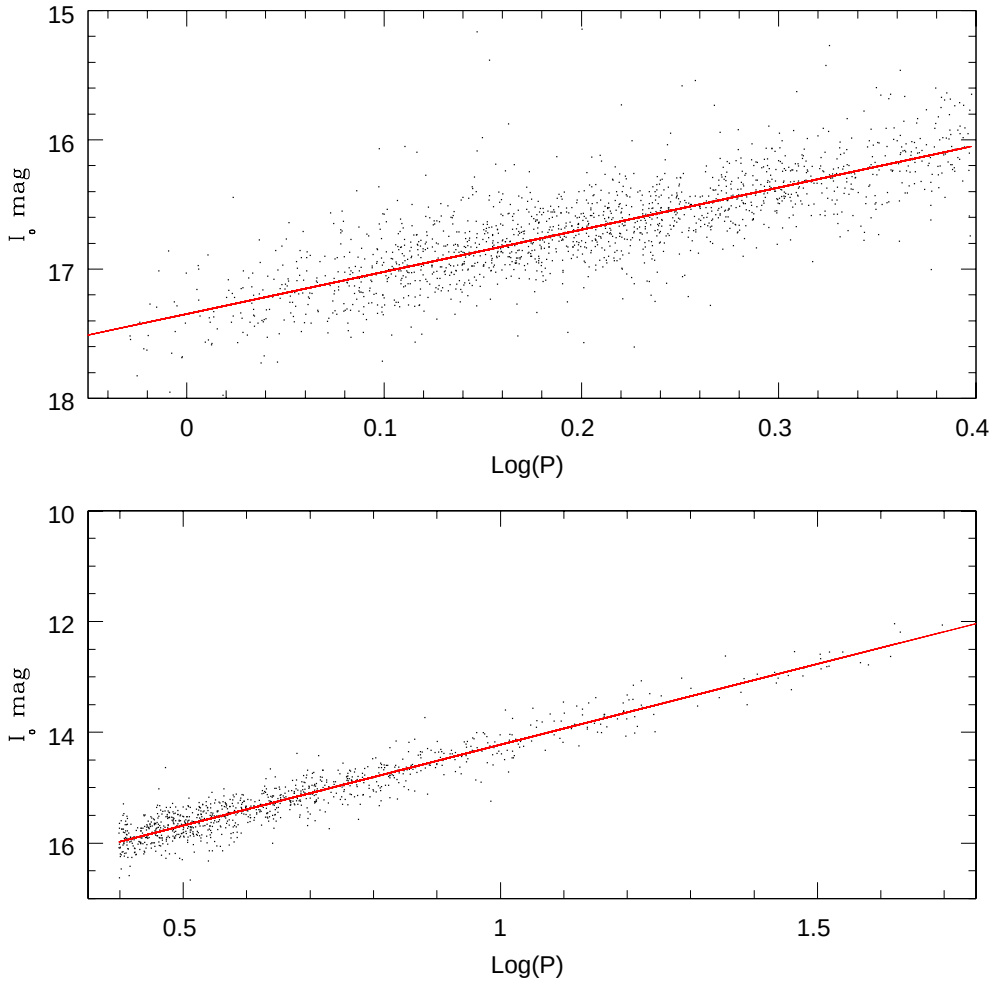

Figure 9.3: The Log(P) vs I_0 PL diagrams of longer (P > 2.5 days) and shorter (P < 2.5 days) period fundamental mode Cepheids are shown in lower and upper panels respectively.

in both the plots at a logP value of ~ 0.4 (P ~ 2.5 days). A break in the PL relation of the SMC fundamental mode Cepheids at about 2.5 days was first reported by Bauer et al. (1999) and confirmed by Udalski et al. (1999), Sharpee et al. (2002), Sandage et al. (2009) and Soszyñski et al. (2010a). As this feature indicates that the SMC hosts two different populations of classical Cepheids we divided the data set into two. One with Cepheids with P> 2.5 and the other with P< 2.5. The first group contains 965 stars and the latter group contains 1638 stars.

The PL relations for these groups are separately obtained using least square fit with 3σ clipping. The results are given in Table 9.1. The PL diagrams of the shorter and longer

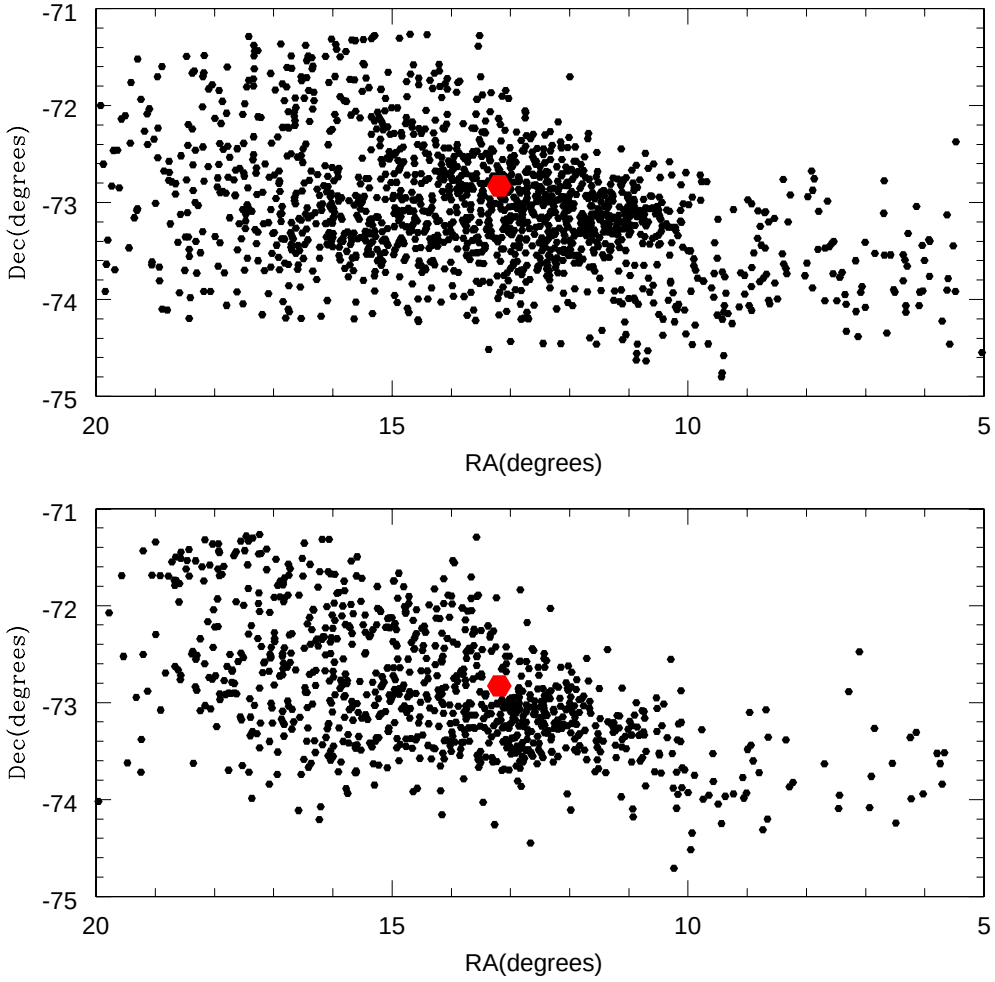

Figure 9.4: The spatial distribution of fundamental mode Cepheids in the SMC. The lower panel shows the distribution of Cepheids with longer period (P>2.5) and the upper panel shows the distribution of Cepheids with shorter period (P< 2.5).

period Cepheids in both the V and I bands are shown in Fig. 9.2 and Fig. 9.3. The best fit line is also shown in the plots. From the plots as well as from the table we can see that the slope of the sample with shorter period Cepheids is steeper than that of the longer period Cepheids. This confirms the previous results obtained by (Udalski et al. 1999) and Groenewegen (2000). The above result suggests that the two group of Cepheids are two different populations. Fig. 9.4 shows the spatial distribution of fundamental mode Cepheids. The distribution of Cepheids with longer period (P > 2.5) is shown in the lower panel and the distribution of Cepheids with shorter period (P < 2.5) is shown in the upper panel. The optical center of the SMC (de Vaucouleurs & Freeman 1972) is shown as red

Table 9.1: The coefficients of PL relations of fundamental mode Cepheids

Data	α_λ	β_λ	σ
V band data with P > 2.5	-2.65±0.037	17.62±0.027	0.28
V band data with P < 2.5	-3.02±0.068	17.87±0.015	0.26
I band data with P > 2.5	-2.92±0.029	17.14±0.029	0.22
I band data with P < 2.5	-3.26±0.055	17.35±0.012	0.21

hexagon in both the plots. The shorter period Cepheids are distributed all over the galaxy. On the other hand, the longer period Cepheids are concentrated more near the bar region.

The estimated coefficients are substituted in the respective PL relations of V and I bands (given in section 2.2.1) and these simultaneous equations are solved to obtain the variation of distance and reddening of each star from the mean value. For shorter and longer period Cepheids we used their respective PL relations. The R.A, Dec and variation in the distance are converted into x,y,z coordinates using the relations given in 2.2.2. Here we took the optical center of the SMC as the center of the system. The z coordinate represents the relative distance of the star with respect to the center of the SMC. The distance towards the SMC center is taken as 60 kpc. The convention used is such that the +ve z axis is towards us and the -ve z axis is away from us. The error in z has contributions from the errors in the PL coefficients and photometric errors. The average error in z is 2.35 kpc.

The distribution of Cepheids with longer periods (P>2.5) in the XZ and YZ planes are shown in the lower and upper panels of Fig. 9.5. A similar plot for the Cepheids with shorter periods (P<2.5) is shown in Fig. 9.6. From the lower panels (XZ distribution) of both the plots we can see that the Cepheids in the eastern part of the SMC are brighter. This in turn suggests that the eastern part of the SMC is closer to us. We can also see a gradient in the relative distances of the Cepheids from east to west. The linear drift in the relative distances is the effect of the inclination of the SMC disk. The YZ distributions shown in the upper panels of Fig. 9.5 and Fig. 9.6 suggest that there is a symmetric distribution of Cepheids with respect to the center in the southern side (Y < 0) of the SMC. On the other hand, more number of stars are closer to us in the northern side. This mildly suggest that on an average the northern side of the SMC is closer to us than the southern side. We do not see any gradient from north to south.

9.3.2 Reddening Map

The actual reddening towards each star is estimated using the relation, E($B - V$) =

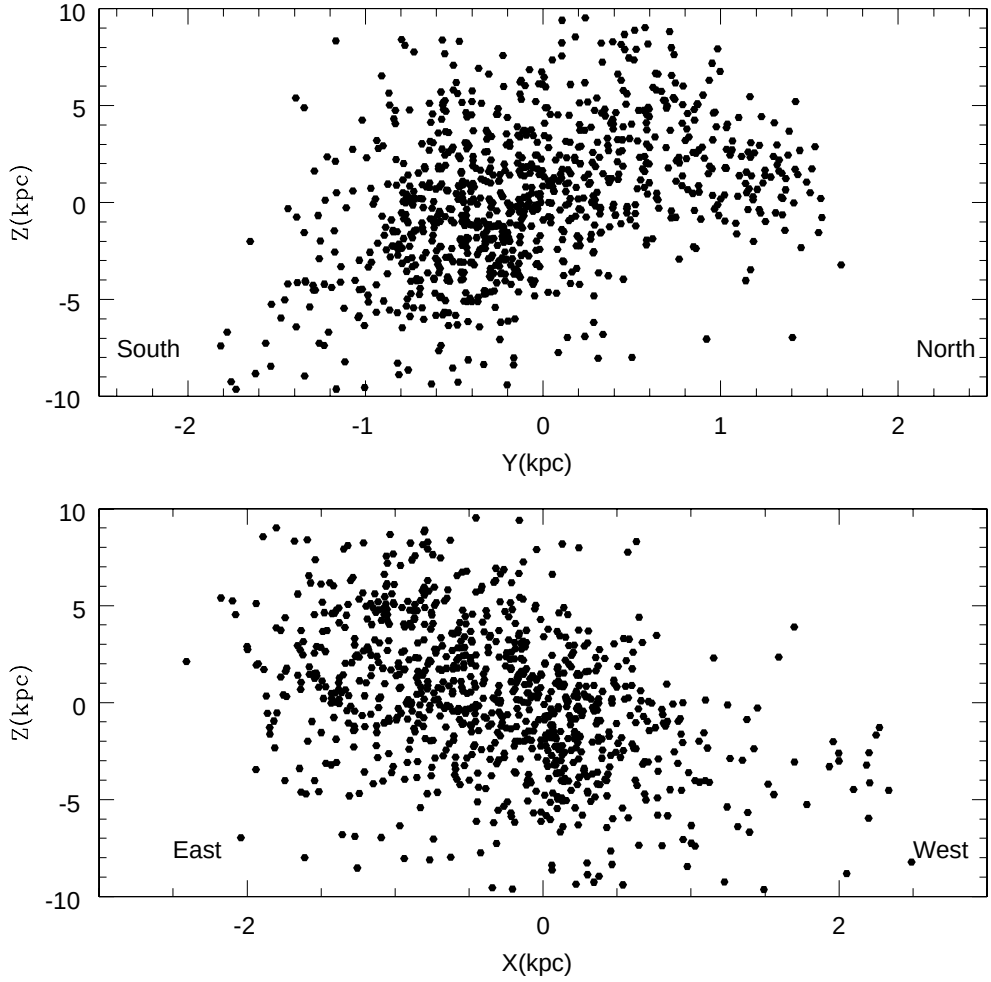

Figure 9.5: The distribution of fundamental mode Cepheids with P>2.5. The lower and the upper panels show the XZ and YZ distributions repectively.

E$(B-V)_{mean}$ + δE(B-V). The data are binned with a bin size of 0°.2 x 0°.2 square kpc and the average reddening within each bin is obtained. The E$(B-V)$ has a range from 0.01 to 0.14 mag with an average value of 0.064 mag. The reddening map is shown in Fig. 9.7. The size of the point is a measure of the reddening such that the bigger points represent regions which have larger reddening and smaller points represent regions with less reddening. From the figure we can see that the central regions have larger reddening than the surrounding regions. This result is consistent with the reddening map (Indu & Subramaniam 2011) obtained from the stars younger than 100 Myr. The reddening map obtained from the RC stars given in Fig.8.1 also shows large reddening in the central regions. Eventhough the regions with large reddening are coinciding in the reddening

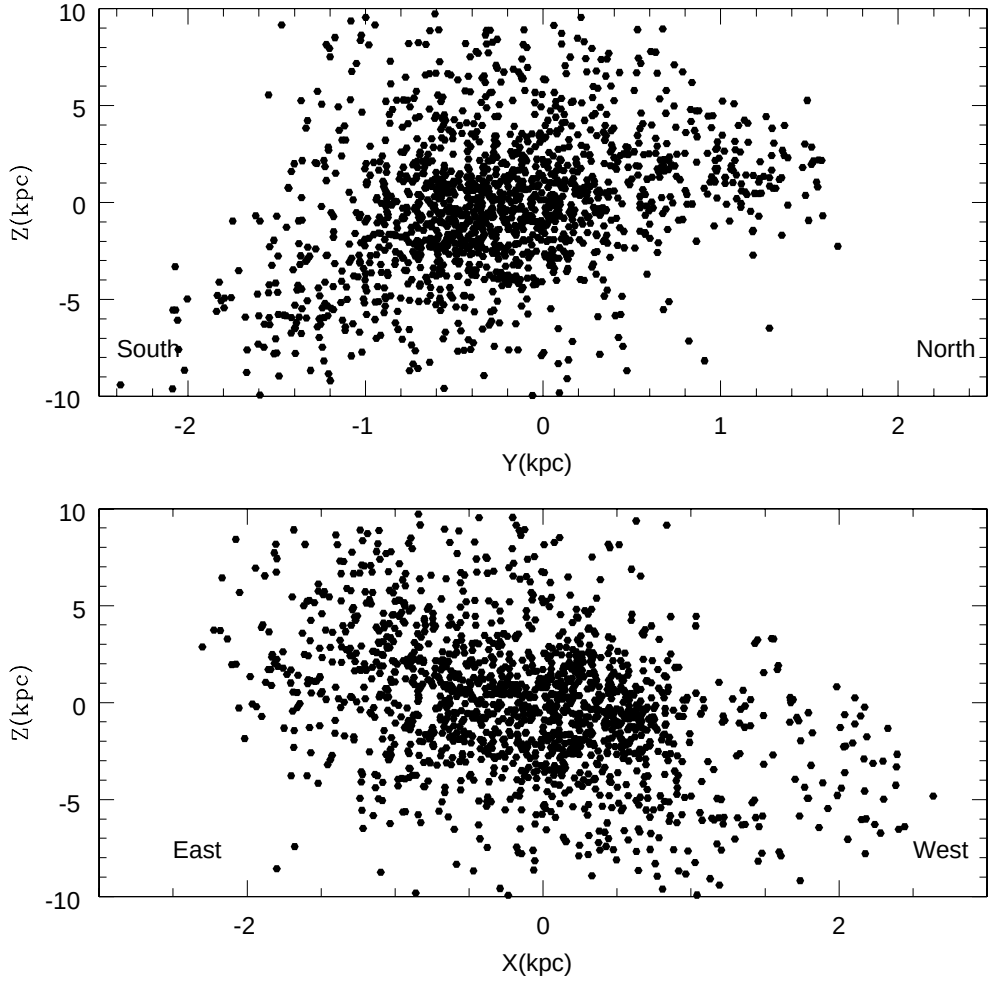

Figure 9.6: The distribution of fundamental mode Cepheids with P<2.5. The lower and the upper panels show the XZ and YZ distributions repectively.

maps obtained using different tracers, the values are different. The mean E($B-V$) obtained from the study of young stars (Indu & Subramaniam 2011) is $\sim$ 0.13 mag and from the study of RC stars (section 8.3) the value obtained is 0.037 mag. The variation in the values may be due to the differences in the reference values used for each study. The important point is that the relative variation of reddening in the SMC is similar in all the reddening maps.

9.3.3 Orientation mesaurements

A plane fitting procedure explained in section 2.2.4 is applied to the cartesian coor-

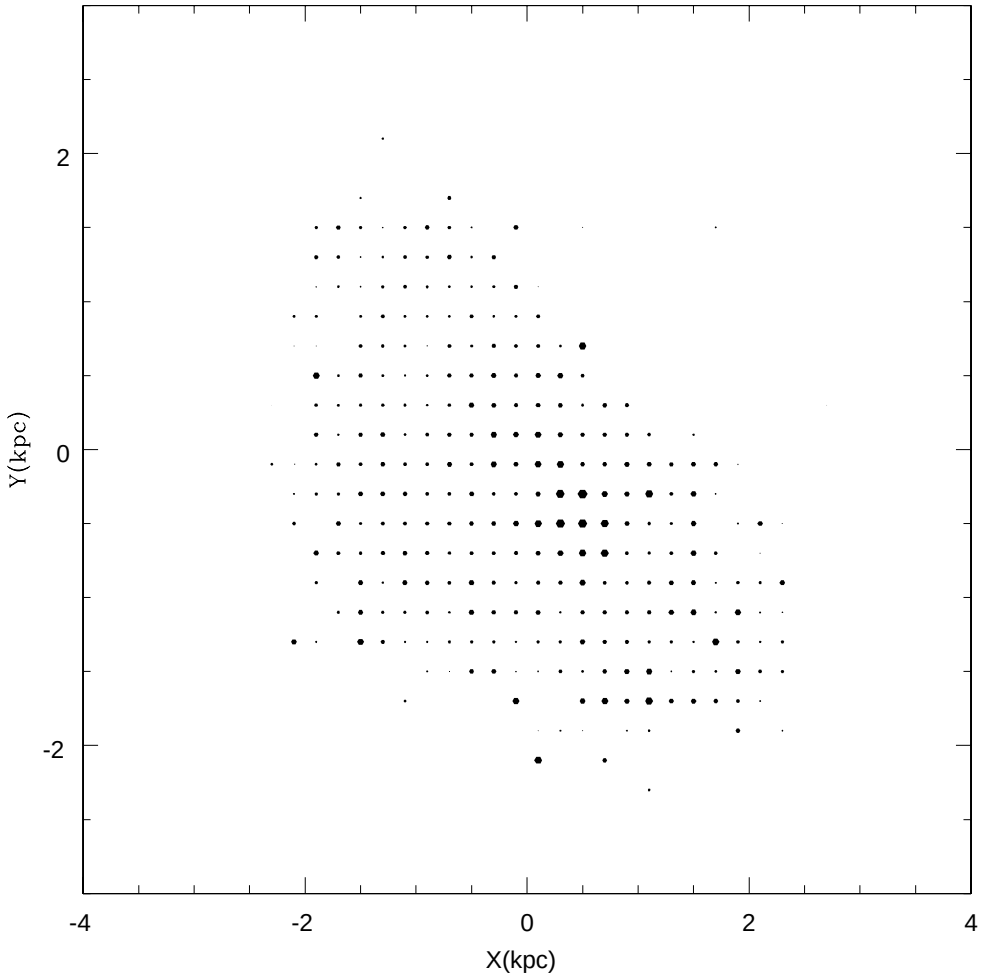

Figure 9.7: The E(B-V) reddening map towards the SMC derived from Cepheids is shown. The size of the point is proportional the the amplitude of reddening. The bigger points represent the regions with large reddening and the small points represent the regions with less reddening.

dinate system. From the coefficients of the equation of plane, the structural parameters such as the inclination i and the position angle of the line of nodes, ϕ are estimated. These parameters are estimated using the shorter and longer periods Cepheids separately. The orientation measurements are also estimated from the combined sample of longer and shorter period Cepheids. The values obtained are given in Table 9.2. The i and ϕ values obtained from the analysis of shorter period Cepheids are different from that obtained from longer period Cepheids. The i value is less and ϕ value is more for the plane obtained from shorter period Cepheids than those obtained from longer period ones.

The extra-planar features in the SMC disk are estimated as explained in section 9.2. The average error in z is 2.35 kpc and the deviations greater than 7 kpc (which corresponds to 3 times the error in z) are considered as real deviations. The extra-planar features are obtained for two groups (shorter and longer period Cepheids) separately. The two dimensional plots of deviations obtained from two groups are plotted in the upper and lower panels of Fig. 9.8. The black points in the figure are the Cepheids which are on the plane, the blue are those which are infront of the fitted plane and the red are those which are behind the fitted plane. There are 138 Cepheids in the shorter period group which are far away (> 7kpc) from the main disk. Out of these 138 outliers, 55 stars are behind the disk and 88 are infront of the disk. In the longer period group, 67 stars are far away from the main disk with 42 stars behind the disk and 35 infront of the disk. After the removal of outliers from the sample the planar parameters for the two groups are re-estimated. The parameters obtained are given in Table 9.2. From the table we can see that the re-estimated parameters of the two groups match well within the errors. This suggests that the variation in the planar parameters we saw before the removal of extra-planar features is due to the presence of outliers in these groups. From the combined sample we also estimated the extra-planar features. After the removal of these outliers, the planar parameters are re-estimated. These values are also given in Table 9.2. From the table we can see that the two groups as well as the combined sample give similar estimates of planar parameters.

The z values of the combined sample are plotted along the axis perpendicualr to the line of nodes, the axis maximum gradient and is shown in Fig. 9.9. Stars which are on the plane are shown as black points and the outliers (which are far away from the fitted plane) are shown as red dots. The effect of inclination is clearly seen in the plot. The slope estimated for the gradient is 2.14±0.08 kpc, which converts into an inclination of 65°.0 ± 4°.4. The inclination obtained matches with the inclination values obtained from the plane fitting procedure.

9.4 Discussion

From the study of the fundamental mode Cepheids we estimated an i of 61°.35±0°.5 and ϕ of 132°.5±10°.5 for the SMC disk. Our results are consistent with previous estimations derieved from Cepheids. Caldwell & Coulson (1986) obtained an inclination of 70°.0±3°.0 and position angle of the closest part to be 58°±10° from the study of 63 Cepheids. From the study of Cepheids in the bar region of the SMC, Groenewegen

Table 9.2: Orientation measurements of the SMC disk

Data	Number of stars	i (degrees)	ϕ (degrees)
Cepheids with P > 2.5 (Caldwell & Coulson 1986)	63	70 ± 3	148 ± 10
Cepheids with P > 2.5 (Groenewegen 2000)	464	68 ± 2	148 ± 7
Our results: Before the removal of extra-planar features			
Cepheids with P > 2.5	954	64.9 ±0.1	124±1.0
Cepheids with P < 2.5	1610	58.7 ± 0.1	145.5 ± 0.8
Combined sample	2603	60.5±0.5	137.2±2.1
Our results: After the removal of extra-planar features			
Cepheids with P > 2.5	887	62.4 ±1.2	132.7±12.0
Cepheids with P < 2.5	1472	61.4 ± 0.8	133.0 ± 10.0
Combined sample	2356	61.35±0.5	132.5±10.5

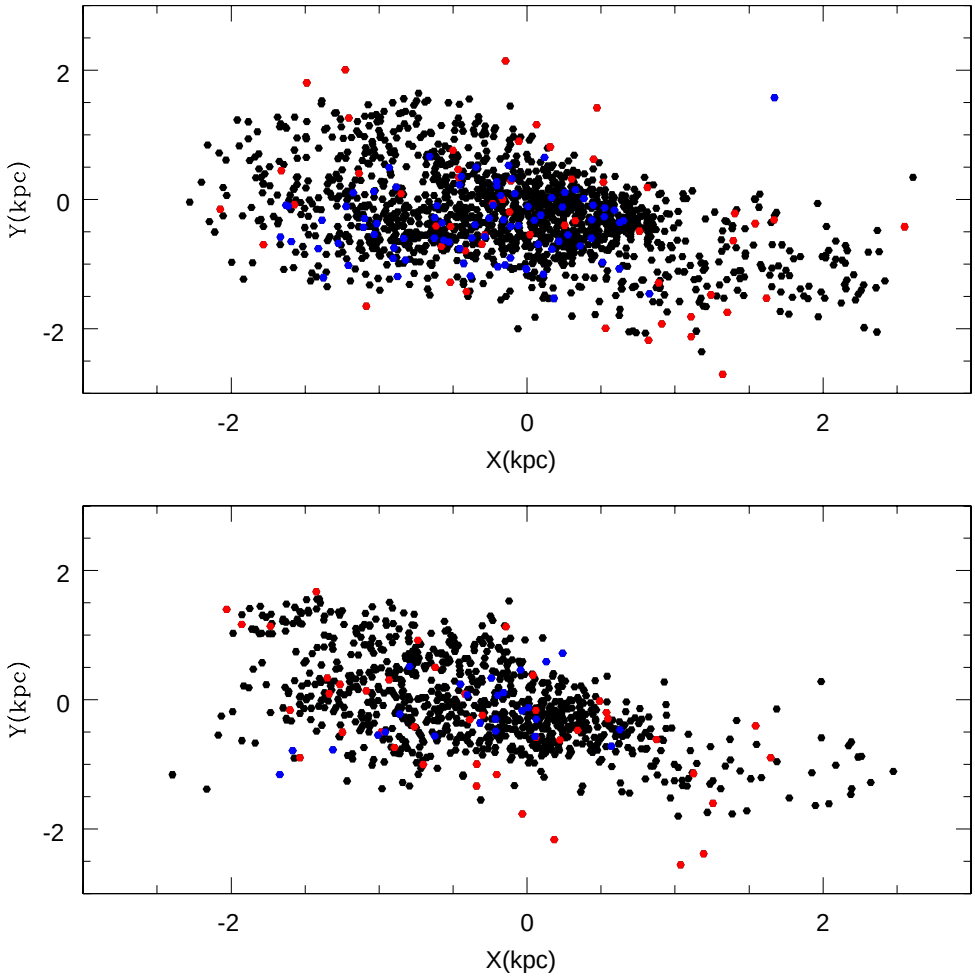

Figure 9.8: The two dimensional plot of deviation is shown. Th lower and upper panels are the deviation plots obtained from the Cepheids with P>2.5 and with P<2.5 repectively. The black points are those which are on the plane. The red and blue points are those which are behind and infront of the fitted plane.

(2000) estimated an inclination of 68°.0±2°.0 and position angle of the line of nodes to be 148°.0±7°.0. Compared to the previous studies our sample has more number of Cepheids.

The other tracer for the estimation of planar parameters of the disk is the H I gas. The high resolution H I observations of the SMC (Stanimirović et al. 2004) show that the SMC has significant amount of circular rotation and a velocity gradient from northeast to southwest. This study gives a ϕ of $\sim 45°$ for the H I disk of the SMC. The ϕ obtained in our analysis is almost orthogonal to that seen in the H I . This suggests that the kinematical line of nodes is perpendicular to the photometric line of nodes. Evans & Howarth (2008)

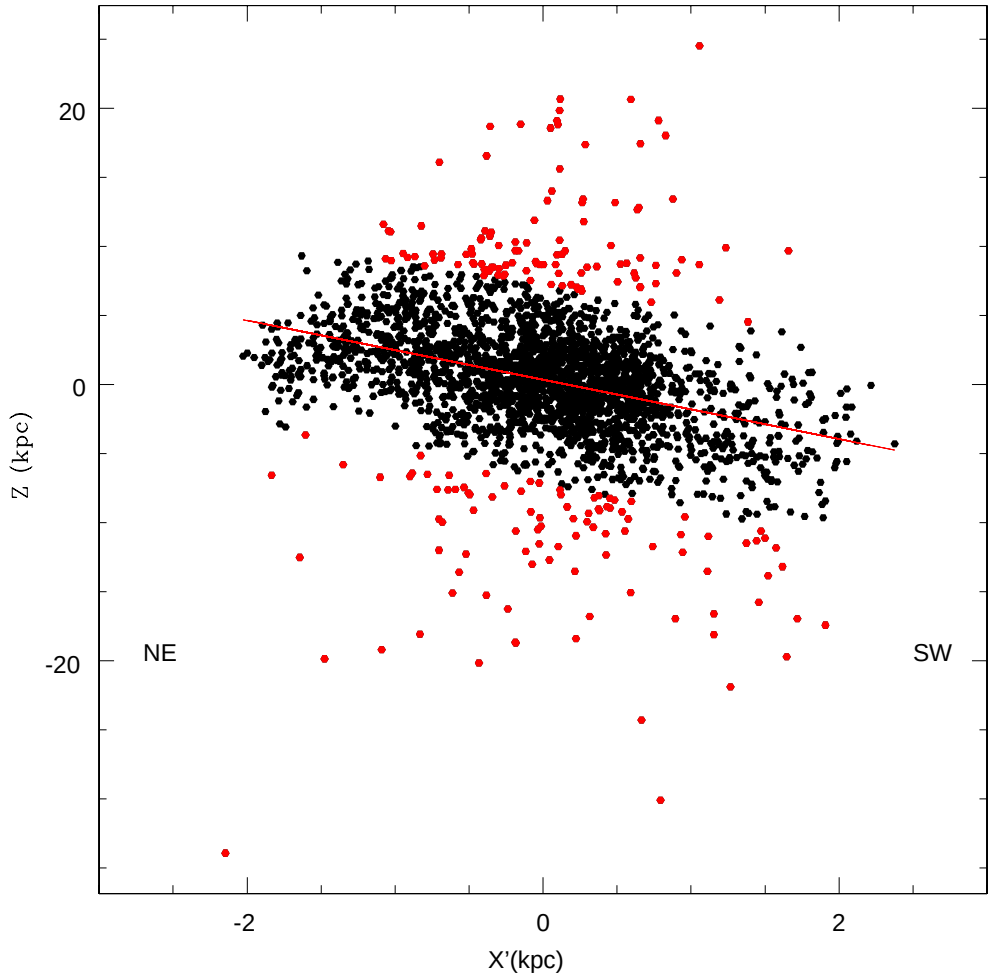

Figure 9.9: The relative distances (z) are plotted against the axis of maximum gradient. The red points are stars which show deviation larger than 3 times the error in z. The direction of inclination is shown as red line.

obtained a position angle ($\sim 126^o$) for the line of maximum velocity gradient, which is similar to the ϕ we obtained. van der Marel et al. (2009) suggested that the difference in the position angles of the line of maximum velocity gradient obtained from the H I (Stanimirović et al. 2004) and that from the young stars (Evans & Howarth 2008) may be an artifact of the different spatial coverage of the two studies (Evans & Howarth (2008) did not observe in the North-East region where the H I velocities are the largest), since it would be difficult to find a physical explanation for a significant difference in kinematics between H I gas and young stars. Our sample as well as the previous photometric data sets used for the estimation of the planar parameters of the SMC disk have less coverage

in the northeast. Thus a larger sample particularly with NE of the SMC is required to settle the above issue and estimate the planar parameters of the SMC accurately.

9.5 Conclusions

• We estimated the structural parameters of the SMC disk using the PL realtion of the 2603 fundamental mode Cepheids from the OGLE III catalog.

• The slope of the PL relation obtained for the shorter (P<2.5 days) period Cepheids is steeper than that obtained for the longer (P>2.5 days) period Cepheids. This suggests that the shorter and longer period Cepheids belong to two different populations.

• The planar parameters are estimated using the PL relations of shorter and longer period Cepheids separately. When the outliers are removed and the planar parameters are re-estimated, the values match within errors.

• For the combined sample, we find an inclination, $i = 61^{\circ}.35 \pm 0^{\circ}.5$ and $\phi = 132^{\circ}.5 \pm 10^{\circ}.5$.

• We find that about 207 stars in our sample are far away from the SMC main disk. Out of 207 stars, 97 are behind the disk and 110 are infront of the disk.

• The position angle, ϕ we estimated is almost orthogonal to that obtained for the HI disk of the SMC. A larger data set which covers the NE of the SMC is required for better estimates of the parameters of the stellar disk of the SMC.

CHAPTER 10

CONCLUSIONS

10.1 Summary

In this thesis study, the stellar populations in the MCs are used as a tool to understand the structure and evolution of these galaxies as well as to understand the evolution of the Magellanic system as a whole. The structure of the MCs are studied using stellar populations (standard candles) of different ages (Cepheids - 100 Myr, Red clump stars: 2-9 Gyr & RR Lyrae stars > 9 Gyr) and the quantitative estimates of the structural parameters are derived. From this study, the structural changes in the two galaxies as a function of time and the processes, such as interactions as well as mergers experienced by MCs at different epochs, which are responsible for these structural changes are identified.

The RC stars in the MCs are studied using the V and I pass band photometric data from the OGLE II, OGLE III and the MCPS catalogues. Along with the optical data the J and H pass band near infrared data from the IRSF MCPSC catalogue are also used for the analysis of RC stars in the LMC. The catalogue of RRLS identified in the MCs from the OGLE III survey are used in our study. The intermediate age RC stars and the old RRLS in both the galaxies are studied in detail. The catalogue of Cepheids, which represent the young stars, from the OGLE III survey are studied only in SMC. As the Cepheids in the LMC were stuided in great detail Nikolaev et al. (2004) using the photometric data in five bands (V,R,J,H and K bands) from the MACHO (combined with 2MASS), which covers a larger area of the LMC than that of OGLE III we did not analyze the OGLE III Cepheids of the LMC. The results from Nikolaev et al. (2004) are taken into account while deriving the conclusions on the structural evolution of the LMC.

The important results obtained from this thesis study are summarised below:

- **Large Magellanic Cloud**

  - **Disk**: The disk of the LMC is studied using the five band photometric data (V,I,J,H and K bands) of the RC stars. The line of sight depth of different regions in the disk is estimated only using the optical data.

    * The structural parameters of the disk, such as the inclination i and the position angle of the line of nodes, PA_{lon} are obtained. We found an i = 23°.0 ± 0°.8 and PA_{lon} = 163°.7 ± 1°.5 from the OGLE III data and an i = 37°.4 ± 2°.3 and PA_{lon} = 141°.2 ± 3°.7 from the MCPS data. From the IRSF MCPSC data we obtained an i = 26°.0 ± 0°.6 and PA_{lon} = 150°.9 ± 0°.5.
    * Extra planar features which are infront as well as behind the fitted plane are found. Regions in the north-west, south-west and south-east of the disk are warped with respect to the disk plane. We also identify a symmetric but off-centered warp in the inner LMC.
    * Reddening varies across the disk and it has to be accounted properly for the estimation of the structural parameters as well as for the detection of extra planar features.
    * The structure of the LMC disk inside the 3 degree radius is found to be different from the outside disk such that the inner disk has relatively less inclination and relatively large PA_{lon}. We found that the variation in the estimated planar parameters of the LMC disk is caused by the differences in coverage and the complicated inner structure of the disk.
    * A large line of sight depth is found for the LMC disk (3.44 ± 1.16 kpc and 2.88 ± 1.78 kpc from OGLE III and MCPS data sets respectively). The northern disk is found to have larger depth compared to other regions. These results suggest that the LMC has experienced heating, probably due to minor mergers.
    * The structural parameters and the extra planar features of the LMC disk obtained from the intermediate age RC are similar to that found from the study of Cepheids (which represent young stars) by Nikolaev et al. (2004) and HI gas.

- **Bar**: The V and I bands data of the RC stars in the bar region are studied to understand the location of the bar with respect to disk and to estimate the line of sight depth.
  - We found that the bar is coplanar with the disk, within ∼ 460 pc. Thus, this study confirms that the bar is very much a part of the intermediate age disk of the LMC and not another component located in front of the disk.
  - For the bar region, an average line of sight depth of 3.95 ± 1.42 kpc is estimated. The ends of the bar are found to be flared.
- **Halo**: The halo of the LMC has been an elusive component so far and one of the ideal proxy to study the halo are the RRLS. We studied the RRLS in the LMC to identify the halo of the LMC.
  - The distribution of RRLS in the inner LMC is found to have a major axis (= 125 ^{o} ± 17^{o}) and inclination (= 31^{o}.3 ± 3^{o}.5) similar to that of the disk. These suggest that the RRLS are not in spheroidal system, but on an equatorial plane, similar to that of the disk.
  - From the scale height estimates we found that 43% of stars in the sample follow disk like scale height. There is another fraction (47%) of RRLS which has puffed up distribution which probably traces the inner halo. Only a small fraction (10%) is likely to trace the extended halo of the LMC.
  - We suggest that a major star formation event happened at 10-12 Gyr ago in the LMC, probably with a gas rich merger to explain the disk-like distribution of the major fraction of the RRLS.

- **Small Magellanic Cloud**: The structure of the SMC is studied using the Cepheids, RC stars and RRLS. The SMC is found to be a two component system with the intermediate-age and old stellar populations distributed in a spheroidal or slightly ellipsoidal system and the young stars in a disk.
  - **Spheroidal component**: The properties of the RC stars and RRLS are studied and compared to understand the spheroidal component.
    - The line of sight depth estimated using the RC stars and the RRLS is found to be ∼ 14 kpc. The depth profiles of both the population are found

to be similar indicating that these two populations are located in the similar volume of the SMC.

* The surface density distribution and the radial density profile of the RC stars suggest that they are distributed in a nearly spheroidal system. The tidal radius estimated for the SMC system is ∼ 7-12 kpc. An elongation from NE -SW is also seen in the surface density map of the RC stars in the SMC.
* The data of RRLS and RC stars are restricted in XY plane due to finite coverage. But the data along the line of sight is fully sampled. Thus the observed SMC is approximated as a triaxial ellipsoid and the parameters of the ellipsoid are obtained. An axes ratio of 1:1.5:8.04 , inclination of the longest axis with the line of sight, $i = 0^o.5$ and the position angle of the projection of the ellipsoid on the plane of the sky, $\phi = 58^o.3$ are estimated from the analysis of RRLS. Similarly an axes ratio of 1:1.5:7.88 , $i = 0^o.6$ and $\phi = 55^o.5$ are estimated from the analysis of the RC stars assuming them to be also extended to a depth of 3.5-sigma.
* The study of data only within concentric spheres of radii 2, 2.5 and 3 degrees from the center, where the extent in all the three axes becomes equal, shows that the relative lengths of the z' and y' axes are comparable. Our tidal radius estimates and various observational studies of the outer regions suggest that the full extent of the SMC in the XY plane is similar to the front to the back distance estimated along the line of sight. These results suggest that the actual structure of the SMC is spheroidal or slightly ellipsoidal.
* We propose that the SMC experienced a merger with another dwarf galaxy at about 4−5 Gyr ago, and the merger process was completed in another 2-3 Gyr. This resulted in a spheroidal distribution comprising of stars older than 2 Gyr.

– **Disk**: Cepheids are used as the tracer to estimate the disk parameters.

* We found an inclination, $i = 61^\circ.35 \pm 0^\circ.5$ and $PA_{lon} = 132^\circ.5 \pm 10^\circ.5$ for the disk.
* The Cepheids with period, P < 2.5 days and with period, P> 2.5 days are found to be two different populations.

10.2 Conclusions

Based on the results obtained from the study of different stellar populations in the MCs summarised above, we come to the following conclusions on their formation and early evolution.

• The LMC experienced a major star formation event around 10-12 Gyr ago, probably due to a merger with a gas rich galaxy. This resulted in the formation of most of the RRLS and also the disk of the LMC. We did not find a prominent stellar halo for the LMC. The structural parameters of the disk obtained in our study from the RRLS and the RC stars, which represent the old and intermediate age disk parameters, match well with the parameters obtained from the young stars, Cepheids (Nikolaev et al. 2004). These results suggest that the disk of the LMC has not evolved much through its lifetime. The highly structured disk and warps in the disk suggest that the LMC has experienced heating due to minor mergers and interactions with the SMC & the Milky Way.

• The SMC is a dwarf galaxy without a prominent stellar halo. It experienced a major merger with another dwarf galaxy at about 4-5 Gyr ago. The merger process was completed in 2-3 Gyr and resulted in the spheroidal distribution of stars older than 2 Gyr and in the formation of extended gas disk along the line of sight. The stars younger than 2 Gyr were formed in this disk of the SMC which is highly inclined.

• The formation and early evolution of the LMC and the SMC are found to be different. The LMC and the SMC seems to have experienced major mergers individually at different epochs. Thus it is quite possible that the LMC and the SMC came closer after the major event experienced by the SMC. It is possible that the LMC and the SMC are formed and evolved separately and were interacting with each other only in the last 4 Gyr or less. The new tidal model of the Magellanic system by Diaz & Bekki (2011) suggests that the LMC and SMC have been separate entities when they formed and their binary state is a recent phenomenon occurred within the last $\sim$ 1.6 Gyr. This model is consistent with our result.

10.3 Future Work

The results obtained in our thesis study lead to certain specific studies of stellar populations in the MCs which will provide more information on the structure and evolution

of the MCs separately as well as on the evolution of the MS as a whole. These studies which can also substantiate our results are mentioned below.

- **Large Magellanic Cloud**
  - The extra-planar features, like the warps and structures identified in the disk of the LMC from the study of the RC stars may be interpreted as due to different stellar populations. Also the large line of sight depth estimated in the bar and the northern disk may also be considered due to different stellar populations. A detailed spectroscopic study of intermediate age stars in these regions will help to deconvolve the effect of metallicity from these features.
  - The RRLS in the inner LMC belong to three different components of the LMC, namely the disk, inner halo and the real halo. The three components can be separated spatially based on the scale height. The spectroscopic study of the RRLS in regions with different scale heights will provide the kinematic information of these components which is very important to trace the real stellar halo of the LMC.
- **Small Magellanic Cloud**
  - Regions near the optical center of the SMC are of great interest for further study, as they show large line of sight depth from the study of the RC stars as well as the RRLS. The density enhancement is also seen in these regions. The spectroscopic study of redgiants will provide both the kinematic and the metallicity information of stars in these regions.
  - The NIR study of the Cepheids in the SMC is important to understand the structure and line of sight depth.

Along with the specific studies mentioned above, the study of outer regions of the MCs are important to understand the signatures of interactions and the structure. The wider and larger ongoing/future photometric surveys (OGLE IV, VISTA and Outer limits survey of the LMC) which cover the outer regions of the MCs will help to provide the complete structure of the Magellanic system.

REFERENCES

Abbe, C. 1867, MNRAS, 27, 257

Alves, D. R. 2004a, New A Rev., 48, 659

—. 2004b, ApJ, 601, L151

Alves, D. R. & Nelson, C. A. 2000, ApJ, 542, 789

Barnes, D. G., Staveley-Smith, L., de Blok, W. J. G., Oosterloo, T., Stewart, I. M., Wright, A. E., Banks, G. D., Bhathal, R., Boyce, P. J., Calabretta, M. R., Disney, M. J., Drinkwater, M. J., Ekers, R. D., Freeman, K. C., Gibson, B. K., Green, A. J., Haynes, R. F., te Lintel Hekkert, P., Henning, P. A., Jerjen, H., Juraszek, S., Kesteven, M. J., Kilborn, V. A., Knezek, P. M., Koribalski, B., Kraan-Korteweg, R. C., Malin, D. F., Marquarding, M., Minchin, R. F., Mould, J. R., Price, R. M., Putman, M. E., Ryder, S. D., Sadler, E. M., Schröder, A., Stootman, F., Webster, R. L., Wilson, W. E., & Ye, T. 2001, MNRAS, 322, 486

Bauer, F., Afonso, C., Albert, J. N., Alard, C., Andersen, J., Ansari, R., Aubourg, É., Bareyre, P., Beaulieu, J. P., Bouquet, A., Char, S., Charlot, X., Couchot, F., Coutures, C., Derue, F., Ferlet, R., Gaucherel, C., Glicenstein, J. F., Goldman, B., Gould, A., Graff, D., Gros, M., Haissinski, J., Hamilton, J. C., Hardin, D., de Kat, J., Kim, A., Lasserre, T., Lesquoy, É., Loup, C., Magneville, C., Mansoux, B., Marquette, J. B., Maurice, É., Milsztajn, A., Moniez, M., Palanque-Delabrouille, N., Perdereau, O., Prévot, L., Renault, C., Regnault, N., Rich, J., Spiro, M., Vidal-Madjar, A., Vigroux, L., & Zylberajch, S. 1999, A&A, 348, 175

Bekki, K. & Chiba, M. 2008, ApJ, 679, L89

Besla, G., Kallivayalil, N., Hernquist, L., Robertson, B., Cox, T. J., van der Marel, R. P., & Alcock, C. 2007, ApJ, 668, 949

Besla, G., Kallivayalil, N., Hernquist, L., van der Marel, R. P., Cox, T. J., & Kereš, D. 2010, ApJ, 721, L97

Borissova, J., Rejkuba, M., Minniti, D., Catelan, M., & Ivanov, V. D. 2009, A&A, 502, 505

Braun, R. & Thilker, D. A. 2004, A&A, 417, 421

Brüns, C., Kerp, J., Staveley-Smith, L., Mebold, U., Putman, M. E., Haynes, R. F., Kalberla, P. M. W., Muller, E., & Filipovic, M. D. 2005, A&A, 432, 45

Buscombe, W. 1954, Leaflet of the Astronomical Society of the Pacific, 7, 9

Caldwell, J. A. R. & Coulson, I. M. 1985, MNRAS, 212, 879

—. 1986, MNRAS, 218, 223

Carrera, R., Gallart, C., Aparicio, A., & Hardy, E. 2011, AJ, 142, 61

Carrera, R., Gallart, C., Hardy, E., Aparicio, A., & Zinn, R. 2008, AJ, 135, 836

Chiosi, E. & Vallenari, A. 2007, A&A, 466, 165

Cioni, M.-R. L., Girardi, L., Marigo, P., & Habing, H. J. 2006a, A&A, 448, 77

—. 2006b, A&A, 452, 195

Cioni, M.-R. L., Habing, H. J., & Israel, F. P. 2000a, A&A, 358, L9

Cioni, M.-R. L., van der Marel, R. P., Loup, C., & Habing, H. J. 2000b, A&A, 359, 601

Clementini, G., Gratton, R., Bragaglia, A., Carretta, E., Di Fabrizio, L., & Maio, M. 2003, AJ, 125, 1309

Cole, A. A. 1998, ApJ, 500, L137+

Combes, F., Debbasch, F., Friedli, D., & Pfenniger, D. 1990, A&A, 233, 82

Crowl, H. H., Sarajedini, A., Piatti, A. E., Geisler, D., Bica, E., Clariá, J. J., & Santos, Jr., J. F. C. 2001, AJ, 122, 220

De Propris, R., Rich, R. M., Mallery, R. C., & Howard, C. D. 2010, ApJ, 714, L249

de Vaucouleurs, G. & Freeman, K. C. 1972, Vistas in Astronomy, 14, 163

Demers, S. & Battinelli, P. 1998, AJ, 115, 154

Diaz, J. & Bekki, K. 2011, MNRAS, 413, 2015

Dolphin, A. E. 2000, MNRAS, 313, 281

Dolphin, A. E., Walker, A. R., Hodge, P. W., Mateo, M., Olszewski, E. W., Schommer, R. A., & Suntzeff, N. B. 2001, ApJ, 562, 303

Dopita, M. A., Lawrence, C. J., Ford, H. C., & Webster, B. L. 1985, ApJ, 296, 390

Dottori, H., Bica, E., Claria, J. J., & Puerari, I. 1996, ApJ, 461, 742

Eddington, Sir, A. S. 1941, MNRAS, 101, 182

Evans, C. J. & Howarth, I. D. 2008, MNRAS, 386, 826

Feitzinger, J. V., Schmidt-Kaler, T., & Isserstedt, J. 1977, A&A, 57, 265

Freeman, K. C. 1999, in IAU Symposium, Vol. 192, The Stellar Content of Local Group Galaxies, ed. P. Whitelock & R. Cannon, 383–+

Freeman, K. C., Illingworth, G., & Oemler, Jr., A. 1983, ApJ, 272, 488

Gallart, C., Zoccali, M., & Aparicio, A. 2005, ARA&A, 43, 387

Gardiner, L. T. & Hawkins, M. R. S. 1991, MNRAS, 251, 174

Gardiner, L. T. & Noguchi, M. 1996, MNRAS, 278, 191

Gardiner, L. T., Turfus, C., & Putman, M. E. 1998, The Astrophysical Journal Letters, 507, L35

Girardi, L., Bressan, A., Bertelli, G., & Chiosi, C. 2000, A&AS, 141, 371

Girardi, L. & Salaris, M. 2001, MNRAS, 323, 109

Glatt, K., Grebel, E. K., Sabbi, E., Gallagher, III, J. S., Nota, A., Sirianni, M., Clementini, G., Tosi, M., Harbeck, D., Koch, A., Kayser, A., & Da Costa, G. 2008, AJ, 136, 1703

Graff, D. S., Gould, A. P., Suntzeff, N. B., Schommer, R. A., & Hardy, E. 2000, ApJ, 540, 211

Graham, J. A. 1975, PASP, 87, 641

Grieve, G. R. & Madore, B. F. 1986, ApJS, 62, 427

Grocholski, A. J., Cole, A. A., Sarajedini, A., Geisler, D., & Smith, V. V. 2006, AJ, 132, 1630

Groenewegen, M. A. T. 2000, A&A, 363, 901

Hardy, E., Suntzeff, N. B., & Azzopardi, M. 1989, ApJ, 344, 210

Harris, J. 2007, ApJ, 658, 345

Harris, J. & Zaritsky, D. 2004, AJ, 127, 1531

—. 2006, AJ, 131, 2514

Harris, J., Zaritsky, D., & Thompson, I. 1997, AJ, 114, 1933

Haschke, R., Grebel, E. K., & Duffau, S. 2011, AJ, 141, 158

Hatzidimitriou, D., Cannon, R. D., & Hawkins, M. R. S. 1993, MNRAS, 261, 873

Hatzidimitriou, D., Croke, B. F., Morgan, D. H., & Cannon, R. D. 1997, A&AS, 122, 507

Hatzidimitriou, D. & Hawkins, M. R. S. 1989, MNRAS, 241, 667

Herschel, Sir, J. F. W. 1847, Results of astronomical observations made during the years 1834, 5, 6, 7, 8, at the Cape of Good Hope; being the completion of a telescopic survey of the whole surface of the visible heavens, commenced in 1825, ed. Herschel, J. F. W., Sir

Hindman, J. V., McGee, R. X., Carter, A. W. L., Holmes, E. C. J., & Beard, M. 1963, Australian Journal of Physics, 16, 552

Holtzman, J. A., Gallagher, III, J. S., Cole, A. A., Mould, J. R., Grillmair, C. J., Ballester, G. E., Burrows, C. J., Clarke, J. T., Crisp, D., Evans, R. W., Griffiths, R. E., Hester, J. J., Hoessel, J. G., Scowen, P. A., Stapelfeldt, K. R., Trauger, J. T., & Watson, A. M. 1999, AJ, 118, 2262

Irwin, M. J., Kunkel, W. E., & Demers, S. 1985, Nature, 318, 160

Kallivayalil, N., van der Marel, R. P., & Alcock, C. 2006a, ApJ, 652, 1213

Kallivayalil, N., van der Marel, R. P., Alcock, C., Axelrod, T., Cook, K. H., Drake, A. J., & Geha, M. 2006b, ApJ, 638, 772

Kato, D., Nagashima, C., Nagayama, T., Kurita, M., Koerwer, J. F., Kawai, T., Yamamuro, T., Zenno, T., Nishiyama, S., Baba, D., Kadowaki, R., Haba, Y., Hatano, H., Shimizu, H., Nishimura, M., Nagata, T., Sato, S., Murai, Y., Kawazu, T., Nakajima, Y., Nakaya, H., Kandori, R., Kusakabe, N., Ishihara, A., Kaneyasu, N., Hashimoto, J., Tamura, M., Tanabé, T., Ita, Y., Matsunaga, N., Nakada, Y., Sugitani, K., Wakamatsu, K.-I., Glass, I. S., Feast, M. W., Menzies, J. W., Whitelock, P. A., Fourie, P., Stoffels, J., Evans, G. P., & Hasegawa, T. 2007, PASJ, 59, 615

Kim, S., Dopita, M. A., Staveley-Smith, L., & Bessell, M. 2000, in IAU Joint Discussion, Vol. 1, IAU Joint Discussion

Kim, S., Staveley-Smith, L., Dopita, M. A., Freeman, K. C., Sault, R. J., Kesteven, M. J., & McConnell, D. 1998, ApJ, 503, 674

King, I. 1962, AJ, 67, 471

Kinman, T. D., Stryker, L. L., Hesser, J. E., Graham, J. A., Walker, A. R., Hazen, M. L., & Nemec, J. M. 1991, PASP, 103, 1279

Koerwer, J. F. 2009, AJ, 138, 1

Kunkel, W. E. 1980, in IAU Symposium, Vol. 85, Star Clusters, ed. J. E. Hesser, 353–+

Kunkel, W. E., Irwin, M. J., & Demers, S. 1997, A&AS, 122, 463

Lah, P., Kiss, L. L., & Bedding, T. R. 2005, MNRAS, 359, L42

Leavitt, H. S. & Pickering, E. C. 1912, Harvard College Observatory Circular, 173, 1

Lequeux, J., Maurice, E., Prevot-Burnichon, M.-L., Prevot, L., & Rocca-Volmerange, B. 1982, A&A, 113, L15

Lotz, J. M., Jonsson, P., Cox, T. J., & Primack, J. R. 2008, MNRAS, 391, 1137

Luks, T. & Rohlfs, K. 1992, A&A, 263, 41

Maragoudaki, F., Kontizas, M., Morgan, D. H., Kontizas, E., Dapergolas, A., & Livanou, E. 2001, A&A, 379, 864

Martinez-Valpuesta, I., Shlosman, I., & Heller, C. 2006, ApJ, 637, 214

Massey, P., Lang, C. C., Degioia-Eastwood, K., & Garmany, C. D. 1995, ApJ, 438, 188

Mastropietro, C. 2010, in American Institute of Physics Conference Series, Vol. 1240, American Institute of Physics Conference Series, ed. V. P. Debattista & C. C. Popescu, 150–153

Mastropietro, C., Burkert, A., & Moore, B. 2009, MNRAS, 399, 2004

Mastropietro, C., Moore, B., Mayer, L., Wadsley, J., & Stadel, J. 2005, MNRAS, 363, 509

Mathewson, D. S., Cleary, M. N., & Murray, J. D. 1974, ApJ, 190, 291

Mathewson, D. S., Ford, V. L., & Visvanathan, N. 1986, ApJ, 301, 664

—. 1988, ApJ, 333, 617

Meatheringham, S. J., Dopita, M. A., Ford, H. C., & Webster, B. L. 1988, ApJ, 327, 651

Meurer, G. R., Bicknell, G. V., & Gingold, R. A. 1985, Proceedings of the Astronomical Society of Australia, 6, 195

Minniti, D., Borissova, J., Rejkuba, M., Alves, D. R., Cook, K. H., & Freeman, K. C. 2003, Science, 301, 1508

Misselt, K. A., Clayton, G. C., & Gordon, K. D. 1999, ApJ, 515, 128

Moore, B. & Davis, M. 1994, MNRAS, 270, 209

Murai, T. & Fujimoto, M. 1980, PASJ, 32, 581

Nagashima, C., Nagayama, T., Nakajima, Y., Tamura, M., Sugitani, K., Nagata, T., Hirao, T., Nakaya, H., Yanagisawa, K., & Sato, S. 1999, in Star Formation 1999, ed. T. Nakamoto, 397–398

Nagayama, T., Nagashima, C., Nakajima, Y., Nagata, T., Sato, S., Nakaya, H., Yamamuro, T., Sugitani, K., & Tamura, M. 2003, in Society of Photo-Optical Instrumentation Engineers (SPIE) Conference Series, Vol. 4841, Society of Photo-Optical Instrumentation Engineers (SPIE) Conference Series, ed. M. Iye & A. F. M. Moorwood, 459–464

Nandy, K. & Morgan, D. H. 1978, Nature, 276, 478

Nidever, D. L., Majewski, S. R., & Burton, W. B. 2008, ApJ, 679, 432

Nidever, D. L., Majewski, S. R., Butler Burton, W., & Nigra, L. 2010, ApJ, 723, 1618

Nidever, D. L., Majewski, S. R., Muñoz, R. R., Beaton, R. L., Patterson, R. J., & Kunkel, W. E. 2011, ApJ, 733, L10+

Nikolaev, S., Drake, A. J., Keller, S. C., Cook, K. H., Dalal, N., Griest, K., Welch, D. L., & Kanbur, S. M. 2004, ApJ, 601, 260

Noël, N. E. D., Aparicio, A., Gallart, C., Hidalgo, S. L., Costa, E., & Méndez, R. A. 2009, ApJ, 705, 1260

Noël, N. E. D., Gallart, C., Costa, E., & Méndez, R. A. 2007, AJ, 133, 2037

North, P. L., Gauderon, R., & Royer, F. 2009, in IAU Symposium, Vol. 256, IAU Symposium, ed. J. T. van Loon & J. M. Oliveira, 57–62

Olsen, K. A. G. & Salyk, C. 2002, AJ, 124, 2045

Pagel, B. E. J. & Tautvaisiene, G. 1998, MNRAS, 299, 535

Paz, D. J., Lambas, D. G., Padilla, N., & Merchán, M. 2006, MNRAS, 366, 1503

Pejcha, O. & Stanek, K. Z. 2009, ApJ, 704, 1730

Persson, S. E., Madore, B. F., Krzemiński, W., Freedman, W. L., Roth, M., & Murphy, D. C. 2004, AJ, 128, 2239

Pfenniger, D. & Friedli, D. 1991, A&A, 252, 75

Piatek, S., Pryor, C., & Olszewski, E. W. 2008, AJ, 135, 1024

Piatti, A. E., Geisler, D., Bica, E., Clariá, J. J., Santos, Jr., J. F. C., Sarajedini, A., & Dottori, H. 1999, AJ, 118, 2865

Putman, M. E., Gibson, B. K., Staveley-Smith, L., Banks, G., Barnes, D. G., Bhatal, R., Disney, M. J., Ekers, R. D., Freeman, K. C., Haynes, R. F., Henning, P., Jerjen, H., Kilborn, V., Koribalski, B., Knezek, P., Malin, D. F., Mould, J. R., Oosterloo, T., Price, R. M., Ryder, S. D., Sadler, E. M., Stewart, I., Stootman, F., Vaile, R. A., Webster, R. L., & Wright, A. E. 1998, Nature, 394, 752

Putman, M. E., Staveley-Smith, L., Freeman, K. C., Gibson, B. K., & Barnes, D. G. 2003, ApJ, 586, 170

Quinn, P. J. & Goodman, J. 1986, ApJ, 309, 472

Rieke, G. H. & Lebofsky, M. J. 1985, ApJ, 288, 618

Rohlfs, K., Kreitschmann, J., Feitzinger, J. V., & Siegman, B. C. 1984, A&A, 137, 343

Saha, A., Olszewski, E. W., Brondel, B., Olsen, K., Knezek, P., Harris, J., Smith, C., Subramaniam, A., Claver, J., Rest, A., Seitzer, P., Cook, K. H., Minniti, D., & Suntzeff, N. B. 2010, AJ, 140, 1719

Sandage, A. & Tammann, G. A. 1968, ApJ, 151, 531

Sandage, A., Tammann, G. A., & Reindl, B. 2009, A&A, 493, 471

Sarajedini, A. 1999, AJ, 118, 2321

Schlegel, D. J., Finkbeiner, D. P., & Davis, M. 1998, ApJ, 500, 525

Schommer, R. A., Suntzeff, N. B., Olszewski, E. W., & Harris, H. C. 1992, AJ, 103, 447

Shapley, H. 1956, Vistas in Astronomy, 2, 1564

Sharpee, B., Stark, M., Pritzl, B., Smith, H., Silbermann, N., Wilhelm, R., & Walker, A. 2002, AJ, 123, 3216

Smecker-Hane, T. A., Cole, A. A., Gallagher, III, J. S., & Stetson, P. B. 2002, ApJ, 566, 239

Smith, H. A., Silbermann, N. A., Baird, S. R., & Graham, J. A. 1992, AJ, 104, 1430

Sofue, Y. 1994, PASJ, 46, 431

Soszyński, I., Poleski, R., Udalski, A., Szymański, M. K., Kubiak, M., Pietrzyński, G., Wyrzykowski, Ł., Szewczyk, O., & Ulaczyk, K. 2010a, Acta Astron., 60, 17

Soszyński, I., Udalski, A., Szymański, M. K., Kubiak, J., Pietrzyński, G., Wyrzykowski, Ł., Ulaczyk, K., & Poleski, R. 2010b, Acta Astron., 60, 165

Soszynski, I., Poleski, R., Udalski, A., Szymanski, M. K., Kubiak, M., Pietrzynski, G., Wyrzykowski, L., Szewczyk, O., & Ulaczyk, K. 2008, Acta Astron., 58, 163

Soszynski, I., Udalski, A., Szymanski, M., Kubiak, M., Pietrzynski, G., Wozniak, P., Zebrun, K., Szewczyk, O., & Wyrzykowski, L. 2002, Acta Astron., 52, 369

Soszyński, I., Udalski, A., Szymański, M. K., Kubiak, M., Pietrzyński, G., Wyrzykowski, Ł., Szewczyk, O., Ulaczyk, K., & Poleski, R. 2009, Acta Astron., 59, 1

Stanek, K. Z., Zaritsky, D., & Harris, J. 1998, ApJ, 500, L141+

Stanimirovic, S., Staveley-Smith, L., Dickey, J. M., Sault, R. J., & Snowden, S. L. 1999, MNRAS, 302, 417

Stanimirović, S., Staveley-Smith, L., & Jones, P. A. 2004, ApJ, 604, 176

Staveley-Smith, L., Kim, S., Calabretta, M. R., Haynes, R. F., & Kesteven, M. J. 2003, MNRAS, 339, 87

Subramaniam, A. 2003, ApJ, 598, L19

—. 2004, ApJ, 604, L41

—. 2005, A&A, 430, 421

—. 2006, A&A, 449, 101

Subramaniam, A. & Anupama, G. C. 2002, A&A, 390, 449

Subramaniam, A. & Prabhu, T. P. 2005, ApJ, 625, L47

Suntzeff, N. B., Friel, E., Klemola, A., Kraft, R. P., & Graham, J. A. 1986, AJ, 91, 275

Tosi, M., Gallagher, J., Sabbi, E., Glatt, K., Grebel, E. K., Christian, C., Cignoni, M., Clementini, G., Cole, A., Da Costa, G., Harbeck, D., Marconi, M., Meixner, M., Nota, A., Sirianni, M., & Smecker-Hane, T. 2008, in IAU Symposium, Vol. 255, IAU Symposium, ed. L. K. Hunt, S. Madden, & R. Schneider, 381–386

Tsujimoto, T. & Bekki, K. 2009, ApJ, 700, L69

Udalski, A. 1998, Acta Astron., 48, 383

—. 2003, Acta Astron., 53, 291

Udalski, A., Kubiak, M., & Szymanski, M. 1997, Acta Astron., 47, 319

Udalski, A., Soszynski, I., Szymanski, M. K., Kubiak, M., Pietrzynski, G., Wyrzykowski, L., Szewczyk, O., Ulaczyk, K., & Poleski, R. 2008a, Acta Astron., 58, 89

Udalski, A., Soszyński, I., Szymański, M. K., Kubiak, M., Pietrzyński, G., Wyrzykowski, Ł., Szewczyk, O., Ulaczyk, K., & Poleski, R. 2008b, Acta Astron., 58, 329

Udalski, A., Szymanski, M., Kubiak, M., Pietrzynski, G., Soszynski, I., Wozniak, P., & Zebrun, K. 1999, Acta Astron., 49, 201

—. 2000, Acta Astron., 50, 307

Udalski, A., Szymanski, M., Kubiak, M., Pietrzynski, G., Wozniak, P., & Zebrun, K. 1998, Acta Astron., 48, 147

van den Bergh, S. 2004, AJ, 127, 897

van der Marel, R. P. 2006, in The Local Group as an Astrophysical Laboratory, ed. M. Livio & T. M. Brown, 47–71

van der Marel, R. P., Alves, D. R., Hardy, E., & Suntzeff, N. B. 2002, AJ, 124, 2639

van der Marel, R. P. & Cioni, M.-R. L. 2001, AJ, 122, 1807

van der Marel, R. P., Kallivayalil, N., & Besla, G. 2009, in IAU Symposium, Vol. 256, IAU Symposium, ed. J. T. van Loon & J. M. Oliveira, 81–92

Velazquez, H. & White, S. D. M. 1999, MNRAS, 304, 254

Wannier, P., Wrixon, G. T., & Wilson, R. W. 1972, A&A, 18, 224

Weinberg, M. D. 2000, ApJ, 532, 922

Welch, D. L., McLaren, R. A., Madore, B. F., & McAlary, C. W. 1987, ApJ, 321, 162

Westerlund, B. E. 1997, The Magellanic Clouds, ed. Cambridge Press

Yoshizawa, A. M. & Noguchi, M. 2003, MNRAS, 339, 1135

Zaritsky, D. 2004, ApJ, 614, L37

Zaritsky, D., Harris, J., Grebel, E. K., & Thompson, I. B. 2000, ApJ, 534, L53

Zaritsky, D., Harris, J., & Thompson, I. 1997, AJ, 114, 1002

Zaritsky, D., Harris, J., Thompson, I. B., & Grebel, E. K. 2004, AJ, 128, 1606

Zaritsky, D., Harris, J., Thompson, I. B., Grebel, E. K., & Massey, P. 2002, AJ, 123, 855

Zaritsky, D., Schectman, S. A., & Bredthauer, G. 1996, PASP, 108, 104

Zhao, H. & Evans, N. W. 2000, ApJ, 545, L35